Fire Imposed Heat Fluxes for Structural Analysis

Allan Jowsey

Doctor of Philosophy

The University of Edinburgh

2006

In memory of my mother, Margo Jowsey.

Declaration

This thesis and the research described and reported within has been completed solely by Allan Jowsey under the supervision of Professor Jose L. Torero, Dr. Asif S. Usmani and Dr. Barbara Lane. Where other sources are quoted, full references are given.

Allan Jowsey
September, 2006

Abstract

The last two decades have seen new insights, data and analytical methods to establish the behaviour of structures in fire. These methods have slowly migrated into practice and now form the basis for modern quantitative structural fire engineering. The events of the World Trade Center collapse have increased interest on the expected performance of large structures and other buildings under fire conditions but simultaneously question the adequacy of classic and modern methodologies.

Among the issues of debate is the treatment of the heat input provided by the fire to the structural elements. Current methods employed in the design of structures in fire treat the fire phenomenon as a simplified boundary condition. Levels of simplification vary depending on methodologies used but it is becoming increasingly recognised that capturing the correct thermal input to structural elements is a necessary requirement for an accurate evaluation of the mechanical response for the given fire.

A study of the underlying parameters implicit in heat transfer calculations for both convection and radiation provides the basis for an analysis of heat fluxes imposed on a structure during a series of large scale fires. These tests demonstrated the large spatial variations that exist in fully developed fires to further emphasise the need to define a fire at a greater resolution.

This study presents a novel methodology for determining the imposed heat fluxes on structural members. To properly characterise the temperature

rise of the structural elements, a post-processing model for computational fluid dynamics tools was developed to establish the heat fluxes imposed on all surfaces by a fire. This model acts as a tool for any computational fluid dynamics model and works on the basis of well resolved local gas conditions. Analysis of the smoke layer and products of combustion allow for heat fluxes to be defined based on smoke absorption coefficients and temperatures. These heat fluxes are defined at all points on the structure by considering full spatial and temporal distributions. Furthermore, heat fluxes are defined by considering directionality and both characteristic length and time scales in fires. Length scales are evaluated for different structural member geometries, while time scales are evaluated for different structural materials including applied fire protection. It is the output given by this model that provides the input for the thermal analysis of the structural members that is a necessary step prior to the structural analysis to be undertaken.

The model is validated against the experimental results of the previously mentioned large scale fire tests, showing good agreement. In addition, comparisons are made to current methods to highlight their potential inadequacies.

In terms of a structural engineering application, two scenarios are evaluated; a large scale fire in a multi-storey building and a complex geometrical structural member provide examples of defining a realistic thermal input within a structural fire engineering context.

Publications

Journal Papers

Jowsey A.I., Welch S., Torero J.L., Usmani A.S., Lane B., Lamont S., Structures in Fire and Example of the Boundary Condition, Submitted to Fire Safety Journal, in review.

Welch S., Jowsey A.I., Deeny S., Morgan R., Torero J.L., BRE Large Compartment Fire Tests – Characterising Post-Flashover Behaviour for Model Validation, Submitted to Fire Safety Journal, in review.

Lamont S., Lane B., Jowsey A.I., Torero J.L., Usmani A.S., Flint G.R., Innovative Structural Engineering for Tall Buildings in Fire, Structural Engineering International, **16**, 2, 142-147, 2006

Books

Jowsey A.I., Welch S., Torero J.L. Heat and Mass Transfer Effects to be Considered when Modelling the Effect of Fire on Structures Transport Phenomena in Fires. Sunden and Faghri Editors, WIT Press, 2007 (in press).

Conference Papers

Jowsey A.I., Rein G., Abecassis-Empis C., Cowlard A., Reszka P., Steinhaus T., Torero J.L., Usmani A.S., Lane B. An Analytical Approach to Define Surface Heat Fluxes to Structural Members in Post-Flashover

Fires. Submitted to the 5th International Seminar on Fire and Explosion Hazards, Edinburgh, UK, 2007.

Rein G., Abecassis-Empis C., Amundarain A., Biteau H., Cowlard A., Chan A., Jowsey A.I., Reszka P., Steinhaus T., Welch S., Torero J.L., Stern-Gottfried J., Coles A., Lazaro M., Alvear D., Capote J.A., Ryder N.L., Mowrer F., Hostika S., Lautenberger C., Joyeux D., Kumar S. Round-Robin Study of Fire Modelling Blind-Predictions Using the Dalmarnock Fire Experiments. Submitted to the 5th International Seminar on Fire and Explosion Hazards, Edinburgh, UK, 2007.

Jowsey A.I., Torero J.L., Usmani A.S., Lane B., Lamont S. Structural Fire Design of Tall Buildings in Fire Conference Proceedings, Cantabria, Spain, 2006.

Usmani A.S., Flint G.R., Jowsey A.I., Roben C., Torero J.L. Collapse Scenarios of WTC 1 & 2 With Extension to Generic Tall Buildings. Conference Proceedings, Cantabria, Spain, 2006.

Rini D., Jowsey A.I., Torero J.L., Lane B., Lamont S. Critical Behaviour of Long Span Cellular Beams in Fire, Proceedings of the 4th International Workshop - Structures in Fire, **1**, 259-272, Aveiro, Portugal, 10-12 May 2006.

Usmani A.S., Roben C.C., Johnston L., Flint G.R., Jowsey A.I. Tall Building Collapse Mechanisms Initiated by Fire, Proceedings of the 4th International Workshop - Structures in Fire, **1**, 527-538, Aveiro, Portugal, 10-12 May 2006.

Lamont S., Lane B., Jowsey A.I., Flint G.R., Torero J.L., Usmani A.S. Innovative Structural Engineering for Tall Buildings in Fire, JCSS and

IABSE Workshop on Robustness of Structures, BRE, Watford, UK, 28-29th November 2005.

Usmani A.S., Flint G.R., Jowsey A.I., Lamont S., Lane B., Torero J.L. Modelling of the Collapse of Large Multi-Storey Steel Framed Structures in Fire, The 4th International Conference on Advances in Steel Structures, **2**, 991-998, Shanghai, China, 13-15 June, 2005.

Jowsey A.I., Torero J.L., Usmani A.S., Lane B., Lamont S., Determination of Fire Induced Collapse Mechanisms of Multi-Storey Steel Framed Structures, 4th European Conference on Steel and Composite Structures, **C**, 5.1-69 - 5.1-76, Maastricht, The Netherlands, 8-10th June 2005.

Jowsey A.I., Torero J.L., Usmani A.S., Modelling of Structures in Fire: An Example of the Boundary Condition, Conference Proceedings, 297-313, Cantabria, Spain, 2004.

Lane B., Lamont S., Usmani A.S., Torero J.L., Flint G.R., Jowsey A.I., Robust Design of Tall Buildings in Fire - The Use of Analysis for Structural Fire Engineering Solutions, Interflam 2004, Edinburgh, July 2004.

Jowsey A.I., Drange L.A., Torero J.L., A Case Study on Building Specifications, 5th International Conference on Performance Based Codes and Fire Safety Design Methods in Fire Safety Engineering, Luxemburg, October 2004.

Jowsey A.I., Torero J.L., Determination of Fire Triggered Collapse Mechanisms of Multi-Story Steel Framed Structures: A Case Study, Fire Service College Annual Conference (RE04), Moreton-in-Marsh, UK, November 2004.

Awards

- **David B. Gratz Scholarship 2005**

  This award comprises a scholarship of $5,000 (USD) and is awarded to a graduate student enrolled in fire science or fire engineering programs at an institution outside of the United States. A committee appointed by the NFPA's Board of Directors selects the recipient based on their academic achievement, leadership qualities, concern for others, commitment to volunteerism, and pursuit of careers in fire safety.

- **Foundation Student Scholar Award 2006**

  This award was established in 2006 by the Board of Governors of the SFPE Educational and Scientific Foundation to recognise students that are performing research to advance the science and practice of Fire Protection Engineering.

Acknowledgements

First of all I'd like to thank my supervisor, Professor Jose Torero for his incredible guidance, expert advice, kindness and patience. I'd also like to thank Dr. Asif Usmani for his support and valuable insight.

I'd like to thank my industrial supervisor, Dr. Barbara Lane for her support and Dr. Susan Lamont for her kindness and patience.

Thank you to Dr. Stephen Welch and Dr. Guillermo Rein for their time, support and guidance for which I am very grateful. Thanks also to Dr. Graeme Flint, everybody in the Fire Group here at The University of Edinburgh and the staff at Arup Fire in London.

Thank you to all my friends and most of all my family for their support over the last three years.

This research was jointly funded by an EPSRC CASE Award through Arup Fire and is gratefully acknowledged.

Contents

List of Figures

List of Tables

Nomenclature

A	area (m^2)
Bi	Biot number
C_1	constant in Planck's spectral energy distribution ($W.\mu m^4 / m^2$)
C_2	constant in Planck's spectral energy distribution ($\mu m.K$)
c	specific heat (J/kg.K), speed of light (m/s)
c_p	specific heat at constant pressure (J/kg.K)
d_i	insulation thickness (m)
E	emission (W/m^2)
$\dot{E}_{in}$	rate of energy transfer into a control volume (W)
$\dot{E}_{out}$	rate of energy out of a control volume (W)
$\dot{E}_{st}$	rate of increase of energy stored within a control volume (W)
F	force (N); fraction of blackbody radiation in a wavelength band; view factor; burning factor
Fo	Fourier number
f_v	soot volume fraction
G	irradiation (W/m^2)
Gr	Grashof number
g	gravitational acceleration (m^2/s)
H	height (m); heated
h	heat transfer coefficient ($W/m^2.K$); Planck's constant
h_c	convective heat transfer coefficient ($W/m^2.K$)
h_r	radiative heat transfer coefficient ($W/m^2.K$)

I	incident radiation (W/m^2)
J	radiosity (W/m^2)
k	thermal conductivity (W/m.K); Boltzmann constant
k_0	soot concentration (absorption coefficient at λ_0) (m^{-1})
L	characteristic length (m)
m	mass (kg); complex index of refraction
$\dot{m}$	mass flow rate (kg/s)
Nu	Nusselt number
O	opening factor ($m^{0.5}$)
Pe	Peclet number
Pr	Prandtl number
P	pressure (N/m^2); partial pressure (atm)
Q	heat transfer rate (W)
q	rate of heat release (W/m^2)
$\dot{q}$	rate of energy generation per unit volume (W/m^3)
q''	heat flux (W/m^2)
r	radius (m)
Ra	Rayleigh number
Re	Reynold's number
T	temperature (^oC) and (K)
t	time (s)
u, v, w	fluid velocity components (m/s)
V	volume (m^3)
x, y, z	rectangular coordinates
X, Y, Z	components of the body force per unit volume (N/m^3)
x_c	critical location for transition to turbulence (m)
x	distance (m); thickness (m)

Greek letters

α	thermal diffusivity (m^2/s); absorptivity; fire growth coefficient (kW/s^2)
β	volumetric thermal expansion coefficient (K^{-1})
χ	burning efficiency factor
δ	hydrodynamic boundary layer thickness (m)
ε	emissivity
ϕ	azimuthal angle (rad)
η	air excess factor
$\varphi^{(3)}$	the Pentagamma function
κ	extinction coefficient (m^{-1})
λ	wavelength (m)
μ	viscosity (kg/s.m)
ν	kinematic viscosity (m^2/s); frequency of radiation (s^{-1})
π	pi
θ	zenith angle (rad); temperature difference (K)
ρ	mass density (kg/m^3); reflectivity
σ	Stefan-Boltzmann constant
τ	transmissivity
ω	solid angle (sr)
Δ	change in
Φ	viscous dissipation function (s^{-2})
Ω	scattering coefficient

Subscripts

a	ambient
abs	absorption
b	blackbody
C	combustion
ch	chemical
f	fire; flame; flow; film
g	gas
L	losses
m	member
net	net
p	pressure; perimeter
$plastic$	plastic
R	radiation
ref	reflectivity
s	surface
sur	surroundings
TC	thermocouple
tr	transmissivity
v	ventilation
w	windows; openings, walls
$wood$	wood
∞	distant gas conditions
0	initial conditions

Superscripts

$*$	dimensionless quantity

Overbar

$\bar{}$	surface average conditions; time mean

Chapter One

1. Introduction

1.1. Background to the Project

Fire-resistance calculations have often been conducted, both in the past and currently, on the basis of a representation of the fire by means of specified gas-phase temperature-time histories. Variations in heating arising from any feedback coupling due to the effect of the surface temperatures on the gas-phase processes are neglected, and therefore deemed to be of second-order importance. For example, the standard ISO-834 [1] or parametric [2] temperature-time curves can be adopted, with the actual heat transfer to the structure being defined according to the resulting convective and radiative fluxes. The energy equation of the structural element can be solved on this basis [3] and can be defined in two different forms, depending on the thermal response capacity of the boundary material,

$$\rho c_p V \frac{dT}{dt} = A\dot{q}_s'' \quad \text{(Thermally - thin material e.g. steel)} \tag{1.1}$$

$$\rho c_p \frac{\partial T}{\partial t} = k\frac{\partial^2 T}{\partial x^2} \quad \text{(Thermally - thick material e.g. concrete)} \tag{1.2}$$

where the boundary condition for both cases corresponds to the input from the fire and is given by,

$$\dot{q}_s'' = h\left(T_g - T_s\right) + \varepsilon_g \sigma T_g^4 - \varepsilon_s \sigma T_s^4 \quad \text{(Thermally - thin)} \tag{1.3}$$

$$\dot{q}_s'' = h\left(T_g - T_s\right) + \varepsilon_g \sigma T_g^4 - \varepsilon_s \sigma T_s^4 = -k\left.\frac{\partial T}{\partial x}\right|_{x=0} \quad \text{(Thermally - thick)} \tag{1.4}$$

where T_g is the imposed temperature of the gas as defined by the temperature-time curve. The emissivity of the solid surface is given by ε_s

and that of the gas by ε_g. For simplicity direct heat exchanges with the environment outside of the compartment, where these components constitute enclosure boundaries, have been ignored here, but could also be included in these expressions. For the thermally-thin elements A will be the exposed area. The unexposed area can be ignored or treated as a loss to some ambient temperature. For thermally-thick materials the boundary condition at the unexposed face will be fixed based on the conditions established for this side of the element. If a fire is present at the other side then a similar boundary condition will be included here; if no fire is imposed, a heat loss to an ambient temperature can be assumed.

The essence of the thermal response problem is now to determine the surface temperature evolution of the structure. In the case of thermally-thick materials, which are the main interest in structural fire engineering, this is a non-trivial problem due to the highly non-linear nature of the applied boundary condition as represented by equation (1.4). In general, this can only be solved by adopting numerical heat transfer procedures, preferably adopting implicit algorithms, which solve the coupled equation set to obtain the evolution of the thermal conditions at the surface, and hence within the solid.

Depending on the application and the accuracy required there are also two other approaches which bypass the above complexity. Firstly, the thermal boundary condition may be imposed by equating the surface temperature of the structural element to the local gas temperature, so that it does not need to be calculated. This approach is highly attractive due to its simplicity in that it reduces the thermal modelling problem to a simple conduction analysis, but it will in many cases significantly overestimate the temperature of the structure, hence providing an overly conservative result. Secondly, in the context of validation using test data, it may be possible to use the measured surface temperatures. This procedure was

adopted by many modellers, including Usmani & Lamont [4] and Moss & Clifton [5] when modelling the Cardington frame tests. Obviously, appropriately positioned monitoring equipment was able to be used in these cases and in real fire situations this type of data is not generally available. For design methods, there is generally no alternative to undertaking a detailed thermal analysis, especially if the members are protected.

1.2. Aims of the Research

This project undertakes the task of resolving the thermal boundary condition between the gas-phase environment of a fire and the solid-phase that represents structural members using a novel methodology to determine the imposed heat fluxes.

Figure 1.1 shows the results of illustrative CFD simulations, using FDS, in which an identical fire is embedded in compartments with three different aspect ratios, for 'post-flashover' conditions. It can be observed that temperature variations greater than 600°C exist throughout the compartment in each case. Furthermore, an analysis of the predicted soot volume fraction also shows well-defined distributions. These observations highlight that the basic premise of a single compartment temperature might be over simplified, even beyond the growth phase of a fire. The consequence of this is the need to compute the local temperatures and to solve the radiative transport equation to establish true boundary fluxes. This can only be done using appropriate compartment fire models or through experimental characterisation of the radiative fluxes to the different surfaces.

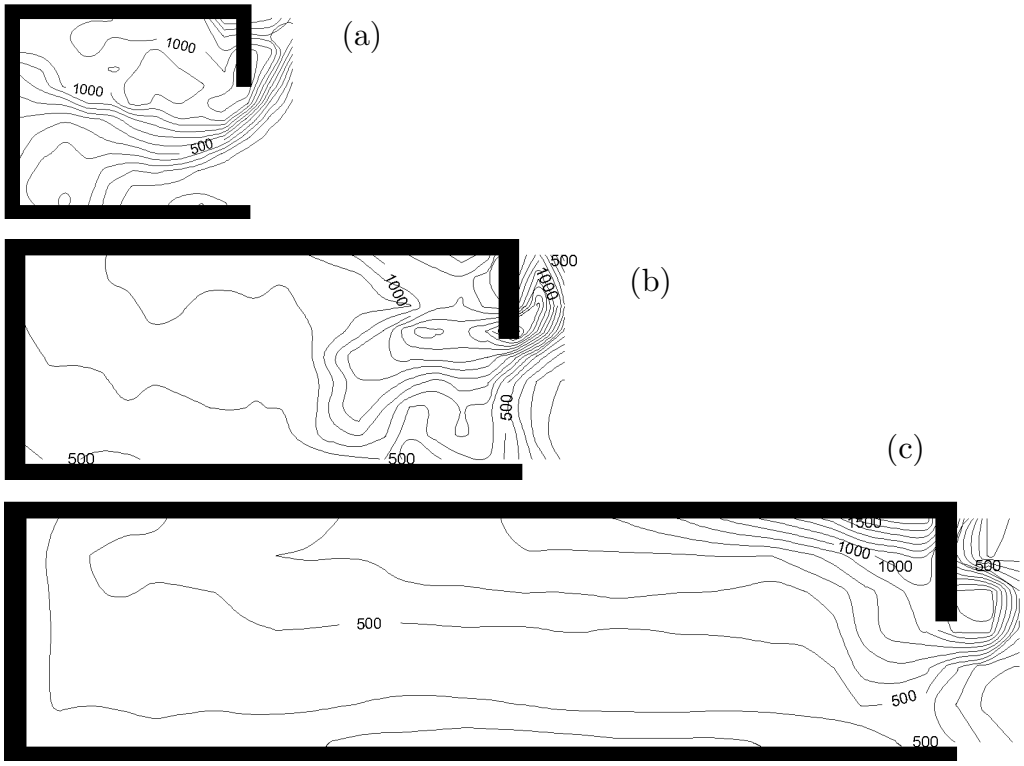

Figure 1.1: Temperature contours for three similar FDS calculations for a compartment with different lengths (a) 4m, (b) 8m, (c) 16m. Contour lines are in °C.

The project examines the underlying parameters commonly employed in heat transfer calculations for both convection and radiation to understand at a greater level the effect that they can have on structural fire engineering applications.

In order to be able to properly characterise the temperature rise of structural elements, a post-processing model for computational fluid dynamics tools allows the establishment of heat fluxes imposed on all surfaces by a fire. The premise of this model requires well resolved local gas conditions. Analysis of the smoke layer and products of combustion allow for heat fluxes to be defined based on smoke absorption coefficients and temperatures. These heat fluxes are defined at all points on the

structure by considering full spatial and temporal distributions. It is the output given by the model that provides the input for the thermal analysis of the structural members.

1.2.1. Outline of Chapters

Chapter 2

Overview of Heat Transfer to Structural Elements

An overview is provided of current practices in evaluating compartment fires from definition of the fire through to heat transfer methods. The basic concepts behind the compartment fire are introduced before techniques to develop temperature-time curves are discussed. Heat transfer methodologies are reviewed including simple models through to complex numerical methods. Compartment fire models are reviewed with emphasis given to their ability to model the post-flashover behaviour of a fire.

Chapter 3

Convective Heat Transfer

An introduction is given for the definition of convective heat transfer to structural elements. Background theory is presented and then an investigation in the form of a parametric study of all the underlying parameters to define their influence is undertaken. Both free and forced convection are considered and different correlations for a variety of structural elements are evaluated. All parameters are investigated in terms of the heat transfer coefficient.

Chapter 4

Radiative Heat Transfer

The concept of radiative heat transfer to structural elements is introduced. Background theory is given and this provides the basis to undertake a study of all the underlying parameters to determine their influences in context of structural fire engineering.

Chapter 5

Analysis of the Cardington Large Scale Fire Tests

Experimental data of the Cardington large scale fire tests undertaken at BRE in 1999 provides the basis for an analysis of heat fluxes on the internal compartment walls. Due to the limited number of heat flux measurements in the test, a methodology is developed to define radiative intensity maps within the compartment based on corrected thermocouple gas temperatures taken throughout the volume. These are in turn correlated with heat flux measurements to validate their appropriateness. Heat flux maps can reveal interesting phenomena during post-flashover conditions that would not normally be noticed given a temperatures map.

Chapter 6

Characteristic Heating Times of Solids

The response of thermally thick and thermally thin structural elements is analysed based on conduction theory. By analysing a material's thermal properties it is possible to define a characteristic heating time that allows data such as heat fluxes to be averaged, allowing for speed of computation when interpreting CFD results.

Chapter 7

Heat Flux Model Development

The methodology behind the development of the heat flux post-processing model is explained. A brief introduction to the model is given, followed by

how to extract the necessary data from CFD programs such as FDS. Definition of control volumes and the calculation of convective and radiative fluxes are given based on the studies of Chapters 3 and 4, while characteristic heating times are used from the definitions developed in Chapter 6.

Chapter 8

Model Validation

To demonstrate the accuracy and validity of the model, the Cardington large scale fire tests form the basis for a comparison. One test is recreated in FDS and the heat flux model is applied to get structural surface heat fluxes. These are then compared to the measured test fluxes, the FDS fluxes and the fluxes that could be expected using the Eurocode methods.

Chapter 9

Structural Analysis Applications

The application of the heat flux model is presented in the context of a full structural analysis. The main application is that of a large multi-storey building in which surface heat fluxes are used as the boundary condition to calculate the solid-phase temperatures for input into a finite element model. Another application is that of structural members with complex geometry including cellular beams and truss systems. A comparison is given of the structural behaviour when the full spatial and temporal resolution over the member is defined to the response when the Eurocode heating methodology is adopted.

Chapter 10

Conclusions and Further Work

A summary of the work undertaken and outcomes of the study is presented. Ideas for future research needs and focus is given.

Chapter Two

2. Overview of Heat Transfer to Structural Elements

2.1. Introduction

This chapter introduces and discusses the methods available to resolve the thermal boundary condition for a structural analysis from the definition of thermal environment to the heat transfer methods available.

2.2. The Compartment Fire

The evolution of a compartment fire can be divided into three periods [3];

1. growth or pre-flashover stage in which the average compartment temperature is relatively low and the fire is localised in the vicinity of its origin;
2. the fully developed or post-flashover fire, during which all combustible items in the compartment are involved and flames appear to fill the volume;
3. the decay period, often identified as the stage of the fire after the average temperature has fallen to 80% of its peak value.

Figure 2.1 illustrates these three periods in the context of a heat release rate (power) of the fire. The transition to stage 2 occurs when the interaction between the fire and the compartment boundaries becomes significant. This transition is known as 'flashover' and it involves a rapid spread of the fire from the area of localised burning to all combustible surfaces within the room. A structural analysis in compartment fires focuses on the heat transferred from the fire environment into the structural element, thus two main variables are of concern; temperatures and the duration of the fire. The fully developed fire poses the greatest threat to structural elements as this is when temperatures are at their highest. In structural fire analyses, the decay period is often neglected due to the relatively low temperatures and moderate influence on structural

behaviour. However, the decay period can also present a substantial risk to structural members in terms of associated contraction stresses and strains as cooling develops.

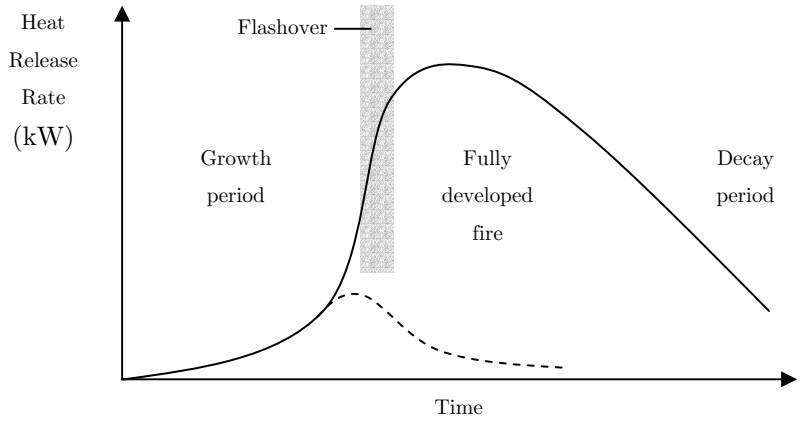

Figure 2.1: Development of a well-ventilated compartment fire where the broken line represents either depletion of the fuel prior to flashover or an extinguished fire [3]

The following sections consider the pre- and post-flashover stages of a fire. The majority of the focus is given to the latter as this is when structural members are subject to the critical extremes of the fire.

2.2.1. Pre-flashover

Following the ignition of the fire within a compartment, one of three events may take place;

1. the fire may burn itself out (not enough fuel) without involving any other items, such as the broken line in Figure 2.1;
2. if there is inadequate ventilation, the fire may self-extinguish or continue to burn at a very slow rate, dictated by the low availability of oxygen;

3. given sufficient fuel and ventilation, the fire may progress to a fully developed state (provided that fire-fighters do not intervene).

If order for the latter (event 3) to occur, flashover needs to take place. The mechanisms leading to flashover has been studied extensively by Waterman [3;6] with the research concluding that a heat flux of about 20kW/m^2 at floor level is required. Additional indicators of flashover include an average compartment temperature of 500-600^{o}C and exterior flaming. The value of heat flux proposed by Waterman is of the same order of magnitude that is taken as the critical heat flux for piloted ignition of most fuels. This is especially the case for 'thermally thin' items such as paper, however for 'thermally thick' items such as wood and other thick combustible solids, a far higher value would be needed. Waterman noted that most of the heat was radiated from upper levels within the compartment to the lower levels. Most of the radiative flux originates from; hot surfaces in the upper part of the enclosure, flames under the ceiling and hot combustion products trapped under the ceiling. The relative importance of each of these however, depends on nature of the fuel and the degree of ventilation.

The Fire Commission (W14) of the Conseil Internationale du Batiment (CIB) undertook a study of the variables affecting fire growth during the 1960s involving nine laboratories around the world [7]. Tests were carried out using small-scale compartments with wood cribs as the fuel load. The results of the study showed that a high fuel bed allows flames to reach the ceilings much more rapidly and thus promotes the spread of fire over the combustible surfaces at an earlier stage. Other conclusions related to the bulk density of fuel; cribs with a low bulk density increase the spread of fire, while combustible lining materials also reduce the time to flashover. The role of the compartment linings was found to have a large influence on the rate of development of the fire. Further work by Thomas and Bullen

[8] suggested that the time to flashover was directly proportional to the square root of the thermal inertia ($k\rho c$) of the compartment bounding material.

The study of fire growth has led to its representation in terms of a parabolic growth rate (commonly referred to as a *t*-squared fire) [9] after an initial incubation period, given,

$$\dot{Q} = \alpha_f (t - t_0)^2 \tag{2.1}$$

where α_f is the fire-growth coefficient (kW/s^2) and t_0 is the length of the incubation period (s). Typical values for α_f are presented in Table 2.1 while Figure 2.2 represents the fires schematically.

Description	Typical Scenario	α_f (kW/s^2)
Slow	Densely packed paper products	0.00293
Medium	Mattress / Armchair	0.01172
Fast	Pallets stacked 1m high	0.04690
Ultrafast	High rack storage	0.18760

Table 2.1: Parameters used for *t*-squared fires [8]

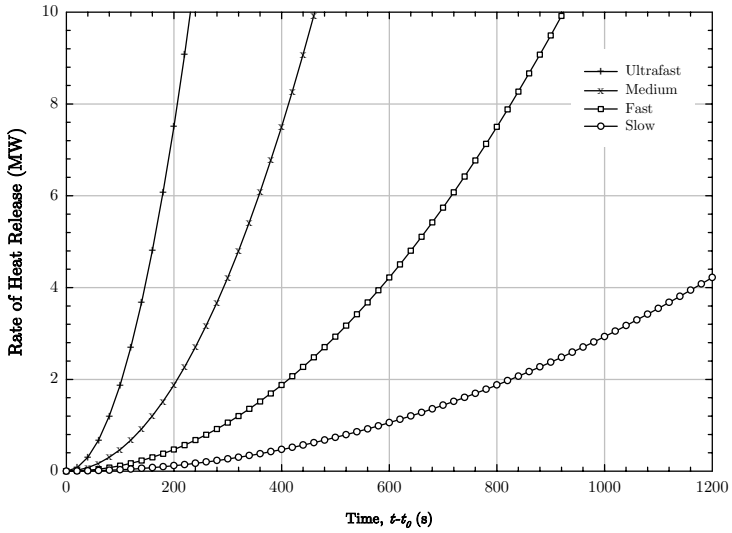

Figure 2.2: Parabolic fire growth for the different *t*-squared coefficients presented in Table 2.1

2.2.2. Post-flashover

Following flashover, most exposed surfaces of combustible items are assumed to be burning and the rate of heat release develops to a maximum producing high temperatures.

Kawagoe [10] considered the rate of burning of wood cribs contained within compartments with different sizes of ventilation opening. This research found that the mass burning rate ($\dot{m}$) was found to depend on the size and shape of the wall ventilation opening, giving the following relationship,

$$\dot{m} = 0.09 A_w H^{1/2} \quad \text{(kg/s)} \tag{2.2}$$

where A_w is the area (m^2) and H is the height (m) of the opening. When the rate of burning is controlled by the rate at which air can flow into the compartment, a fire is said to be 'ventilation controlled'. In contrast, when

a ventilation opening is enlarged, a condition will be reached beyond which the rate of burning becomes independent of the size of the opening and is determined instead by the surface area and burning characteristics of the fuel. Such a condition is referred to as a 'fuel controlled' fire. The work of Kawagoe led to the semi-empirically deduced ventilation factor $A_w H^{1/2}$ as expressed in equation (2.2).

It is important to be able to distinguish between ventilation and fuel controlled fires as a fuel controlled fire is generally less severe except in comparison with fires in which the ventilation is very poor. The CIB tests [7] highlight the difference in two regimes. Figure 2.3 by Thomas and Heselden [11] shows a plot of average gas temperature inside the compartment for a number of fully developed fires as a function of the ventilation. They include in their analysis an opening factor in which A_T is the total area of the walls and ceiling of the compartment, excluding the ventilation area. When the opening factor is less than 8-10$m^{-1/2}$ then the fire is fuel controlled. In this situation, excess air that enters the compartment has the effect of moderating the gas temperature. The cross-over to a ventilation controlled regime depends on the relationship between the mass burning rate ($\dot{m}$) and the rate of inflow of air. The scatter in Figure 2.3 is attributed by Law and O'Brien [12] to be the result of some particularly extreme experimental conditions.

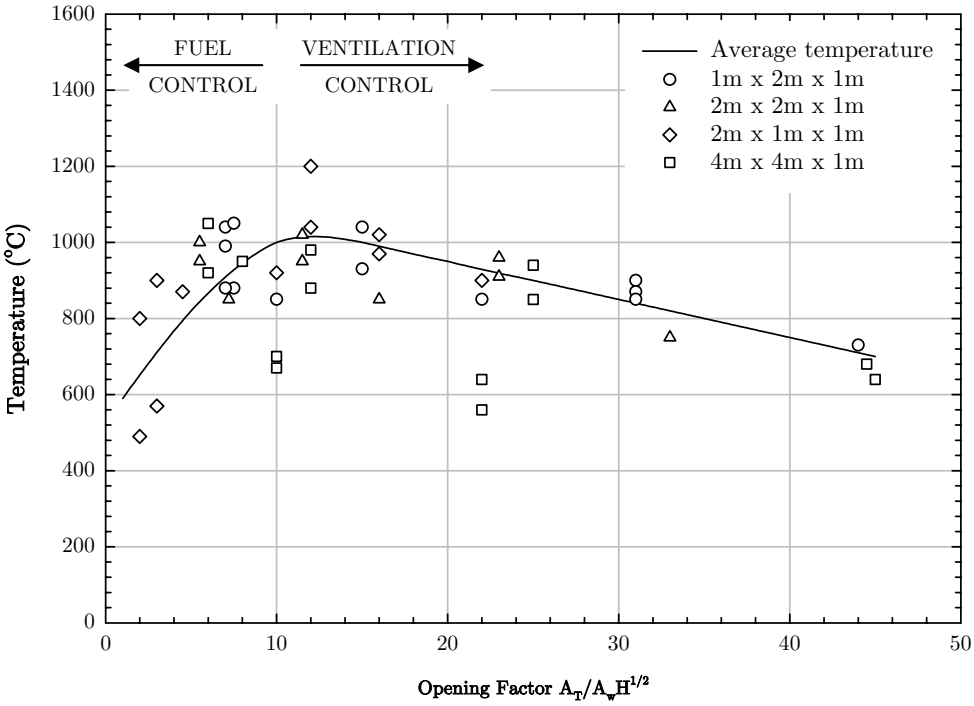

Figure 2.3: Average compartment temperatures during the steady burning of wood crib fires as a function of the opening factor; symbols in the key refer to compartment dimensions in meters (width x depth x height) [11].

In order to be able to predict gas temperatures achieved within compartment fires for use in structural engineering design calculations, it is important to understand the mechanisms at work in a fully developed scenario. Figure 2.4 shows the heat gains and losses within a compartment which allows the following heat balance to be written,

$$\dot{q}_C = \dot{q}_L + \dot{q}_W + \dot{q}_R \tag{2.3}$$

where

$\dot{q}_C$ = rate of heat release due to combustion

$\dot{q}_L$ = rate of heat loss from replacement of hot gases by cold gases

$\dot{q}_W$ = rate of heat loss through boundaries

$\dot{q}_R$ = rate of heat loss by radiation through openings

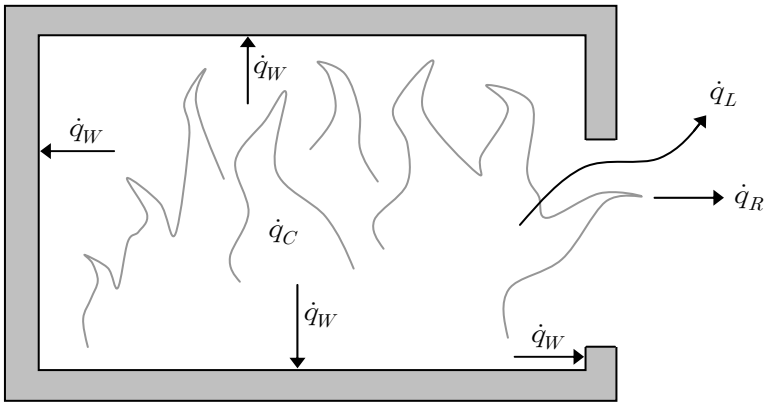

Figure 2.4: Heat losses during a fully developed fire [2]

The rate of heat due to combustion $\dot{q}_C$ can be evaluated by multiplying equation (2.2) by the heat of combustion for the fuel ΔH_c [2], giving,

$$\dot{q}_C = 0.09 A_w H^{1/2} \cdot \Delta H_c \tag{2.4}$$

It is assumed that $\dot{q}_C$ remains constant throughout the duration of the fully developed fire and that it is ventilation controlled. Equation (2.4) describes the global behaviour within the compartment and is based on the experimental observations during flashover, that there is generally an excess of pyrolyzate (combustible gases from solid fuels).

Heat loss by radiation through the openings is given by,

$$\dot{q}_R = A_w \varepsilon_F \sigma T_g^4 \tag{2.5}$$

in which T_g is the gas temperature within the compartment (K), σ is the Stefan-Boltzmann constant and ε_F is the emissivity of the gases within the compartment. This can be calculated from,

$$\varepsilon_F = 1 - \exp(-\kappa x_F) \tag{2.6}$$

where x_F (m) is the flame thickness (generally taken as the depth of the room) and κ (m^{-1}) is the extinction coefficient. By assuming a single value for the extinction coefficient, the method implies that the radiation field is in thermal equilibrium with the gas phase, in that there is no radiative exchange between soot particles and the gas. The adoption of a single flame thickness also implies that the optical depth within the gas is much smaller than the characteristic length of the compartment to therefore allow heat radiation to be treated as a local phenomenon. Chapter 4 considers radiative heat transfer to a far greater detail and examines the influence of the underlying parameters in the context of structural elements.

The heat loss due to convective flow can be determined from,

$$\dot{q}_L = \dot{m}_F c_p (T_g - T_0) \tag{2.7}$$

in which $\dot{m}_F$ is the outflow of the fire gases. A detailed review of the heat transfer boundary conditions for convective flows is given Chapter 3.

Heat loss through the compartment boundaries depends on the gas temperature within the compartment T_g and on the internal surface temperature T_i and the thermal properties of the bounding materials. In order to evaluate this process, conductive heat transfer into the boundary

must be solved numerically. Heat transfer texts [3] provide methods on how to undertake this. Conductive heat transfer with relation to structural elements is discussed in Chapter 6.

Having defined all the terms of the heat balance, it is possible to solve for the gas temperature within the compartment. The following section discusses methods available to define compartment gas-phase temperatures. The limitations of the above method include, in addition to those discussed above, the assumptions; that combustion is complete and occurs entirely within the confines of the compartment, that the temperature is uniform within the compartment at all times, that a single surface heat transfer coefficient may be used for the entire inner surface of the compartment and that heat flow to and through compartment boundaries is one-dimensional, in that the effects of heat transfer at corners and edges are neglected.

2.3. Temperature-Time Relationships

Current structural fire engineering analyses work on the basis of a design fire in the form of a characteristic temperature-time curve that is expected not to be exceeded during the lifetime of the structure. Pettersson [2] and Magnusson & Thelandersson [13] developed a set of temperature-time curves, for which a typical set is presented in Figure 2.5. These curves were derived from the above equations for a 'standard compartment' constructed from materials of 'average thermal properties'. Each curve corresponds to different 'fire load' expressed in terms of a net heat of combustion. An empirical correction factor can be applied to take account of lightweight insulating materials. The model assumes ventilation controlled burning throughout the fully developed stage and as a consequence will overestimate the burning rate of a fire for which fuel controlled conditions actually exist. The result of this is likely to be an

over-estimate of the 'severity' of the fire with respect to its potential for damaging structural elements.

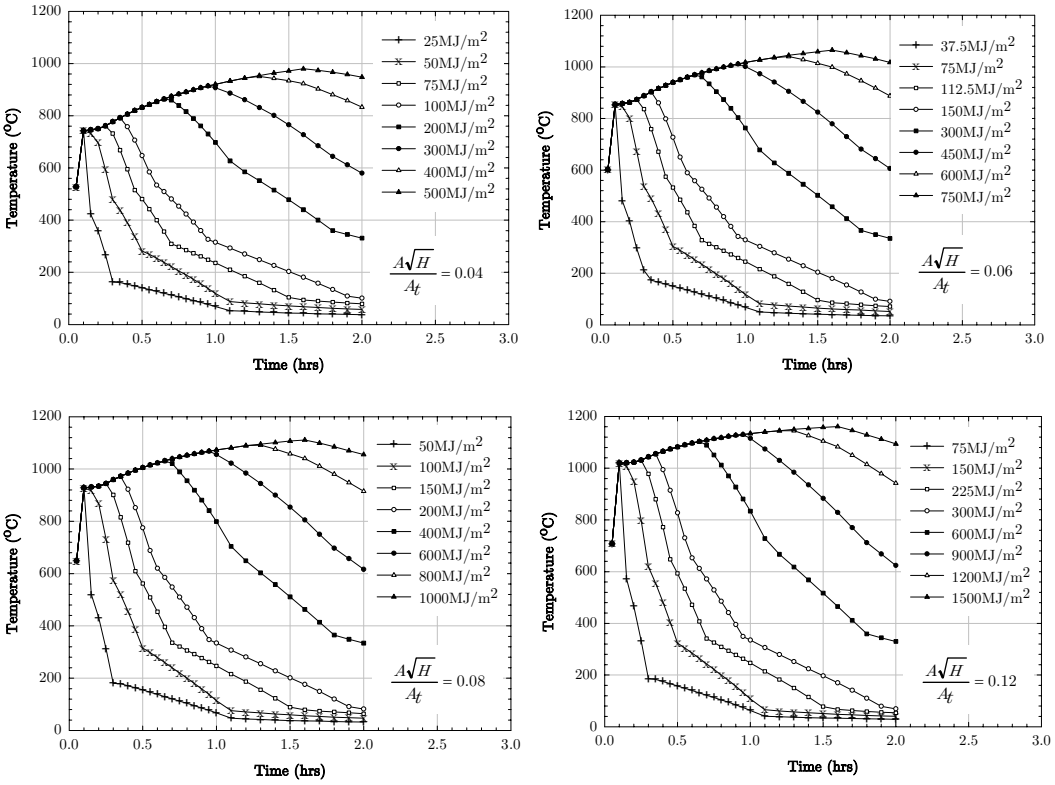

Figure 2.5: Theoretical temperature-time curves for compartment fires with different floor fire load densities and opening factors [2]; wall thickness 0.2m, $k = 0.8\text{W/m.K}$ and $\rho c = 1700\text{W/m}^3\text{.K}$.

Similar approaches to define temperature-time curves have been developed by Kawagoe and Sekine [14] and Lie [15] incorporating both ventilation factors and fuel burning rates, while Babrauskas and Williamson [16] developed a model that considers fuel nature and distribution together with allowing definition of ventilation controlled and fuel controlled scenarios.

Law [17] derived a method to predict fully developed compartment fire temperatures from the tests undertaken under the auspices of CIB. The

method takes into account the compartment geometry by considering the total internal compartment surface area and the fuel loading expressed in terms of an equivalent wood load.

Ma and Makelainen [18] created a parametric temperature-time curve for compartments with floor area of less than $100m^2$. The parametric curve is based on a general shape function that defines the evolution of a compartment fire by taking into consideration fuel loading, ventilation conditions, geometry of the compartment and the properties of the wall linings. In a comparison [19], the method was found to under predict much of the CIB data although the CIB report only average temperature.

The concept of a shape constant is developed further by Barnett [20;21] to define a temperature-time curve that requires only one equation to describe both growth and decay periods of a fire. The curve appears to fit the CIB data and other tests [22] extremely well; however the recent emergence of this new method suggests that a comprehensive study of its effectiveness is required before it is considered for design purposes.

2.3.1. Nominal temperature-time curves

In the context of structural engineering, the term 'fire-resistance' is associated with the ability of an structural element to perform its function during the course of a fire. This ability is tested by considering a large scale sample subjected to a 'standard fire' defined by the temperature-time variation of hot gases within a furnace. The standard fire is also commonly used as a design fire to define possible compartment fires within buildings, and as such, nominal temperature-time curves exist to describe the fire evolution.

For the case of a fully developed fire, the Eurocodes describe the action of the fire in terms of temperature-time curves. Three nominal curves are given in Eurocode 1 [1] with additional guidance provided by Franssen & Zaharia [23]. The most common method for representing a post-flashover compartment fire is that of the standard curve, also referred to as the standard ISO-834 curve, given by,

$$T_g = 20 + 345\log_{10}(8t + 1) \tag{2.8}$$

where t is the time in minutes. For the case of external walls that may be exposed to fire plumes, the external fire curve may be used,

$$T_g = 20 + 660(1 - 0.686e^{-0.32t} - 0.313e^{-3.8t}) \tag{2.9}$$

If a more severe fire is anticipated in which the fuel is predominantly hydrocarbon, the Eurocodes provide the hydrocarbon curve, given by,

$$T_g = 20 + 1080(1 - 0.325e^{-0.167t} - 0.675e^{-2.5t}) \tag{2.10}$$

For comparison, the three nominal temperature-time curves are shown in Figure 2.6. Both the external and hydrocarbon are seen to quickly reach a plateau temperature, while the standard fire continues to increase in temperature, although this rate of increase slows with time. For a two hour period, none of the curves reach a gas temperature in excess of 1100°C.

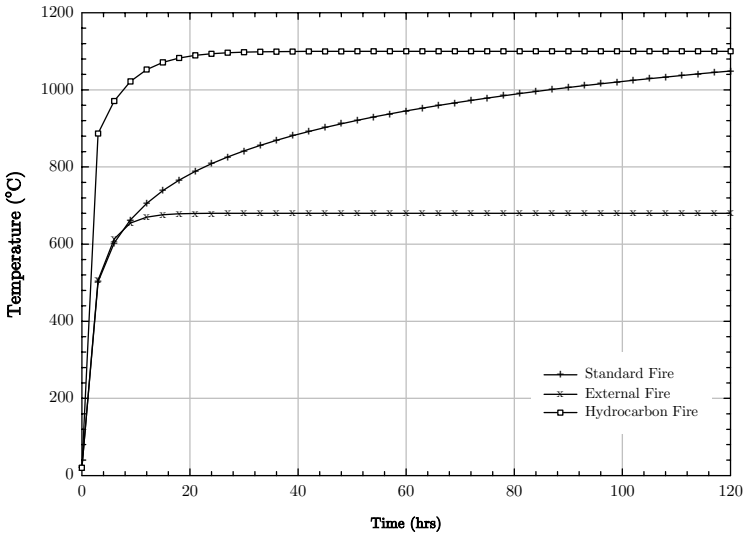

Figure 2.6: Nominal temperature-time curves

If a decay phase of the fire is to considered in addition to a heating phase, then Annex A of Eurocode 1 [1] provides a method for determining an appropriate temperature-time curve by,

$$T_g = 20 + 1325\left(1 - 0.324e^{-0.2t^*} - 0.204e^{-1.7t^*} - 0.472e^{-19t^*}\right) \qquad (2.11)$$

where $t^* = t\Gamma$ and $\Gamma = (O/b)^2(0.04/1160)^2$. The opening factor is given by $O = A_v\sqrt{H_{eq}}/A_t$, while b incorporates the thermal properties of the compartment linings $(k\rho c)^{1/2}$. The duration of the heating phase can be defined in relation to the fire growth rate and fuel load densities. Parametric temperature-time curves are however limited to compartments with floor areas of up to 500m^2 and a maximum height of 4m. An example of a typical parametric fire curve with respect to the standard fire curve is given in Figure 2.7.

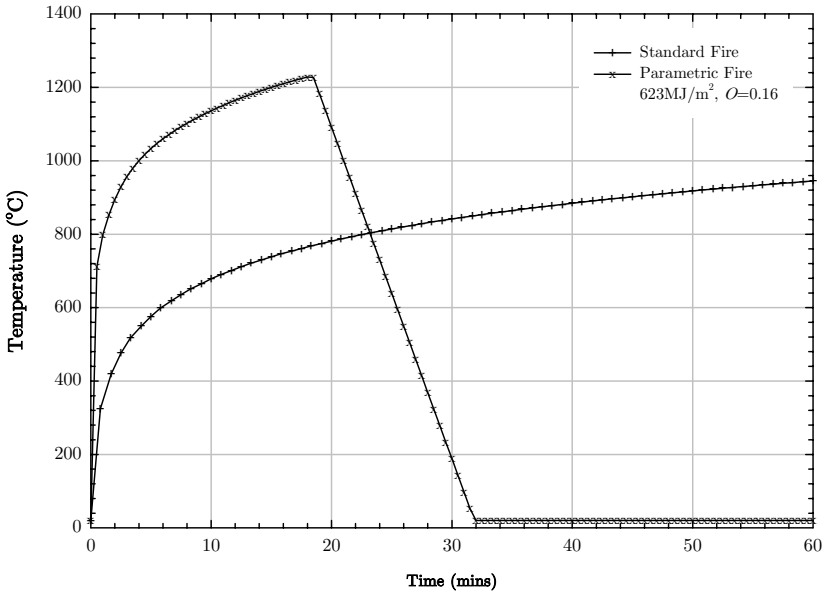

Figure 2.7: Standard fire temperature-time curve and parametric fire curve for a specified fuel load and opening factor

For the case of a localised fire, the length of a flame is determined using the Heskestad flame height correlation [24]. Annex C of Eurocode 1 [1] provides a methodology for undertaking this calculation for the cases of flames not impacting and impacting on a ceiling.

Both the magnitude of the temperature and the duration of the fire are important elements in determining the severity of a given fire. The duration of a fire is directly related to the amount of fuel available to burn or the amount of the amount of air available. In contrast, the magnitude of the temperature is generally a function of the ventilation available, the ignition scenarios and the fuel load and its properties.

2.4. Heat Transfer to Structural Elements

Guidance for the evaluation of the thermal analysis for structures including the heat transfer phenomena which defines the thermal boundary condition is given in many sources including industry-orientated publications [25] and in the standard design guides [26]. Solutions can be obtained at several levels; from tabular or graphical data, through simple numerical calculations to detailed numerical methods performed by computer. The following sections discuss aspects of each method.

2.4.1. Pre-Computed and Graphical methods

Due to the potential tedious nature of numerical methods and the complexities associated with computer programs, graphical solutions are favoured for their ability to provide quick results. Several graphical methods exist for the determination of steel temperature with an applied insulation.

Malhotra [27] developed a series of graphs, presented in Figure 2.8, for estimating the steel temperature of members exposed to the standard fire exposure, based on the lumped heat capacity. Steel temperatures are plotted against the element's P_s / A_s ratio. This is the ratio of the heated perimeter to the cross-sectional area of the steel and can be considered analogous to the section factor employed within the Eurocodes. The curves in the figure represent selected times of exposure while each graph is for a specific thermal resistance ranging from 0.05 to 0.30 ($W/m^2.^oC$). The thermal resistance is determined by the ratio of the insulation thickness d_i to its thermal conductivity k_i. The method is limited to the standard fire exposure and considers a limited knowledge of the fire protection material.

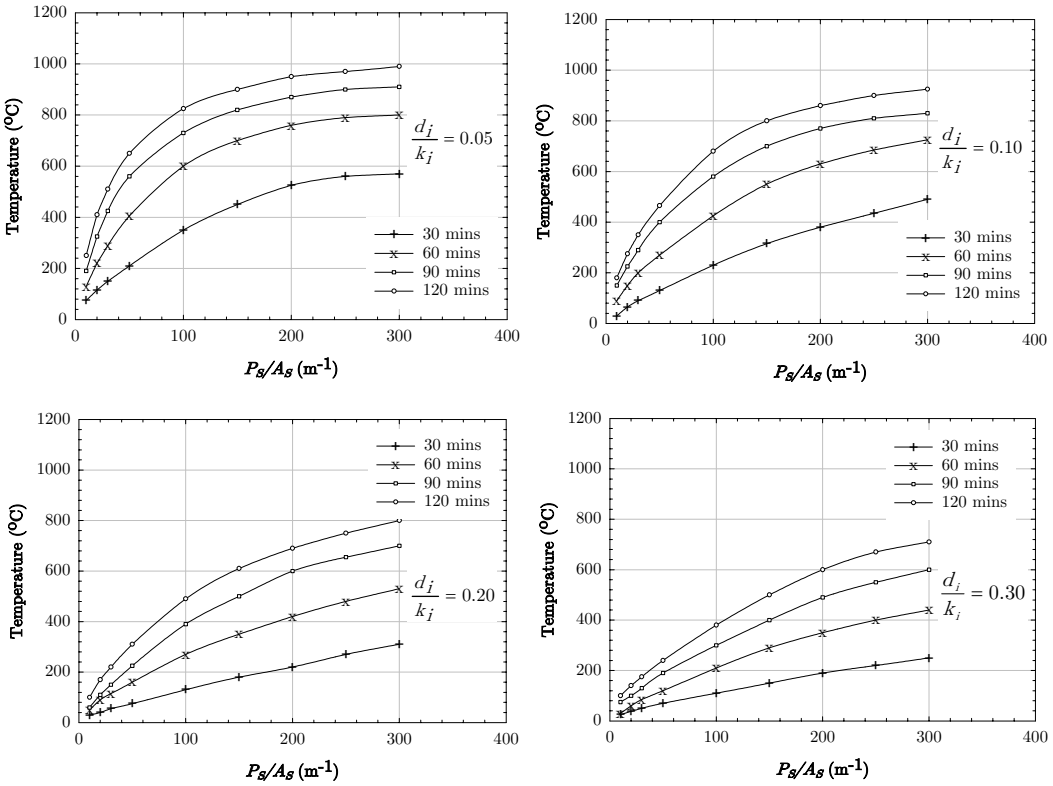

Figure 2.8: Temperature of protected steel members with relation to section size and insulation properties at selected time periods [27]

Jeanes [28] created a series of temperature-time graphs of protected steel beams. The results are based on a specific spray-applied cementitious protection material with a range of thicknesses of 12.7 to 38.1mm. Graphs are available for a large variety of beam shapes, with an example given in Figure 2.9 – it should be noted that these charts are designed for American W-shape beams (similar to I-beams) in which W is the self weight of the section (lb/ft) and D is the heated perimeter (ft). These graphs use the average steel temperature based on the ASTM E-119 fire exposure [29]. Their use allows for the determination of a thickness of fire protection material required to achieve a desired level of fire resistance. Alternatively, they can be used to estimate the fire endurance for a particular steel beam and insulation thickness design which has not been tested. Figure 2.10 shows an alternate way of presenting the data where

the fire resistance can be determined from the member size and thickness of insulation.

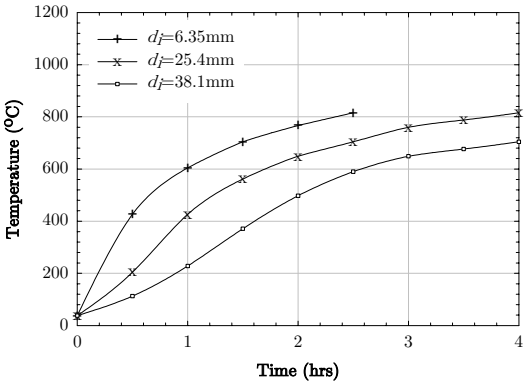

Figure 2.9: Average section temperature of a W12x14 (305x102x25UC with P_s/A_s=320m^{-1}) beam (W/D=0.4) for various thicknesses of applied fire protection [28]

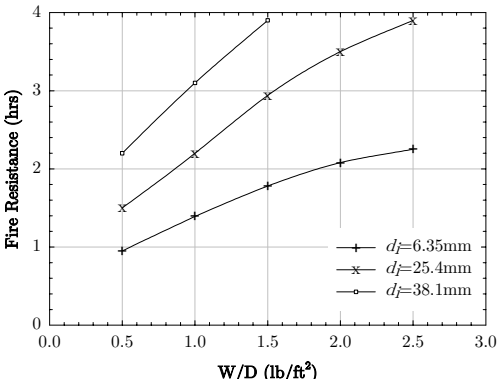

Figure 2.10: Fire endurance of steel beams for different insulation thicknesses for an average section temperature of 538°C [28]

Lie [30] presents graphical representations of the exact solutions to the governing differential equations for the temperature of protected steel members exposed to the standard fire. Similar to method of Jeanes, this method applies to American W-shape sections. It is assumed that heat transfer is one-dimensional through the insulation layer and that there is a uniform temperature throughout the steel cross-section. Figure 2.11 and Figure 2.12 show how the graphical method can be applied using the given ranges of the Fourier number, Fo, for the insulation layer. It is required to evaluate the dimensionless parameters Fo, N and θ to use the graphs;

$$Fo = \frac{\alpha t}{d_i^2} \tag{2.12}$$

where t is the heating time (hrs), d_i is the thickness of insulation (m) and $\alpha = k_i/(\rho_i c_i)$ is the thermal diffusivity of the insulation (m^2/hr).

$$N = \frac{\rho_i c_i d_i}{c_s (W/D)} \tag{2.13}$$

in which c_s is the specific heat of steel.

$$\theta = \frac{T - T_0}{T_m - T_0} \tag{2.14}$$

where T is the temperature of the steel at time t (°C), T_0 is the initial temperature of the steel and T_m is the mean temperature of the fire which can be calculated from the standard temperature-time curve in which t is given in hrs, by,

$$T_m = 150(\ln 480t - 1) - 30/t \tag{2.15}$$

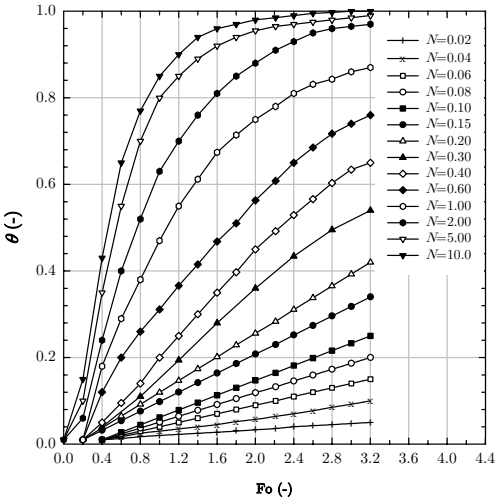

Figure 2.11: Dimensionless steel temperatures for low Fourier numbers [30]

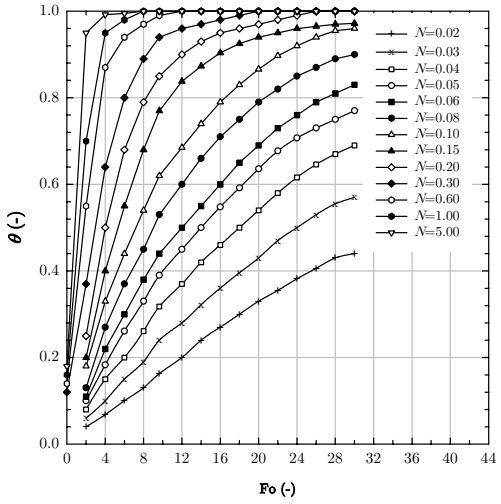

Figure 2.12: Dimensionless steel temperatures for high Fourier numbers [30]

Although useful in some cases, graphical methods are limited by their applicability only to one design fire, namely the standard fire. They can not be used if the design fire incorporates different growth, maximum temperature and decay characteristics with respect to the standard fire temperature-time curve.

2.4.2. Method for unprotected steelwork

If it is assumed that the temperature distribution throughout the cross-section of a structural member is uniform then the temperature rise $\Delta T_{s,t}$ of the element per time-step Δt can be determined by [26],

$$\Delta T_{s,t} = k_{sh} \frac{A_m / V}{c_a \rho_a} \dot{h}_{net,d} \Delta t \tag{2.16}$$

in which k_{sh} is a correction factor for the shadow effect [31]. Although the shadow effect applies only to radiative fluxes, in equation (2.16) it is applied to total fluxes. This is justified in that radiation becomes the dominant mode of heat transfer in post-flashover fires in comparison to convective fluxes. A_m / V is referred to as the section factor or massivity factor and relates the exposed surface area of the member to its volume. The higher this value, the faster it heats. Section factors can be evaluated using tables in Eurocode 3 [26] that allow for different shapes and directional exposures, however, they don't contain any information regarding the physical characteristics that they represent. The variable $\dot{h}_{net,d}$ is the design value of the net heat flux per unit area comprising convective and radiative components as outlined in the Eurocodes.

2.4.3. Method for protected steelwork

The steel temperature of a member encased in fire protection material can be evaluated, assuming a uniform temperature distribution, by [32],

$$\Delta T_{s,t} = \frac{k_p A_p / V}{d_p c_a \rho_a} \frac{\left(T_{g,t} - T_{s,t}\right)}{\left(1 + \phi/3\right)} \Delta t - \left(e^{\phi/10} - 1\right) \Delta T_{g,t} \tag{2.17}$$

with

$$\phi = \frac{c_p \rho_p}{c_a \rho_a} d_p A_p / V \tag{2.18}$$

The derivation of this equation was undertaken by Wickstrom [33]. There is no heat flux variable in equation (2.17) because the underlying assumption is that the surface temperature of the insulating material is the same as that of the gas. The only thermal resistance to the steel section is assumed to be within the insulation material by means of conduction. The section factor A_p / V is determined by considering the method in which the steel section is encased in the protection material. In the case of a rectangular box-type protection surrounding an I-beam, radiation from the inner surface of the insulation material to the member is not taken into consideration. As an alternative, an approximation to the section factor is made to account for the radiative spacings involved.

The Eurocode calculation of member heating when insulated with protection material is limited to I-beam or H-beam type sections. Corrections need to be applied if alternative shapes such as T-shapes and rectangular shapes are to be evaluated.

Figure 2.13 shows the typical temperature rise of an unprotected and a protected steel member with respect to the standard fire while Figure 2.14 shows the same but for a parametric fire curve.

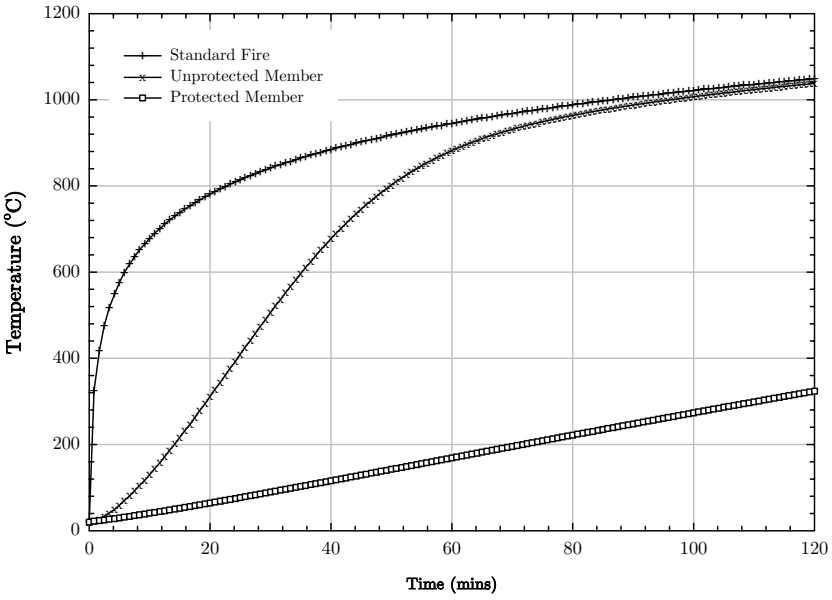

Figure 2.13: Typical heating response of an unprotected member and a protected member with respect to the standard fire (A_p/V =50m^{-1})

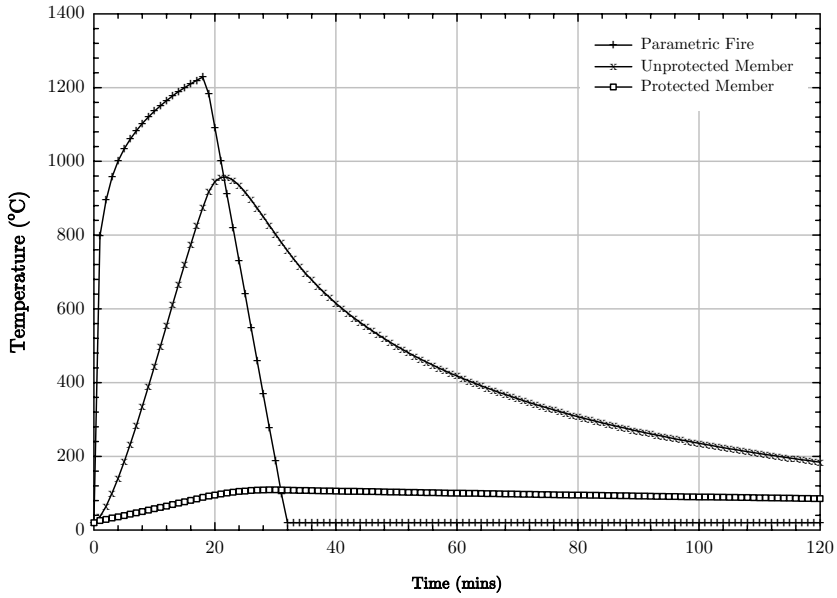

Figure 2.14: Typical heating of an unprotected member and a protected member with respect to a parametric fire (623MJ/m^2 and O=0.16) including a decay period (A_p/V =50m^{-1})

2.4.4. Computer models for heat transfer

A number of computer-based models exist for estimating structural temperatures in fires. Such models range from simple spreadsheets to finite element models. Spreadsheet models [34] perform simple and iterative calculations in one spatial dimension assuming quasi-steady-state conditions in a similar manner to equations (2.16) to (2.18).

More complex models can be used to solve the appropriate differential equations. Lie and Harmathy [35] developed a two-dimensional finite difference model to predict the temperature rise of protected steel columns based on the ASTM E119 curve, in which heat transfer by radiation is considered between any air gaps enclosed by the insulation and the steel.

General heat transfer finite element programs including FIRES-T3 [36], TASEF-2 [37] and SAFIR have been developed to specifically address the heating of structural members exposed to fire conditions. These models examine the heat conduction through structural elements; however, as a boundary condition they require appropriate input of the fire environment and exposure. This is usually built into the program or can be user defined and takes the form of a temperature time curve together with appropriate heat transfer coefficients. Geometrical factors for the element can be specified and thermal material property data is considered. Good comparison to standard test fires is seen for the majority of models [25], however, their accuracy for large full-scale fires relies on the correct definition of the thermal exposure as a boundary condition.

2.5. Compartment Fire Models

As described in the sections above, the current practice for input to thermal and structural calculations is normally to ignore the fire growth period and concentrate on the fully developed fire. As a first order of magnitude approach, this might be appropriate but if Compartment Fire Models (CFM's) are going to be used to evaluate the fire environment and heating behaviour then this simplification is unnecessary. The objective of a CFM will be to provide a much more detailed evolution of the conditions within the compartment where the fire originated and in adjacent areas. For a particular fire scenario it is possible that flashover might be attained within the compartment of origin before any structural element has undergone significant heating; nevertheless none of the adjacent compartments will be expected to have reached fully-developed conditions. Furthermore, the growth of the fire beyond the compartment of origin will generally be within the same timescales as the heating of structural members. Given the principle that fire resistance is given directly by the temperature of the structural element, it is possible that neglecting the growth period might not matter and would result simply in conservative requirements for fire protection. However, if the behaviour of the structure is to be studied dynamically and in an integral manner [38] then the results are uncertain. Alternatively, if the objective is to fully integrate CFM's with structural analysis, then significant effort is necessary to establish realistic timescales and characteristic conditions of fire growth beyond the compartment of origin. Experimental validation should follow because little or no useful data exists.

Since the early 1970's a wide variety of CFM's have been developed. Initially the term 'model' referred to either analytical or empirical formulations that allowed simple calculations associated with the growth of a fire within a compartment. Computer-based models rapidly followed and

built upon the framework established by these analytical expressions and experimental data. Computer tools available for fire modelling in the 1970's favoured the development of zone-models. Zone models require multiple, but simple computations; as a result they provide appropriate solutions given some constrained computational resources. A number of variants emerged and their use became generalised towards the end of this decade.

It is only since the 1980's that advancement in computer technology has made Computational Fluid Dynamics (CFD) or Field Models a viable alternative for fire-related calculations [39]. Currently, a wide range of CFD computer-models, including fire-dedicated programs, exist and they compete well with traditional zone models. Analytical and experimental formulations form the basis to calculate the behaviour of fires within compartments, but due to the multiple variables and complexities of the problem, quantitative predictions are now mostly obtained from numerical computations. However, due to the great sophistication of field models and the complexity of the input data, simulations cannot be run blindly and their application requires the supervision of qualified individuals.

The following sections dissect the particular application of CFM's to structural analysis with reference given to the heat transfer to structural elements. The advantages of this approach will be introduced and a number of limitations of the different methodologies will be highlighted.

2.5.1. General remarks

Compartment Fire Models have traditionally been divided in two groups; Zone Models (ZM) and Computational Fluid Dynamics (CFD) or Field Models. This division is still relevant and is used in the following sections. Reviews available in the literature are of two types; surveys and

summaries of features. Surveys present data on all existing models and together with some brief description of the code, its developers and typical applications. Friedman [40] has published a comprehensive survey of this type, which has more recently been updated and extended by Olenick & Carpenter [41]. Both surveys provide a complete list of all known existing models, their sources and applications although no critical review of the models is given. Summaries of the features of CFM's are more common in the literature, including reviews by Walton [42] and Cox and Kumar [39], covering zone and CFD models respectively. In most cases limitations are presented only within a general context. The rapid increase on the usage of CFD codes for fire prompted more detailed reviews, of which the more comprehensive are those of Novozhilov [43] and Luo [44].

2.5.2. Zone Models

Zone models treat compartments as a control volume sub-divided into two smaller control volumes, within which all properties and conditions are assumed homogeneous. The upper control volume considers the mixture of hot products of combustion and the lower one, the colder fresh air. Flow, temperature and species fields within these control volumes are not spatially resolved and therefore are assumed uniform. Any adjacent compartments are linked by mass and energy transfer between them. The solution of the flow, which is the most computationally intense aspect of these calculations, is thus avoided by this simple two-zone approach. A fire in the enclosure is treated as a pump of mass and energy from the lower layer to the upper layer. As energy and mass are pumped into the upper hot layer its volume increases, causing the interface between the layers to move toward the floor. Significant experimental validation of the principles of this methodology has been generated in the last three decades and its limitations have been many times described [42].

Two-zone models are by definition limited when analysing the convective heat transport from the gas phase to the solid phase since they avoid the solution of the fluid mechanics equations, thus allowing for faster computations. Nevertheless they rely on empirical correlations at all levels of heat and mass transfer. These empirical correlations have in general no direct link with the burning conditions and as a result the convective heat transfer coefficients and radiation heat transfer representations used for a small fire will be the same as for a large fire.

Calculation of the convective coefficient (assumed to be natural convection) is via correlations for walls, ceilings and floors (hot surface up or cold surface down) and ceilings and floors (cold surface up or hot surface down). A series of particular details extracted from CFAST are presented below for illustration from Jones et al. [45] and Cooper [46]; similar approaches can be found in other Zone Models. The convective transfer coefficient is generally defined in terms of the Nusselt number, for example,

$$h = \frac{Nu_L k}{L} = C \cdot Ra_L^n \tag{2.19}$$

where the Rayleigh number is defined as,

$$Ra_L = Gr_L \cdot Pr = \frac{g\beta\left(T_s - T_g\right)L^3}{\nu\alpha} \tag{2.20}$$

This number is based on a characteristic length, L. The power n is typically 0.25 and 0.33 for laminar and turbulent flow, respectively. All properties are evaluated at the film temperature; $T_f = \left(T_s + T_g\right)/2$. The thermal diffusivity and thermal conductivity of air are also defined as a function of T_f, given by Atreya [47],

$$\alpha = 1.0 \times 10^{-9} T_f^{7/4} \tag{2.21}$$

$$k = \left(\frac{0.0209 + 2.33 \times 10^{-5} T_f}{1 - 0.000267 T_f} \right) \tag{2.22}$$

Table 2.2 presents the different correlations employed within CFAST.

Geometry	Correlation	Restrictions
Walls	$Nu_L = \left(0.825 + \frac{0.387 Ra_L^{1/6}}{\left(1 + \left(0.492/Pr\right)^{9/16}\right)^{8/27}} \right)^2$ $\approx 0.12 Ra^{1/3}$	None
Ceilings and floors (hot surface up or cold surface down)	$Nu_L = 0.13 Ra^{1/3}$	$2 \cdot 10^8 \le Ra_L \le 10^{11}$
Ceilings and floors (cold surface up or hot surface down)	$Nu_L = 0.16 Ra^{1/3}$	$10^8 \le Ra_L \le 10^{10}$

Table 2.2: Different heat transfer correlations employed in CFAST [45;46]

In Zone Models, the Reynolds number (see Chapter 3) cannot be calculated properly since velocity fields are not determined within the two zones. For this reason, the convective heat transfer and the boundary layer have to be calculated in a different way. The thickness of the boundary layer is determined by the temperature difference between the gas zone and the wall or object being heated [45]; therefore, convective heat transfer is calculated based only on the temperature difference between the zone and the object. From the principles of the model it is impossible to improve this approach; nevertheless it is important to

establish if these correlations could be accurately used to define the thermal evolution of structural elements in fire. There is no evidence in the literature that there has been any systematic evaluation of the performance of Zone Models for predicting heating of structural elements in compartment fires.

Thermal radiation tends to be treated in a more complex manner. Methods such as the four-wall algorithm, derived by Siegel & Howell [48], that solve the net radiation equation, are present in Zone Models. The objects that participate in the radiation exchange are walls, gases and fires. Heat exchange between layers is also possible. The zones and surfaces are assumed to radiate and absorb like a grey body. Absorption within the gas layer can be evaluated and indeed, this method can show adequate results when appropriate absorbance coefficients are applied (e.g. 0.5 and 0.01 for the upper and lower layers, respectively). These coefficients represent reasonable approximations for fires with sooty upper layers and clean lower layers; they are nevertheless fully empirical. For fully-developed conditions these coefficients have never been validated [49].

Zone Models generally do not include pyrolysis models, and the onus is on the user to set pyrolysis rates. Approximate pyrolysis rates for pre-flashover fires are defined by empirical heat-release rates and abundant data is available in the literature. In the case of fully-developed fires however, heat-release rates are ultimately defined by ventilation and a very restricted set of data is available. This is very important because the burning time, and thus the total heat transfer, is strongly influenced by the pyrolysis rates. The emissivity and optical properties of the thermal environment will also be strongly influenced by the soot absorption coefficient and thus by the soot yield of the fire under each specific condition. This information is currently very limited for fully-developed fires.

The validity of these models depends on the general applicability of the two-zone representation and of the relevant empirical correlations. The limits of the two-zone approximation have not been studied extensively. Among the empirical correlations, such as those corresponding to the fire plume, the expressions for entrainment rates are critical and their validation under conditions other than free axi-symmetric or line fires is limited [50].

The use of Zone Models for complicated geometries has not been validated and thus is questionable for extreme cases. Because of the enforced condition of constant properties in each zone, complicated geometries have to be treated in the same way as less complicated ones. The absence of velocity fields and lack of a turbulence model implies that the convective heat transfer will in any case not be affected by any details of a complicated geometry.

Zone model assumptions have also been found to break down in flashover fire scenarios [43], leading to predicted heat-release rates that are lower than the actual ones.

In summary, Zone Models are inherently limited by their basic assumptions, however, they are simple to use, robust in nature and can provide good insight on fire development for simple scenarios. Extensive validation is available in the literature and clear estimates of error can be generated. Even so, the intrinsic limitations of zone models are clearly of importance when addressing the application to modelling of structures exposed to fires.

2.5.3. CFD Models

CFD modes are characteristically defined by the way the in which turbulence is modelled. Thus, CFD codes can simplistically be divided into three groups, with models based on Reynolds-Averaged Navier-Stokes (RANS), Large Eddy Simulation (LES) and Direct Numerical Simulation (DNS).

For the modelling of an environment such as a compartment fire, and given the computational resources currently available, DNS simulations are not feasible for a number of reasons. DNS requires the grid resolution to be as fine as the Kolmogorov microscale. All eddies, down to the dissipation length scale, must be simulated explicitly with sufficient accuracy. The number of DNS grid points required for the resolution of all scales increases approximately with the cube of the Reynolds number (Re^3). The Reynolds number for typical fire and smoke movement in a compartment is approximately 10^5, and the total number of cells necessary for solving fire and smoke movement in a room is of the order of 10^{13}. Current supercomputers however, have the capability to provide a maximum grid resolution of 10^8 cells. Therefore, current computing technology is still completely insufficient to solve such detailed fire flows. DNS, therefore, cannot be used to simulate complicated fire spread and smoke movement in a full-scale compartment.

Since full resolution of the Navier-Stokes equations is not practically possible, it is necessary to model only some aspects of the flow. The choices of which aspects of the flow will be modelled, and thus the approach to be followed, is difficult and implies inevitable subjectivity. RANS takes the option of solving the ensemble-averaged Navier-Stokes equations by using turbulence modelling, thereby approximating the fluid flow fluctuations via a modelled state. In a RANS solution, all dynamical degrees of freedom smaller than the size of the largest (energy-containing)

eddies are averaged, so there is no dynamic information about the smaller scales. RANS can be further divided into turbulent viscosity models (such as the $k-\varepsilon$ model) and Reynolds-stress models. The most widely used turbulent viscosity model in fire is the standard buoyancy-modified $k-\varepsilon$ model.

LES, pioneered in the early 1960-1970s by Smagorinsky [51] and Deardorff [52], assumes that turbulent motion can be separated into large-eddies and small-eddies. The motion of the large eddies (super-grid scale) is directly simulated while that of the small eddies (sub-grid scale) is approximated. Since LES solves time-dependent flow, it can provide detailed information on turbulence, such as three-dimensional instantaneous velocities.

The key step in both LES and RANS is the derivation of the underlying dynamical equations averaged over small scales. The fundamental difference between LES and (transient) RANS is the definition of small scales. In LES, the small lengthscales are smaller than the grid size and in RANS, the small lengthscales are smaller than the largest eddies. If the grid size of an LES simulation is taken to be progressively larger, self-consistency requires that the LES results approach the RANS results [53]. LES techniques always need to be three-dimensional and must have a time-step short enough to capture most of the important turbulent motion. As a result, LES is computationally more expensive than RANS, especially for the case of essentially time-invariant problems where RANS codes can be run in a quasi steady-state mode. Nevertheless, recent advances in computer performance and numerical methods have meant that LES is becoming more feasible for such fire and smoke flow problems.

Some general limitations for both RANS and LES approaches to the modelling of turbulent flows relevant to fires can be established:

- RANS codes average locally over time and space, thus all dynamic information for scales smaller than the large turbulence scales is lost. For the calculation of the thermal response of structural elements this might not be too significant, given that the time-scales of solid heating are much larger than those of gases. Nevertheless, the loss of dynamic information could significantly affect the predictions of fire growth and therefore needs to be handled with great care.

- LES does not average over time so it allows modelling the time evolution of the sub-grid scales. This can be seen as providing a good resolution of the time evolution of the fire. To achieve computations within reasonable computational time constraints, this requires an increase in the cell size; thus large grid cells typically characterize LES solutions. The grid cells can be much larger than the flame thickness; therefore the temperatures of each cell typically represent an average of reactive and non-reactive regions. Thus, the capability of these codes to properly predict the temperatures of combusting mixture, and therefore the radiative heat transfer, is questionable. Furthermore, LES modelling implies a proper definition of the grid size that is consistent with the model parameters and with the computational constraints. A reduction of the grid does not always produce an improvement in precision, indeed determination of the grid may require pre-acquired empirical knowledge, or independent computations [43].

- RANS relies on numerous empirical model coefficients (between 7 to 12 different coefficients) that will describe turbulent viscosity and fluid wall interactions. These functions are well defined for high Reynold's numbers with homogeneous turbulence but can be difficult to establish for transitional flows with constraint

boundaries such as those to be expected close to the surfaces of structural elements. Wall functions have been established to address these areas but their accuracy and generality is still questionable [54].

- Diffusion flames representative of fires are generally considered (spatially) thick, thus the validity of the direct application of RANS flamelet models and simple LES combustion models could be questioned [54]. Despite this statement, proficient use of these models can provide adequate results.

- LES also relies on empirical model coefficients (e.g. the Smagorinsky constant) but their calibration is easier and is expected to be independent of the Reynold's number. In fact, the Smagorinsky constant can be avoided entirely with a dynamic sub-grid model [53]. Calibration of the model coefficients has been done for many scenarios but these rarely include conditions typical of fires. Dynamic sub-grid models are beginning to appear in the fire literature but are still a topic of ongoing research and are not fully validated.

- Proper combustion models are necessary to generate correct heat-release rates (thus temperatures) and species distributions. To achieve proper temperature predictions it is also necessary to adequately represent radiative heat transfer. For radiation to be properly modelled the most important aspects are temperature and soot concentrations. Significant work on the development of combustion models, radiation models, and soot models is currently underway [43;44;55;56]. These models are being incorporated into numerical tools on a constant basis. Currently, existing combustion models have been validated only in simple scenarios, for simple fuels

and with very limited diagnostics. Common validations rely on simple comparison with temperature measurements [57;58] that in many cases are decades old [59]. These validation exercises are clearly not sufficient to determine the adequacy of the complex models proposed.

- The relatively long timescales which are relevant to structural behaviour imply in most cases fully-developed fires. Although validation exercises under these conditions exist [60;61] they still remain insufficient. The data available for post-flashover, fully-developed fires, is generally in the form of average point measurements of temperature [11;62] which is more suited for the validation of Zone Models than of CFD codes. Combustion and soot models are greatly sensitive to the burning conditions; therefore the capability of existing models to provide reasonable predictions under fully-developed fire conditions remains largely untested.

Whichever model is used, all numerical tools are severely limited by any improper definition of the fundamental properties of materials controlling fire growth. An analysis of the input variables for all flammable materials shows a fundamental dependence on values in databases which are typically very simple and approximate [3;63;64]. The errors that can be induced by an improper or incomplete selection of material properties can be more important than those generated by an incorrect specification of the parameters of the numerical flow and combustion models. In addition, the conclusion of CIB W14 'Round Robin for Code Assessment' exercise was that the effect of user choices on uncertain inputs, including numerical parameters, can have a dominant effect on the outputs obtained from numerical codes in general [65].

The general limitations outlined above are by no means insurmountable, but improvement and confidence can only be achieved with systematic and careful validation and by improved guidance and training for users. In their current state, all CFD codes are research tools that require great proficiency in their use and by far the biggest challenge is to guarantee that the users apply them correctly.

2.5.4. Heat Transfer within CFD Models

The CFD code FDS defines a number of methods for applying thermal exposures [66] to a structure, depending on the expected material behaviour (i.e. thermally-thin sheet or a thermally-thick solid). For the most relevant case of a thermally-thick solid exposed to an arbitrary flux, a one-dimensional heat transfer analysis is performed across the thickness of the material. The cell resolution within the wall is non-linear, with clustering near the surface where initial thermal gradients are steeper. The surface temperature is determined according to the appropriate convective and radiative fluxes and the solid-phase conduction, i.e. it is a locally varying parameter. This treatment is best suited to planar surfaces such as enclosure boundaries where localised heating does not induce significant thermal gradients in the plane of the wall.

Radiation calculations within FDS are undertaken via the solution of the radiation transport equation for a non-scattering grey gas, and in some cases using a narrow-band model [67]. The radiation transport is based on a ray-tracing method using a large number of discrete rays. In common with other DTRM methods [55], computational limits of the total numbers of rays can lead to a non-uniform distribution of the radiant energy, for example in the case of a target far away from a localised source of radiation like a small growing fire, a numerical error generally known as the 'ray effect' [55]. More detail on the heat transfer processes in FDS is

given Chapters 3 and 4 considering convective and radiant heat transfer respectively.

2.6. Applications in Structural Fire Engineering

Of the examples of fire definitions and heat transfer methods outlined above, varieties are used by structural fire engineers both in the commercial and research sectors. Lim et al. [68] simply use the ISO-834 fire gas temperature as a direct thermal boundary condition for the analysis of fire-exposed floor systems. Temperature distributions within the slab are then evaluated using the finite-element program SAFIR. Usmani et al. [69] adopted a parametric gas-phase temperature-time relationship for the design fire as described in the Eurocodes [1], i.e. the parametric approach. Post-flashover conditions were assumed so that a single representative temperature could be used but the authors admit that this method does not take into account the different convective and radiative heat exchanges between surfaces, the fire and combustion products, nor local variations of the empirical coefficients. Similar approaches are adopted by Franssen [70] and Liew and Ma [71] using the standard, hydrocarbon and parametric fire curves in Eurocode 1, with decay periods also considered.

Prasad and Baum [72] have recognised the need for the thermal boundary condition to be defined by the appropriate incident heat flux, which in turn is determined from solutions of the radiative transport equation. This is possible within the scope of CFD calculations, which they consider is the only realistic method that one might achieve an adequate representation of the temporal and spatial variations associated with temperature and combustion products derived from a natural fire in a compartment. They recognise that for more challenging large-scale applications, such as the World Trade Center scenarios, with fire impingement on large truss

systems, simplifications may often be needed. They present a method which considers the spatial distribution of the temperature and combustion products and also takes into account the geometry of the enclosure. This involves the classification of a compartment into the hot upper layer and cool lower layer. From these layers, representative temperatures and radiative properties can be determined with the use of CFD modelling and applied to a radiative transport model to determine heat fluxes to a target surface. Two major simplifications are embedded within this procedure; the first is use of the concept of a grey gas, the properties of which are independent of spectral frequency, hence allowing a simple approximation of the average absorption coefficient. The second is to assume a vertically stratified distribution of temperature and combustion products throughout the compartment. This two-zone classification model however ignores some important details of the spatial differences created during large-scale enclosure fires and indeed it is these distributions that may have a marked impact on the way a structure may behave in fire. Hence by averaging CFD output over time and space, potentially large variations in exposure conditions are inevitably lost.

Tofilo et al. [73] have considered the distribution of heat fluxes on the walls on an enclosure for fuels with different soot yields. Their experimental set-up allowed for the separation of convective and radiative heat fluxes from the hot gases and also the radiative fluxes from the fire plume. The effect of different ventilation characteristics and fuel pan sizes were also investigated. Variations in heat flux are demonstrated for the different fire scenarios, however only single point measurements are given and no attempt is made to map the surface flux spatial distributions.

Lattimer [74-77] and Back [78] have undertaken extensive work on characterising heat flux distributions including spatial maps that have been successfully recreated using FDS [79]. Correlations in the form of;

flat vertical walls, flat unconfined and confined ceilings, parallel flat vertical walls, corner walls at 90°, corner walls at 90° with a ceiling and horizontal I-beams beneath a ceiling are considered. The aim of the research was to consider combustible materials with regard to flame spread and fire development. For the different configurations, peak heat fluxes were around 100kW/m^2 with considerable spatial variations. It must be highlighted though that all the fires were localised and originated from small ignition sources that are relatively small in size when compared to full-scale post-flashover scenarios.

2.7. Conclusions

A review of the different approaches used to establish the thermal boundary condition required to make a detailed analysis of a structure in the event of a fire has been discussed. This has been placed within the context of defining the thermal environment and undertaking the heat transfer to a structural element. A review of current graphical, numerical and computer based solutions has been presented.

The validity and limits of the different current approaches provides a guideline to areas that need further attention. Indeed, from this evaluation it emerges that the only general way to precisely model the thermal boundary condition is via numerical models. Other techniques need to resort to strong simplifications. The impact of those simplifications on accuracy could be minor, but has not been fully established. Numerical models can be of significant use in assessing the relevance of many of the assumptions embedded in current calculation methodologies.

A review of the most commonly used modelling approaches then reveals that currently these techniques also have important limitations. Many of

these can be circumvented by proficient and experienced use, but the lack of detailed validation still remains a serious problem.

Chapter Three

3. Convective Heat Transfer

3.1. Introduction

Convective heat transfer plays an important role in fires by transporting chemical energy released during a fire to the surrounding environment through the motion of hot gases. In basic terms, convection describes the energy transfer between a surface and a fluid moving over that surface as a result of an imposed temperature difference. The motion of hot gases may be driven by the fire itself, commonly referred to as natural or free convection, alternatively some external source may drive the gases and this is known as forced convection. The combination of both is referred to as mixed convection.

Strictly, convection is not a basic mode of heat transfer, rather it can be considered as a combined effect of conduction and the motion of some transmitting medium. In general however, convection is treated as a separate mode of heat transfer involving complex relationships between velocity, temperature and concentration distributions.

This Chapter discusses the basic concepts of convective heat transfer and studies the parameters necessary for calculating the imposed convective surface heat fluxes on structural elements.

3.2. Basic Concept

Consider the case of Figure 3.1 in which an arbitrary shape of surface area A_s and temperature T_s experiences a flow of fluid at higher temperature T_∞ and velocity V over its surface. Convection will occur if $T_s \neq T_\infty$ and heat will flow from the hot surrounding gas to the colder wall at the rate of heat transfer Q which is proportional to both the surface area and the

temperature difference. This allows the local convective heat flux to be written as,

$$q'' = \frac{Q}{A_s} = h\left(T_\infty - T_s\right) \tag{3.1}$$

which is referred to as Newton's law of cooling and the proportionality constant h is the heat transfer coefficient. T_∞ and V are characteristic values representative of the conditions external to the boundary layers formed in the immediacy of the solid.

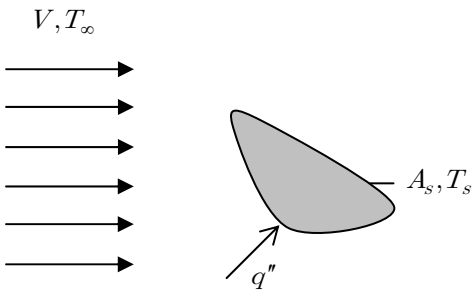

Figure 3.1: Convective heat transfer to a surface of an arbitrary shape

Under normal conditions there is zero relative velocity between the fluid and the wall and the fluid temperature equals the wall temperature. This means that at the wall, the fluid can not experience any slip or temperature jump. It has been experimentally observed that the heat transfer coefficient is not a constant in that it is sensitive to flow conditions. The magnitude of the heat transfer coefficient is dependent on the rate at which the fluid can convect a particle to the surface of the solid. Since the fluid experiences no slip at the solid and assuming radiation is negligible, then heat flow to the solid boundary is by conduction only. At a greater distance from the surface into the gas, the velocity is higher and convection of particles becomes more significant until near the outer edge of the boundary layer where almost all energy

transport occurs by convection. It is sometimes considered that equation (3.1) obscures the basic phenomena that are active, however its convenience is responsible for its continued use [80;81].

The concept of the boundary layer is depicted in Figure 3.2. The particles in contact with the surface at zero velocity retard the motion of particles in the adjecent layer and so on, until at some distance $y = \delta$ from the surface the effect becomes negligible. The quantity δ represents the boundary layer thickness within which velocity gradients and shear stresses are large. The surface shear stress can be calculated with knowledge of the velocity gradient at the surface as,

$$\tau_s = \mu \left. \frac{\partial u}{\partial y} \right|_{y=0} \tag{3.2}$$

where μ is a fluid property known as the dynamic viscosity.

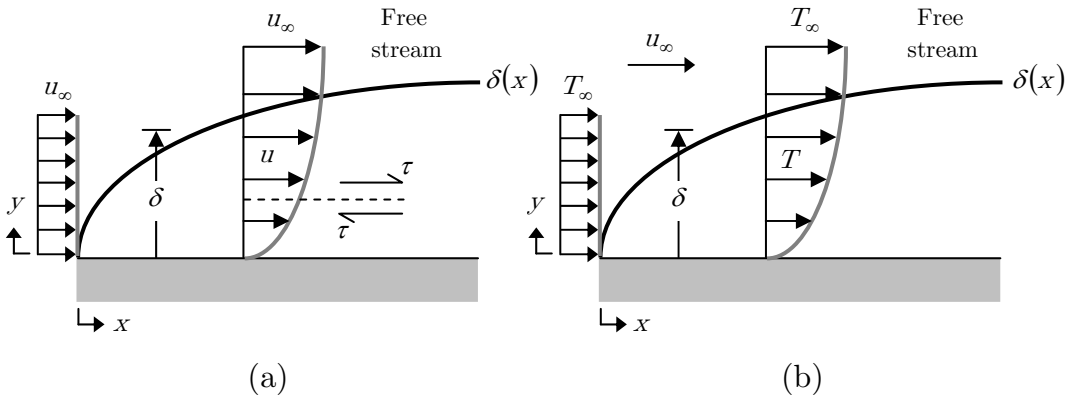

Figure 3.2: Velocity boundary layer (a) and thermal boundary layer (b) development over a flat plate

In a similar sense to that of the velocity boundary layer in Figure 3.2 (a), the temperature boundary layer is seen in Figure 3.2 (b). In this case, particles exchange energy with those in the adjacent fluid layer causing

temperature gradients to develop. The convective heat flux can be evaluated applying Fourier's law to the fluid at $y = 0$ for any position x from the leading edge by,

$$q_s'' = -k_{fluid} \left. \frac{\partial T}{\partial y} \right|_{y=0} \tag{3.3}$$

where k is the thermal conductivity of the fluid. By combining equation (3.1) and (3.3) and rearranging, the heat transfer coefficient can be written as,

$$h = \frac{-k_{fluid} \cdot \partial T / \partial y \big|_{y=0}}{T_\infty - T_s} \tag{3.4}$$

It is clear that conditions within the thermal boundary layer have a strong influence on the wall temperature gradient and also determine the rate of heat transfer across the boundary layer.

3.3. Laminar and Turbulent Flows

For any convection problem it is important to characterise the flow within the boundary layer as being laminar or turbulent [82]. Surface friction and convection transfer rates depend strongly on these conditions. Figure 3.3 shows the difference between laminar and turbulent flow conditions. Laminar flows are characterised by streamlines with velocity components in the x and y directions while in contrast, turbulent flows are highly irregular and are characterised by velocity fluctuations. Indeed intense fluid mixing results in a larger layer thickness than laminar flows. When calculating boundary layer behaviour it is assumed that the transition zone begins at some location x_c which can be determined by a dimensionless grouping of variables called the Reynold's number. The critical Reynold's

number is the value of Re_x for which transition begins and for flow over a flat plate, is known to vary from approximately 10^5 to 3×10^6. However, a representative value of,

$$Re_x = \frac{\rho u_\infty x_c}{\mu} = 5\times10^5 \tag{3.5}$$

is often used for boundary layer approximations [82].

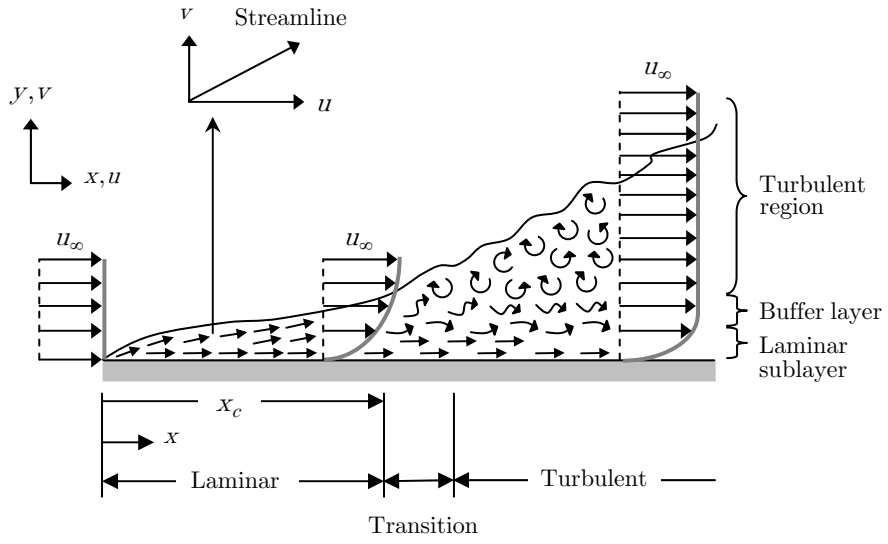

Figure 3.3: Velocity boundary layer development on a flat plate showing laminar and turbulent regions

3.4. Boundary Layer Equations

By considering steady, two-dimensional flow of a viscous, incompressible fluid in a Cartesian coordinate system it is possible to obtain a set of differential equations that govern the velocity, temperature and species concentration fields within a fluid. The complete derivation of these equations can be found in any standard heat transfer textbook [81;82] and as such are not presented here.

3.4.1. Convection Transfer Equations

At each point in the fluid, the conservation of mass and energy as chemical species, together with Newton's second law of motion, must be satisfied. Applying the laws to a differential control volume allows the following results to be obtained,

$$\frac{\partial u}{\partial x} + \frac{\partial v}{\partial y} = 0 \tag{3.6}$$

$$\rho\left(u\frac{\partial u}{\partial x} + v\frac{\partial v}{\partial y}\right) = -\frac{\partial p}{\partial x} + \mu\left(\frac{\partial^2 u}{\partial x^2} + \frac{\partial^2 u}{\partial y^2}\right) + X \tag{3.7}$$

$$\rho\left(u\frac{\partial u}{\partial x} + v\frac{\partial v}{\partial y}\right) = -\frac{\partial p}{\partial y} + \mu\left(\frac{\partial^2 v}{\partial x^2} + \frac{\partial^2 v}{\partial y^2}\right) + Y \tag{3.8}$$

$$\rho c_p\left(u\frac{\partial u}{\partial x} + v\frac{\partial v}{\partial y}\right) = k\left(\frac{\partial^2 T}{\partial x^2} + \frac{\partial^2 T}{\partial y^2}\right) + \mu\Phi + \dot{q} \tag{3.9}$$

$$\mu\Phi = \mu\left\{\left(\frac{\partial u}{\partial x} + \frac{\partial v}{\partial y}\right)^2 + 2\left[\left(\frac{\partial u}{\partial x}\right)^2 + \left(\frac{\partial v}{\partial y}\right)^2\right]\right\} \tag{3.10}$$

Equation (3.6) results due to the application of the conservation of mass to the differential control volume. The two terms represent the net outflow of mass in *x*- and *y*-directions, which must be zero for steady flow. Equation (3.7) represents the rate at which the *x*-momentum leaves the control volume due to fluid motion across surfaces normal to the *x*- and *y*-directions respectively. This net outflow of momentum must be balanced by the sum of the *x*-components of forces acting on the fluid in the control volume. The first term on the right-side of the equation represents the net pressure force, the second term represents the net effect of viscous and shear stresses. The last term provides the body force acting on the fluid per unit volume and for gravity would correspond to $X = \rho g_x$

where ρ is the total mass density of the fluid and g_x is the component of the gravitational constant in the x-direction. The terms of equation (3.8) have equivalent interpretations, but for the y-direction. Equation (3.9) results from the application of the conservation of energy to the differential control volume. Terms on the left-hand side account for the net rate at which thermal energy leaves the control volume due to bulk fluid motion (advection), while terms on the right-hand side account for net inflow due to conduction, viscous dissipation and generation. Viscous dissipation, which is given by equation (3.10) represents the net rate at which mechanical work is irreversibly converted to thermal energy due to viscous effects in the fluid. The generation term characterises the conversion of other forms of energy to thermal energy.

These transfer equations can be solved for the velocity $u(x,y)$ and $v(x,y)$, and temperature $T(x,y)$ fields. Their solution is only possible using finite-difference or finite-element methods and there are only a few cases for which exact solutions may be obtained.

3.4.2. The Forced Flow Boundary Layer Approximations

The equations in the previous section can be simplified in many applications for which body forces are negligible $(X = Y = 0)$ and because the boundary layer thicknesses are known to be typically very small $(Re_x << 1)$, the following approximations can be applied,

$$\left.\begin{array}{c} u >> v \\ \dfrac{\partial u}{\partial y} >> \dfrac{\partial u}{\partial x'}\,\dfrac{\partial v}{\partial y'}\,\dfrac{\partial v}{\partial x} \end{array}\right\} \text{ Velocity boundary layer}$$

$$\left.\begin{array}{c} \dfrac{\partial T}{\partial y} >> \dfrac{\partial T}{\partial x} \end{array}\right\} \text{ Thermal boundary layer}$$

That is, the velocity component in the direction along the surface is far greater than that normal to the surface, and gradients normal to the surface are much larger than those along the surface. These simplifications and approximations lead to the overall continuity equation (3.6) remaining unchanged but the *x*-momentum equation (3.7) being reduced to,

$$u\frac{\partial u}{\partial x}+v\frac{\partial v}{\partial y}=-\frac{1}{\rho}\frac{\partial p}{\partial x}+v\frac{\partial^2 u}{\partial y^2} \tag{3.11}$$

The *y*-momentum equation (3.8) reduces to,

$$\frac{\partial p}{\partial y}=0 \tag{3.12}$$

that is that pressure does not vary in the direction normal to the surface. Finally, the energy equations (3.9) and (3.10) reduce to,

$$u\frac{\partial T}{\partial x}+v\frac{\partial T}{\partial y}=\alpha\frac{\partial^2 T}{\partial y^2}+\frac{v}{c_p}\left(\frac{\partial u}{\partial y}\right)^2 \tag{3.13}$$

Given that p is not a function of y as in equation (3.12) then in equation (3.11) it can be written $(\partial p/\partial x)=(dp/dx)$ so that the pressure gradient may be treated as a known quantity. Also, the last term of equation (3.13) is what remains of the viscous dissipation and in most situations this can be neglected relative to those that account for advection and conduction. Therefore the boundary layer equations can be summarised as: -

Continuity: -

$$\frac{\partial u}{\partial x}+\frac{\partial v}{\partial y}=0 \tag{3.14}$$

Momentum: -

$$u\frac{\partial u}{\partial x}+v\frac{\partial v}{\partial y}=v\frac{\partial^2 u}{\partial y^2} \tag{3.15}$$

Energy: -

$$u\frac{\partial T}{\partial x}+v\frac{\partial T}{\partial y}=\alpha\frac{\partial^2 T}{\partial y^2} \tag{3.16}$$

These simplifications allow for ease of calculation for the spatial variations of u, v and T in the different boundary layers.

3.5. Dimensionless Parameters

The equations of continuity, momentum and energy presented in the previous section are all of the same form. As such, similarity parameters can be developed that allow the application of results obtained for a surface experiencing one set of conditions to the scenario of geometrically similar surfaces experiencing entirely different conditions. Dimensionless independent variables are defined by normalising the boundary layer equations in the form of,

$$x^* = \frac{x}{L} \quad \text{and} \quad y^* = \frac{y}{L} \tag{3.17}$$

in which L is a characteristic length for the surface of interest. Other dependent dimensionless variables can be defined as,

$$u^* = \frac{u}{V} \quad \text{and} \quad v^* = \frac{v}{V} \tag{3.18}$$

where V is the upstream velocity of the surface and as,

$$T^* = \frac{T_s - T}{T_s - T_\infty} \tag{3.19}$$

Substituting these variables into the boundary layer equations allows the identification of the dimensionless group ν/VL, whose reciprocal is the Reynold's number.

$$Re_L \equiv \frac{VL}{\nu} \tag{3.20}$$

It can also be inferred that the term α/VL is a dimensionless group that may be expressed as $(\nu/VL)(\alpha/\nu) = (Re_L)^{-1}(\alpha/\nu)$ where the ratio α/ν is dimensionless and its reciprocal is referred to as the Prandtl number.

$$Pr \equiv \frac{\nu}{\alpha} \tag{3.21}$$

Using these dimensionless parameters, a solution to the momentum equation (3.15) will be of the function form,

$$u^* = f\left(x^*, y^*, Re_L, \frac{dp^*}{dx^*}\right) \tag{3.22}$$

Similarly, a solution to the energy equation (3.16) can be written,

$$T^* = f\left(x^*, y^*, Re_L, Pr, \frac{dp^*}{dx^*}\right) \tag{3.23}$$

From the definition of the convective coefficient in equation (3.4) a solution can be written,

$$h = -\frac{k}{L}\frac{(T_s - T_\infty)}{(T_\infty - T_s)}\left.\frac{\partial T^*}{\partial y^*}\right|_{y^*=0} = +\frac{k}{L}\left.\frac{\partial T^*}{\partial y^*}\right|_{y^*=0} \tag{3.24}$$

which in turn allows the definition of a dependent dimensionless parameter termed the Nusselt number.

$$Nu \equiv \frac{hL}{k} = +\frac{\partial T^*}{\partial y^*}\bigg|_{y^*=0} \tag{3.25}$$

The Nusselt number can be thought of as the dimensionless temperature gradient at a surface and it allows for a measure of the convection heat transfer occurring at that location. It follows that for a prescribed geometry,

$$Nu = f\left(x^*, Re_L, Pr\right) \tag{3.26}$$

If the function of equation (3.26) is known it could be used to calculate the value of Nu for different values of V and L. Indeed from knowledge of Nu, the local convection coefficient h can be found and therefore the local heat flux to a surface determined.

The above discussion has provided a means of evaluating the convective heat transfer coefficient h which is the largest uncertainty in calculating convective heat fluxes to structural elements.

3.6. Forced Convection

This section considers the flow of gases over structural elements that could include flat surfaces, and curved surfaces such as spheres and cylinders. Forced convection considers the situation whereby the relative motion between the surface and the gas is maintained by some external means such as a pump or a fan. This however, does not include buoyancy forces that are due to temperature gradients in the gas itself. Forced convection is not normally associated directly with fires although there may be situations in which the ventilation characteristics result in increased velocities near to openings that necessitate its consideration.

Relationships in the form of equation (3.26) are considered in this section to obtain average heat transfer coefficients that are essentially averaged over the surface area of the body and is therefore independent of the spatial variable x^*. Average heat transfer coefficients are obtained from the average Nusselt number, denoted $\overline{Nu}$.

3.6.1. Flat plate

Flat plates are encountered in many structural engineering applications such as walls, ceilings, webs of beams, flanges of beams, etc. As previously discussed, a laminar boundary layer is initially created until at some location a transition to turbulent conditions is encountered. A simple boundary layer represented for this geometry is shown in Figure 3.4. The Nusselt number correlation for laminar flow is given as: -

$$\overline{Nu} = 0.644\, Re^{\frac{1}{2}} Pr^{\frac{1}{3}} \qquad Pr \geq 0.6 \tag{3.27}$$

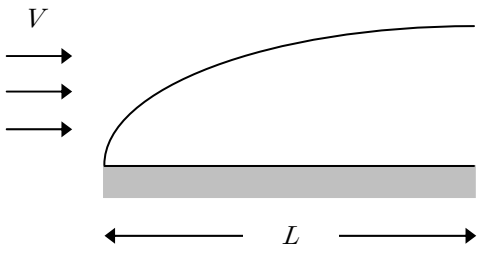

Figure 3.4: Flow over a flat plate

It is possible to develop a single equation to account for all Prandtl numbers for laminar flow over an isothermal plate [83].

$$\overline{Nu} = \frac{0.6774 Re^{\frac{1}{2}} Pr^{\frac{1}{3}}}{\left[1 + \left(0.0468 / Pr\right)^{\frac{2}{3}}\right]^{\frac{1}{4}}} \qquad Pe \geq 100 \tag{3.28}$$

where $Pe \equiv RePr$ is the Peclet number.

In the case of flow over a flat plate in which there are both laminar and turbulent boundary layers or rather mixed boundary layer conditions, it is also possible to use approximations to define a single Nusselt number correlation [82],

$$\overline{Nu} = 0.037\, Re^{\frac{4}{5}} Pr^{\frac{1}{3}} \tag{3.29}$$

3.6.2. Cylinder in cross-flow

Cylinders in cross-flow are also encountered in structural engineering with truss members being a typical example. As shown in Figure 3.5, flow is brought to rest at a stagnation point before circumventing the cylinder as a result of induced pressure gradients. The boundary layer on the opposite side to the normal flow is seen to separate slightly creating a wake until at some point further downstream of the flow returns to normal.

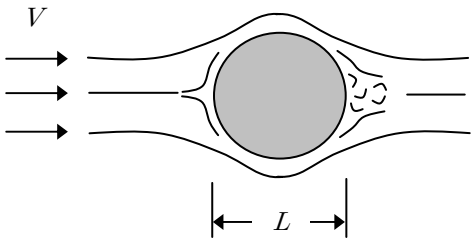

Figure 3.5: Boundary layer formation and separation resulting from flow around a cylinder

The Nusselt number correlation for this geometry is given as [84],

$$\overline{Nu} = CRe^{m} Pr^{\frac{1}{3}} \tag{3.30}$$

where the constants C and m are found from Table 3.1 [85;86].

Re	C	m
0.4-4	0.989	0.330
4-40	0.911	0.385
40-4000	0.683	0.466
4000-40,000	0.193	0.618
40,000-400,000	0.027	0.805

Table 3.1: Constants for circular cylinder in cross-flow

Again, using certain approximations, it is possible to define a single equation to describe the Nusselt number correlation to account for a large range of conditions [87]. The following expression can be used provided $Re \cdot Pr > 0.2$,

$$\overline{Nu} = 0.3 + \frac{0.62 Re^{\frac{1}{2}} Pr^{\frac{1}{3}}}{\left[1 + \left(0.4 / Pr\right)^{\frac{2}{3}}\right]^{\frac{1}{4}}} \left[1 + \left(\frac{Re}{282{,}000}\right)^{\frac{5}{8}}\right]^{\frac{4}{5}} \tag{3.31}$$

3.6.3. Non-circular cylinders in cross-flow

Equation (3.30) can also be applied to shapes other than circular cross sections, where the constants are defined in Table 3.2 [86].

Geometry	*Re*	*C*	*m*
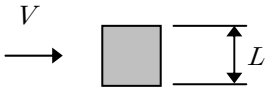	$5\times10^3-10^5$	0.246	0.588
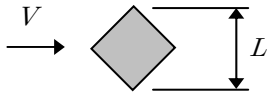	$5\times10^3-10^5$	0.102	0.675
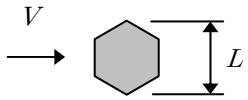	$5\times10^3-1.95\times10^4$ $1.95\times10^4-10^5$	0.160 0.0385	0.638 0.782
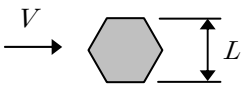	$4\times10^3-1.5\times10^4$	0.153	0.638

Table 3.2: Constants for non-circular cylinder cross-flow

3.6.4. Sphere in cross-flow

The boundary layer effects for a sphere in cross-flow are very similar to those for a circular cylinder as shown in Figure 3.6. Although perhaps not common in structural engineering applications, for completeness its Nusselt number is presented here. Commonly it is used to evaluate convective heating of thermocouple beads.

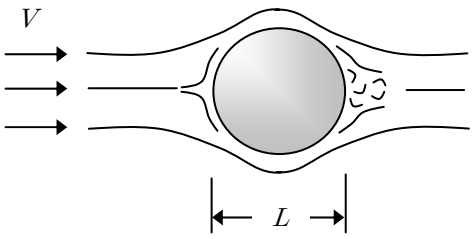

Figure 3.6: Boundary layers caused by a sphere in a cross-flow

The Nusselt number correlation for a sphere is given as [88],

$$\overline{Nu} = 2 + \left(0.4 Re^{\frac{1}{2}} + 0.06 Re^{\frac{2}{3}} \right) Pr^{\frac{2}{5}} \left(\frac{\mu}{\mu_s} \right)^{\frac{1}{4}} \quad \begin{bmatrix} 0.71 < Pr < 380 \\ 3.5 < Re < 7.6 \times 10^4 \end{bmatrix} \tag{3.32}$$

3.7. Application to the Heat Transfer Coefficient

Having defined the Nusselt number correlations for a range of geometries that could be present in structural elements, it is now possible to investigate the role that all the underlying parameters play on the outcome of the convective heat transfer coefficient. The preceding sections show that in the case of forced convection, h_c is a function of the gas properties (k, μ, ρ, Pr), the gas velocity V and the geometrical length scale L. The gas properties are all temperature dependent [89] and are shown in Figure 3.7 to Figure 3.10.

A parametric study of the temperature, length scale and velocity parameters is undertaken in the section below.

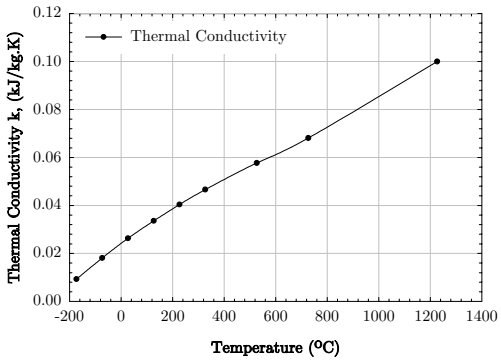

Figure 3.7: Thermal conductivity of air with temperature

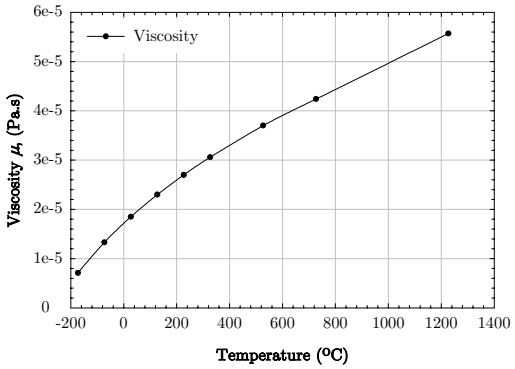

Figure 3.8: Viscosity of air with temperature

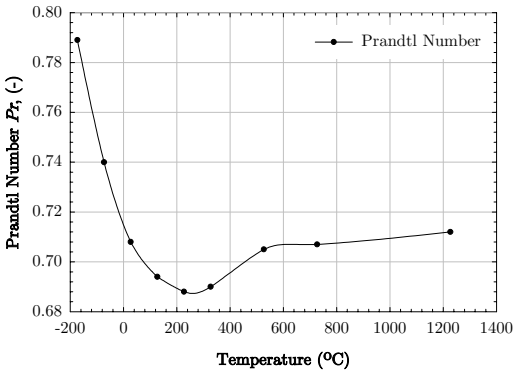

Figure 3.9: Prandtl number of air with temperature

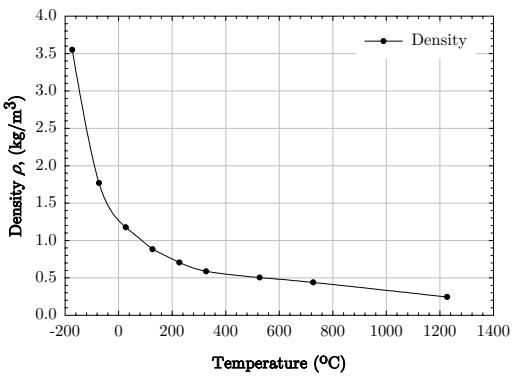

Figure 3.10: Density of air with temperature

3.7.1. Temperature dependence

A range of structural temperatures commonly encountered in structural fire engineering, including cooling for interest results in a limit of -200 to approximately 1300°C. The dependence of the convective heat transfer coefficient on this range can be explored by keeping the length scale and velocity constant. In this case the length scale is set to 0.1m. This represents the order of magnitude associated with typical structural elements such as beam flanges and webs [88]. The velocity is set to 8m/s to represent the typical flow associated with ventilation openings and the upper limits of velocities that could potentially be present in large scale compartment fires [90;91]. This allows the relationship shown in Figure 3.11 to be determined.

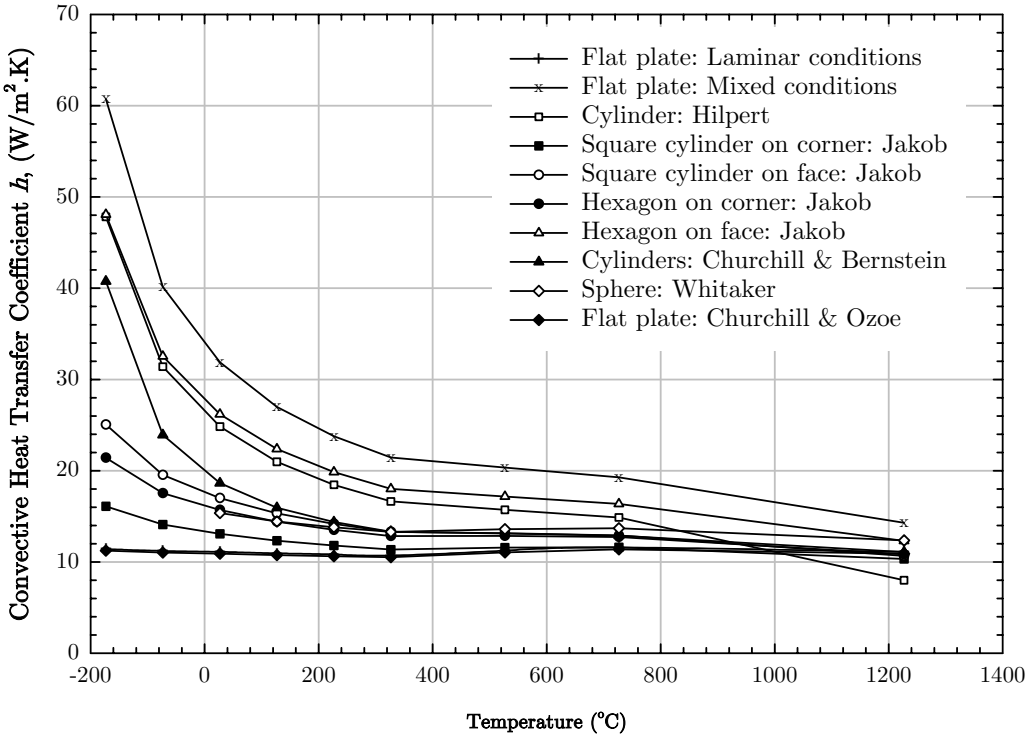

Figure 3.11: Convective heat transfer coefficient dependence on temperature for multiple geometrical conditions in forced convection

From Figure 3.11 it is clear that the convective heat transfer is strongly influenced at very low temperatures. However, if the low temperatures are ignored and focus is given to temperatures expected in compartment fires, typically anything in excess of ambient (20°C) then reasonably little variation is present with changing temperature and in most cases this decreases to negligible difference at very high typical compartment temperatures. In the case of the flat plate correlations, which are very common in structural applications, the heat transfer coefficient remains almost constant for the pure laminar and for the universal laminar correlation developed by Churchill and Ozoe [83]. From the plot it seems reasonable to assume that for hot temperatures a constant heat transfer coefficient can be used in heat transfer calculations. For the following parameters the choice of temperature is not an issue, providing a temperature at or above ambient is used.

3.7.2. Length scale dependence

A study of the dependence of the convective heat transfer coefficient on the length scale is undertaken for a range of length scales that could be encountered in structural members from the widths of beam flanges in the order of millimetres through to longer lengths that could comprise entire lengths of continuous walls of the order of tens of meters. Figure 3.12 is created assuming an ambient temperature and a velocity of 8m/s as outlined in section 3.7.1.

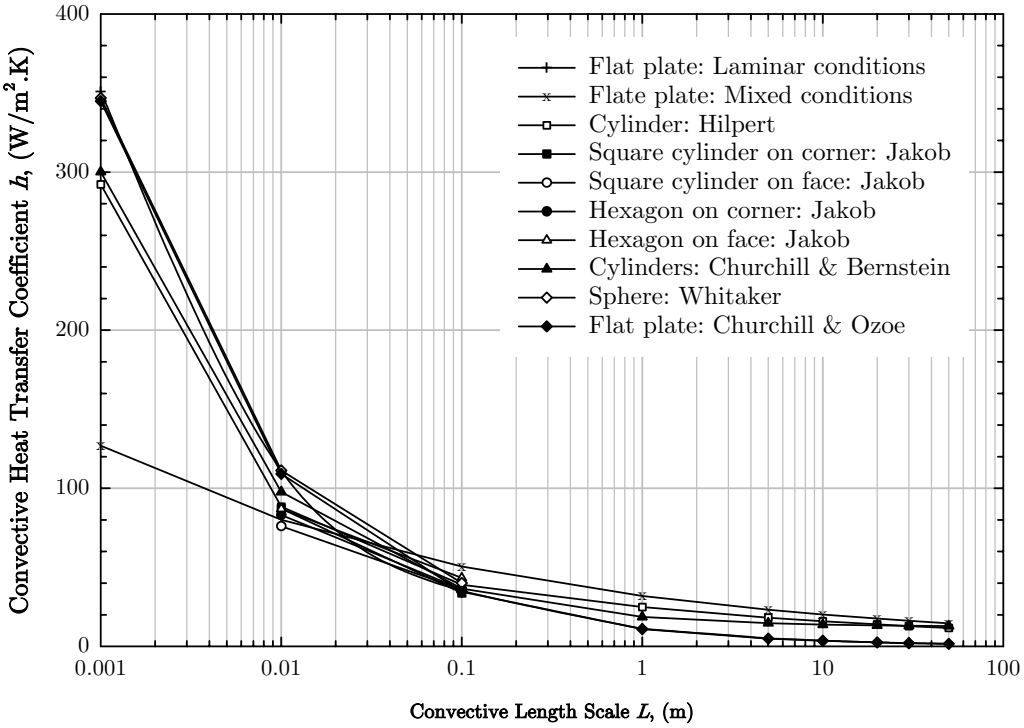

Figure 3.12: Convective heat transfer coefficient dependence on length scale for multiple geometrical conditions in forced convection

For each geometrical condition, as convective length is increased, there is a significant reduction in the average heat transfer coefficient until approximately L=0.1m when this reduction begins to stagnate. The reduction follows a significant decay and highlights the importance of the coefficient at small length scales. In terms of heat transfer to structural

elements this implies that small elements such as truss members that could have length scales of approximately 25mm would heat at a more rapid rate than, for example the web of an I-beam made of the same material subject to a flow along its primary axis.

3.7.3. Velocity dependence

In investigating the dependence of the heat transfer coefficient on velocity of the gas it is assumed that the velocity is induced by some external source such as a broken window providing a source of ventilation or from some other external opening. Velocity measurements in large scale fires are relatively scarce in the available literature, however several sources [90;91] provide data from which a range of possible velocities can be established. As a result, in this study a range of 2m/s to 25m/s are investigated although it is extremely unlikely that a velocity of 25m/s will ever be created without some extreme external source.

Figure 3.13 is created assuming a constant ambient temperature and a typical length scale of 0.1m to represent a structural element as outlined in section 3.7.1. The heat transfer coefficient is seen to increase monotonically with velocity. The rate of increase is associated with the flow type of the gas around the structural element being considered. For turbulent flow regimes such as that over the flat plate and those induced by impinging on non-circular geometry [83;86] the rate of increase is slightly higher than laminar flow situations. The increase in turbulence leads to an increased boundary layer thickness, for which conditions are characterised by highly random, three-dimensional motion of relatively large parcels of gas that cause significant increases in wall shear stresses and convection coefficients [82].

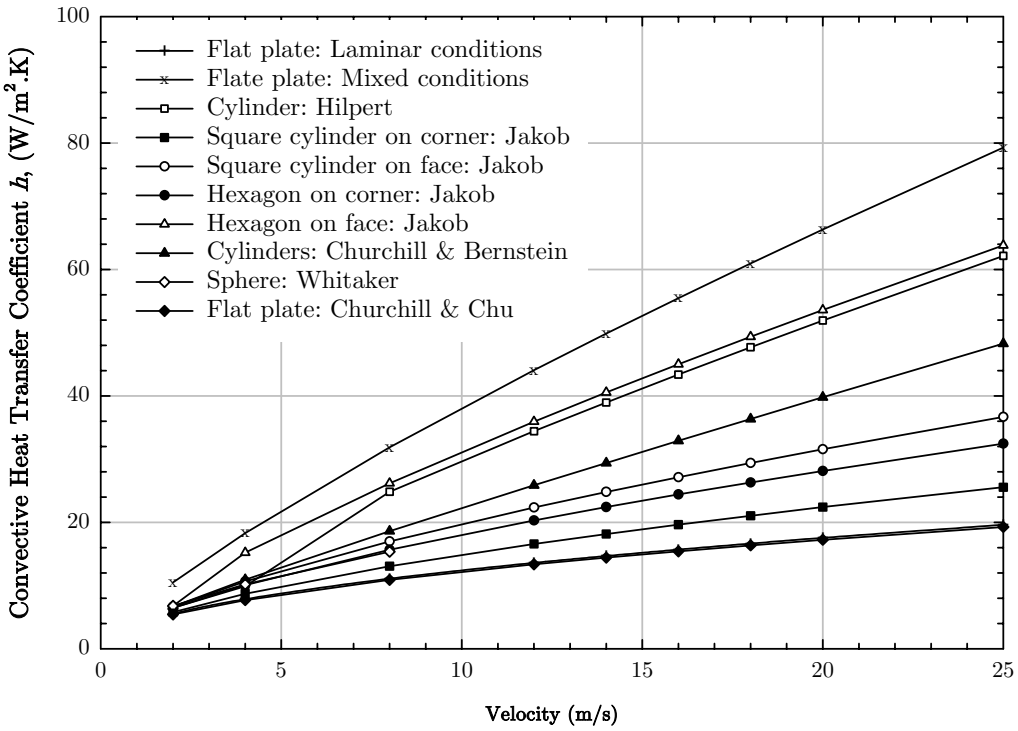

Figure 3.13: Convective heat transfer coefficient dependence on velocity for multiple geometrical conditions in forced convection

3.8. Free Convection

In the situation where there is no forced velocity, convection currents may still exist in the gas. These are known as free or natural convection and occur when a body force acts on a fluid in which there are density gradients resulting in a buoyancy force causing free convection currents. In the case of compartment fires, the density gradient is due to temperature gradients and the body force is due to the gravitational field creating quiescent flow conditions. Due to the fact that free convection flow velocities are lower than those associated with forced convection, the corresponding heat transfer rates are also lower.

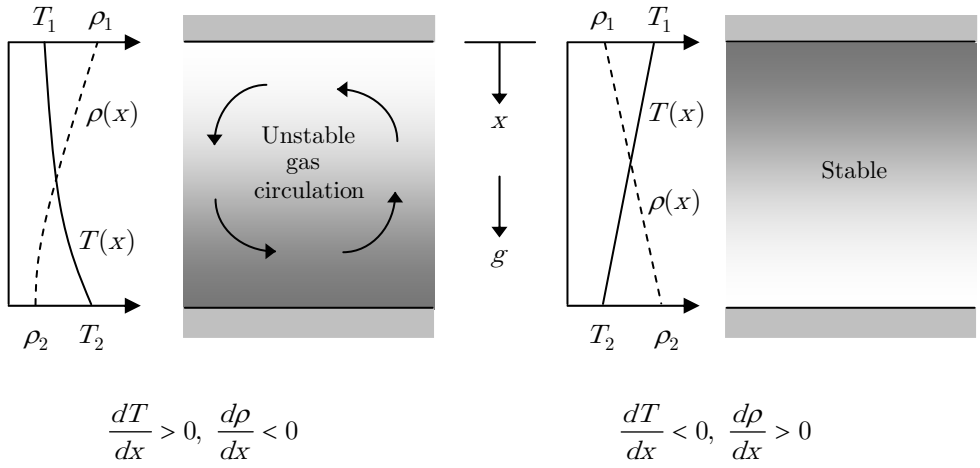

Figure 3.14: Conditions in a gas between two horizontal plates at different temperatures. (a) Unstable temperature gradient. (b) Stable temperature gradient.

The conditions of free convection are shown in Figure 3.14 where in (a) the temperature of the lower plate exceeds that of the upper plate and density is seen to decrease in the direction of gravity. If the temperature difference is sufficiently high then conditions in the gas become unstable and buoyancy forces are able to overcome the viscous forces. The force of gravity on the denser gas in the upper layers is greater than that acting on the lighter fluid in the lower layers causing the heavier gas to descend and increase in temperature during the process, while the lighter fluid rises and cools. This process induces circulation patterns as shown in the figure. In the case of the upper plate which is hotter than the lower plate (b) this situation creates stable conditions where there is no bulk gas motion and heat transfer is seen to occur from top to bottom by means of conduction.

In the case of the governing conservation equations, the continuity equation (3.14) and energy equation (3.15) remain the same as for forced

convection. However, the buoyancy effects of free convection are incorporated into the momentum equation which is written as,

$$u\frac{\partial u}{\partial x}+v\frac{\partial u}{\partial y}=g\beta\left(T_{\infty}-T\right)+v\frac{\partial^{2}u}{dy^{2}} \tag{3.33}$$

where g is the force due to gravity and β is the expansion coefficient calculated from the absolute temperature as is given,

$$\beta=\frac{1}{T} \tag{3.34}$$

If the similarity considerations outlined in section 3.5 are applied to the equations of free convection then the momentum equation can be rewritten,

$$u^{*}\frac{\partial u^{*}}{\partial x^{*}}+v^{*}\frac{\partial u^{*}}{\partial y^{*}}=\frac{g\beta\left(T_{\infty}-T_{s}\right)L}{u_{0}^{2}}T^{*}+\frac{1}{Re}\frac{\partial^{2}u^{*}}{dy^{*2}} \tag{3.35}$$

The unknown reference velocity u_0^2 is inconvenient and it is commonly multiplied by $Re^2=(u_0^2L/v)^2$ to create the Grashof number,

$$Gr\equiv\frac{g\beta\left(T_{\infty}-T_{s}\right)L}{u_{0}^{2}}\left(\frac{u_{0}^{2}L}{v}\right)^{2}=\frac{g\beta\left(T_{\infty}-T_{s}\right)L^{3}}{v^{2}} \tag{3.36}$$

The Grashof number is the ratio of buoyancy force to the viscous force and has a similar role in free conduction to the Reynold's number in forced convection. These two parameters can be used to determine which flow conditions are present and hence deduce what form the heat transfer correlations will take. The scenarios are presented in Table 3.3.

Condition	Flow Type	Correlation Form
$(Gr / Re^2) << 1$	Forced	$Nu = f(Re, Pr)$
$(Gr / Re^2) \approx 1$	Combined free and forced	$Nu = f(Re, Gr, Pr)$
$(Gr / Re^2) >> 1$	Free	$Nu = f(Gr, Pr)$

Table 3.3: Free and forced convection definitions

Free convection boundary layers can also be turbulent, arising from hydrodynamic instabilities that can become amplified. The transition from laminar flow to turbulent can be defined in terms of the Rayleigh number, which for vertical plates is,

$$Ra = Gr \cdot Pr \approx 10^9 \tag{3.37}$$

3.8.1. Vertical plates

Vertical plates are extremely common in structural engineering, comprising walls, and exposed column faces. Figure 3.15 shows the case of the plate being exposed to hot and cool atmospheric surroundings.

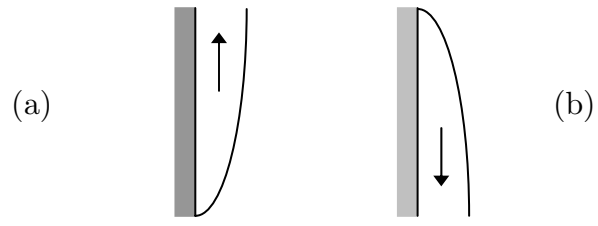

Figure 3.15: Free convective flow over (a) hot vertical plate exposed to cooler surroundings and (b) cold plate exposed to hotter surroundings

The Nusselt number correlation for a vertical plate is given in the form,

$$\overline{Nu} = C \cdot Ra^{n} \tag{3.38}$$

Where the constants C and n can be taken from Figure 3.16 [82;92-94].

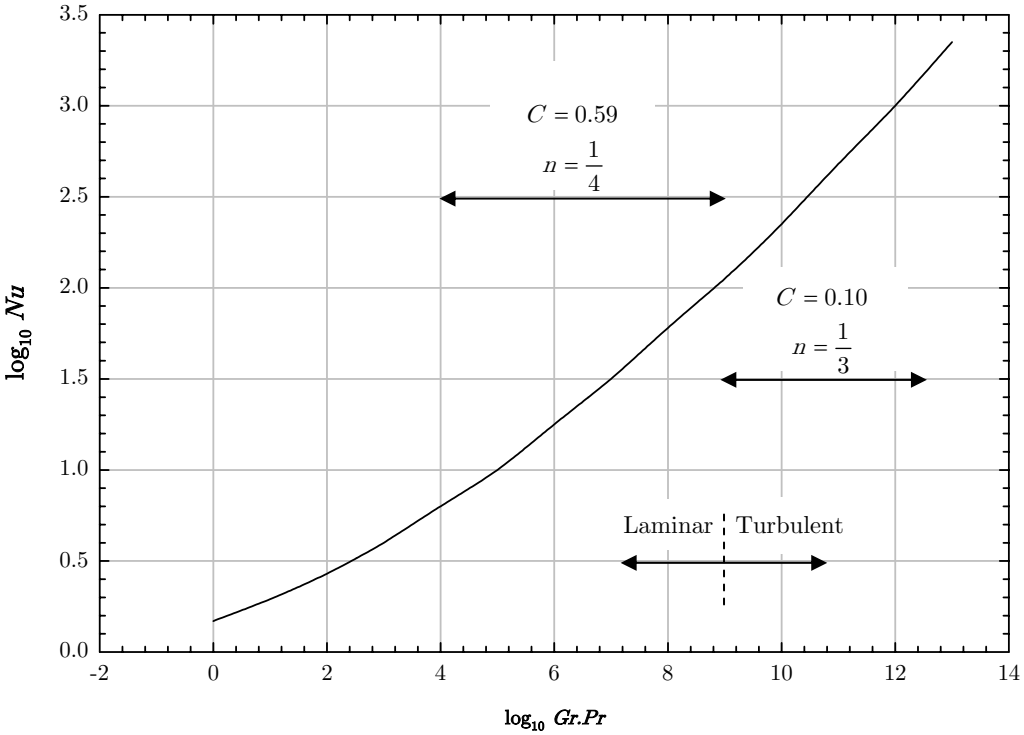

Figure 3.16: Nusselt number for free convection heat transfer from a vertical plate

A correlation that can be applied over the entire range of Ra [95] is in the form of,

$$\overline{Nu} = \left\{ 0.825 + \frac{0.387 Ra^{\frac{1}{6}}}{\left[1 + \left(0.492 / Pr \right)^{\frac{9}{16}} \right]^{\frac{2}{27}}} \right\}^{2} \tag{3.39}$$

However, slightly better accuracy for laminar flows [95]is given by,

$$\overline{Nu} = 0.68 + \frac{0.670 Ra^{\frac{1}{4}}}{\left[1 + \left(0.492 / Pr\right)^{\frac{9}{16}}\right]^{\frac{4}{9}}} \qquad Ra \le 10^9 \tag{3.40}$$

3.8.2. Inclined plates

Structural elements that can be approximated as inclined plates as shown in Figure 3.17 exhibit a very similar behaviour to vertical plates. The only difference is that the buoyancy force has a component normal, as well as parallel to the surface. As such the gravitational acceleration g must be reduced to $g\cos\theta$ where $0 \le \theta \le 60^{\circ}$. The Nusselt number correlation in equation (3.39) is applicable for this geometry.

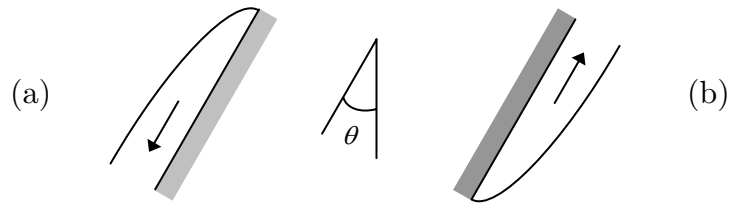

Figure 3.17: Free convection flow over inclined plates (a) cold surface up and (b) hot surface down

3.8.3. Horizontal plates

Horizontal plates are common in many structural engineering applications, including ceilings, floors and lower flanges of beams. Depending on the orientation of the structural element and temperature with respect to its surroundings, two distinct scenarios can be identified [93] as shown in Figure 3.18. In the case of the upper surface of a plate of the lower surface of a cooled plate being subject to convective flows (a), the following Nusselt number correlations can be applied,

$$\overline{Nu} = 0.54 Ra^{\frac{1}{4}} \qquad (10^4 \le Ra \le 10^7) \tag{3.41}$$

$$\overline{Nu} = 0.15 Ra^{\frac{1}{3}} \qquad (10^7 \le Ra \le 10^{11}) \tag{3.42}$$

In the case of convective flows to the lower surface of a heated plate or the upper surface of a cooled plate (b), the following Nusselt number correlation is given,

$$\overline{Nu} = 0.27 Ra^{\frac{1}{4}} \qquad (10^5 \le Ra \le 10^{10}) \tag{3.43}$$

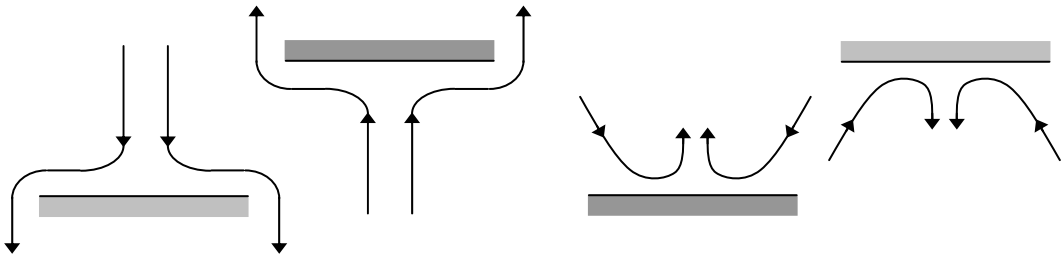

(a) (b)

Figure 3.18: Free convection flow over horizontal plates (a) cold surface up or hot surface down (b) hot surface up or cold surface down

3.8.4. Cylinder

As mentioned above in the discussion of forced convection, cylinders (Figure 3.19) are common to structural engineering problems, most notably in the use of truss systems. The long horizontal cylinder has been the focus of much work in heat transfer and correlations are expressed in the form of equation (3.38) where the constants are found in Table 3.4 [96].

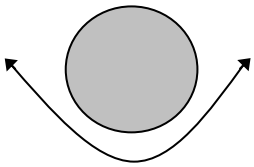

Figure 3.19: Horizontal cylinder exposed to free convective flow

Ra	C	m
$10^{-10} - 10^{-2}$	0.675	0.058
$10^{-2} - 10^{2}$	1.020	0.148
$10^{2} - 10^{4}$	0.850	0.188
$10^{4} - 10^{7}$	0.480	0.250
$10^{7} - 10^{12}$	0.125	0.333

Table 3.4: Constants for free convection on a horizontal circular cylinder

Other research [97] has led to a proposed solution to take account of all a wide range of Rayleigh numbers,

$$\overline{Nu} = \left\{ 0.60 + \frac{0.387 Ra^{\frac{1}{6}}}{\left[1 + \left(0.559 / Pr \right)^{\frac{9}{16}} \right]^{\frac{8}{27}}} \right\}^{2} \qquad Ra \le 10^{12} \qquad (3.44)$$

3.8.5. Sphere

The case of a sphere in free convection is very similar to that of a horizontal cylinder as shown in Figure 3.20. Although a sphere may not

be commonly found in structural engineering applications, it is included here in terms of completeness from a heat transfer perspective.

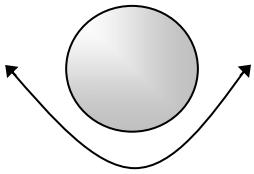

Figure 3.20: Sphere exposed to free convective flow

Research [98] has lead to the following Nusselt number correlation,

$$\overline{Nu} = 2 + \frac{0.589 Ra^{\frac{1}{4}}}{\left[1 + \left(0.469 / Pr\right)^{\frac{9}{16}}\right]^{\frac{4}{9}}} \qquad Ra \le 10^{11} \; and \; Pr \ge 0.7 \qquad (3.45)$$

3.9. Application to the Heat Transfer Coefficient

Having defined the Nusselt number correlations in free convection for a range of structural geometries it is now possible to investigate the role that all the underlying parameters play on the convective heat transfer coefficient. The preceding sections show that in the case of free convection, h_c is a function of the gas properties (v, β, Pr) and the geometrical length scale L. The gas properties are all temperature dependent and are represented in Figure 3.21 and Figure 3.22. These allow for a parametric study of temperature and length scale parameters in free convection. In the case of free convection, air is assumed to be quiescent and therefore the heat transfer coefficient is not affected by the velocity of the gas.

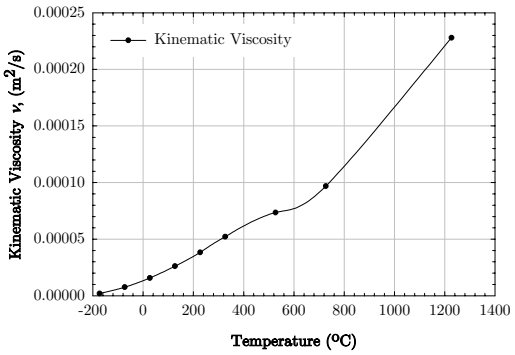

Figure 3.21: Kinematic viscosity of air with temperature

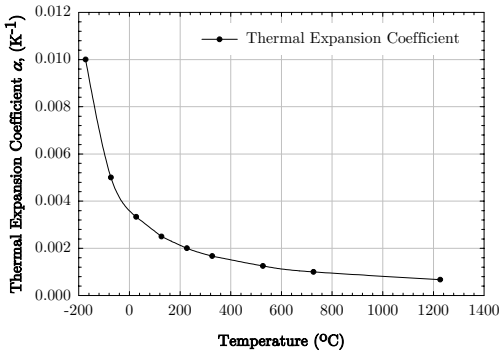

Figure 3.22: Thermal expansion coefficient of air with temperature

3.9.1. Temperature dependence

For each of the geometrical arrangements discussed above, the variation of the heat transfer coefficient is determined for a range of temperatures common to structural fire engineering as discussed in section 3.7.1. In all cases, a constant length scale of 0.1m is again adopted to represent an order of magnitude associated with a typical structural element. Figure 3.23 shows the relationship with temperature. A very similar pattern is found for free convection in comparison to forced convection, although the magnitude of the heat transfer coefficient is generally of a lower order due to the lack of influence of gas velocity that helps to create turbulent flows that increase the efficiency of heat transfer from the gas to the structure.

At high temperatures that are typical of compartment fires, the heat transfer coefficient is relatively stable and can be assumed to take a single representative value for each geometrical correlation. At lower temperatures, the heat transfer coefficient is seen to increase with decreasing temperature, however this relationship really only becomes pronounced below ambient conditions and can therefore be neglected in the case of compartment fires.

In the cases of the vertical plate, approximating a wall and horizontal plate with its lower side heated, approximating a slab – two of the most common geometries in structural engineering, there is almost no variation over the whole temperature range. This further suggests that a single heat transfer coefficient for a given length scale is sufficient to describe the heat transfer.

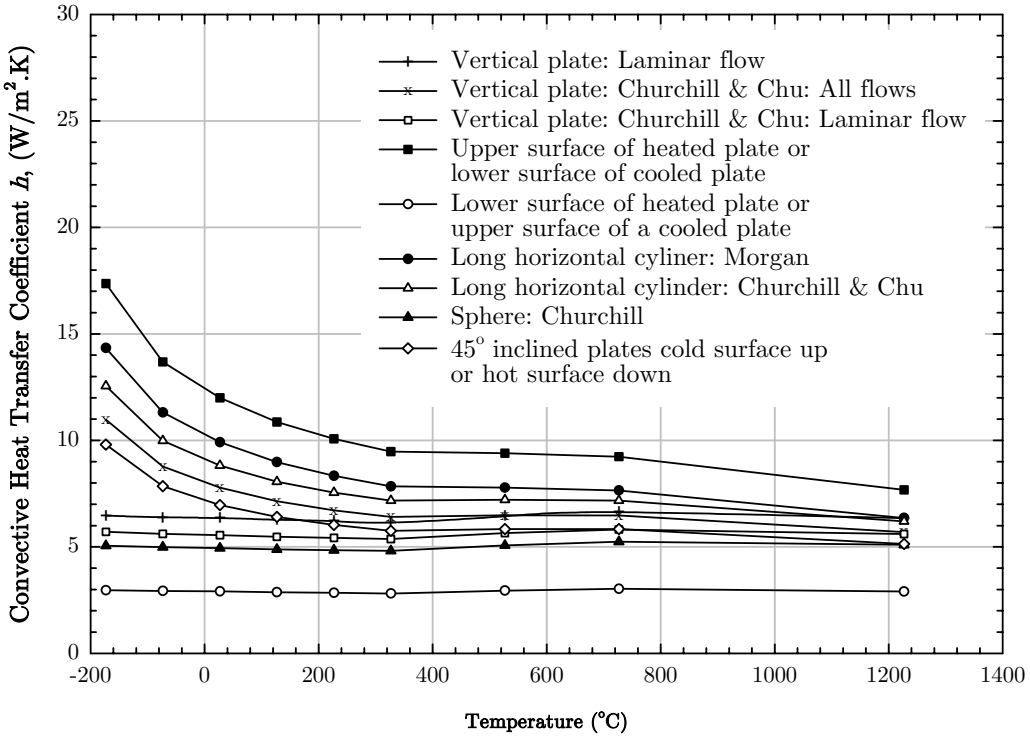

Figure 3.23: Convective heat transfer coefficient dependence on temperature for multiple geometrical conditions in free convection

3.9.2. Length scale dependence

The dependence of the heat transfer coefficient on length scale has been undertaken at ambient temperature for the range of likely structural scales as outlined in section 3.7.2. The correlations for different geometrical conditions are shown in Figure 3.24.

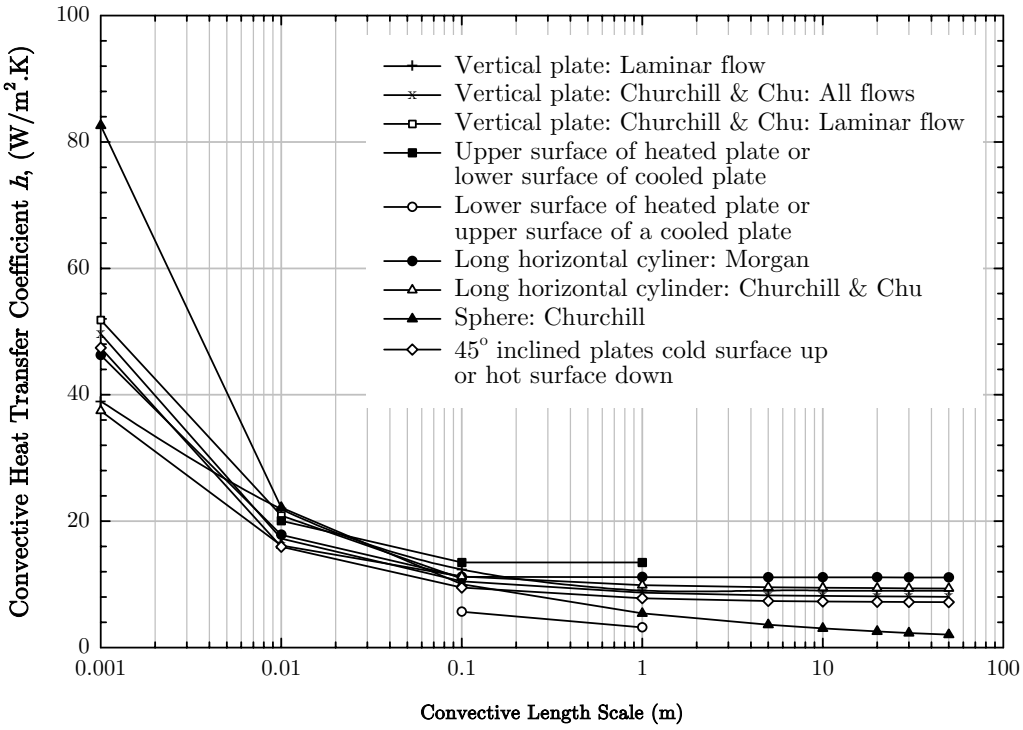

Figure 3.24: Convective heat transfer coefficient dependence on length scale for multiple geometrical conditions in free convection

A similar relationship to that of forced convection is observed, again with the magnitude of the coefficient being lower due to the lack of associated velocity. In general, a strong relationship is observed whereby the heat transfer coefficient appears to decay exponentially to constant value at about L=0.1m. If the case of the sphere is neglected due to its infrequent occurrence in structural applications, then a similar trend is found for the remaining geometrical conditions.

3.10. Convection within FDS

When estimating convective heat transfer using numerical models, strong approximations are necessary. These approximations are related mostly to the principles used to solve the transport equations, thus need to be discussed in the context of the specific techniques.

The convective heat transfer to the walls for a large eddy simulation (LES) code is very difficult to establish because cell sizes are defined to correspond to the characteristic length scale of a large eddy. Large eddies are generally several centimetres in size, thus they tend to be greater than the boundary layers. Several techniques have been reported in the literature. Given that the most commonly used LES numerical tool in fire is FDS, attention is given toward the treatment of given to this boundary condition by this code.

Within FDS [66] the convective heat transfer coefficient is obtained from a combination of natural and forced convection correlations. The convective flux is calculated as,

$$\dot{q}_c'' = h\Delta T \tag{3.46}$$

where ΔT is the temperature difference between the wall and the gas and is taken at the centre of the grid cell abutting the wall. The convective coefficient h, is determined by,

$$h = \max\left[C\left|\Delta T\right|^{\frac{1}{3}} \ , \ \frac{k}{L} 0.037 Re^{\frac{4}{5}} Pr^{\frac{1}{3}} \right] \tag{3.47}$$

where C is the coefficient for natural convection given as 1.43 for a horizontal surface and 0.95 for a vertical surface. The latter case correlation of equation (3.47) uses a Nusselt number correlation for a flat plate in a mixed laminar and turbulent flow. The FDS Technical Reference [66] states that: 'because the Reynold's number is proportional to the characteristic length L, then the heat transfer coefficient is weakly related to L. For this reason L is taken to be 1m for most calculations.' With reference to Figure 3.24, assuming L to be 1m may be justified when

large grid cells are used – commonly greater than 0.1m. This ensures that convective heat fluxes are evaluated in an accurate manner. However, if structural elements of smaller length scale than the grid size resolution are to be investigated, then a higher heat transfer coefficient is required resulting in convective and therefore total heat fluxes being underestimated.

Furthermore, for convective heat transfer correlations to be valid, the basic premise of an external flow and a boundary layer has to be respected. Therefore, calculations could be strongly grid dependent. If the cell size is too big, then the average value is not representative of the external flow condition. Alternatively, if the cell size is too small then the temperature might not correspond to a location internal to the boundary layer. The former condition is common when modelling large volumes, while the latter will generally not occur in LES simulations where cell sizes tend to be significantly larger than the boundary layers. This is more relevant for DNS computations.

3.11. Conclusions

Empirical correlations for the convective heat transfer coefficient have been reviewed for both forced and free convection with emphasis being given to the impact on structural elements. A parametric study of both flow conditions revealed relationships of the transfer coefficient in terms of temperature, length scale and velocity. In both cases, temperatures typical to compartment fires do not dramatically alter the coefficient and therefore a single representative value can be adopted. Variation with velocity is generally only applicable to forced convection, the conditions of which are only likely to be encountered in compartment fires near to ventilation openings. Increased velocity is seen to increase the heat transfer coefficient in an almost linear trend. From a structural engineering standpoint,

variation in length scales has the most important relationship to the heat transfer coefficient. Extremely high coefficients can be achieved in both free and forced convection if the length is very small, for example in the order of 1mm. The heat transfer coefficient decreases extremely rapidly with increasing length scale until a constant value is maintained above lengths of approximately 0.1m. This has big implications in that often structural elements such as trusses and flange and web thicknesses can have associated length scales of less than 0.1m. When this is this case, the convective heat transfer coefficient can be high. In the case of FDS, the convective heat transfer to the wall is undertaken assuming a constant length scale of 1m, which for most situations will yield an acceptable coefficient, however if results are to be extracted and applied to structural elements that are too small to be represented within the adopted grid resolution then convective and therefore total heat fluxes may be under predicted.

It has been demonstrated that when calculating convective heat fluxes, the length scale must be carefully taken into account, especially when CFD results provide the basis of the analysis.

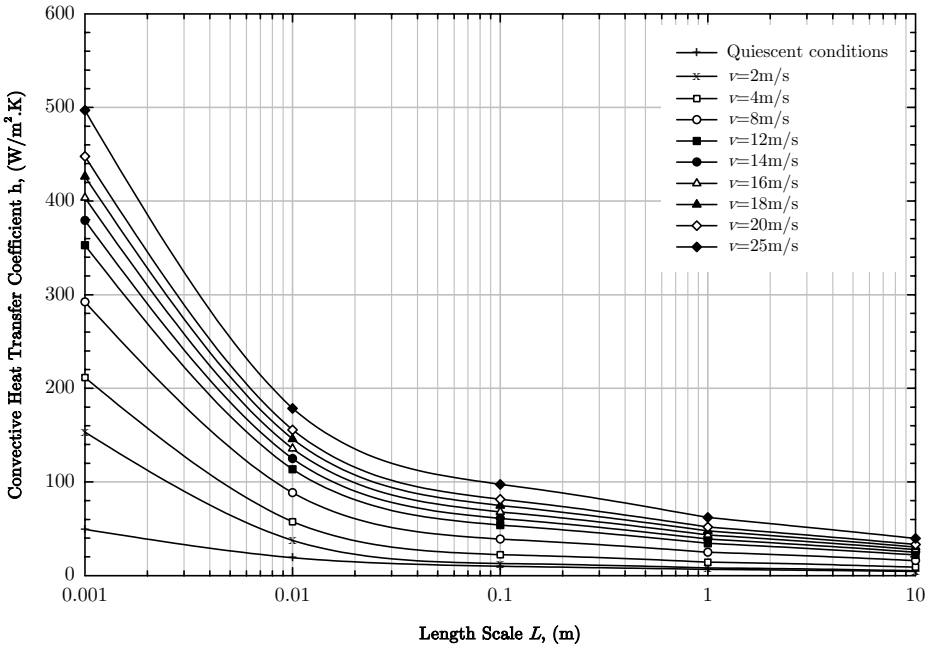

Figure 3.25: Simplified relationship between convective heat transfer coefficient with length scale and velocity

As it has been shown that length scale and velocity are the two main influences on the convective heat transfer coefficient, it is entirely plausible that a single fit could be applied to these curves that could account for any structural geometry that would consider the increased heat transfer coefficient for small length scales that are familiar with structural member such as trusses and flange thicknesses. As a result, a summary plot as shown in Figure 3.25 can be produced to determine the heat transfer coefficient based on a given length scale and flow velocity.

Chapter Four

4. Radiative Heat Transfer

4.1. Introduction

In large scale fires, radiation is often considered the dominant mode of heat transfer with the process involving the exchange of energy between surfaces together with the emission and absorption by various gases and soot particles.

This chapter introduces the basic framework of thermal radiation before investigating the underlying parameters to demonstrate their influence in terms of heat transfer to structural elements. This is achieved by considering typical thermal environments in compartment fires.

4.2. Fundamental Concepts

Figure 4.1 represents a solid that is situated in a vacuum and is initially at a lower temperature than its surroundings. The presence of a vacuum prevents energy loss from the surface of the solid by conduction or convection. The solid heats due to the interception and absorption of thermal radiation emitted from the surroundings while in turn, the surroundings will intercept and absorb radiation emitted from the solid. The net heat transfer is seen to be from the surroundings to the solid until T_s reaches T_∞.

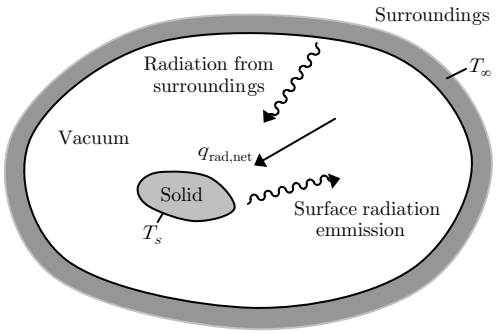

Figure 4.1: Radiative heating of a solid within a vacuum surrounded by a hot gas

Thermal radiation is generally associated with the rate at which energy is emitted by matter as a result of its finite temperature. In reality emission is due to the oscillations or transitions of the many electrons that constitute matter. Therefore radiation can be considered due to the thermally excited conditions within the matter.

Two theories exist as to the nature in which radiation is transported. One theory considers radiation as the propagation of particles called photons or quanta, the second views radiation as the propagation of electromagnetic waves. In the latter case, radiation can be linked to the standard wave properties of frequency υ and wavelength λ which are related as,

$$\lambda = \frac{c}{\upsilon} \tag{4.1}$$

where c is the speed of light in the intervening medium. For a vacuum, $c_0 = 2.998 \times 10^8$ m/s. The entire range of the electromagnetic spectrum is shown in Figure 4.2 in which thermal radiation is associated with heat transfer in compartment fires, most notably the near infrared region that ranges from visible region to about $\lambda = 25\mu$m [48]. The magnitude of radiation varies with wavelength and this dependence is referred to with the term spectral.

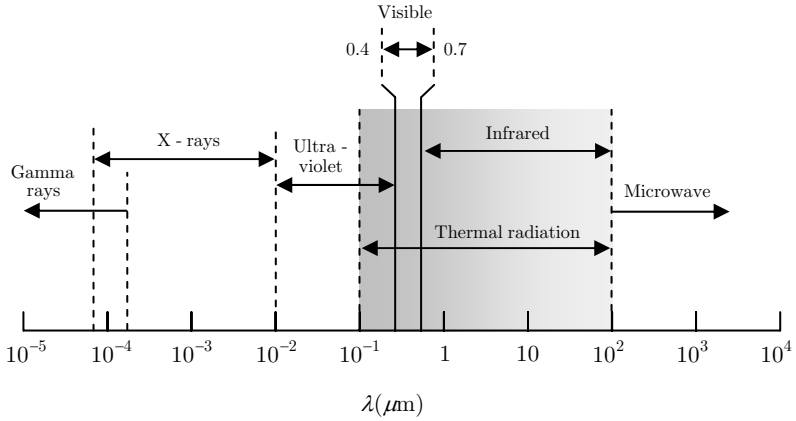

Figure 4.2: Spectrum of electromagnetic radiation

4.3. Radiative Intensity

The directionality associated with radiation can have a large effect on the surface on which it is incident and this is characterised using the concept of radiative intensity. Figure 4.3 (a) shows emission in a particular direction from element dA_1 which can be specified in terms of the zenith and azimuth angles, θ and ϕ respectively, of a spherical coordinate system as in Figure 4.3 (b). A differentially small surface in space dA_n through which the radiation passes, subtends a solid angle $d\omega$ when viewed from a point on dA_1. It can be written that,

$$d\omega = \frac{dA_n}{r^2} \tag{4.2}$$

As the area dA_n is normal to the (ϕ, θ) direction, it may be represented as $dA_n = r^2 \sin\theta d\theta d\phi$ for a spherical surface. Therefore,

$$d\omega = \sin\theta \, d\theta \, d\phi \tag{4.3}$$

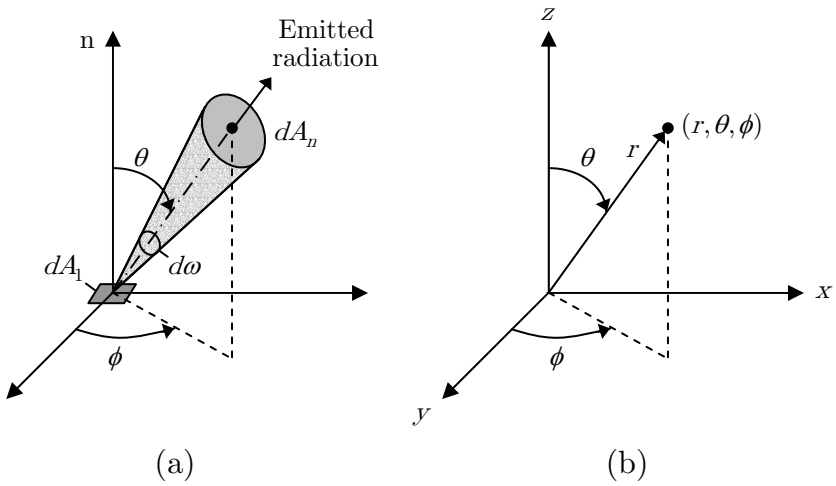

Figure 4.3: Directional nature of radiation. (a) Emission from differential area into a solid angle. (b) Spherical coordinate system

The rate at which emission from dA_1 passes through dA_n is expressed in terms of the spectral intensity $I_{\lambda,e}$ of the emitted radiation. The formal definition of spectral intensity is *'the rate at which radiant energy is emitted at the wavelength λ in the (ϕ,θ) direction, per unit area of the emitting surface normal to this direction, per unit solid angle about this direction, and per unit wavelength interval $d\lambda$ about λ'* [82]. The area that is used to define the intensity is the component of dA_1 perpendicular to the direction of the radiation which defines the spectral intensity as,

$$I_{\lambda,e}(\lambda,\theta,\phi) = \frac{dq}{dA_1 \cos\theta \cdot d\omega \cdot d\lambda} \tag{4.4}$$

where $(dq/d\lambda) \equiv dq_\lambda$ is the rate at which radiation of wavelength λ leaves dA_1 and passes through dA_n, giving,

$$dq_\lambda = I_{\lambda,e}(\lambda,\theta,\phi) dA_1 \cos\theta d\omega \tag{4.5}$$

4.3.1. Emission

The concept of emmissive power allows the amount of radiation emmitted per unit surface area to be quantified. The spectral, hemispherical emissive power E_λ ($\mathrm{W/m^2 \cdot \mu m}$) is defined as the rate at which radiation of wavelength λ is emitted in all directions from a surface per unit wavelength $d\lambda$ about λ and per unit surface area. It is written,

$$E_\lambda(\lambda) = \int_0^{2\pi} \int_0^{\pi/2} I_{\lambda,e}(\lambda,\theta,\phi) \cos\theta \sin\theta d\theta d\phi \tag{4.6}$$

and the total, hemispherical emissive power, E ($\mathrm{W/m^2}$), is the rate at which radiation is emitted per unit area at all possible wavelengths and in all possible directions, giving,

$$E = \int_0^\infty E_\lambda(\lambda) d\lambda \tag{4.7}$$

The term 'emissive power' implies emission in all directions and allows for the adjective 'hemispherical' to be dropped so that references are made to spectral emissive power E_λ or the total emissive power E.

If the intensity of the emitted radiation is independent of direction, then a surface can be referred to a diffuse emitter. In this case $I_{\lambda,e}(\lambda,\theta,\phi) = I_{\lambda,e}(\lambda)$ and therefore $I_{\lambda,e}$ can be removed from the integrand of equation (4.6), giving,

$$E_\lambda(\lambda) = \pi I_{\lambda,e}(\lambda) \tag{4.8}$$

4.3.2. Irradiation

The foregoing concepts consider radiation emitted by a surface, however they may be extended to incident radiation as in the case of fire environments to structural elements. Such radiation may originate from emission and reflection occuring at other surfaces and will have spectral and directional distributions determined by the spectral intensity $I_{\lambda,i}(\lambda,\theta,\phi)$. Spectral irradiation can be written in a similar manner to equation (4.6),

$$G_\lambda(\lambda) = \int_0^{2\pi}\int_0^{\pi/2} I_{\lambda,i}(\lambda,\theta,\phi)\cos\theta\sin\theta d\theta d\phi \tag{4.9}$$

and total irradiation is given in a similar manner to equation(4.7) by,

$$G = \int_0^\infty G_\lambda(\lambda)d\lambda \tag{4.10}$$

while if the incident radiation is diffuse,

$$G_\lambda(\lambda) = \pi I_{\lambda,i}(\lambda) \tag{4.11}$$

4.3.3. Radiosity

The term radiosity accounts for all of the radiant energy leaving a surface. This includes direct emission together with the reflected portion of the irradiation as shown in Figure 4.4.

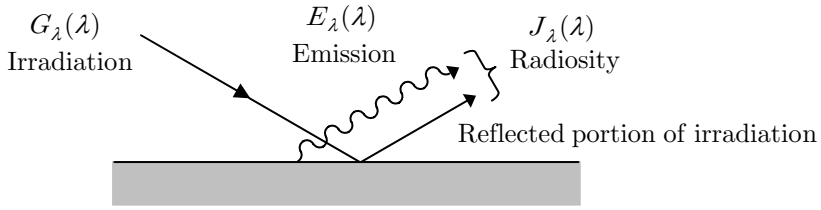

Figure 4.4: Surface radiosity

Following on from the previous definitions, the spectral radiosity is written,

$$J_\lambda(\lambda) = \int_0^{2\pi} \int_0^{\pi/2} I_{\lambda,e+r}(\lambda,\theta,\phi)\cos\theta \sin\theta d\theta d\phi \tag{4.12}$$

and the total radiosity is given,

$$J = \int_0^\infty J_\lambda(\lambda) d\lambda \tag{4.13}$$

and if the surface is both a diffuse emitter and a diffuse reflector, then,

$$J_\lambda(\lambda) = \pi I_{\lambda,e+r}(\lambda) \tag{4.14}$$

4.4. Blackbody Radiation

A blackbody is considered an ideal radiating surface and its concept is used to describe the characteristics of real surfaces and indeed serves as the standard against which they can be compared. A blackbody can be characterised by: -

- Absorbs all incident radiation, regardless of wavelength and direction

- For a given temperature and wavelength, no surface can emit more energy than a blackbody
- A blackbody is a diffuse emitter in that it is independent of wavelength

The spectral distribution of a blackbody emission takes the form,

$$I_\lambda(\lambda,T)=\frac{2hc_o^2}{\lambda^5\left[\exp\left(hc_o/\lambda kT\right)-1\right]} \tag{4.15}$$

where $h=6.6256\times10^{-34}\,\mathrm{J\cdot s}$ and $k=1.3805\times10^{8}\,\mathrm{J/K}$ are the universal Planck and Boltzmann constants respectively, c_o is the speed of light in a vacuum and T is the absolute temperature of the blackbody. From equation (4.8), the spectral emissive power is of the form,

$$E_{\lambda,b}(\lambda,T)=\pi I_{\lambda,b}(\lambda,T)=\frac{C_1}{\lambda^5\left[\exp\left(C_2/\lambda T\right)-1\right]} \tag{4.16}$$

with the first and second constants $C_1=2\pi hc_o^2=3.742\times10^{8}\,\mathrm{W\cdot\mu m^4/m^2}$ and $C_2=\left(hc_o/k\right)=1.439\times10^{4}\,\mu\mathrm{m\cdot K}$. Equation (4.16) is known as the Plank distribution and is plotted in Figure 4.5.

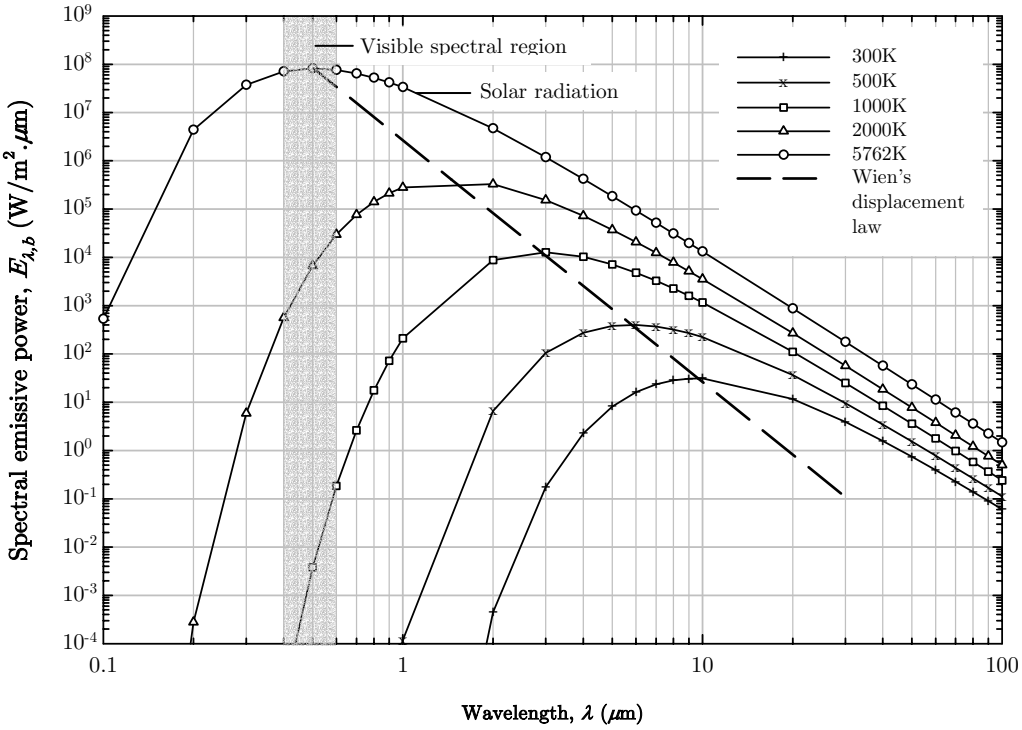

Figure 4.5: Spectral blackbody emissive power

A significant fraction of the radiation emitted by the sun, which may be approximated as a blackbody at 5762K, is in the visible region of the spectrum. In contrast, for temperatures less than 1000K, emission is predominantly in the infrared region of the spectrum and is therefore not visible to the eye.

The locus of points described by Equation (4.16) can be obtained using Wien's displacement law,

$$\lambda_{\max} T = C_3 \tag{4.17}$$

where $C_3 = 2897.8 \mu\text{m} \cdot \text{K}$.

If equation (4.16) is substituted into equation (4.8), the total emissive power of a blackbody can be expressed as,

$$E_b = \int_0^\infty \frac{C_1}{\lambda^5 \left[\exp\left(C_2 / \lambda T\right) - 1\right]} d\lambda \tag{4.18}$$

and performing the integration, it may be shown that,

$$E_b = \sigma T^4 \tag{4.19}$$

where $\sigma = 5.670 \times 10^{-8} \mathrm{W/m^2 \cdot K^4}$ is known as the Stefan-Boltzmann constant and enables the calculation of the amount of radiation emitted in all directions and over all wavelengths simply from the knowledge of the temperature of the blackbody.

4.5. Surface Emissivity

The emissivity of a surface is a radiative property that is defined as the ratio of the radiation emitted by a surface to the radiation emitted by a blackbody at the same temperature. Spectral, directional emissivity is written,

$$\varepsilon_{\lambda,\theta}(\lambda, \theta, \phi, T) \equiv \frac{I_{\lambda,e}(\lambda, \theta, \phi, T)}{I_{\lambda,b}(\lambda, T)} \tag{4.20}$$

In a similar manner, a total, directional emissivity which represents a spectral average of $\varepsilon_{\lambda,\theta}$ can be defined as,

$$\varepsilon_{\theta}(\theta, \phi, T) \equiv \frac{I_e(\theta, \phi, T)}{I_b(T)} \tag{4.21}$$

Most calculations involve surface properties that represent directional averages. Therefore, a spectral, hemispherical emissivity is defined as,

$$\varepsilon_{\lambda}(\lambda,T) \equiv \frac{E_{\lambda}(\lambda,T)}{E_{\lambda,b}(\lambda,T)} \tag{4.22}$$

The total, hemispherical emissivity, which represents an average over all possible directions and wavelengths, is defined as,

$$\varepsilon(T) \equiv \frac{E(T)}{E_{b}(T)} \tag{4.23}$$

If $\varepsilon(T)$ is known, then it can be used with equation (4.19) and equation (4.23) to evaluate the total emissive power of any surface at any temperature by,

$$E(T_s) = \varepsilon(T_s)E_b(T_s) = \varepsilon(T_s)\sigma T_s^4 \tag{4.24}$$

4.6. Absorption, Reflection and Transmission

The preceding sections have discussed the concepts of radiation from the perspective of irradiation incident on a surface and emission from that surface. It is very likely that in reality radiation will be intercepted by some solid or liquid medium. In the case of a semi-transparent medium such as a glass plate as shown in Figure 4.6, for a spectral component of the irradiation, portions of this radiation may be reflected, absorbed and transmitted. If a medium is opaque then $G_{\lambda,tr} = 0$ and the remaining absorption and reflection processes can be treated as surface phenomena.

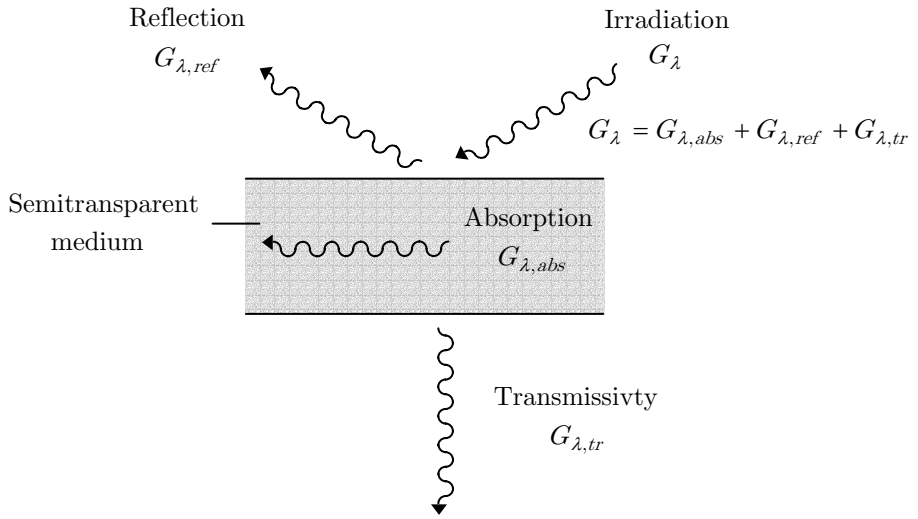

Figure 4.6: Absorption, reflection and transmission processes associated with a semitransparent medium

Absorptivity is a property that determines the fraction of the irradiation absorbed by the surface. The total, hemispherical absorptivity α represents an integrated average over both direction and wavelength is defined as,

$$\alpha \equiv \frac{G_{abs}}{G} \tag{4.25}$$

Reflectivity is the property that determines the fraction of the incident radiation reflected by a surface and the total, hemispherical reflectivity ρ is given as,

$$\rho \equiv \frac{G_{ref}}{G} \tag{4.26}$$

Transmissivity can be a complicated problem [48], although reasonable approximations can be achieved using,

$$\tau \equiv \frac{G_{tr}}{G} \tag{4.27}$$

From the radiation balance in Figure 4.6 and the foregoing definitions it can be written for a fire within an enclosure of uniform temperature containing a medium that has reached its equilibrium state,

$$\alpha_\lambda + \rho_\lambda + \tau_\lambda = 1 \tag{4.28}$$

The assumption of the local dynamic equilibrium is used extensively in heat transfer calculations. Kirchoff's law states that in order to maintain equilibrium, absorptivity and emissivity must be related by,

$$\alpha_\lambda = \varepsilon_\lambda \tag{4.29}$$

The above relation remains valid when total properties are considered and the incident radiation is independent of the incident angle and has the same spectral proportions as the blackbody radiator. When this is the case, the surface is described as a diffuse, grey body.

4.7. Participating Media

The preceding sections have all assumed the medium that separates surfaces to be non-participating in that it neither absorbs nor scatters surface radiation and it emits no radiation itself. However, in the case of compartment fires, the gas environment can have a large effect on the outcome of the heat transfer and its influence results in it being termed a participating media.

The equation of transfer can be used to describe the variation in intensity of a radiant beam at any position along its path in an absorbing-emitting-

scattering medium. In the subsequent sections, irradiation is referred to as radiant intensity and is denoted I. For a given direction line in the medium, the equation of heat transfer is,

$$\frac{1}{\kappa_\lambda(T,L)}\frac{dI_\lambda(L)}{dL} + I_\lambda(L) = I_{\lambda,b}(T) \tag{4.30}$$

where L is the physical path length and κ_λ represents the spectral extinction coefficient. The intensity $I_\lambda(L)$ is coupled with the spatial distribution of the extinction coefficient and temperature through conservation of energy in the medium.

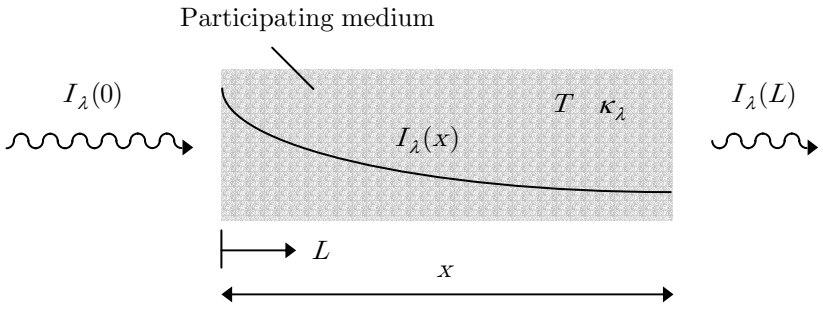

Figure 4.7: Reduction of radiative intensity due to a participating medium

Consider the case of Figure 4.7 where a monochromatic beam of radiation passes through a radiating layer of thickness L; providing that the temperature and properties of the medium are uniform along the path, the intensity of the radiant beam at point x is given by integration of equation (4.30) as,

$$I_\lambda(x) = I_\lambda(0)\exp(-\kappa_\lambda x) + I_{\lambda,b}\left[1-\exp(-\kappa_\lambda x)\right] \tag{4.31}$$

The extinction coefficient is generally the sum of the absorption coefficient and the scattering coefficient,

$$\kappa_\lambda(\lambda,T,P) = a_\lambda(\lambda,T,P) + \sigma_{\lambda,s}(\lambda,T,P) \tag{4.32}$$

The absorption coefficient varies strongly with wavelength and substantially with temperature and pressure since for a gas, it depends on density. The effects of scattering in most engineering applications are found to be negligible, although as discussed in the following section, for the effects of smoke it can play an important role.

The spectral emissivity for a path length L, in a uniform gas volume can be expressed as,

$$\varepsilon_\lambda = \frac{I_{\lambda,L}}{I_{\lambda,b}} = 1 - \exp(-\kappa_\lambda L) \tag{4.33}$$

The term $\kappa_\lambda L$ is called the optical path length or opacity. If $\kappa_\lambda L << 1$ then the medium is optically thin. However if $\kappa_\lambda L >> 1$ then the medium is optically thick, which implies that the mean penetration distance is much less than the characteristic length L. When this is the case, local radiation results only from local emission.

The exponential decay of radiative intensity, termed Beer's law is used to infer the overall spectral absorptivity of the medium, with the transmissivity defined as,

$$\tau_\lambda = \frac{I_{\lambda,L}}{I_{\lambda,0}} = \exp(-\kappa_\lambda L) \tag{4.34}$$

4.8. Radiation Properties of Combustion Gases

The total emissivity of a gas-soot mixture requires knowledge of the soot volume fraction, extinction coefficients, temperatures, path length and the partial pressure of the participating media. These are briefly discussed in the following sections.

4.8.1. Properties of Gases

The emissivity of any gas is a strong function of wavelength and can vary by as much as several orders of magnitude over very small changes in wave number. Uncertainties involved in estimating parameters to calculate radiative heat flux make average properties such as total emissivity a useful tool. Comprehensive total emissivity charts were first developed by Hottel [99], while modern formulations have been summarised for the emissivity of gases [100-102]. Total emissivity charts for water vapour and carbon dioxide allow the determination based on knowledge of partial pressure and temperature of each gas and the associated path length. Correction factors for the emissivities are provided [103] for the effect of the band overlap of water vapour and carbon dioxide.

4.8.2. Properties of Soot

In a non-homogeneous medium such as soot, the effects of scattering become an important radiative mechanism in addition to absorption and emission. The main assumptions are that soot particles can be described as perfectly spherical spheres and that inter-particle spacing is sufficiently large that radiation for each particle can be treated independently. In reality, soot particles are produced as a result of incomplete combustion and are usually observed to be in the form of spheres, agglomerated chunks and long chains. With diameters in the range of

$50-1000\times10^{-4}\,\mu$m, in comparison to infrared wavelengths it can be shown that the Rayleigh limit is applicable to the calculation of radiation [104;105]. Soot particles are generally characterized by their optical properties, including chemical composition (hydrogen-carbon ratio). However, from a heat transfer viewpoint, radiation from a soot cloud is predominantly affected by particle size distribution and can be considered independent of chemical composition [104]. The absorption and scattering behaviour of a single particle can be described by solving the electromagnetic field equations in terms of spectral soot concentration k_λ,

$$k_\lambda = \frac{C_0}{\lambda} f_v \tag{4.35}$$

where f_v is the soot volume fraction and C_0 is a constant between 2 and 6 dependent on the complex index of refraction $m = n - \mathrm{i}k$, given by,

$$C_0 = \frac{36\pi nk}{\left(n^2 - k^2 + 2\right)^n + 4n^2k^2} \tag{4.36}$$

Equation (4.35) and (4.36) can be used to evaluate the absorption extinction coefficient for the entire range of optical thickness by,

$$\kappa = 3.72\frac{C_0}{C_2} f_v T \tag{4.37}$$

While the spectrally integrated absorptivity of soot, assuming scattering to be negligible for a path length L is given by [106],

$$\alpha_s = 1 - \frac{15}{\pi^4}\varphi^{(3)}\left(1 + \frac{\lambda k_\lambda TL}{C_2}\right) \tag{4.38}$$

where $\varphi^{(3)}$ is the pentagamma function [107], expressed as,

$$\varphi^{(n)}(z) = \frac{d^n}{dz^n}\varphi(z) = \frac{d^{n+1}}{dz^{n+1}}\ln\Gamma(z) \qquad (n = 1,2,3\ldots)$$
$$= (-1)^{n+1}\int_0^\infty \frac{t^n e^{-zt}}{1-e^{-t}}dt \qquad (\Re z > 0) \tag{4.39}$$

The following gas-soot mixture total emissivity equation has been shown [104;108] to be an excellent approximation,

$$\varepsilon = \left[1 - \exp(-\kappa L)\right] + \varepsilon_g \cdot \exp(-\kappa L) \tag{4.40}$$

where ε_g is the emissivity of the gas alone.

4.9. Parametric Study of the Underlying Variables

The introduction and definitions of the concepts behind radiation allows a study of parameters to be undertaken to determine the influence they can have in the context of compartment fires. This section examines total emissivities and associated extinction coefficients of radiating mixtures of combustion products. Soot particles and the radiative contribution of carbon dioxide (CO_2) and water vapour (H_2O) are considered for spectral calculations to account for wavelength. The 15, 10.4, 9.4, 4.3, 2.7, 2.0 μm vibration-rotation bands of CO_2 and the pure rotation band (at wavelengths $> 10\mu$m), the 6.3, 2.7, 1.87 and 1.38 μm vibration rotation bands of H_2O are included in the analysis with an applied correction for the overlap region of the 2.7 and 15 μm bands. The method of calculation is based on that Fleske and Tien [106] and presented by Modak [109] for an exponential wide band model assuming scattering effects to be negligible.

The calculation procedure determines the relationships for gaseous emission of carbon dioxide and water vapour developed by Hottel [99] for a range of temperatures and pressures as shown in Figure 4.8 and Figure 4.9 respectively. In addition, the contribution of soot is calculated by equation (4.38). In the case of post-flashover compartment fires, soot will generally be the dominant mode of radiation and the contributions of carbon dioxide and water vapour will be significantly reduced. Nonetheless, the gaseous contributions can not be ignored completely and as such are considered in full in this analysis.

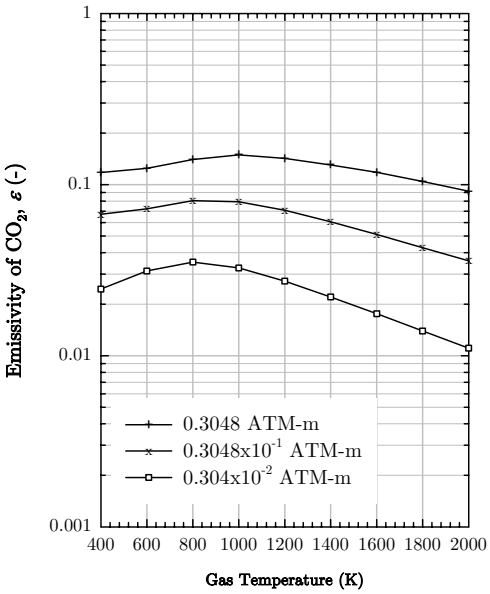

Figure 4.8: Total emissivity of CO_2 with temperature

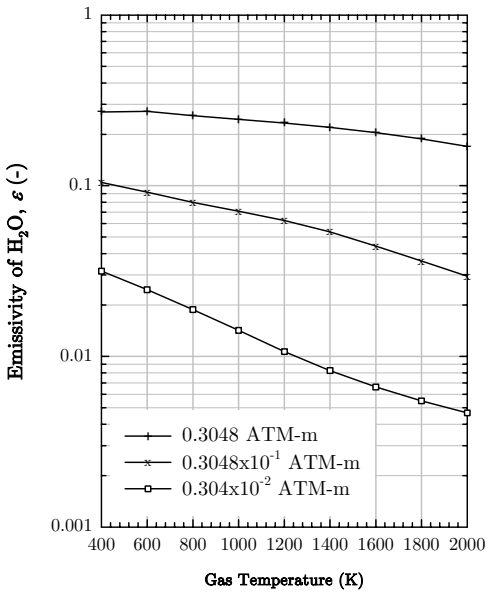

Figure 4.9: Total emissivity of H_2O with temperature

Emissivity and therefore extinction coefficients of gas and soot mixtures are seen to be a function of wavelength λ, soot concentration k, path length L, temperature T and partial pressures of gaseous species p_c and p_w. The extent of influence of each of these parameters on total emissivity and extinction coefficients is investigated below.

4.9.1. Refractive index of soot

Optical properties of soot can be used together with Mie theory [48] and equations (4.35)and (4.36) to evaluate soot concentration. As an example, propane soot is considered here with its optical properties shown in Figure 4.10 with respect to wavelength. In turn, the radiation constant C_0 is shown in Figure 4.11 with respect to wavelength. The description of C_0 as a constant is strictly not true, although as depicted in the figure, its variation is relatively small with wavelength. Common methods assume C_0 to take a constant value of between 2 and 6 and these limits are shown by dashed lines in the figure.

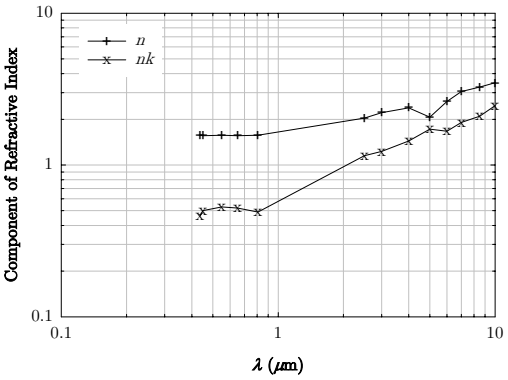

Figure 4.10: Components of refractive index of propane with wavelength

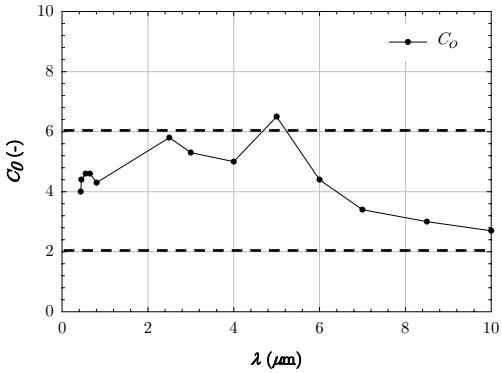

Figure 4.11: Radiation constant C_0 for propane with wavelength

By assuming a constant value of C_0, the influence of the refractive indices of soot can be taken as negligible in further analysis of the calculation of emissivities and extinction coefficients. A knowledge of C_0 allows for the calculation of the soot concentration k to be evaluated and for the case of propane, this is shown in Figure 4.12. At low wavelengths the concentration is high, however, with increasing wavelengths there is an monotonic decay to about $6\,\mu$m after which it is reasonable to assume a

single concentration. For this reason all subsequent analyses focus on wavelengths in the region 0 to 10 μm to capture the important variation. In reality, wavelengths up to 100 μm can be expected in general thermal radiation problems, however it is unlikely that radiation from compartment fires will reach such large infrared wavelengths.

It must be noted though, that soot concentration also depends on the soot volume fraction f_v which can vary markedly in the smoke layer of a compartment fire. The relationship in Figure 4.12 represents a single value of soot volume fraction and although the same trend can be expected for other values, the magnitude of the concentration may change dramatically. It should be noted that soot concentration here represents a monochromatic absorption coefficient at wavelength λ_0 as in equation (4.35). In comparison, the extinction coefficient κ used in the remainder of this chapter is calculated for a specific wavelength, temperature and path length.

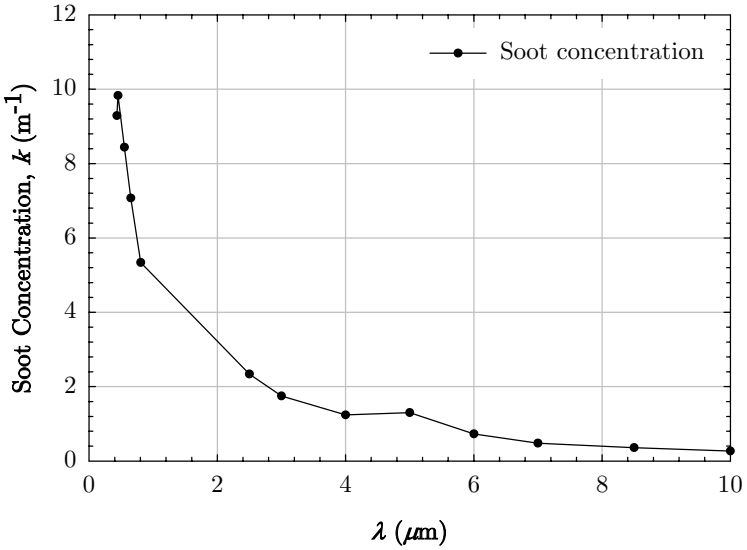

Figure 4.12: Soot concentration k with wavelength for propane with $f_v = 1 \times 10^{-6}$

4.9.2. Wavelength

The total mixture emissivity of a cloud of smoke particles with a constant soot concentration of $k = 2\text{m}^{-1}$ and path length $L = 0.5\text{m}$ is shown in Figure 4.13 with temperature for various wavelengths. For wavelengths typical of the visible region, there is little change in emission with temperature. However, at higher wavelengths, an increase is apparent. This is a direct consequence of the wavelength in equation (4.38) which determines the absorptivity and emissivity of the soot. This increase is also apparent for the associated extinction coefficient shown in Figure 4.14 where increases with temperature only appear to be apparent at wavelengths greater than $1\,\mu\text{m}$.

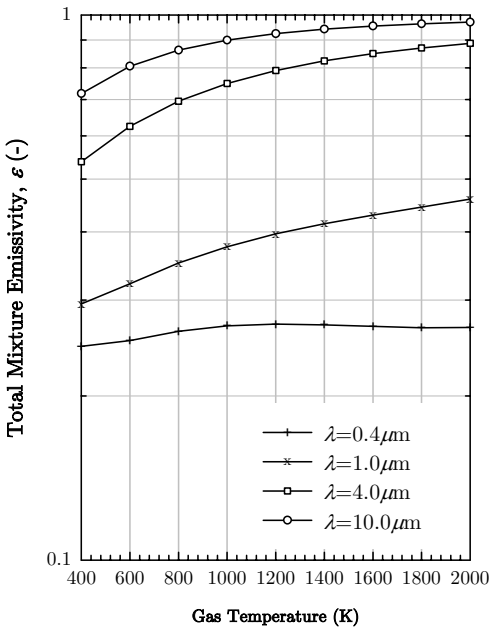

Figure 4.13: Total emissivity with temperature and various wavelengths for $k = 2\text{m}^{-1}$ and $L = 0.5\text{m}$

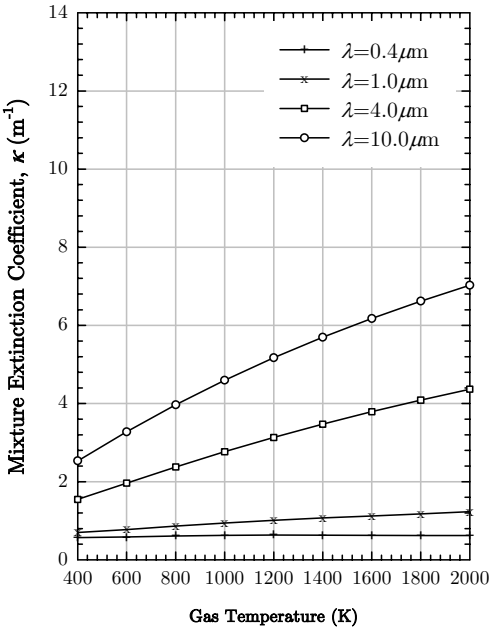

Figure 4.14: Extinction coefficient with temperature and various wavelengths for $k = 2\text{m}^{-1}$ and $L = 0.5\text{m}$

Figure 4.15 and Figure 4.16 show the dependence of emissivity and extinction coefficient with temperature for selected wavelengths. It is seen that for small wavelengths low emissivities occur while for all temperatures a sharp rate of increase is associated with increased wavelength. For wavelengths typical in fires ($< 1\mu$m) the variation in extinction coefficient is negligible.

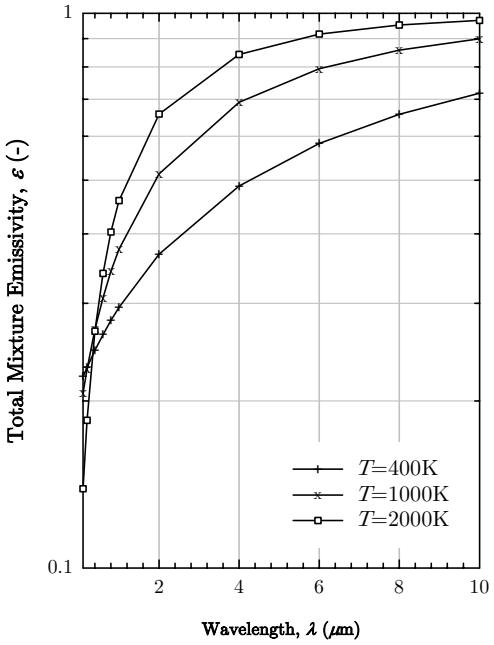

Figure 4.15: Total emissivity with wavelength and various temperatures for $k = 2\text{m}^{-1}$ and $L = 0.5\text{m}$

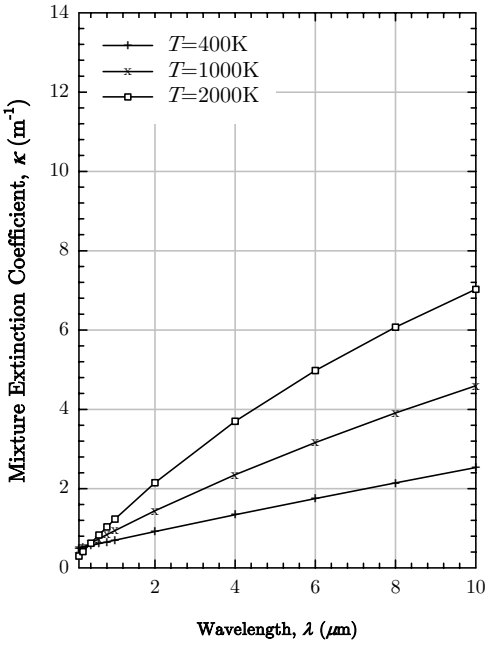

Figure 4.16: Extinction coefficient with wavelength and various temperatures for $k = 2\text{m}^{-1}$ and $L = 0.5\text{m}$

4.9.3. Soot concentration

The variation in total emissivity and extinction coefficient with temperature for different soot concentrations is shown in Figure 4.17 and Figure 4.18 respectively. In the case of no soot $k = 0\text{m}^{-1}$, the effect on emissivity is quite striking, as temperature increases, emissivity is seen to decrease. In this case, emissivity is being described only as a result of the

gaseous contributions of carbon dioxide and water vapour. The decrease can be associated to the correction applied due to the overlap in the spectral bands which is determined based on the spectral absorption coefficient of H_2O which itself is temperature dependent [110]. Indeed this relationship is evident in Hottel's emissivity charts in Figure 4.8 and Figure 4.9. When soot is introduced, the rate of emission is seen to increase with temperature and this rate is more pronounced for higher soot concentrations as shown by the plot of the extinction coefficient.

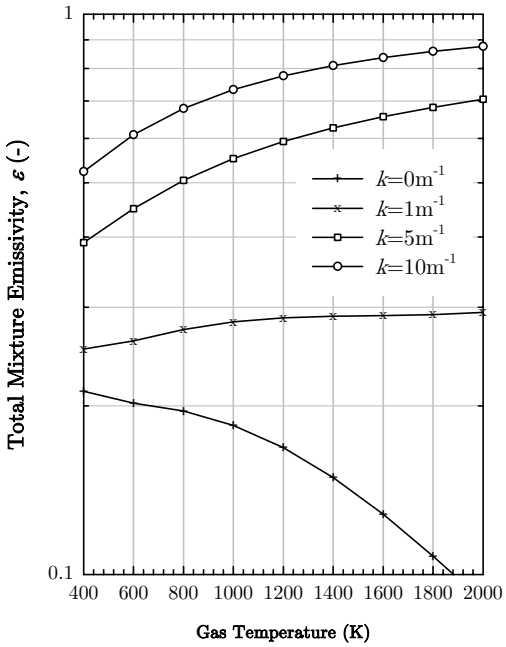

Figure 4.17: Total emissivity with temperature and various soot concentrations for $\lambda = 0.94\mu$m and $L = 0.5$m

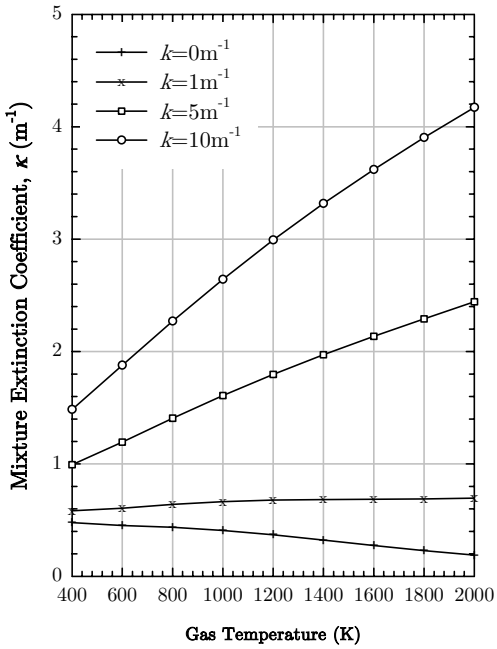

Figure 4.18: Extinction coefficient with temperature and various soot concentrations for $\lambda = 0.94\mu$m and $L = 0.5$m

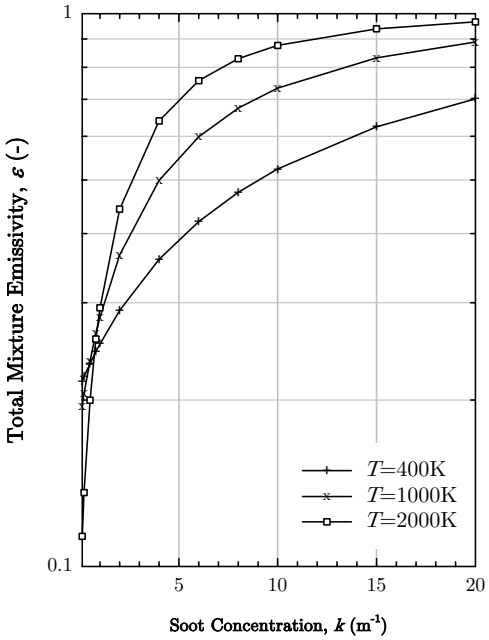

Figure 4.19: Total emissivity with soot concentrations and various temperatures for $\lambda = 0.94\mu$m and $L = 0.5$m

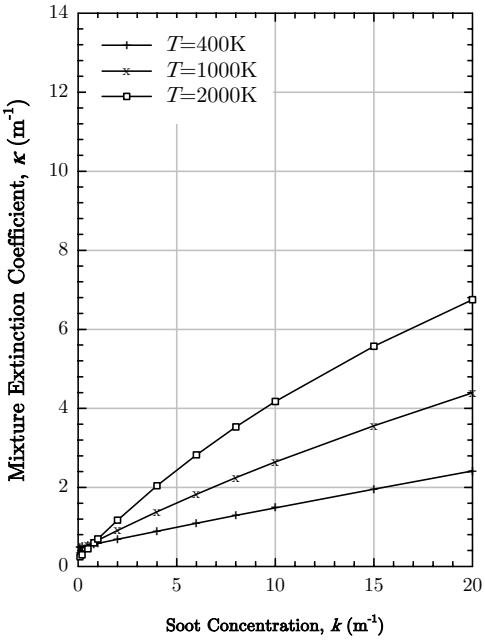

Figure 4.20: Extinction coefficient with soot concentration and various temperatures for $\lambda = 0.94\mu$m and $L = 0.5$m

The variations with soot concentration for emissivity and extinction coefficient are represented in Figure 4.19 and Figure 4.20. Again it is illustrated that higher soot concentrations yield higher emissivities, the rate of which increases with temperature. This is also evident in the extinction coefficient.

4.9.4. Path length

The path length associated with radiation can be thought of as relating to a size of cloud consisting of products of combustion with a larger path length creating a larger cloud. The relatively slow rate of increase of emissivity with temperature shown in Figure 4.21 appears to be uniform for all path lengths over the range of typical compartment temperatures. An increase in the path length results in a greater emissivity. The slow increase in emissivity is mirrored in Figure 4.22 for the extinction coefficient over the range of temperatures.

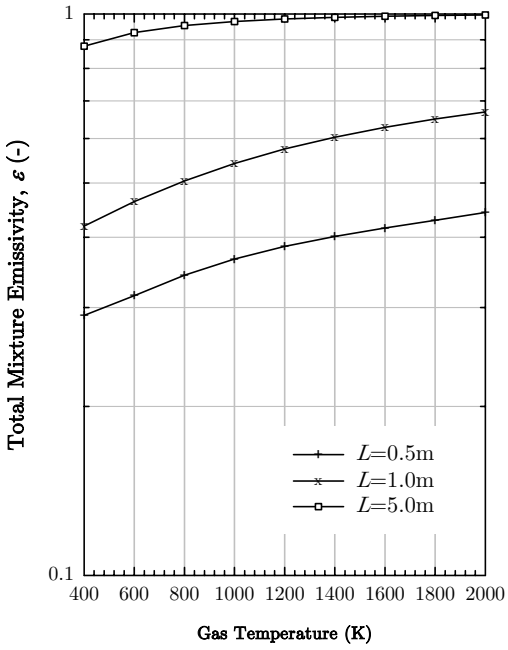

Figure 4.21: Total emissivity with temperature and various path lengths for $\lambda = 0.94\mu$m and $k = 2\text{m}^{-1}$

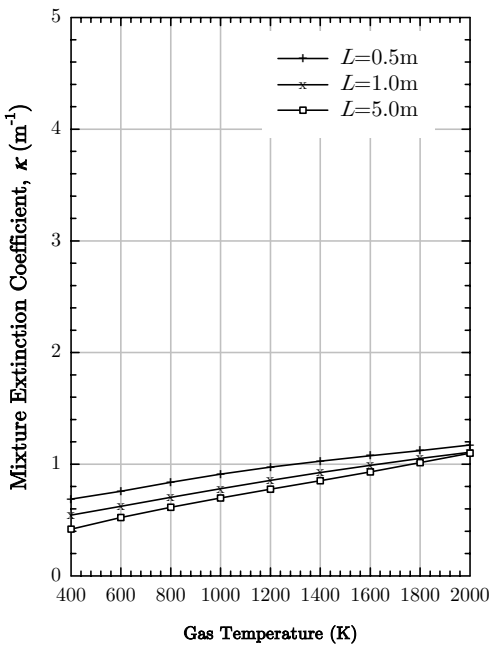

Figure 4.22: Extinction coefficient with temperature and various path lengths for $\lambda = 0.94\mu$m and $k = 2\text{m}^{-1}$

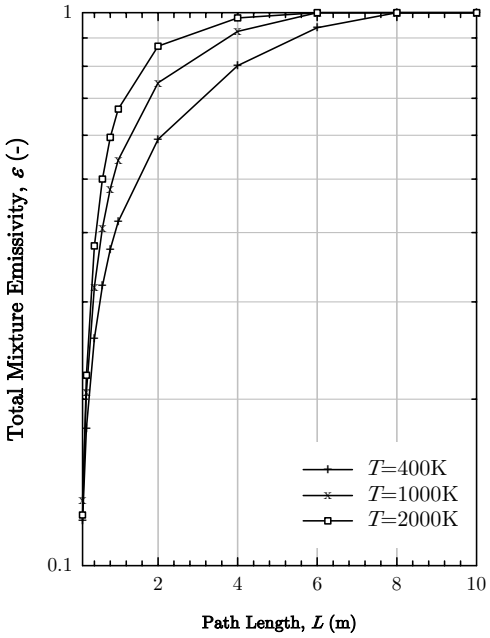

Figure 4.23: Total emissivity with path length and various temperatures for $\lambda = 0.94\mu$m and $k = 2\text{m}^{-1}$

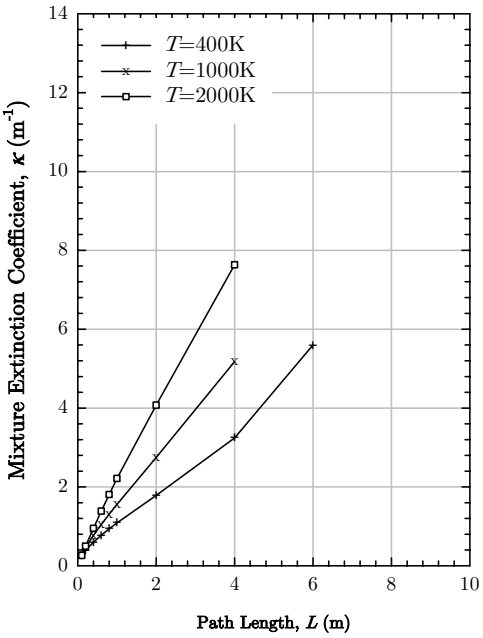

Figure 4.24: Extinction coefficient with path length and various temperatures for $\lambda = 0.94\mu$m and $k = 2\text{m}^{-1}$

The relationship between path length and emissivity for selected temperatures in Figure 4.23 shows that above a certain path length, a cloud of soot and gas can be considered to be totally emissive indicating that in radiative calculations only a certain distance through the cloud of products of combustion needs to be considered to achieve accurate results. For the parameters chosen in this case, a path length of 6m for a temperature of 1000K seems sufficient to capture all the radiation produced. The plot of extinction coefficients in Figure 4.24 is truncated for each temperature plot at certain path lengths due to the emissivity at that point equaling unity for which the extinction coefficient tends toward infinity. The truncation path length values provide the depth for which radiative calculations are needed to be considered totally accurate. This is illustrated in Figure 4.25 in which the ratio of the incident radiation to the

initial radiation is plotted against path length for various extinction coefficients. The dashed line represents an error limit of 10% in the radiation received at the surface allowing for maximum path lengths through smoke of different concentrations to be established. This plot is discussed in greater detail in Chapter 7 in the context of calculating the radiative intensities.

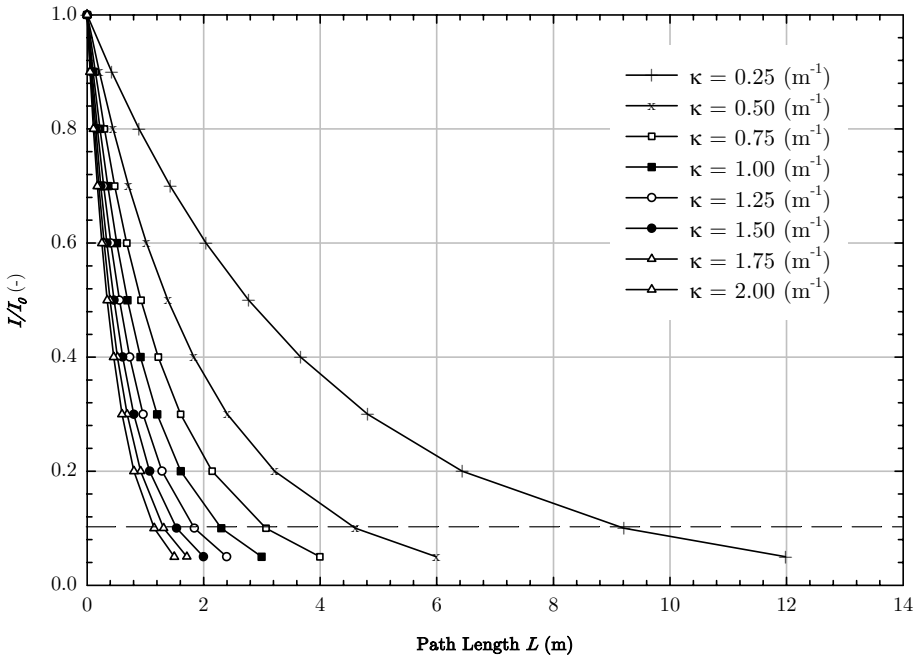

Figure 4.25: Required path lengths based on ratio of radiant intensities and extinction coefficients with an error limit of 10% highlighted

4.9.5. Partial pressures of gases

In evaluating the emissive properties of gas and soot mixtures, the partial pressures of carbon dioxide and water vapour are variables, however, values in the literature do not exist for the case of full scale fire testing. In order to establish what influence they might have on radiative calculations, a CFD simulation of a propane (soot yield of 1%) pool fire covering the entire floor of a 4x4x4m compartment with the heat release

set to achieve instantaneous flashover was undertaken. Point measurements of CO_2 and H_2O concentrations were made at two locations as depicted in the image on the right of Figure 4.26. The plot in the same figure shows the time dependence of the variables. It can be seen that for both locations, a relatively stable value of pressure is achieved in the fully developed fire. From the plot, minimum and maximum values were taken and applied to the parametric study of the radiative properties using the wide band model described above.

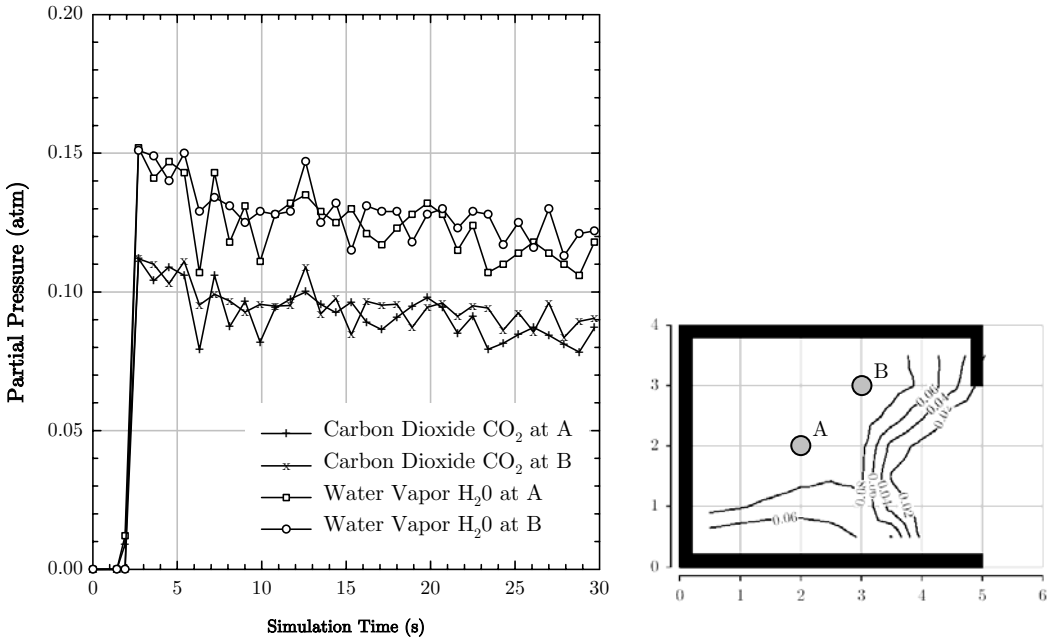

Figure 4.26: Partial pressures of CO_2 and H_2O measured at two points in a fully developed fire with propane fuel

Figure 4.27 shows the variation of total emissivity with temperature for the partial pressure combinations within the key. These combinations were based on a simple CFD model of a fully developed fire as outlined above. Three soot concentrations are considered and the minimum and maximum pressure combinations for each gas shown. It is clear that little difference is observed between the ranges of partial pressures investigated, furthermore any difference is reduced with increased soot concentration.

This relationship allows for the partial pressure variables of carbon dioxide and water vapour to be neglected as an influencing parameter for radiative calculations within typical compartment fires.

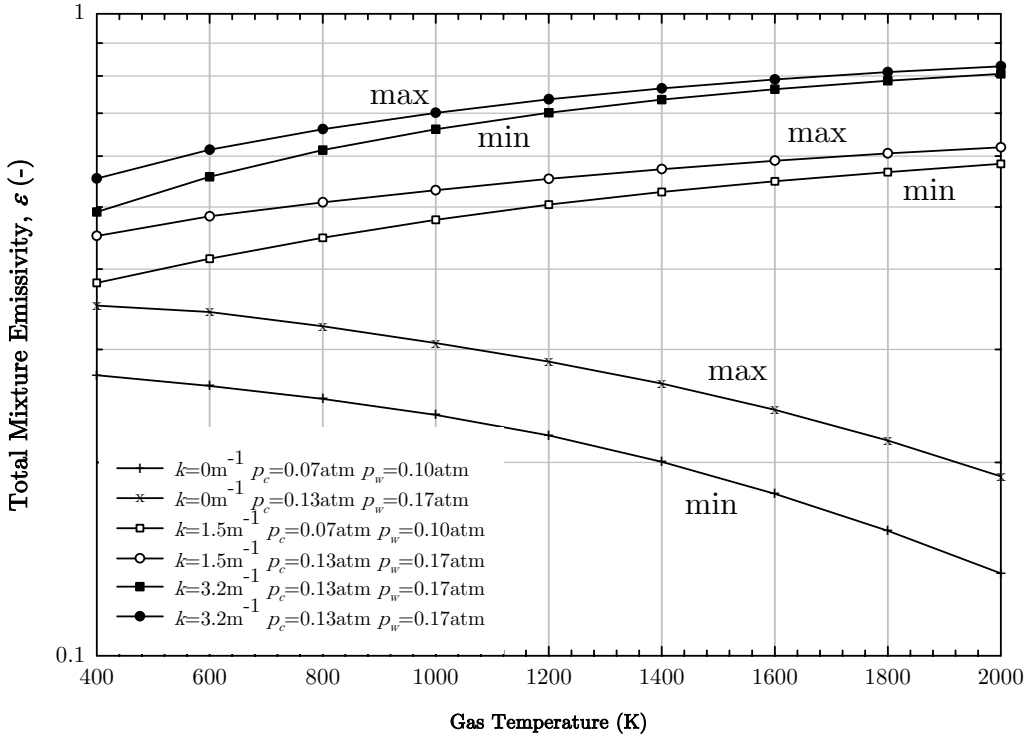

Figure 4.27: Emissivity with temperature for minimum and maximum combinations partial pressures of CO_2 and H_2O for propane with $L = 1.0\text{m}$ and $\lambda = 0.94\mu\text{m}$

4.10. Application to the Heat Transfer Coefficient

Radiative calculations can be thought of in a similar manner to that of convection. Consider the equation to describe the total heat flux to a surface, assuming radiation to come from a single source,

$$\dot{q}_s'' = h_c(T_g - T_s) + \varepsilon\sigma(T_g^4 - T_s^4) \tag{4.41}$$

This can also be re-written as,

$$\dot{q}_s'' = h_c(T_g - T_s) + h_r(T_g - T_s) \tag{4.42}$$

where h_r is the radiative heat transfer coefficient defined as,

$$h_r = \varepsilon\sigma\left(T_g + T_s\right)\left(T_g^2 + T_s^2\right) \tag{4.43}$$

If however, it is assumed that the surface on which the radiation is incident remains cold so that radiative feedback can be neglected then this can simplified to,

$$h_r = \varepsilon\sigma T_g^3 \tag{4.44}$$

This definition of the radiative heat transfer coefficient allows for the inherent complex parameters associated with radiative heat transfer to be simplified to a single parameter. Such a simplification may not always be relevant when performing heat transfer calculations; nonetheless it provides a useful method to help quantify the parameters in this study.

4.10.1. Wavelength

The variation in radiative heat transfer coefficient with temperature and wavelength is shown in Figure 4.28 and is accounted for in equation (4.44) in the emissivity. An increase in temperature for all wavelengths corresponds to increase in the heat transfer coefficient with a more rapid rate for longer wavelengths. With the knowledge that compartment fire will never sustain a temperatures higher than a given value, a hot (1000K) and cold (400K) temperature are used to evaluate the heat transfer

coefficient for a range of wavelengths in Figure 4.29. It can be seen that for each temperature, the heat transfer coefficient increases towards some asymptotic value further highlighting that wavelengths only effect radiation in the near infrared ($< 25\mu m$) region.

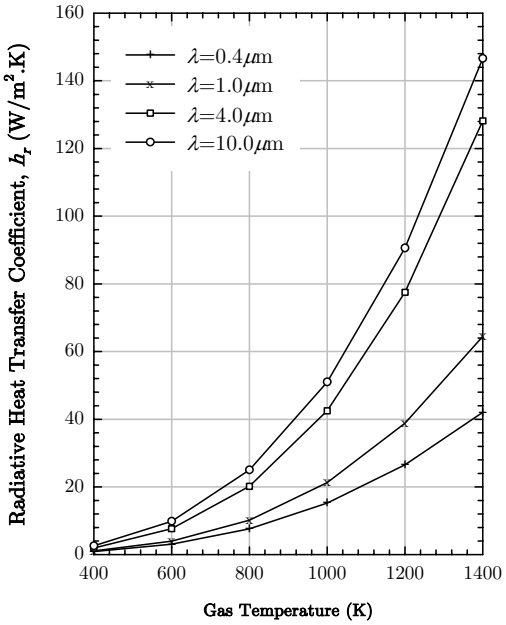

Figure 4.28: Radiative heat transfer coefficient with temperature for various wavelengths with $k = 2\text{m}^{-1}$ and $L = 0.5\text{m}$

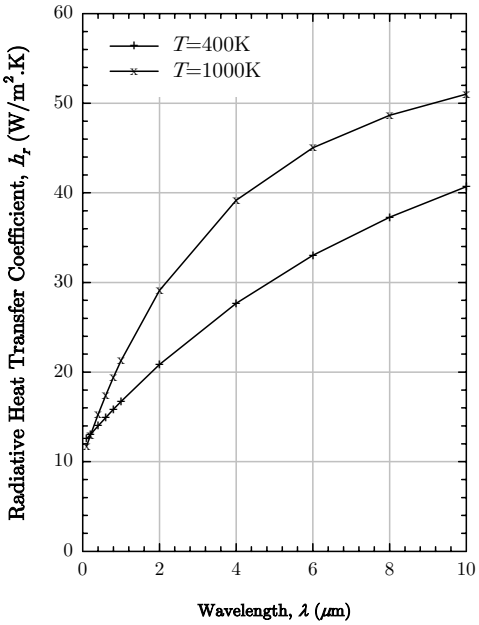

Figure 4.29: Radiative heat transfer coefficient with wavelength for a cool and hot temperature

4.10.2. Soot concentration

The relationship between soot concentration, temperature and the radiative heat transfer coefficient is very similar to that of wavelength and is important in establishing the gas mixture emissivity. An increase is the coefficient is achieved with increasing temperature with higher soot concentrations providing a more rapid increase. Similarly, for each temperature, there appears to be an asymptotic coefficient value which

suggests that for above a certain soot concentration, the increase in radiation from that gas and soot mixture becomes negligible.

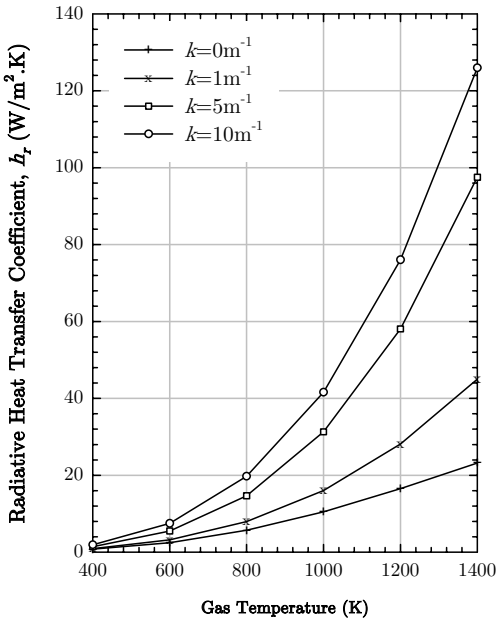

Figure 4.30: Radiative heat transfer coefficient with temperature for various soot concentrations with $\lambda = 0.94\mu$m and $L = 0.5$m

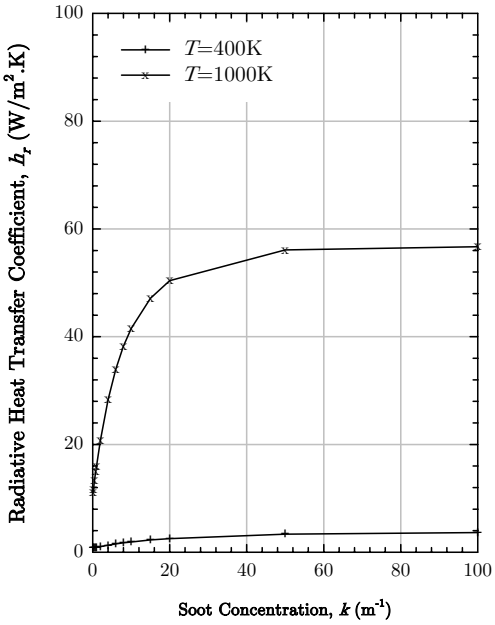

Figure 4.31: Radiative heat transfer coefficient with soot concentration for a cool and hot temperature

4.10.3. Path length

The influence on the radiative heat transfer coefficient by varying the path length with temperature is shown in Figure 4.32 and Figure 4.33. There is definitive increasing relationship for all path lengths with increasing temperature, with all path lengths exhibiting almost the same rate of increase. Again, as in the case of wavelength and soot concentration the radiative heat transfer coefficient reaches an asymptotic value leading to the conclusion that for given conditions, a maximum path length can be used to define radiation accurately.

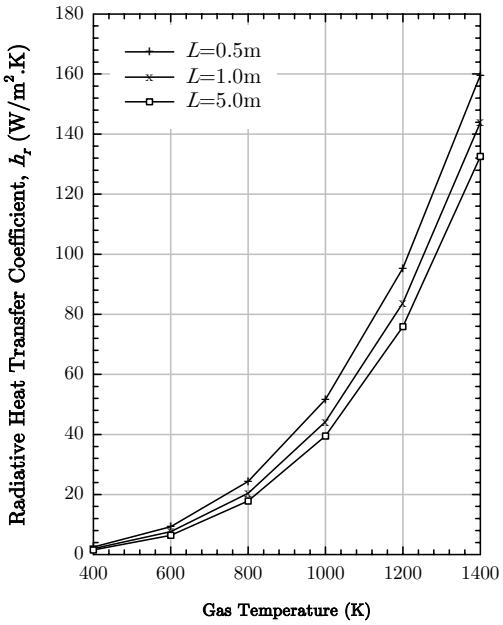

Figure 4.32: Radiative heat transfer coefficient with temperature for various path lengths with $\lambda = 0.94\mu\text{m}$ and $k = 2\text{m}^{-1}$

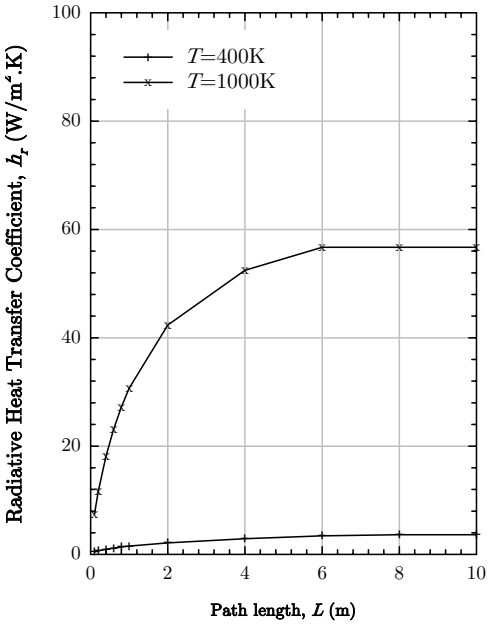

Figure 4.33: Radiative heat transfer coefficient with path length for a cool and hot temperature

4.11. Radiation within FDS

FDS [66] calculates radiation by solving the Radiation Transport Equation (RTE) for an absorbing/emitting and scattering medium. The RTE is given as,

$$\begin{aligned} \mathbf{s}\cdot\nabla I_\lambda(\mathbf{x},\mathbf{s}) = -\left[\kappa(\mathbf{x},\lambda)+\sigma_s(\mathbf{x},\lambda)\right]I(\mathbf{x},\mathbf{s}) + B(\mathbf{x},\lambda) + \cdots \\ \cdots\frac{\sigma_s(\mathbf{x},\lambda)}{4\pi}\int_{4\pi}\Phi(\mathbf{s},\mathbf{s}')I_\lambda(\mathbf{x},\mathbf{s}')d\Omega' \end{aligned} \tag{4.45}$$

where $I_\lambda(\mathbf{x},\mathbf{s})$ is the radiation intensity at wavelength λ, $\mathbf{s}$ is the direction vector of the intensity, $\kappa(\mathbf{x},\lambda)$ and $\sigma_s(\mathbf{x},\lambda)$ are the local absorption and scattering coefficients, respectively, and $B(\mathbf{x},\lambda)$ is the

emission source term. The integral on the right of the equation describes the in-scattering from other directions. In the case of a non-scattering gas, the equation becomes,

$$\mathbf{s} \cdot \nabla I_{\lambda}(\mathbf{x},\mathbf{s}) = \kappa(\mathbf{x},\lambda)\left[I_{b}(\mathbf{x}) - I(\mathbf{x},\mathbf{s})\right] \tag{4.46}$$

The treatment of the spectral dependence involves dividing the radiation spectrum into a relatively small number of bands, and deriving a separate RTE for each. The limits of the bands are selected to give an accurate representation of the most important bands of CO_2 and water vapour. This defines the band specific RTE's as,

$$\mathbf{s} \cdot \nabla I_{\lambda}(\mathbf{x},\mathbf{s}) = \kappa_{n}(\mathbf{x})\left[I_{b,n}(\mathbf{x}) - I(\mathbf{x},\mathbf{s})\right], \quad n = 1...N \tag{4.47}$$

where I_n is the intensity integrated over band n, and κ_n is the appropriate mean absorption coefficient inside the band. The source term can be written as a fraction of the blackbody radiation,

$$I_{b,n} = F_{n}(\lambda_{\min},\lambda_{\max})\sigma T^{4} / \pi \tag{4.48}$$

The calculation of the factors F_n are given in [48]. With the intensities corresponding to the bands, the total intensity can be evaluated by summing over all the bands,

$$I(\mathbf{x},\mathbf{s}) = \sum_{n=1}^{N} I_{n}(\mathbf{x},\mathbf{s}) \tag{4.49}$$

Six bands are considered sufficient ($N = 6$) although if the absorption of the fuel is known to be important, separate bands can be reserved for fuel,

and the total number of bands increased to ten ($N = 10$). Fuel is assumed to be methane (CH_4). Even with a small number of bands, the solution of N RTE's can be very time consuming. In most large-scale fire scenarios, soot is the most important combustion product and can dominate in terms of thermal radiation from the fire and hot smoke. FDS uses the assumption that the gas behaves as a grey medium due to the fact that the radiation spectrum of soot is continuous. This allows the spectral dependence to be lumped into one absorption coefficient ($N = 1$) so that the source term can be given by the blackbody radiation intensity,

$$I_b(\mathbf{x}) = \sigma T(\mathbf{x})^4 / \pi \tag{4.50}$$

For the case of optically thin flames, where the amount of soot is small compared to the amount of CO_2 and water, the grey gas assumption may produce significant over-predictions of the emitted radiation.

The narrow-band model RadCal [67] is implemented within FDS to calculate the grey or band-mean absorption coefficients κ_n. The absorption coefficient using this method is a function of mixture fraction and temperature.

In simulations with limited spatial resolution, the source term I_b, in the RTE requires special treatment near to the flame sheet. This is because the temperatures are smeared out over the grid cell and thus are considerably lower than would be expected. Due to its dependence on the temperature raised to the fourth power, the source term must be modelled in those grid cells cut by the flame sheet. Outside these regions, greater confidence is given in the computed temperature, and the source term can assume its ideal value, giving,

$$\kappa I_b = \begin{cases} \kappa\sigma T^4/\pi & \text{Outside the flame zone} \\ \chi_r \dot{q}'''/4\pi & \text{Inside the flame zone} \end{cases} \tag{4.51}$$

Where $\dot{q}'''$ is the heat release rate per unit volume and χ_r is the local fraction of that energy emitted as thermal radiation.

The boundary condition for the radiation intensity *leaving* a grey diffuse wall is given as,

$$I_b(\mathbf{s}) = \varepsilon I_{bw} + \frac{1-\varepsilon}{\pi}\int_{\mathbf{s}'\cdot\mathbf{n}_w<0} I_w(\mathbf{s}')\left|\mathbf{s}'\cdot\mathbf{n}_w\right| d\Omega \tag{4.52}$$

where $I_w(\mathbf{s})$ is the intensity at the wall, ε is the emissivity, and I_{bw} is the blackbody intensity at the wall.

To obtain the discretised form of the RTE, the unit sphere is divided into a finite number of solid angles. In each grid cell a discretised equation is derived by integrating equation (4.46) over the cell ijk and the control angle $d\Omega^l$ to obtain,

$$\int_{\Omega^l}\int_{V_{ijk}} \mathbf{s}\cdot\nabla I_n(\mathbf{x},\mathbf{s})\,dV d\Omega = \int_{\Omega^l}\int_{V_{ijk}} \kappa_n(\mathbf{x})\left[I_{b,n}(\mathbf{x}) - I_n(\mathbf{x},\mathbf{s})\right] dV d\Omega \tag{4.53}$$

The volume integral on the left is replaced by a surface integral over the cell faces using the divergence theorem. Assuming that the radiation intensity $I(\mathbf{x},\mathbf{s})$ is constant on each of the cell faces, the surface integral can be approximated by a sum over all the cell faces. This allows the radiant heat flux vector to be defined as,

$$\mathbf{q}_r(\mathbf{x}) = \int \mathbf{s} I(\mathbf{x},\mathbf{s})\, d\Omega \tag{4.54}$$

The radiant loss term in the energy equation is,

$$-\nabla \mathbf{q}_r(\mathbf{x}) = \kappa(\mathbf{x})\left[U(\mathbf{x}) - 4\pi I_b(\mathbf{x})\right] \quad ; \quad U(\mathbf{x}) = \int (\mathbf{x}, \mathbf{s}) d\Omega \tag{4.55}$$

This defines the radiant energy gained by a grid cell as the difference between that which is absorbed and that which is emitted.

4.12. Conclusions

The background theory to radiation has been introduced which in turn has provided the basis to undertake a parametric study of the underlying parameters, namely wavelengths, soot concentration, path length and partial pressure of gaseous species. The role of each of these parameters has been quantified in terms of emissivity and extinction coefficient by the use of a spectral wide band absorption model.

In addition, the quantification of parameters has been extended to evaluate the radiative heat transfer coefficient to provide a single correlation for the use of calculating radiative heat transfer to structural surfaces.

It is been shown that partial pressures do not contribute significantly to the evolution of emissivities and extinction coefficients of combined gas and soot mixtures.

Wavelengths have been shown to only influence emissivities in the near infrared region $< 25\mu m$. Soot concentrations have been shown to have an influence on emissivities and associated extinction coefficients, depending on radiative conditions, up to a defined maximum value. The influence of path length has been demonstrated in that a limiting value can be defined

within which radiation can be evaluated accurately. Again, this value depends on the thermal and gaseous environments.

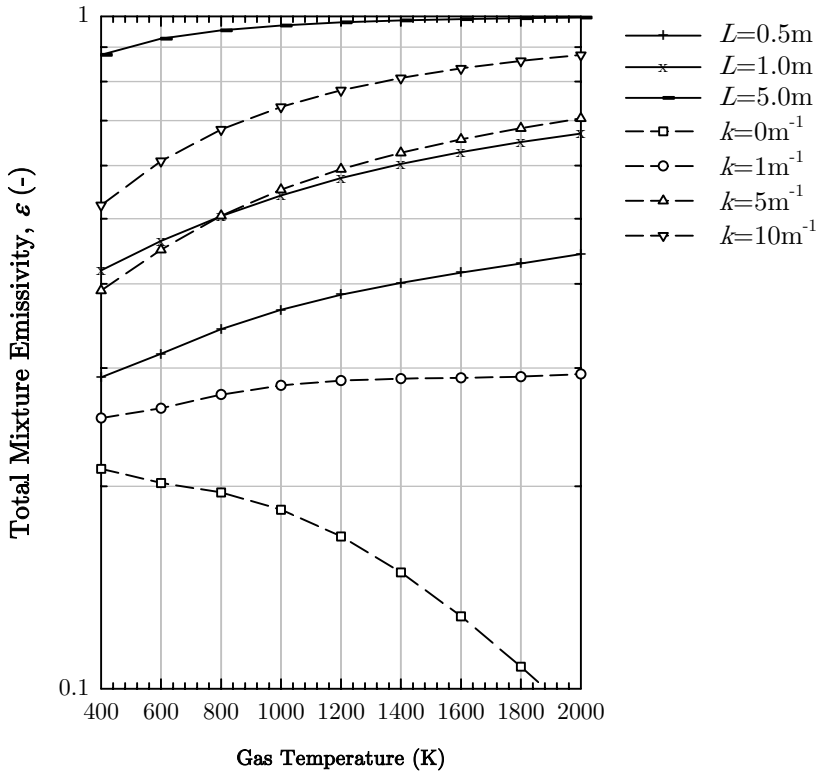

Figure 4.34: Total gas mixture emissivity with temperature for different path lengths and soot concentrations

With knowledge of the compartment fire environment, specifically the spatial and time varying soot distribution and temperature, as can be obtained from a CFD model, it is possible to define limits for the path length through the smoke for which radiative intensity calculations can be undertaken. The plot of Figure 4.34 summarises the dependence of the gas emissivity on both the path length and the soot concentration. These are the two main influencing factors on the emissivity and as such are important input variables to be defined in the calculation of radiative intensity.

Chapter Five

5. Analysis of the Cardington Large Scale Fire Tests

5.1. Introduction

Before any methodology to calculate heat fluxes can be developed and validated for a fire environment, it is essential to be able to establish that all required inputs are correct. In chapter 3 it has been established how to properly define and bracket convective heat transfer coefficients within a typical fire environment. Chapter 4 then addressed the variables involved in the estimation of the radiative heat transfer. In both chapters, the temperature of the gas-phase appears as part of the required calculations. This temperature can be evaluated as the output of CFD tools and needs to be compared to thermocouple measurements for validation. In the present chapter, focus is given to addressing the errors associated to thermocouple measurements to establish a methodology that will permit the use of this data for validation of the heat transfer computations.

The availability of reliable and comprehensive measurement data from large-scale fire tests is essential to increase the understanding of the thermal environment within fully developed fires. Not only is this important from a structural viewpoint but also it can help to form the basis of ongoing validation of computational simulation methodologies in fire, and CFD models in particular.

This chapter creates a methodology whereby given a sufficient number of measurement points it is possible to compute an estimate of the true gas temperatures at each location by post-processing the thermocouple temperature data taking account of the expected interactions in the thermal flowfield. The corrected temperatures can then be used in determining the true opening velocities and may be cross-checked by assuming consistency with measured heat fluxes. However, recognising the theoretical interrelationship of each thermocouple temperature with every other, and the coupling of temperature and velocity via the influence on

the thermocouple error of the velocity-dependent convective heat transfer coefficients, it is apparent that the problem is mathematically complex, requiring a numerical solution. The methodology presented describes and demonstrates a simple method for performing this post-processing, within the scope of a series of large-scale fire tests, in order to establish a self-consistent and reliable dataset of physical parameter values. This analysis also allows for the generation of radiative intensity maps, which can provide valuable insight into the spatial and temporal variability of the thermal exposures within the compartment. These maps can then be compared with simulations and the ultimate predictions of heat flux maps.

The experimental programme was undertaken within the scope of the Natural Fire Safety Concept 2 (NFSC2) series of fire tests at BRE Cardington in 1999-2000, sponsored by the European Coal and Steel Community (ECSC). These were full-scale post-flashover fires performed in a large compartment measuring 12m x 12m in plan by 3m height and involved a total of eight scenarios for which opening position, fire load composition and enclosure boundary thermal insulation were varied. The main purpose of the tests was to characterise a range of fires for the model validation exercise performed within the scope of the NFSC programme, i.e. focusing on zone models [111]. A description of the experiments and the basic instrumentation has been provided by Lennon & Moore [112]. Load cells were used to record mass loss and a large number of thermocouples were located throughout the compartment to monitor gas temperatures. Further thermocouples were placed on and within the enclosure boundaries and supporting steelwork, including special 'indicative' test sections, both with and without protection, to look at the thermal response of the structure.

Zone model validation, specifically of OZone, has thus far been performed entirely in relation to the overall compartment fire temperatures derived

from the tests, i.e. average of all the instantaneous thermocouple values within the compartment volume [113]. This approach presumes that thermocouple errors are either sufficiently small or that errors cancel out. These may be reasonable assumptions, but to what extent they can be supported has not been assessed previously.

In order to more fully characterise the fires for the purposes of CFD model validation additional instrumentation was also installed, including temperature and velocity measurements in the compartment openings, together with heat flux gauges in the enclosure boundaries and in a specially-constructed box suspended from the ceiling near the centre of the compartment (with a flux meter facing in each direction) [60]. Availability of this type of information facilitates checking of key CFD predictions, such as the total fluid flows in and out of the compartment and the distributions of thermal exposures.

Regarding model validation, it is important to recognise that assessment of predicted gas-phase temperatures can in fact be performed in two different ways – by comparing the derived gas temperatures directly with the CFD predictions, or by providing a sub-model in the CFD code for computation of 'thermocouple temperatures'. The latter method has an advantage in terms of describing the spatial variation, since the very detailed information computed by the CFD code can be fully exploited in the calculation, limited only by the resolution of the numerical grid. Countering this, the predictions will clearly be subject to any uncertainties in the representation of the optical properties of the participating media and also to any other numerical errors (e.g. due to the Discrete Transfer Radiation Model (DTRM) 'ray effect').

5.2. The Fire Test Programme

The ECSC NFSC2 fire tests on the BRE large compartment were conducted as part of a European collaboration to develop a new fire safety concept based on the observed behaviour of natural fires. An overview of the experiments and essential measurements is available in the literature [60;112;114]. Table 5.1 provides a summary of the parameters investigated, while Figure 5.1 and Figure 5.2 show conditions in the compartment prior to ignition and during the fire respectively.

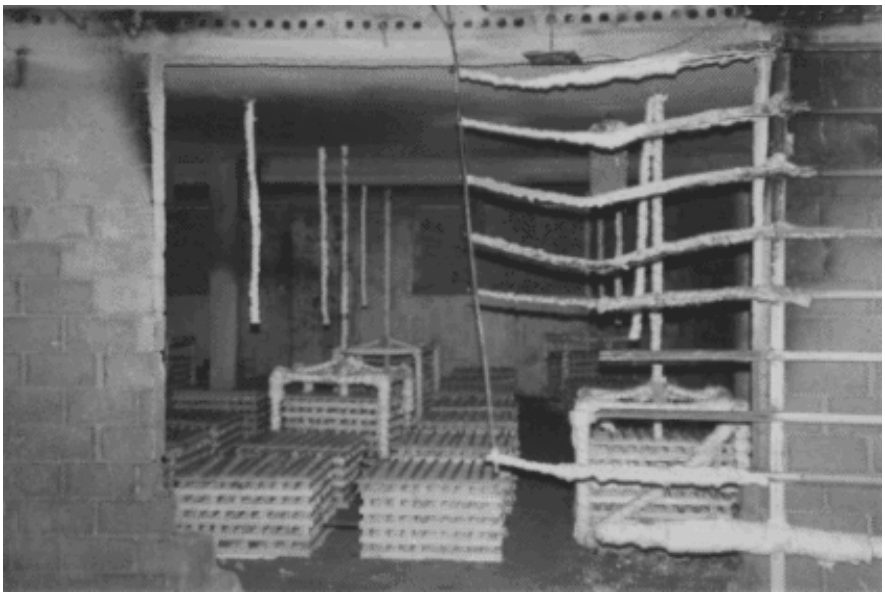

Figure 5.1: Internal view of the Cardington large scale fire tests showing cribs and instrumentation prior to ignition

Figure 5.2: View of the fire growth phase conditions within the compartment during Test 8

Test Number	1	2	3	4	5	6	7	8
Fire load type	W	W	W+P	W	W+P	W	W+P	W+P
Boundaries	I	HI	HI	HI	HI	I+	I+	I+
Opening	F	F	F	F+B	F+B	F+B	F+B	F

Table 5.1: Details of the ECSC NFSC2 fire tests in the BRE large compartment

Key:		
	W	100% wood
	W+P	80% wood, 20% plastic
	I	Compartment lining 'insulating' ($b = 720$)
	HI	Compartment lining 'highly insulating' ($b = 1600$)
	I+	Compartment lining 'insulating', + ceiling
	F	Front opening only ($O = 0.1$)
	F+B	Front and back openings ($O = 0.072$)

where

b is the thermal absorptivity ($\sqrt{k\rho c}$)

O is the opening factor ($A_v\sqrt{h_{eq}}/A_t$)

where

A_v is the total area of openings on all walls

h_{eq} is the weighted average of window heights on all walls

A_t is the total surface area of the enclosure including openings

The effective fuel load, area of ventilation openings and size of compartment were fixed for all tests. In each test, the fuel load was taken to be equivalent to 40kg/m^2 of wood for the full floor area, with tests using wood, denoted 'W' in Table 5.1, using 100% timber but the those with wood & plastic, 'W+P', having 80% timber and 20% plastic by calorific value. A variation in ventilation was provided by moving the opening location from a full height opening at the front only, 'F', to an opening over the upper half of the wall at both front and back, 'F+B', whilst maintaining the same overall ventilation area of A_v=24.48m^2. Despite having equal areas these two alternatives provide for quite different incoming airflows and also represent slightly different opening factors (O), due to the dependence of the latter on opening height. The insulating lining, 'I', consisted of bare blockwork walls and pre-cast concrete slabs for the ceiling, whilst the highly insulating tests, 'HI', involved various sprayed fibre fire protection materials, or in one case (test 5) a proprietary light-weight walling system. Indeed, for tests 6-8, sprayed fibre fire protection was retained on the ceiling of the compartment in order to protect the slabs, which had threatened to collapse in the first test when left unprotected. As a result, the actual insulation condition of these tests was

higher than for Tests 1 to 5 and intermediate between the two b values provided, and this case is denoted 'I+'.

Gas temperatures were measured with thermocouples; 16 thermocouple column trees (labelled from back left corner forwards, in rows, as 1-16) were installed in a grid pattern within the compartment, as represented in Figure 5.3. In each column there were four type-K bare-beaded 3mm diameter thermocouples, capable of accurately measuring temperatures of up to about 1250°C, positioned at distances of 100mm, 300mm, 600mm and 1800mm below ceiling height. Thermocouples were also positioned across the full height of the ventilation openings to the compartment, together with velocity probes. The latter consisted of McCaffrey bi-directional probes, attached to pressure transducers and/or micro-manometers, which are devices which record a pressure difference from which a local velocity can be determined. Different numbers of probes were used in each test, in both of the front openings, and also in the rear openings where relevant. In tests with full height openings, eight probes were located across the centre of the doorways at distances of 50mm, 400mm, 750mm, 1100mm, 1800mm, 2150mm and 2500mm below the ceiling.

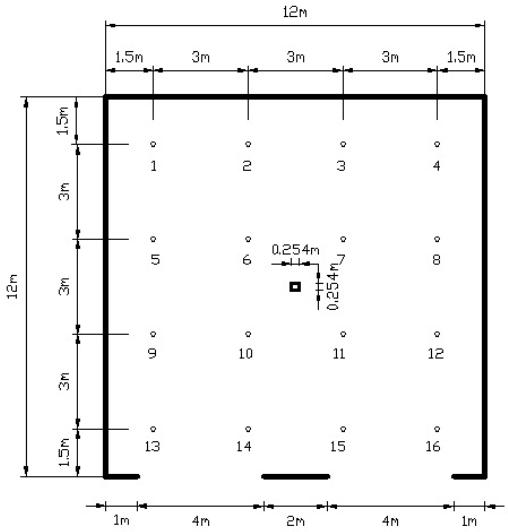

Figure 5.3: Compartment dimensions and thermocouple tree locations

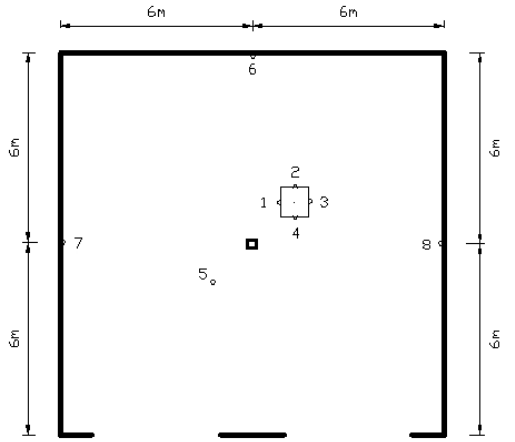

Figure 5.4: Billet locations to measure heat fluxes

Heat flux data was obtained using steel billets installed by the University of Ulster [114]. Since a local atmosphere temperature is recorded adjacent to each billet it is possible to distinguish the convective and radiative components, if this value can be equated to the local gas temperature and assuming an accurate value for the convective heat transfer coefficient. However, significant uncertainties in each of these assumptions means that the ability to distinguish a convective component is rather small, and in any case, even when the surface temperature of the billet lags well behind the gas temperature, the convective component is very small once temperatures exceed 1000°C, usually a lot less that 10%. In practice once the billet has become warm, the estimated convective component drops to less than 1% by the end of the heating phase; therefore, the distinction is ignored and the measured billet fluxes are assumed to represent purely radiative fluxes even though a small convective element may be embedded within them.

In the NFSC2 tests billets 1-4 were placed in the exposed faces of a special insulated box mounted on the ceiling, facing outwards in each horizontal coordinate direction at about 0.2m below the ceiling, billet 5 was in the ceiling itself, facing downwards, and a single billet was placed at a height of 2m from floor level on each of the compartment walls, except those with ventilation openings, as shown in Figure 5.4. Each billet face was positioned flush with the compartment boundary, and blackened in an attempt to ensure a constant surface emissivity throughout the tests. Thermocouples were also stationed at each billet location, projecting approximately 50mm into the room, in order to measure local gas temperatures.

5.3. Method of Analysis

A method for reconstructing the gas-phase temperature field from measured thermocouple temperatures is presented in the following sections.

5.3.1. Temperature measurements

The gas temperatures within the Cardington test were all obtained using thermocouples, however, it is well known that thermocouple temperatures may not be representative of the local true gas temperatures. There is a variety of reasons for this, with the dominant effect due to 'radiation errors' arising from the remote transfer of heat to (or from) a thermocouple bead in an environment which is locally more moderate (or severe). There may also be effects due to the conduction along the length of the thermocouple wire and the transient response of the bead. The former can result in a correction in either direction but its estimation requires a precise knowledge of the conditions along the length of the wire, which is generally insufficiently known. This effect however will generally be small unless the distance between the bead and a heat sink is abnormally short [115]. In a similar sense it can be shown that the transient heating error

will be small for typical fire conditions, i.e. the timescale of the response of the thermocouple is very short in comparison with the timescale of the gas phase environment. Therefore, both errors are typically neglected.

Far greater errors in temperatures can be attributed to radiation effects and may again result in both losses and gains with respect to the true values [116]. A thermocouple placed in a hot gas layer may receive radiation lower than that indicated by the local gas temperature due to the influence of remote, but cool surroundings, such as a cold layer. The result is a recorded temperature slightly lower than the true gas temperature. In a lower layer however, a temperature far higher than expected can often be recorded. This is due to the radiation from the distant flames and the hot gas layer in the environment which can be 'seen' by the thermocouple, i.e. the effective 'surroundings temperature'. In either case, the effect will be more pronounced when heat transfer is highly dominated by radiation, as it normally is in post-flashover fires. By modelling the radiative and convective exchange between the thermocouple and the surroundings, and assuming quasi-equilibrium conditions, it is possible to predict these errors by means of the energy balance theory that is presented in heat transfer texts [82]. In these equations, the 'surroundings temperature' relates the local gas temperatures together with the optical properties of the intervening participating medium – the complication of this is that there is no general solution. The methodology proposed here aims to decouple the phenomena in order to reconstruct the gas temperature field.

Despite the significance of the radiation error, it is often neglected by many fire researchers due to the difficulty in its accurate estimation [117]. Simplifications have sometimes been made to approximate the surroundings temperature, for example by equating it to T_w, the average

temperature of the walls [118]. The disadvantage of this method though is that it takes no account of the optical properties of the fire gases, including the effects of smoke, which will lead to large inaccuracies for typical compartment fires. In addition, the surface emissivities of the compartment boundaries are typically poorly defined.

The use of aspirated thermocouples, with radiation shields, is another possibility for avoiding the problems due to radiation errors [115]. However, some temporal and spatial resolution is sacrificed in these devices and they are not totally effective in eliminating the effects (only an infinite series of shields would be perfectly effective). Given the large number of thermocouples in the BRE large compartment tests, distributed throughout the compartment, and the generally cumbersome nature of aspirated thermocouples, their use in these experiments would have been highly impracticable, as would be true of many large-scale fire tests.

5.3.2. Heat flux measurements

A number of total heat flux meters (steel billets) were placed at various locations within each test compartment. Each billet consisted of a steel cylinder, of dimensions 100mm long by 40mm diameter, with thermocouples installed in pre-drilled holes at distances of 2, 10, 50 and 90mm from the exposed face. Total heat fluxes were computed from the measured temperatures by performing an inverse transient heat flow calculation, defining the temperature gradient into the depth of the billet using the temperature values from the 2 and 10mm thermocouple positions. The incident flux was set equal to the conduction flux through the surface layers plus the transient heating of this region and the re-radiation estimate based on the approximated surface temperature. In order to check the calibration of the billets a Gardon gauge radiometer was

also located adjacent to the billet in the back wall of the compartment in the first test, for the purposes of comparison.

5.3.3. Velocity measurements

Velocity is very important in terms of characterising the temporal layer heights and total compartment flows. Consequently it is of most interest in the openings where these are normally well-defined. Another advantage of estimating velocities at all locations within the compartment is that it can provide knowledge of the influence on convective heat transfer, embedded in the heat transfer coefficient h. For the openings, the velocity measurements also relate to the thermocouple corrections described above, since it is known that the gas temperature must be approximately ambient in locations of strong measured inflow, with any recorded differences attributed to radiation error.

5.4. Model Development

The following section details the calculation methodology employed in establishing the detailed thermal environment.

5.4.1. Gas temperature calculations

By assuming the conduction errors for the thermocouple can be neglected, the heat energy balance equation may be applied,

$$\rho_{TC} C_p V \frac{\partial T}{\partial t} = q''_{net} A \tag{5.1}$$

or, rearranged to represent the response of a spherical thermocouple,

$$\frac{\partial T}{\partial t} = \frac{q''_{net} A}{\rho_{TC} c_p V} = \frac{q''_{net} 4\pi r^2}{\rho_{TC} c_p \, {}^4\!/_3 \pi r^3} = \frac{3q''_{net}}{\rho_{TC} c_p r} \tag{5.2}$$

Appropriate properties for a 3mm Nickel-Chromium/Nickel-Aluminium thermocouple approximated are c_p=440J/kg.K, ρ_{TC}=9000kg/m^3 and r=0.0015m. The properties are assumed constant. A range of the net heat flux of 10-100kW/m^2 will be used as characteristic high heat fluxes typical of a fire environment. This gives the thermocouple's response characteristic as,

$$\frac{3q''_{net}}{\rho_{TC} c_p r} = \frac{3 \times 10 \times 10^3}{9000 \times 440 \times 0.0015} = 5\text{K/s or } 50\text{K/s} \tag{5.3}$$

Considering also that the thermocouple values were recorded once per minute in the tests, with the peak temperature differences between recordings usually being less than 200°C, it is apparent that any error due to transient heating of the thermocouple will be insignificant and therefore steady-state conditions of the thermocouple can be assumed in the analysis. As a result, the summation of the heat transfers, including losses and gains from convection must equal zero,

$$q_{net} = q_{conv} + q_{rad} = 0 \tag{5.4}$$

The convective and radiative transfers are given by,

$$q_{conv} = h_{TC}(T_g - T_{TC}) \tag{5.5}$$

$$q_{rad} = \varepsilon_{TC} \sigma (T_{sur}^4 - T_{TC}^4) \tag{5.6}$$

Substituting equations (5.5) and (5.6) into (5.4) and rearranging for the gas temperature gives,

$$T_g = \frac{\varepsilon_{TC}\sigma}{h_{TC}}(T_{TC}^4 - T_{sur}^4) + T_{TC} \tag{5.7}$$

The convection heat transfer coefficient for the thermocouple h_{TC}, can be obtained from a Nusselt number, rearranged as,

$$h_{TC} = \frac{kNu}{d_{TC}} \tag{5.8}$$

where the thermal conductivity is given,

$$k = \frac{\mu c_p}{Pr} \tag{5.9}$$

giving the convective heat transfer coefficient as,

$$h_{TC} = \frac{\mu c_p Nu}{d_{TC} Pr} \tag{5.10}$$

The Prandtl number is taken to be a constant of 0.7 following detailed studies of non-buoyant flows [119]. The viscosity μ, can be calculated from Sutherland's Law [120],

$$\mu = \frac{C_1 T^{1.5}}{T + C_2} \tag{5.11}$$

where the constants C_1 and C_2 are defined as 1.458×10^{-6} and 110.4 respectively.

The Nusselt number for a sphere can be calculated from the Williams/Kramers expression, using the Reynolds number [93],

$$Nu = 0.37 Re^{0.6} \tag{5.12}$$

where,

$$Re = \frac{\rho_g v d_{TC}}{\mu} \tag{5.13}$$

in which the density can be evaluated from a temperature-density correlation [3] in the form of,

$$\rho_g = \rho_o \left(\frac{T_a}{T} \right) \tag{5.14}$$

Having established the background equations to the model, a method is required to estimate the effective surroundings temperature distribution for each thermocouple. This is necessary because of the finite number of thermocouples available to define heat exchanges between the surrounding environment and the thermocouple.

The method considers a weighted contribution of the latest estimates of the gas temperature at the position of each nearby thermocouple, using an iterative method to progressively update all of the values. The weighting coefficients W_i, represent the influence of the separation between the location of interest and the surrounding thermocouples, $i = 1$ to n, together with the optical properties of the intervening media, characterised by the extinction coefficient κ,

$$T_s = \sqrt[4]{\left(W_1 T_{TC1}^4 + W_2 T_{TC2}^4 + ... + W_n T_{TCn}^4 \right)} \tag{5.15}$$

where the weighting factor, W_i is calculated using,

$$W_i^n = \frac{\exp(-L_i x)}{\sum(\exp(-L_i x))} \tag{5.16}$$

where L_i is the distance to thermocouple TC_i.

The latter parameter is limited to the path distance within the combustion products, as outside this realm, in fresh air, the extinction coefficient disappears. The extinction coefficient κ, can be calculated from the relation,

$$\varepsilon_{sur} = 1 - e^{-\kappa L} \tag{5.17}$$

which can be rearranged to give,

$$\kappa = \frac{-\ln(1-\varepsilon_{sur})}{L} \tag{5.18}$$

An estimation for the emissivity of the surroundings ε_{sur}, was computed using the RadCal narrow band model, with an air excess factor η, taken to be 1 (assuming stoichiometry under ventilation-controlled burning) and the soot yield taken to be between 2% and 5% [4], and the characteristic path length, *L,* is taken as 1.7m which is the vertical distance over which the compartment thermocouples are distributed.

Though the above method is general, and can in principle be extended to include every thermocouple location within the compartment, the weighting calculation was in practice confined to individual thermocouple trees. This is a limitation not imposed by the method but by the current experiments. The spacing on a thermocouple tree included at least one narrow gap (0.1m), with the largest being 1.2m. By comparison, the distance between thermocouple trees was a minimum of 3m; this difference

and the exponential decay associated with the extinction coefficient, meant that it was possible to confine the correction procedure to individual thermocouple trees.

In equation (5.15) the first guess for the gas temperatures at neighbouring thermocouple locations is provided by the local thermocouple temperatures T_{TC}. The resulting gas temperature estimates are then used in the next iteration, in order to obtain an improved prediction of the gas temperature as by,

$$T_s = \sqrt[4]{\left(W_1 T_{1,g-1}^4 + W_2 T_{2,g-1}^4 + \ldots + W_n T_{n,g-1}^4\right)} \tag{5.19}$$

This procedure can be repeated until the individual estimates converge to a single temperature solution. However, in common with most numerical methods, progress towards the solution is subject to certain numerical errors, and may for example exhibit oscillatory behaviour or even divergence. Indeed, an unacceptably large number of iterations may be required in order to find a sufficiently well-converged solution. In order to overcome such problems a conventional under-relaxation procedure was adopted, introducing a relaxation factor r, into equation (5.7), which defines how much of the latest estimate to incorporate into the current approximation to the solution,

$$T_g = \left[\frac{\varepsilon_{TC}\sigma}{h}(T_{TC}^4 - T_{sur}^4) + T_{TC}\right] r + T_{g-1}(1-r) \tag{5.20}$$

Relaxation factors ranging from 0.1 to 1.0 were tested. From these tests, best results were achieved using a value of 0.3 and this value is assumed in all following analyses. The effect of this procedure on the rate of convergence can be seen in Figure 5.5.

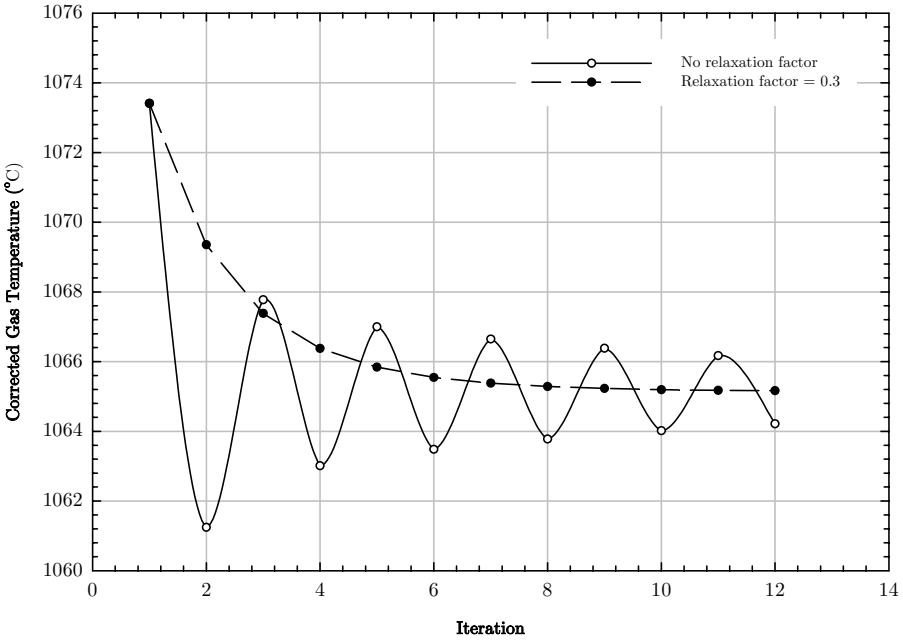

Figure 5.5: Example of the effect of the relaxation factor on convergence of corrected gas temperatures

Finally, it should be noted that when the thermocouple bead is situated in an opening location where there is an inflow from the ambient environment, the true gas temperature can reasonably be assumed to be ambient for all iterations, and therefore the effective temperature of the surroundings can be found by rearranging equation (5.7) to give,

$$T_{urs} = \sqrt[4]{\frac{h_{TC}(T_{TC} - T_g)}{\varepsilon_{TC}\sigma} + T_{TC}^4} \tag{5.21}$$

5.4.2. Heat flux calculations

Having defined the corrected gas temperatures, it is now possible to estimate the resulting associated 'radiative intensity' fields. Radiative intensity is defined as the total radiative energy passing through a region of space, and differs from a flux parameter which can only be defined with

respect to a solid surface, i.e. the latter requires a directional dependence assumption whilst the former is independent of direction. Ignoring convective heat transfer and any re-radiation influences, a first estimate of the local radiative intensity is given as,

$$\dot{q}''_{inc} = \varepsilon_{sur}\sigma T_{sur}^4 \tag{5.22}$$

Note that the estimated surroundings temperature, T_{sur}, is used in this equation, and not the implied local gas temperature, so that the computed parameter represents the true radiation field as far as possible.

In order for direct comparisons to be made with the total heat flux measurements of the billets, a calculation of the effective incident flux is also required at the location of each billet. This involves using the gas temperatures previously derived at each thermocouple location to determine an approximation to the surroundings temperature experienced by each billet. As no single thermocouple tree represented the surroundings that each billet had a sight of, an average of those closest to the billet was taken. An alternative would be simply to equate the surroundings temperature to that measured by the thermocouple located close to the billet; however, it should be considered that this temperature is in turn strongly influenced by the local wall temperature, which might be a lot lower than the average temperature of the gases in the neighbouring region.

5.4.3. Velocity calculations

In determining the velocities, the measured voltages are first converted to pressure differences according to the instrument and calibration range. The calculation of velocity is from the Bernoulli equation,

$$\Delta P = \frac{1}{2}\rho v^2 \tag{5.23}$$

where the multiplication by 0.5 represents ideal flow and which, in the case of a velocity probe is replaced by a calibration factor, K_t, which includes a specific correction to each probe to accommodate the effects of turbulent flow around the head of the probe,

$$\Delta P = K_t \rho v^2 \tag{5.24}$$

The gas density ρ, can then be defined by the equation of state in order to calculate the pressure as a function of temperature,

$$\rho = \frac{P_a}{RT} \tag{5.25}$$

Substituting equation (5.25) into (5.24), and rearranging for velocity gives,

$$v = \sqrt{\frac{\Delta P R T}{K_t P_a}} \tag{5.26}$$

The value of K_t was determined for each probe prior to the tests via calibration in a wind tunnel at BRE. The ambient pressure P_a, is taken as 101325N/m^2 and the gas constant R is 287.5 J/kg/K for air. In order to calculate appropriate gas temperatures for the velocity calculations, the thermocouples next to each velocity probe must be corrected using the theory described above. The theory is identical, and an appropriate weighting can be made over the locations of all the probes in any given opening.

5.5. Results

The majority of the results in the following section are presented for Test 8. This test contained the majority of working heat flux billets against which all output can be compared. Other tests experienced billet malfunctions leading to limited datasets being collected.

5.5.1. Temperature corrections

The temperature evolution of the thermocouples in one vertical rake (column 7, near the middle of the compartment, but offset slightly to the back right) in a single test (test 8) is shown in Figure 5.6, together with the corrected gas temperatures calculated by the methodology described above. It is clear that in the growth and decay regimes of the fire a good agreement is shown between the two different representations of temperature, indicating that thermocouples can be very representative of gas temperatures during these lower temperature regimes. However, during the fully-developed period when temperatures are generally highest, errors can easily be identified, with large overestimation of the lower layer temperatures, but some underestimation in the upper layer. These trends are in the directions expected, and indicate that during this phase of the fire its true severity might not be properly represented by the thermocouple values alone.

The thermocouple corrections, i.e. the differences between the estimated gas temperature and the measured values ($T_g - T_{TC}$), are shown directly in Figure 5.7. The corrected gas temperature of the upper thermocouples is seen to be up to almost 50°C higher than that recorded by the thermocouples. Although this temperature difference is relatively small it should be remembered that if converted directly to a radiative intensity a larger difference results, due to the 4th power dependence on temperature (which translates to about 15% in this particular case).

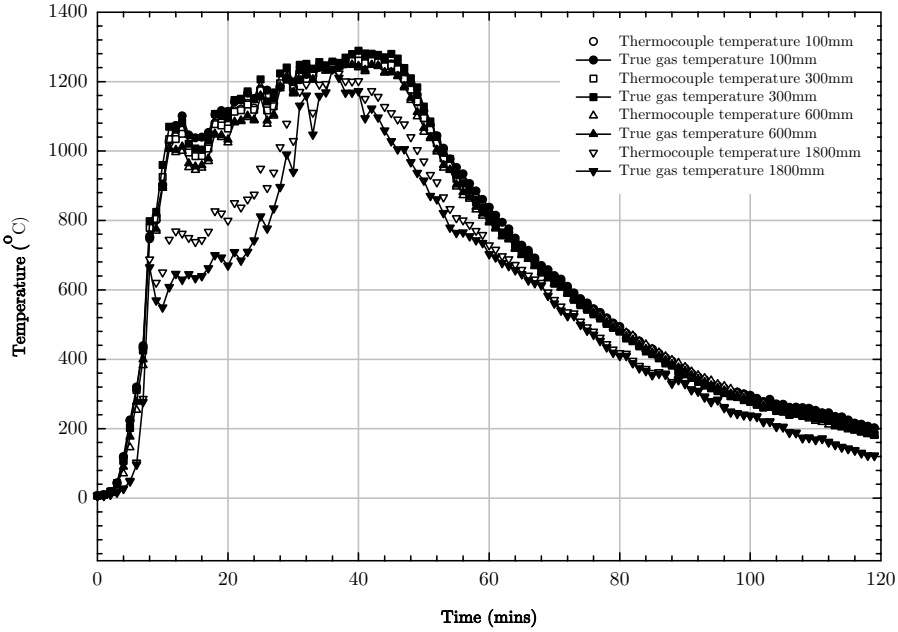

Figure 5.6: Corrected gas temperatures and recorded thermocouple temperatures for thermocouple tree 7, Test 8. Distances in key denote height from ceiling. Room height is 3m.

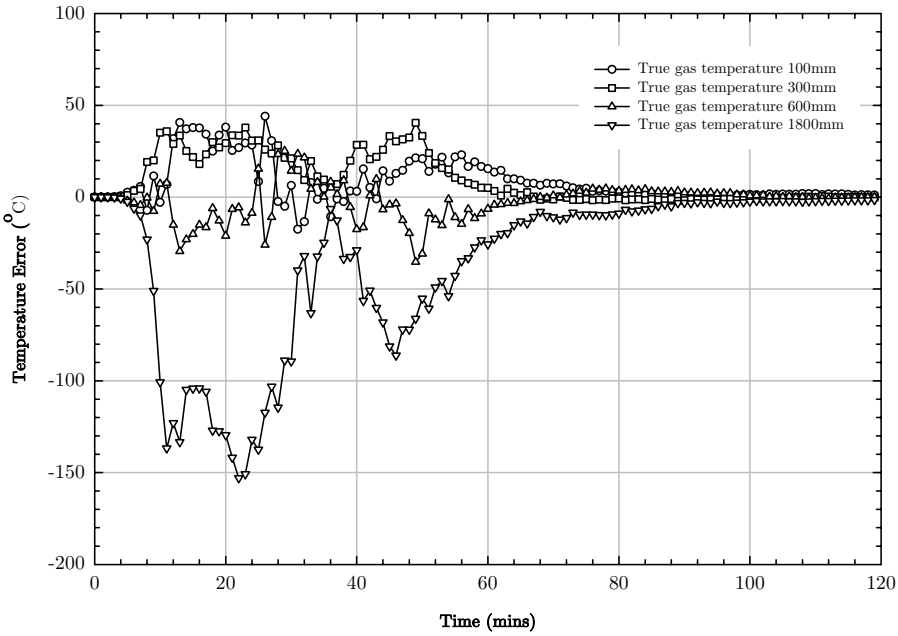

Figure 5.7: Differences between calculated and measured temperatures for thermocouple tree 7, Test 8. Distances in key denote height from ceiling. Room height is 3m.

Similar errors to those highlighted in Figure 5.7 were observed for all locations in the compartment, though with generally larger corrections towards the openings where the greatest variations in the underlying temperature fields are seen, and the influence of the ambient surroundings can be most clearly felt.

5.5.2. Opening velocity and temperature corrections

To be able to correct both the temperatures and the velocities in the opening, it is important to define whether the locations of the probes are in the inflow or outflow. A first approximation of velocity was achieved using the uncorrected thermocouple temperature using equation (5.26), the results of which are shown in Figure 5.8. It can be seen that probes 7-8 lie generally within the strong inflow region (negative velocity), although the measurements are rather erratic during certain phases of the fire. Probe 6, in contrast, recorded a significant outflow during much of the peak burning phase of the fire, when the hot layer is expected to be at its deepest, and reverted to a consistent inflow only during the decay phase. Thus, the assumption is made that probes 7 and below are inflows throughout the fire and vice versa for probes 6 and upwards, the difference between calculated and recorded temperatures ($T_g - T_{TC}$) in the opening is as shown in Figure 5.9. The results clearly demonstrate that the thermocouple errors can be very large indeed in the inflow, but also that they can be much bigger in the hot layer than in comparison to a location within the depth of the compartment, as in Figure 5.7. This observation is very much as expected for this region where the temperature stratification is much stronger than deeper within the compartment.

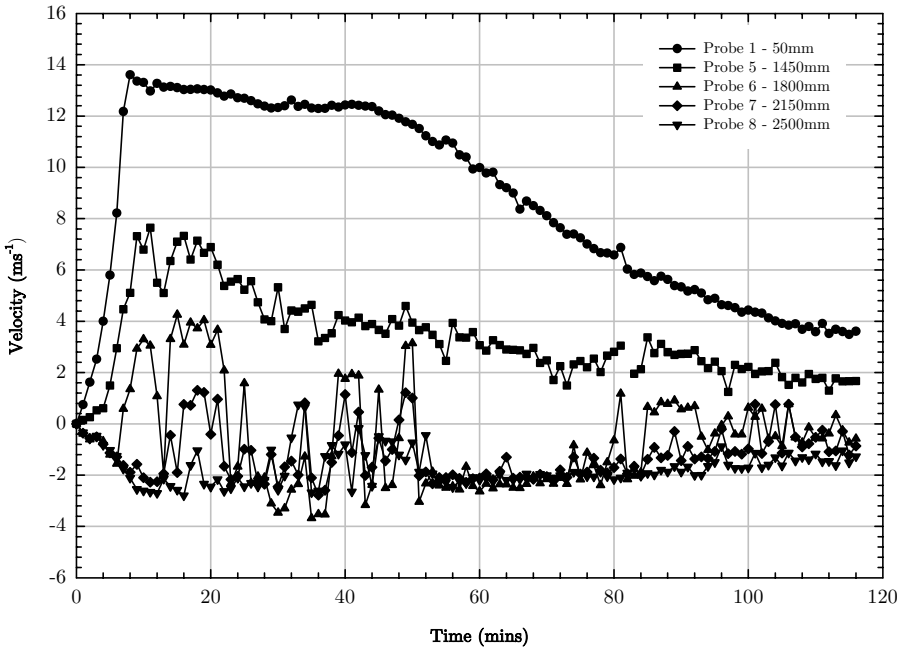

Figure 5.8: Velocities in the opening as calculated from original thermocouple temperatures for Test 8. Distances in key denote height from ceiling

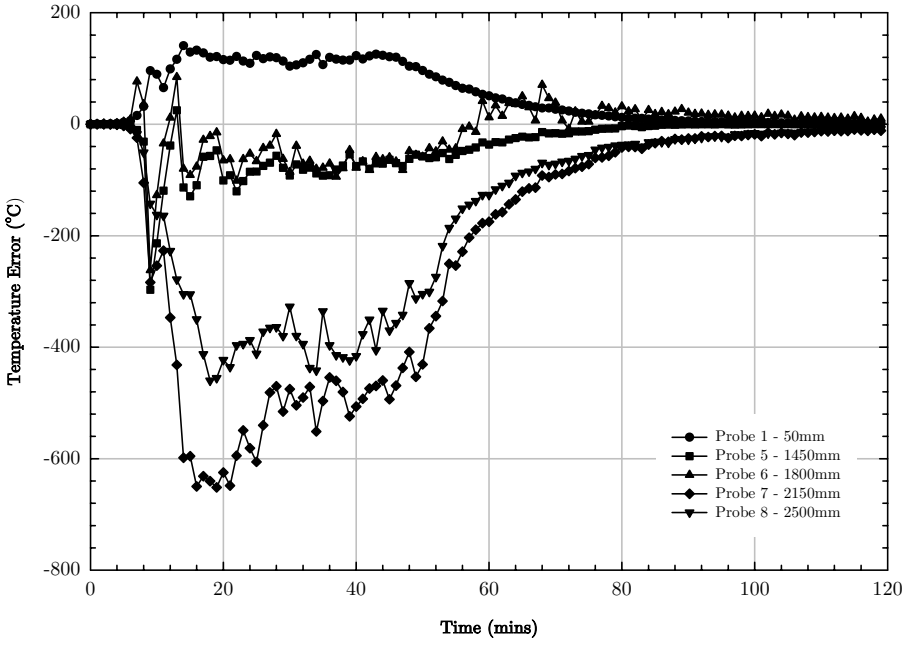

Figure 5.9: Differences between calculated and measured temperatures for thermocouple tree in the opening for Test 8. Distances in key denote height from ceiling

5.5.3. Heat flux comparisons

Up to this point, corrected gas temperatures have only been justified in theoretical terms; however, the recorded heat fluxes provided by the billets allow for a more direct validation by means of comparisons between measured total fluxes and those calculated from the surrounding temperatures based on corrected gas temperatures. Results are presented for billet 7 of Test 8. Here the corrected surroundings temperature at the billet height was evaluated by averaging the estimated gas temperatures from the appropriate thermocouples on trees 5 and 9. Figure 5.10 shows the recorded flux together with that calculated from the method described using the true gas temperatures. Also shown is the heat flux calculated from the thermocouple local to the billet (positioned 50mm away), assuming a surface emissivity of 0.8.

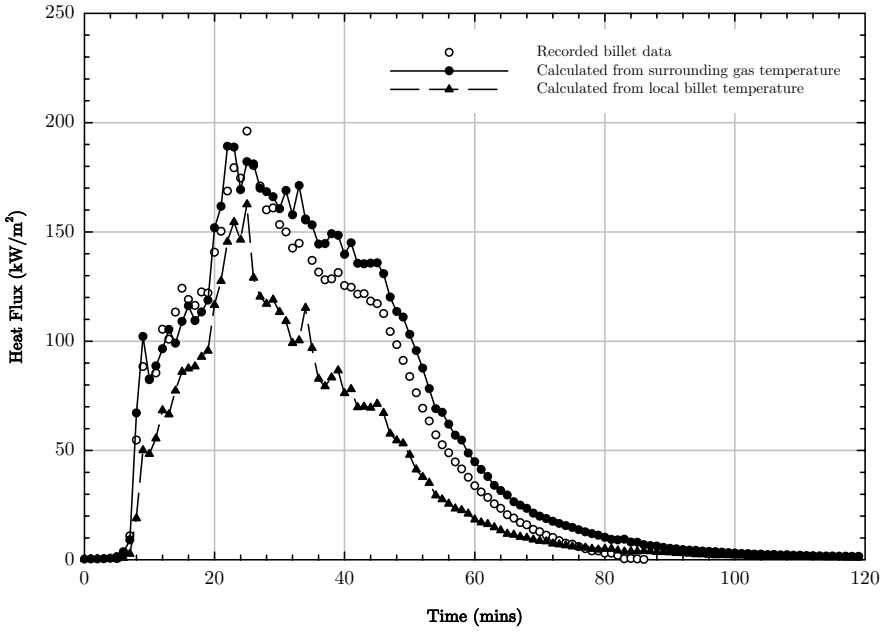

Figure 5.10: Recorded heat fluxes and heat fluxes calculated from the relevant true gas temperature and from the local surrounding gas temperature for billet 7 of Test 8.

The graph shows that the flux computed from the local thermocouple reading is significantly lower than the recorded flux, which might perhaps be attributed to the fact that this thermocouple is influenced by the wall temperature itself which will be lower than the local gas temperatures. The method which uses the corrected temperatures from the neighbouring region, in comparison, shows a good correlation with the recorded data for the first 30 minutes, before diverging slightly. One influence which might be partly responsible for the observed difference later in the test is a change in the gas emissivity. The fire load in this test comprised plastic and wood, with the plastic component experiencing preferential burn off, with denser smoke. The larger drop in measured flux following the peak (after 30 minutes) may be associated with the fact that most of the plastic would have been consumed at that point, with an associated reduction in smoke visibility and emissivity. Another possibility is that the convective component of the total heat flux has, plays a larger role in contributing to the fluxes earlier in the test, but this reduces once the billet surface heats up to close to the gas temperature.

Figure 5.11 through to Figure 5.14 show selected comparisons between measured and calculated heat fluxes at different locations within the compartment for various tests. Good agreement is seen for each case demonstrating that the model is robust enough to be able to reproduce the test measurements spanning the full range of parameters varied in the tests both at the back of the compartment and on the centreline. The trends are also consistent with the physical understanding of the results, with the latest peak, for billet 6 located in the back wall of Test 2 (Figure 5.11), occurring at around 50 minutes when the fire has finally progressed to towards the back of the compartment.

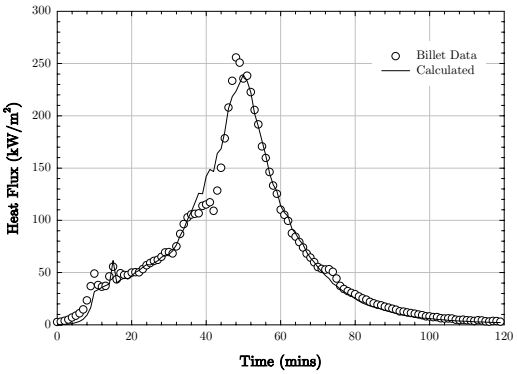

Figure 5.11: Billet 6 (back wall) of Test 2

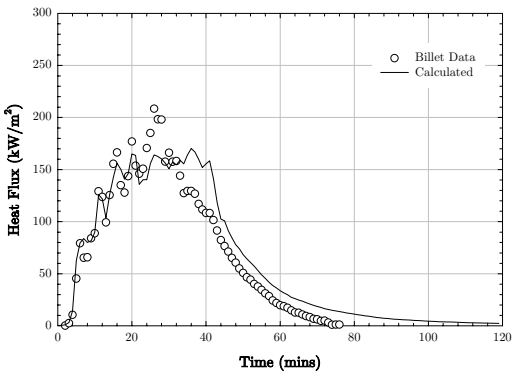

Figure 5.12: Billet 7 (left side wall) of Test 3

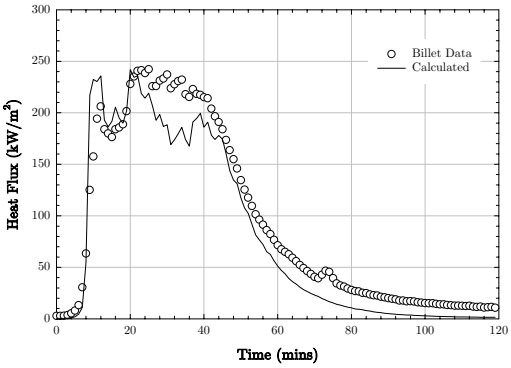

Figure 5.13: Billet 6 (ceiling) of Test 8

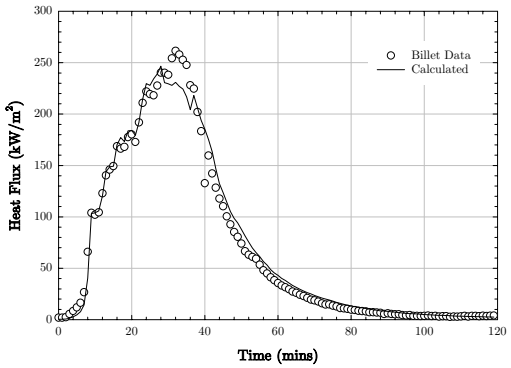

Figure 5.14: Billet 8 (right side wall) of Test 4

5.5.4. Temperature and radiative intensity maps

A good way to view the spatial variation in the thermal fields is to compute two-dimensional contour plots through the compartment. This has been done in the following sections, for both gas temperature and radiative intensity fields. The plots have been separated into three plane cross-sections: -

(a) Into the depth of the compartment, on the doorway centreline
(b) Across the width of the compartment, at mid-depth
(c) Just below the compartment ceiling,

Each cross-section is described in the following sections. For each case, plots are produced at 10 minute intervals from 10 minutes to 40 minutes in order to capture the main post-flashover stage of the fire, defined in Figure 5.6, Figure 5.10 and Figure 5.13. Plot locations are indicated in Figure 5.15.

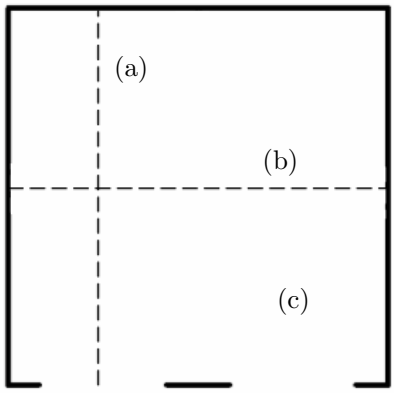

(a) Figure 5.16 and Figure 5.17: cross-section from back wall to opening

(b) Figure 5.18 and Figure 5.19: cross-section through compartment centre

(c) Figure 5.20 and Figure 5.21: entire ceiling of compartment

Figure 5.15: Key to locations of radiative intensity and gas temperature contour plots

Plane through opening

A plot of gas temperatures reveals high values near to the opening (on the right of the plot), as preferential burning takes place there due to the ventilation in the earlier stages of the fire (Figure 5.16a), while the influence of a strong inflow of ambient air is seen in the lower section of the doorway. As the fire continues to burn there is an obvious progression of the highest temperature region (1200°C) towards the rear of the compartment. Overall, strong gradients of temperature are apparent over the height of the compartment and, to a lesser extent, through the depth of the room.

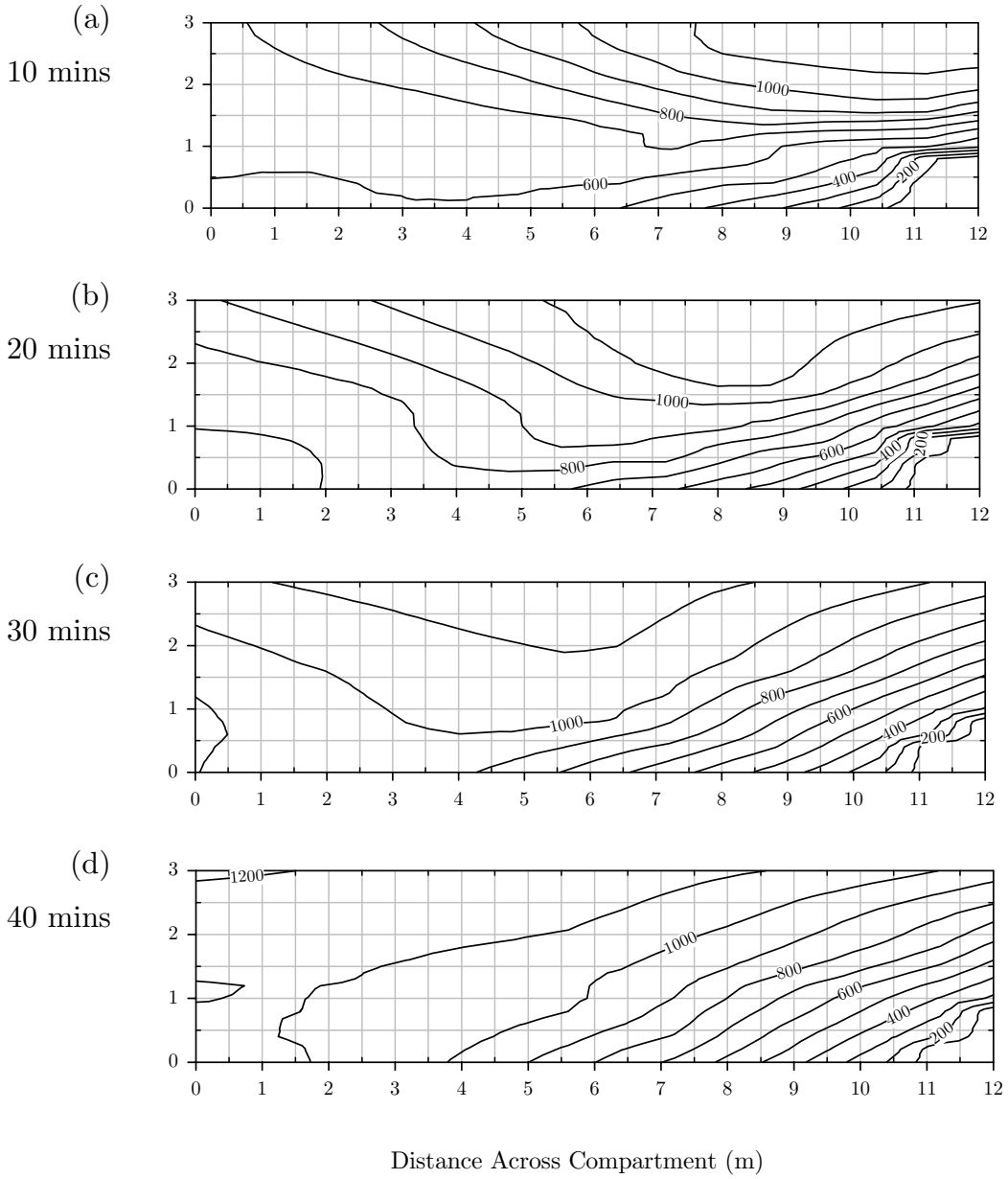

Figure 5.16: Gas temperature map over cross-section through compartment (see Figure 5.15) from back wall (left) to doorway (right). Contour labels are in °C

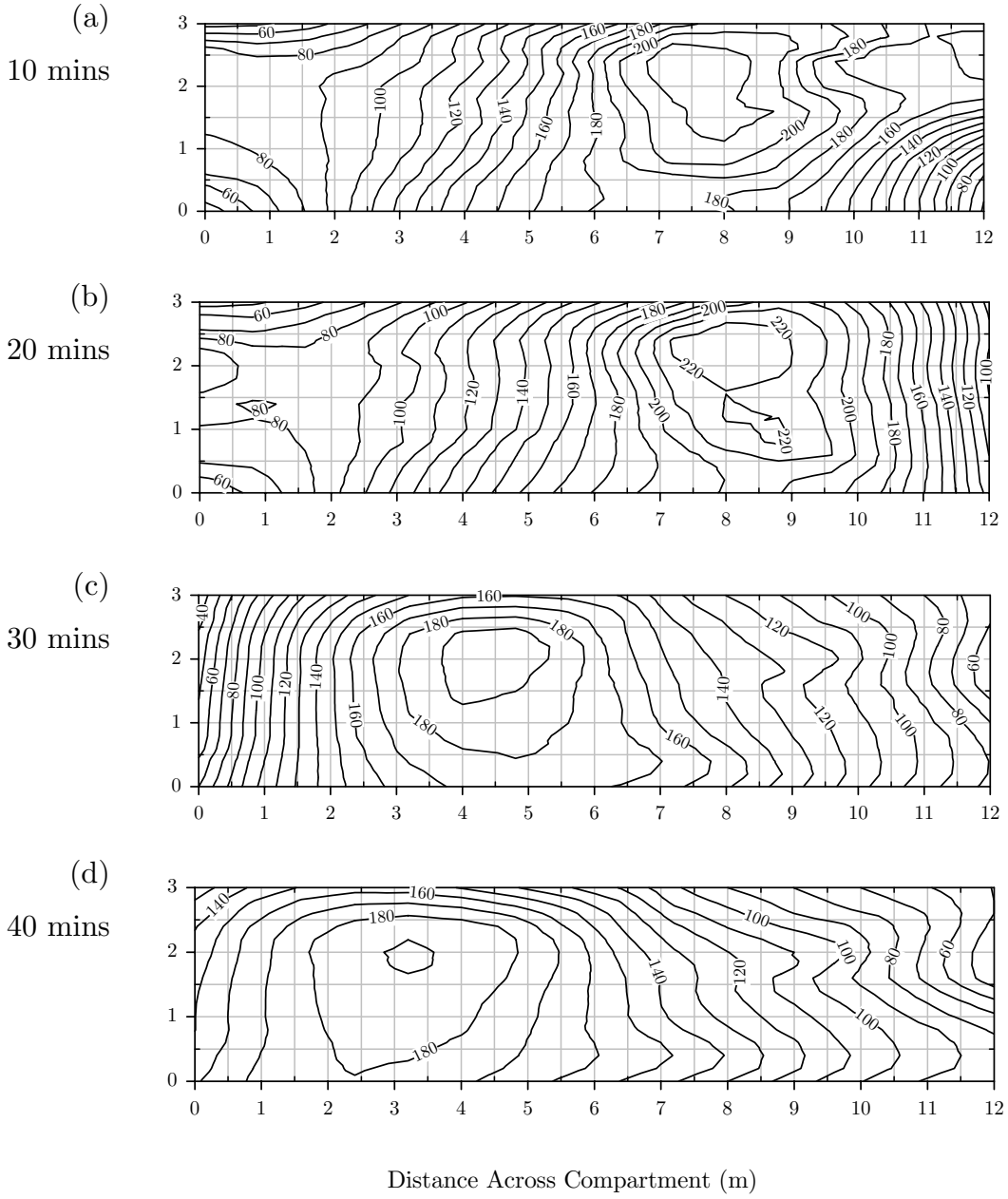

Figure 5.17: Radiative intensity map over cross-section through compartment (see Figure 5.15) from back wall (left) to doorway (right). Contour labels are in kW/m^2

If the equivalent radiative intensity plot is examined (Figure 5.17a) then a rather different pattern is shown. The highest intensities, of the order of 200kW/m^2, are found towards the front of the compartment early in the test but the vertical gradient in the opening is less severe. As the fire continues, the peak radiative intensities are seen to progress towards the rear of the compartment. However, the vertical gradient due to the inflow of air becomes less pronounced. This is due to the dominant effect of the strong radiation from products of combustion in the upper layer at this stage in the test. Indeed, Figure 5.17b indicates an area high radiative intensity of over 200kW/m^2 within what is effectively the lower layer, even though local gas temperatures drop off rapidly through this region. Interestingly, Figure 5.17d also shows relatively high radiative intensities in the lower layer towards the front of the compartment and again this can be attributed to remote radiation, but in this case enhanced by radiation received from the remains of the cribs, glowing white hot in the incoming air stream.

Plane across width

The temperature profiles shown in Figure 5.18 show some vertical stratification but this is less severe than that shown in Figure 5.16. There is considerable asymmetry in the maps, with burning on this plane initially focussed on the right of the plot (i.e. on the right of the test compartment) before moving to the left at 30 minutes, but the effect of inflow from the two openings at the front of the compartment cannot be clearly detected.

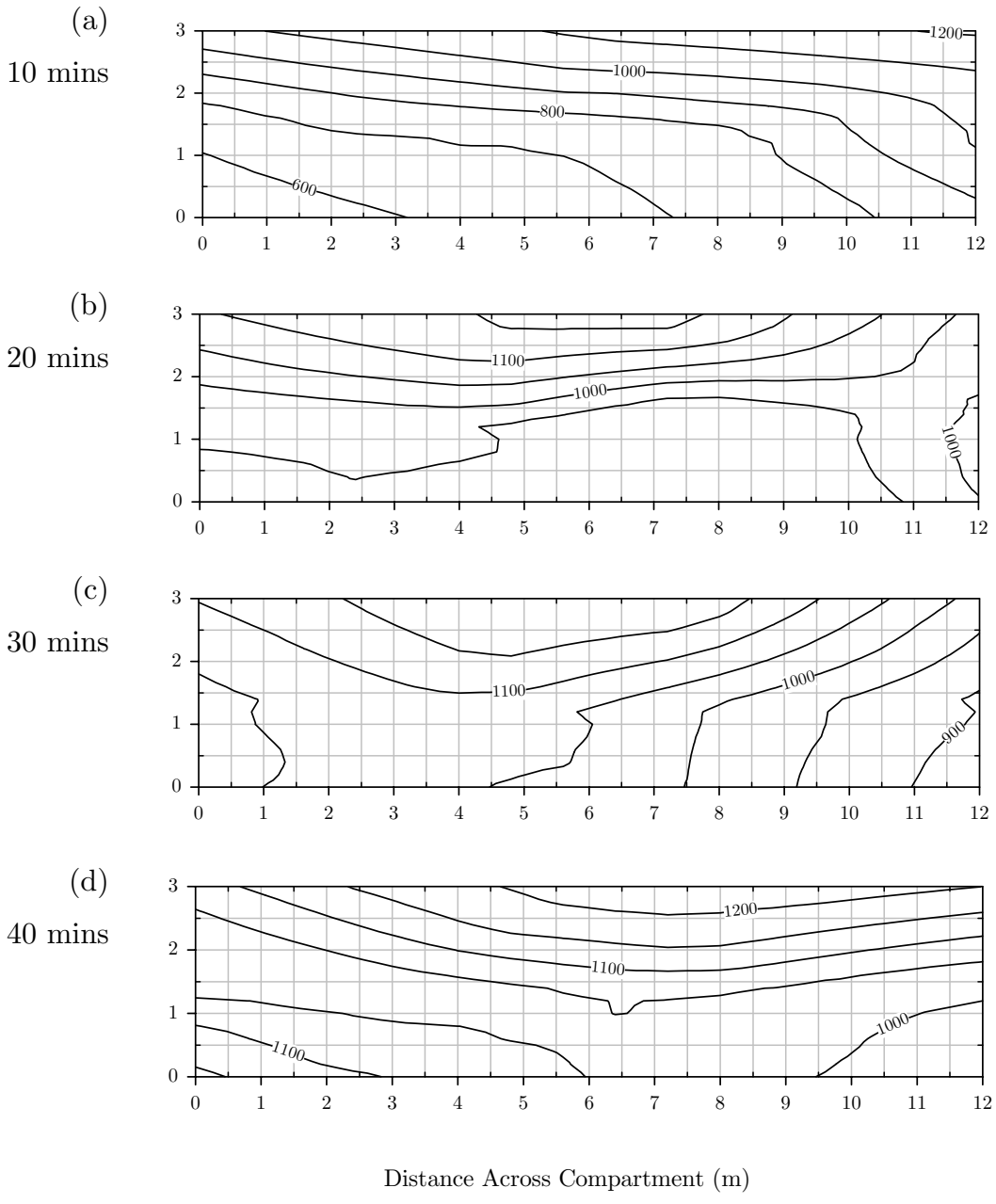

Figure 5.18: Gas temperature map over cross-section through centre of compartment (see Figure 5.15), viewed from front.

Contour labels are in °C

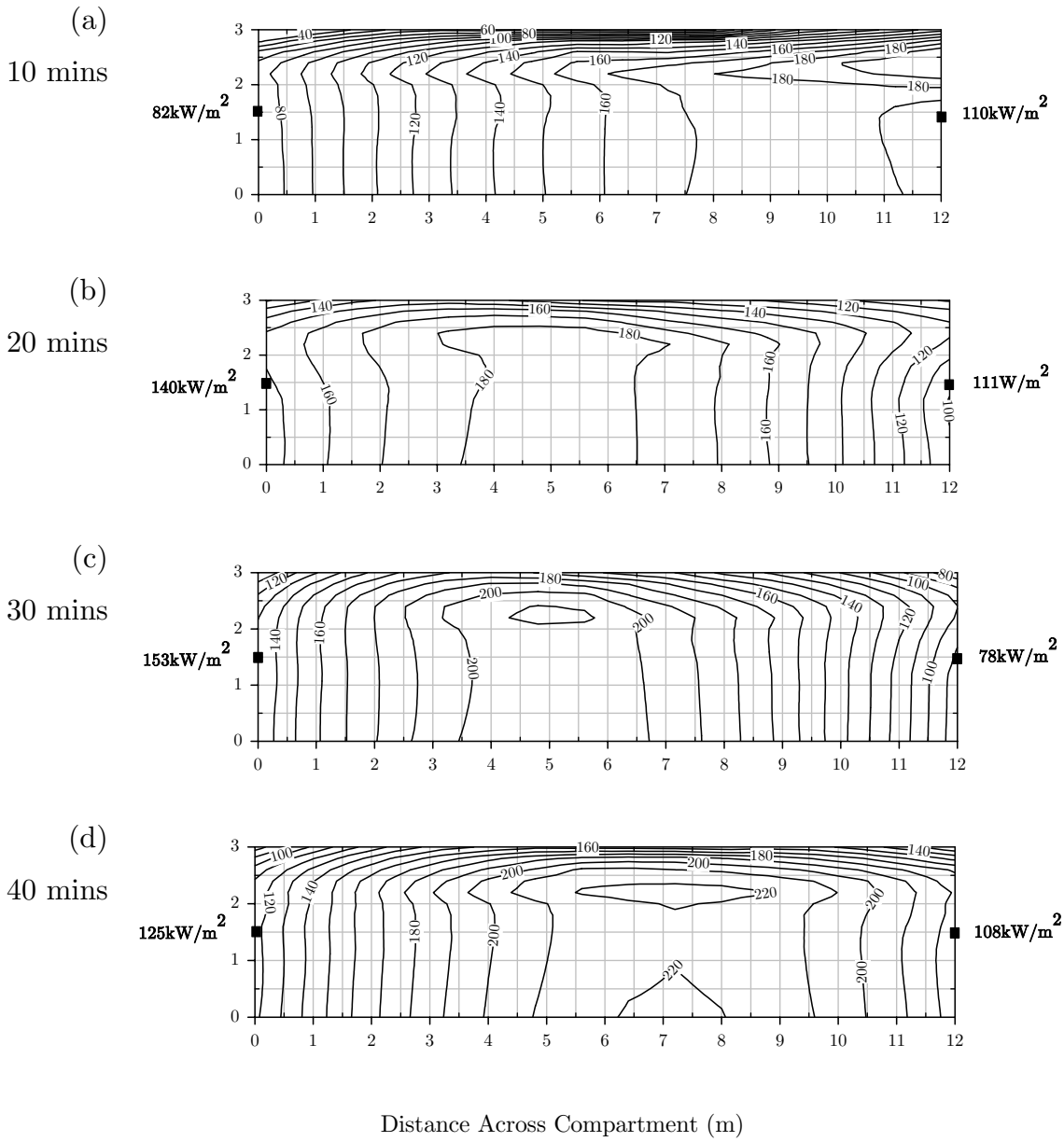

Figure 5.19: Radiative intensity map over cross-section through centre of compartment (see Figure 5.15), viewed from front. Bold numbers at the sides indicate billet reading at the black square at the corresponding time. Contour labels are in kW/m^2

The distribution of radiative intensities with time is shown in Figure 5.19. The advantage of plotting contours in this location is that it allows direct comparison with the recorded billet data on the left and right side walls, included on the plots at the black square locations. As noted earlier, the radiative intensities actually represent the total energy arriving at a region, so are not directly comparable to the wall fluxes; however, the two values will tend to converge unless the compartment walls are very hot, as the former value is dominated by the radiative heat arriving from within the volume of the compartment, with the energy coming from the wall itself often being insignificant. In this respect it can be seen that there is a very good agreement.

Plane below ceiling

Plots of the gas temperatures just below the ceiling are shown in Figure 5.20. Due to the presence of a hot smoke layer, the temperatures in this region are consistently high – all in excess of 600°C. However the results still reveal the dynamic nature of the fire. Highest temperatures are initially seen at the opening, but are then seen to progress towards the rear of the compartment as the fire develops. Maximum temperatures are never in excess of 1300°C. During the initial stages of the fire, the influence of the two doorway openings can be seen in Figure 5.20a. The central supporting pillar between the openings (centre of right side of the plot) forces the flow of smoke and combustion products towards the doorways and as a result comparatively lower temperatures are found in this region. The asymmetry noted in Figure 5.18 can now be seen to be a function of depth, with burning having apparently progressed more deeply into the compartment at the right-hand side and a region of very intense combustion located in the upper left opening at the 10 minute snapshot.

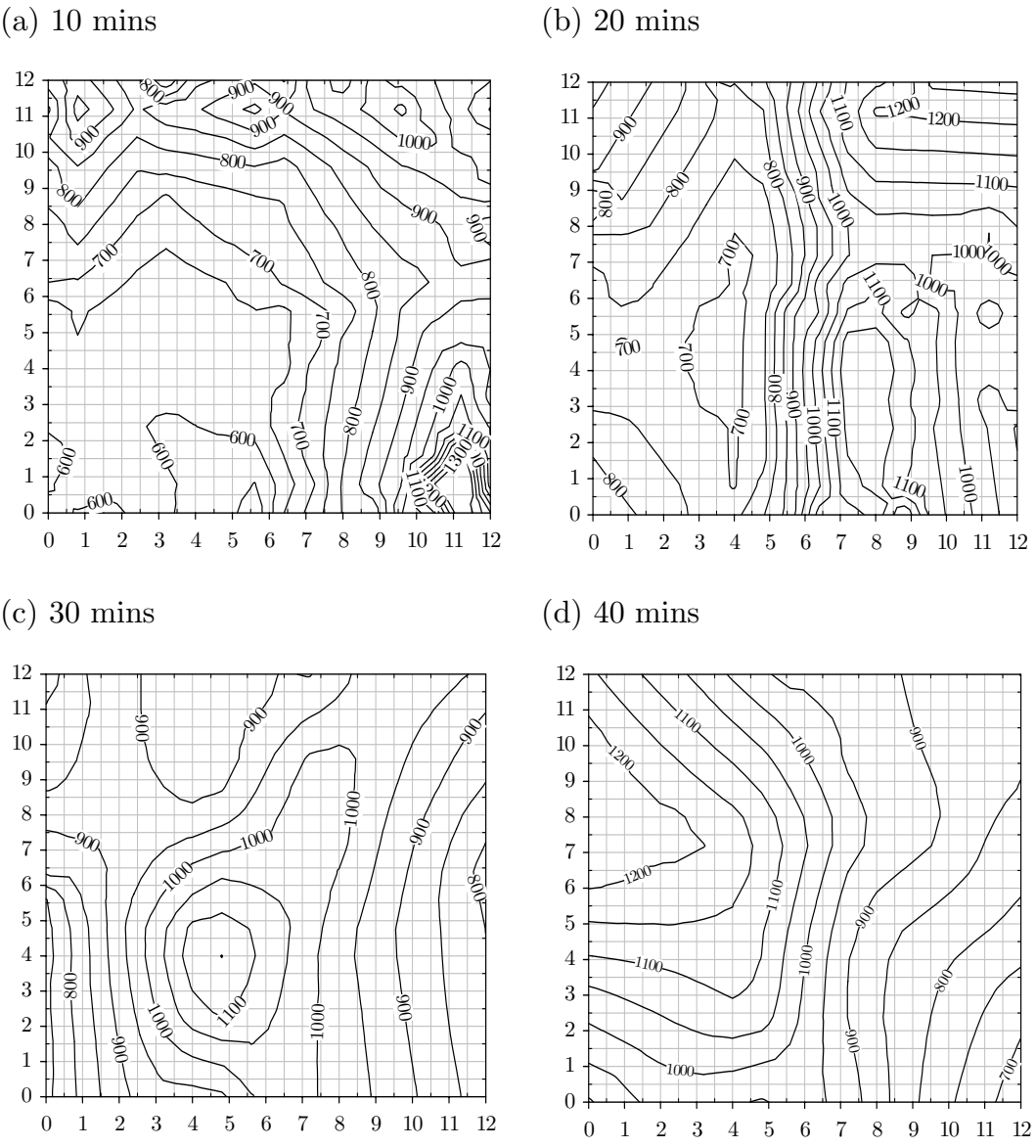

Figure 5.20: Gas temperature map just under compartment ceiling (see Figure 5.15). The openings are located on the right of each plot. Contour labels are in °C and axis labels of room dimensions are in m

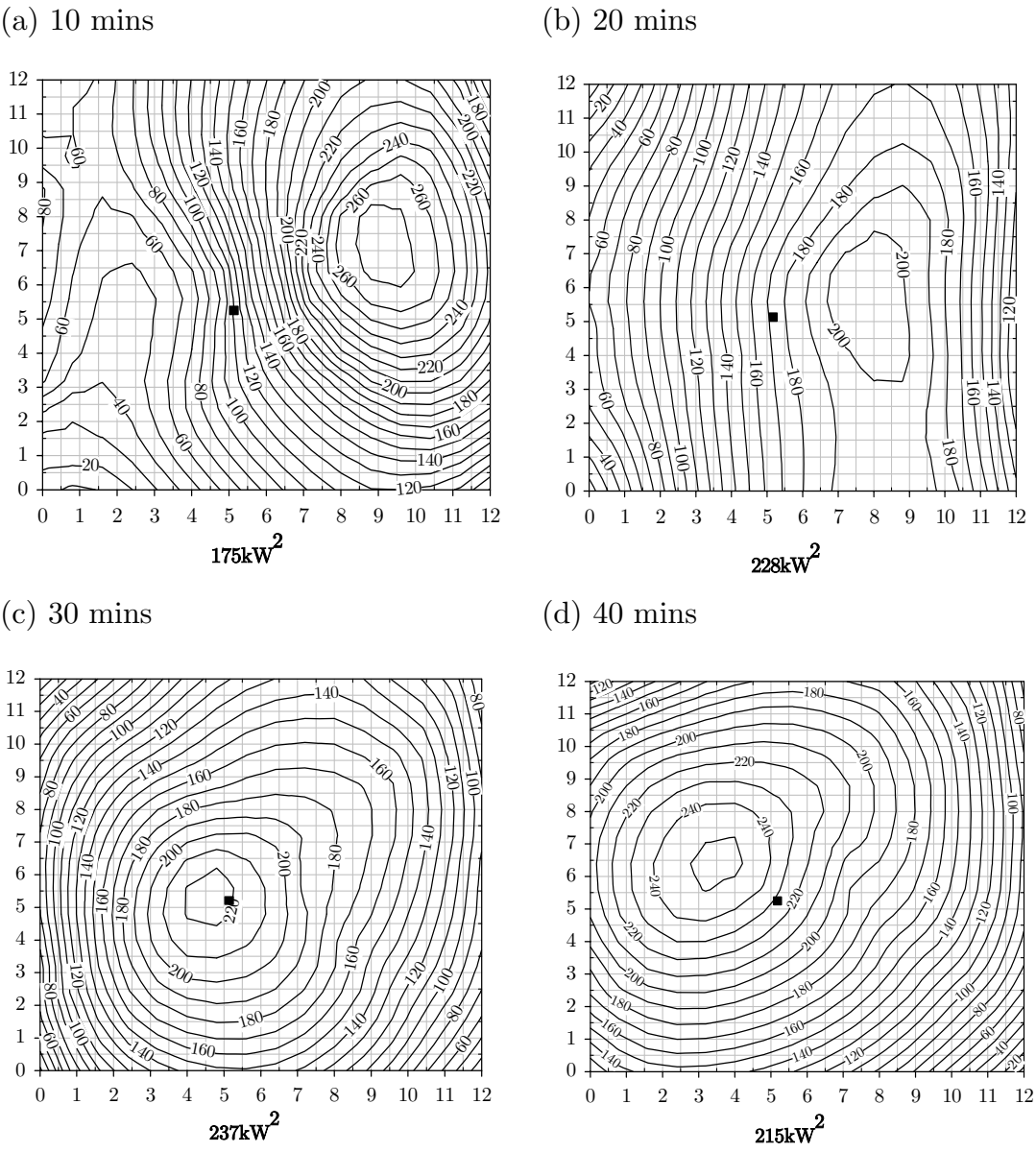

Figure 5.21: Radiative intensity map over compartment ceiling (see Figure 5.15). Bold numbers below the plots indicate billet reading at the black square at the corresponding time. The openings are located on the right of each plot. Contour labels are in kW/m^2 and axis labels of room dimensions are in m

The plot of ceiling radiative intensities reveals some interesting observations – see Figure 5.21. Strong gradients of flux are seen over the entire ceiling at all stages of the fire. The maximum heat flux of 280kW/m^2 is seen towards the front of the compartment in the early stages of the post-flashover fire (i.e., at 10 minutes), some distance behind the regions of peak temperatures located in the openings themselves. Once again, as the fire develops, the peak region moves towards the rear of the compartment, but mirroring the above observation, it does not move as far back as the peak temperature region. A similar phenomenon can be observed laterally, i.e. peak radiative intensities remain near the middle of the compartment even when temperatures are highest towards the edges. The reason for these differences is the influence of the effective configuration factor in the radiative intensity parameter; in the middle of the compartment, heat transfer is effective from both sides, whereas towards the edges the total value becomes increasingly dominated by the energy arriving from only one direction, i.e. from the centre of the compartment. This also accounts for the factor of approximately two which relates the intensities within the depth of the compartment to those at the edge, As for the other plots above, the strong gradients of radiative intensity show that even during the post-flashover stage significant variations of effective thermal exposures may be present.

5.5.5. Comparison with averaged test results

Comparison of the averaged values for gas temperatures and thermocouple temperatures for Test 8 show that there is very little difference when looked at in overall terms, see Figure 5.22. The peak difference is only 13°C. The reason for such a small effect is predominantly due to error cancellation – the differences are only large locally. The result of this comparison highlights the need for a correct spatial definition of temperatures and heat fluxes. The fact that all errors are cancelled, as is

expected due to the conservation of energy, shows just how misleading an average temperature can be. By adopting an average value, extreme gradients of heat flux are being ignored within the compartment.

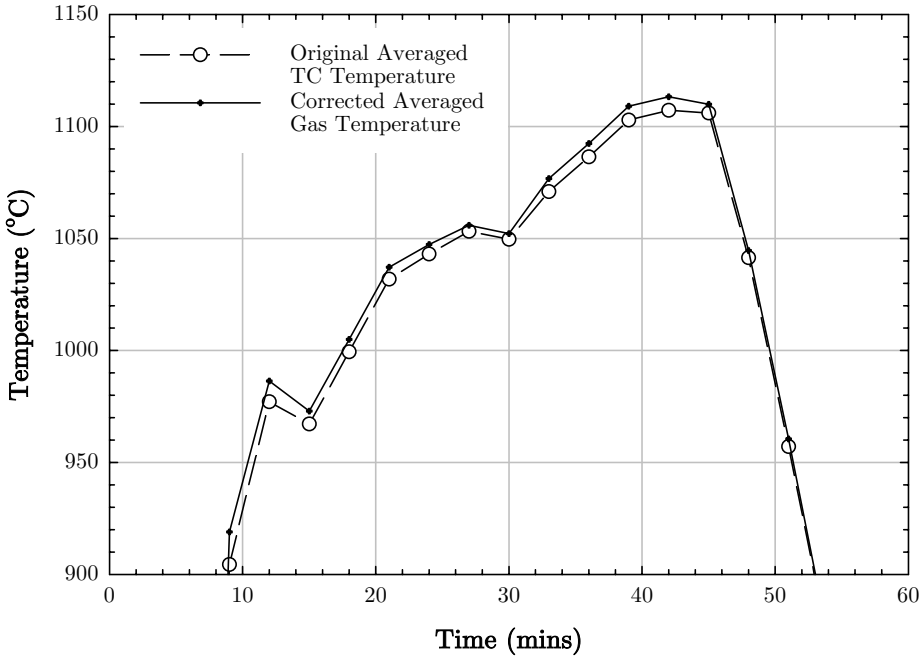

Figure 5.22: Comparison of averaged gas temperatures and averaged thermocouple temperatures for test 8, for high temperature part of curve (>900°C)

5.6. Conclusions

By establishing a reconstruction of the gas temperature field, one of the key motivations of this chapter has been to consider the thermal exposure distributions within post-flashover fires. Conventionally, these are assumed to be uniform, or at best partitioned into two layers, but this simplification would not be supported by the results of the current analysis. Also, heating potential is normally assessed purely in terms of gas temperatures, or if test data are used, thermocouple temperatures. The latter may depart significantly from gas temperatures, particularly

near openings, as shown here, but can be corrected by the method presented if there are sufficient measurement points. A more useful parameter for characterising thermal exposures is the radiative intensity, i.e. the total radiant energy arriving at any point in space, which would be incident upon a structural member if located there – it must be remembered however, that convection can never totally be ignored. The distribution of radiative intensities may be significantly different from that of gas temperature, due to the influence of remote radiation. As has been shown in the preceding sections, the locations where gas temperatures peak, typically near openings, can be significantly offset from the regions of peak radiative intensities which tend to occur, deeper into the compartment fire. This is because the latter parameter is influenced by remote conditions, being enhanced where there are long path-lengths through high temperature combustion products, but can be suppressed where cooler environments exert an influence. In this respect, the radiative intensity parameter mirrors the behaviour of thermocouples in radiation-dominated environments. Thermocouples however, do not provide a direct measure of thermal severities, such as the likely impact of the fire on structural components. They do however, provide an idea of the distribution of heating and can also be converted directly to intensities if an appropriate surface emissivity can be determined.

Whilst local gas temperatures might not be well represented by thermocouple measurements, values which are averaged over the whole fire region might provide a very good approximation to the average gas temperatures. This simply due to the fact that errors cancel due to the fact that energy is lost from one part of the domain is captured in another. The method of using an average compartment temperature can hide extreme variations in the severity of a fire experienced by structural members within the compartment.

Chapter Six

6. Characteristic Heating Times of Solids

6.1. Introduction

It is well known that the heating times of solid-phase structural elements differ greatly than those of the gas-phase environment. Extreme fluctuations in temperature may occur in the gas for a given fire, while for the same scenario, the structural members may exhibit a far more steady change in temperature. This chapter studies the characteristic heating times associated with different types of structural materials to demonstrate that not every time instance of the fire necessarily needs to be considered when analysing the incident surface heat fluxes. An acceptable level of accuracy can be obtained by averaging results over a given time interval.

This method allows the transformation of transient environments into quasi-steady-state conditions that simplify the analysis into the summation of a series of steady-state solutions.

Although the scope of this study intends to define structural surface heat fluxes, characteristic heating times can only be evaluated with some knowledge of an element's ability to conduct heat. If an element is sufficiently thin so that it can be assumed to heat uniformly throughout its section, then one approach to define its characteristic heating time can be adopted. If however the section is sufficiently thick so that thermal gradients are induced over its width, then an alternate approach is required. These methods are outlined in the following section.

6.2. Biot Number

It is important to be able to quantify a structural element's ability to conduct heat through its thickness as a means to characterise whether it can be treated as thermally thick or thermally thin. Consider the plane wall with surface convection in Figure 6.1. If one surface is maintained at

ambient temperature $T_{s,1}$ and the other surface is exposed to a hot fluid of temperature $T_\infty > T_{s,1}$, then this temperature will be some intermediate value, $T_{s,2}$ for which $T_\infty > T_{s,2} > T_{s,1}$. The surface energy balance of this system can be written as,

$$\frac{kA}{L}(T_{s,1} - T_{s,2}) = hA(T_{s,2} - T_\infty) \tag{6.1}$$

where is k the material's thermal conductivity. Rearranging gives,

$$\frac{(T_{s,1} - T_{s,2})}{(T_{s,2} - T_\infty)} = \frac{(L/kA)}{(1/hA)} = \frac{hL}{k} \equiv Bi \tag{6.2}$$

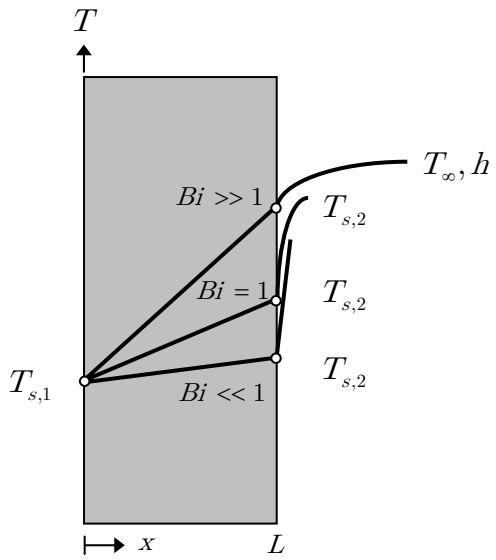

Figure 6.1: Effect of the Biot number on steady-state temperature distribution in a plane wall with surface convection

The dimensionless parameter termed the Biot number can be used to quantify the resistance to conduction within the structural element.

$$Bi = \frac{h_T L_c}{k} \tag{6.3}$$

where h_T is the total heat transfer coefficient given by,

$$h_T = h_c + h_r \tag{6.4}$$

The characteristic length L_c in equation 1.1 can be considered a conduction characteristic length and relates to the length scale corresponding to the maximum spatial temperature difference. It is customary to define this characteristic length as the ratio of the element's solid volume to its surface area,

$$L_c \equiv \frac{V}{A_s} \tag{6.5}$$

The following conditions can be outlined to determine which method should be used to determine a structural element's characteristic heating time.

If $Bi < 0.1$ - Thermally thin

If $Bi > 0.1$ - Thermally thick

This is demonstrated in Figure 6.2 where a plane wall initially at a uniform temperature T_i experiences heating when immersed in a fluid of $T_\infty < T_i$. The problem can be treated as one dimensional in x and the temperature variation with position and time, $T(x,t)$ is shown. The temperature variation throughout the section is seen to a strong function of the Biot number. When the Biot number is small, temperature gradients in the solid are small and the main temperature difference is

between the solid and the fluid, and the solid temperature remains nearly uniform as it increases to T_∞. For large values of the Biot number, temperature gradients within the solid can be significant and the temperature difference across the solid is much larger than that between the surface and the fluid.

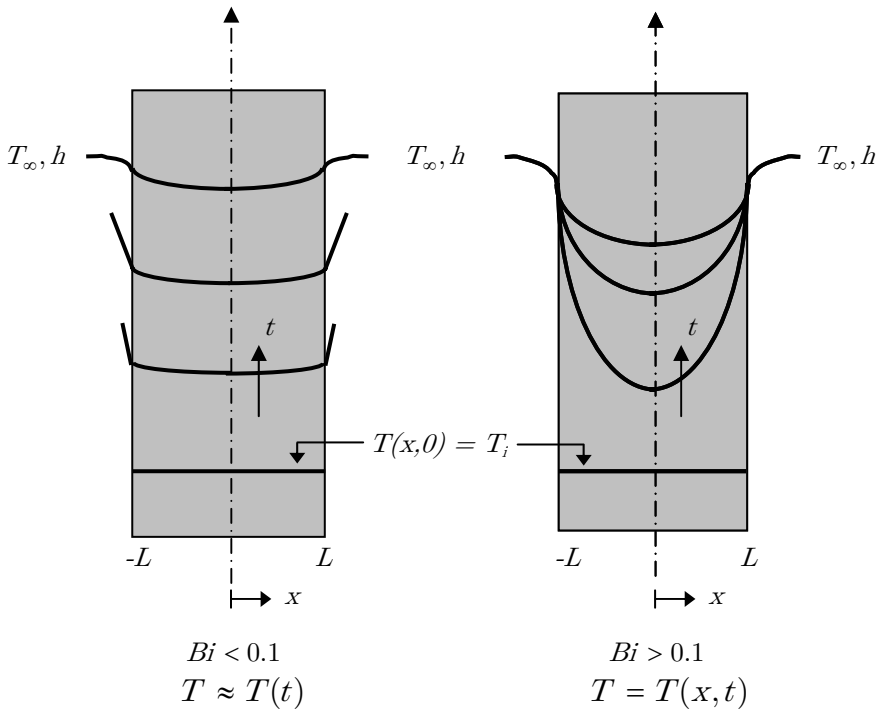

Figure 6.2: Transient temperature distributions for different Biot numbers in a plane wall symmetrically cooled by convection

The total heat transfer coeffcient used in the calcualtion of the Biot number is the sum of the convective and radiative transfer coefficients as shown in equation (6.4). When considering a certain structural element, it is reasonable to assume that the convective coefficient will remain constant throughout the fire. The radiative component however is a function of the local gas – assuming that the element is within an optically dense medium. The radiative heat transfer coefficient can be written as,

$$h_r = \varepsilon\sigma(T_g^2 + T_s^2)(T_g + T_s) \tag{6.6}$$

However, if the surface is assumed to remain cold, the radiative heat transfer coefficient can be defined by,

$$h_r = \varepsilon\sigma T_g^3 \tag{6.7}$$

The dependence of the total heat transfer on the gas-phase temperature is shown in Figure 6.3. A constant convective heat transfer coefficient of 25W/m^2.K has been assumed while the radiative coefficient rises with temperature to the third power. In order to be conservative in evaluating the thermal thickness of a structural element, the maximum value of the total heat transfer coefficient is required. This has been defined for the following section as occurring for a gas-phase temperature of 1200°C.

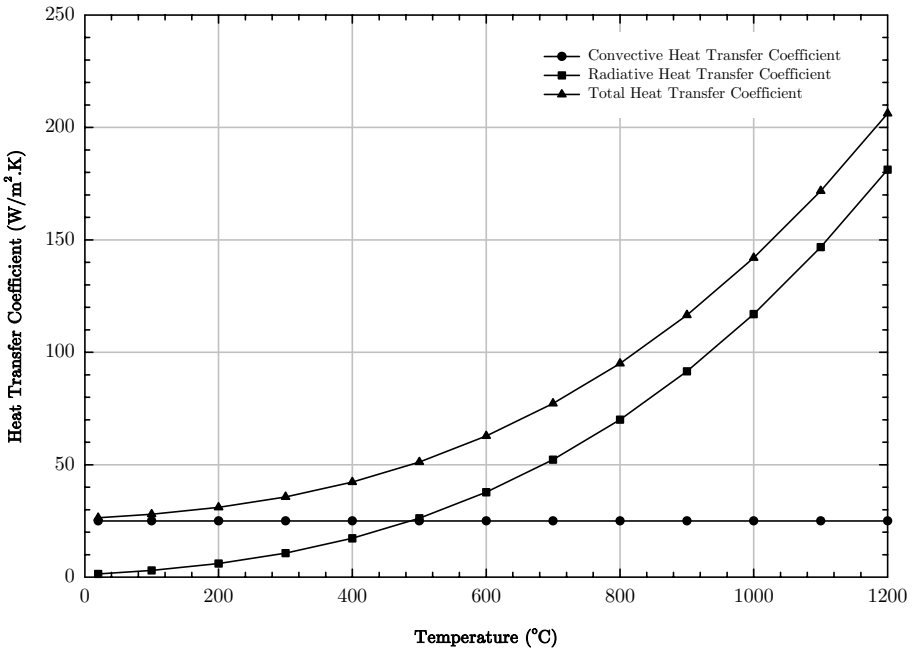

Figure 6.3: Variation of heat transfer coefficients with gas-phase temperature, assuming $\varepsilon_g = 1$

Table 6.1 presents the thermal properties of typical structural materials including steel, concrete and numerous types of insulation.

Material	k (kW/m.K)	c (kJ/kg.K)	ρ (kg/m^3)
Aluminium (pure)	0.206	0.895	2710
Steel (0.5% Carbon)	0.054	0.465	7850
Concrete	0.0016	0.75	2400
Brick	0.0008	0.80	2600
Glass	0.00076	0.80	2710
Brick/Concrete Block	0.00073	0.84	1900
Gypsum Board	0.00017	1.10	960
Plywood	0.00012	2.50	540
Fiber Insulation Board	0.00053	1.25	240
Chipboard	0.00015	1.25	800
Aerated Concrete	0.00026	0.96	500
Plasterboard	0.00016	0.84	950
Calcium Silicate Block	0.00013	1.12	700
Alumina Silicate Block	0.00014	1.00	280
Glass Fiber Insulation	0.000037	0.80	60
Expanded Polystyrene	0.000034	1.50	20

Table 6.1: Common structural materials - thermal properties

For each of the materials in Table 6.1, the Biot number has been calculated assuming a characteristic length scale, $L_c = 0.02\text{m}$ which would typically represent a large I-beam member. The convective heat transfer coefficient has been taken as 25W/m^2.K and the radiative coefficient evaluated for 1200°C. This gives a total heat transfer coefficient of,

$$h_T = 25 + (1 \times 5.67 \times 10^{-8} \times (1200 + 273)^3) = 206\text{W/m}^2\text{.K} \qquad (6.8)$$

The plot of Biot numbers in Figure 6.4 shows that only aluminium and steel can be considered thermally thin for the given characteristic length as their Biot number is lower than 0.1. For all the other materials, their Biot number is greater than one indicating that they are thermally thick. This

is most evident for the insulation materials which exhibit extremely large Biot numbers.

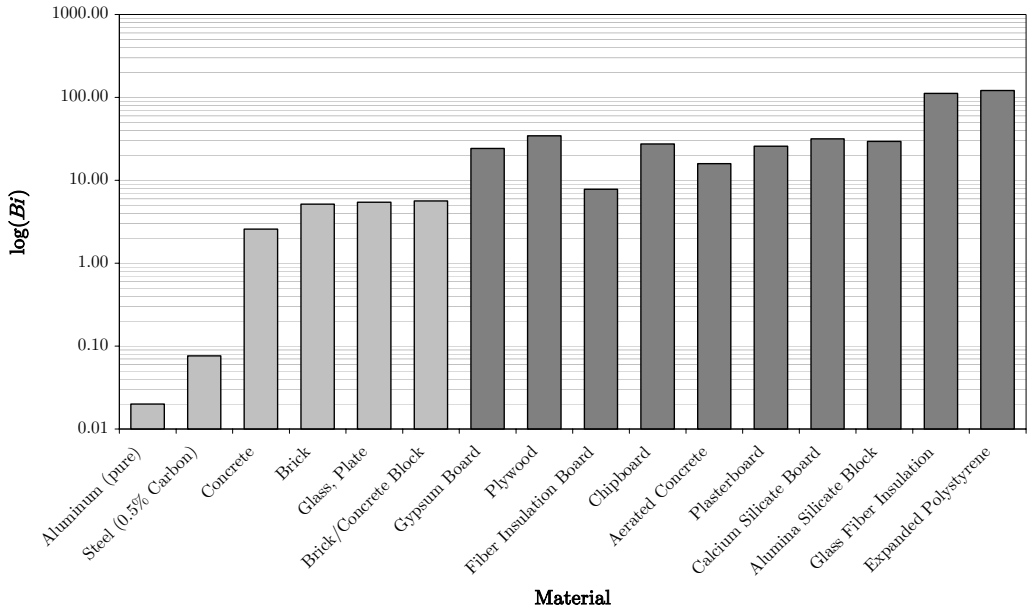

Figure 6.4: Biot number for typical structural materials where light grey bars represent primary structural materials and dark grey bars are insulation materials.

Having established whether an element is thermally thin or thick provides a basis for calculating the characteristic heating time of a structural element. The relevant approach to each is outlined in the following sections.

6.3. Thermally thin

When it is known that the temperature gradients within a solid can be assumed to be negligible so that the temperature can be taken to be spatially uniform, then the approximation of the lumped capacitance method can be applied. Considering the energy balance that relates the

rate of heat input at the surface to the rate of change of internal energy, the temperature response of a structural element can be expressed as,

$$-hA_s(T_s - T_\infty) = \rho Vc\frac{dT_s}{dt} \tag{6.9}$$

In which (ρVc) is termed the *lumped thermal capacitance* of the solid. Further derivation leads to the solution for the temperature reached by the solid at some time, t,

$$\frac{T_s - T_\infty}{T_i - T_\infty} = \exp\left[-\left(\frac{hA_s}{\rho Vc}\right)t\right] \tag{6.10}$$

Where $(\rho Vc / hA_s)$ is defined as the *thermal time constant*. Taking $L_c \equiv V / A_s$, then exponent of equation 6.10 can be written as,

$$\frac{hA_s t}{\rho Vc} = \frac{ht}{\rho cL_c} = \frac{hL_c}{k}\frac{k}{\rho c}\frac{t}{L_c^2} = \frac{hL_c}{k}\frac{\alpha t}{L_c^2} \tag{6.11}$$

or

$$\frac{hA_s t}{\rho Vc} = Bi \cdot Fo = 1 \tag{6.12}$$

where

$$Fo = \frac{\alpha t}{L_c^2} = 1 \tag{6.13}$$

is termed the Fourier number. It is a dimensionless time, which together with the Biot number is used to characterise transient conduction problems. If the Fourier number is set to 1, then a characteristic heating time of the solid can be evaluated as,

$$t_{c_{thin}} = \frac{L_c^2}{\alpha} \tag{6.14}$$

For the materials shown to be thermally thin for the example given in section 6.2, the corresponding characteristic time is presented in Table 6.2.

Material	t_c (s)
Aluminium (pure)	5
Steel (0.5% Carbon)	27

Table 6.2: Characteristic heating times of thermally thin materials with L_c=0.02m

6.4. Thermally thick

When temperature gradients within a structural element are known to be significant, the lumped thermal capacitance approach cannot be used. An alternative method to evaluate the characteristic heating time is to use the analytical solution for a *semi-infinite solid*.

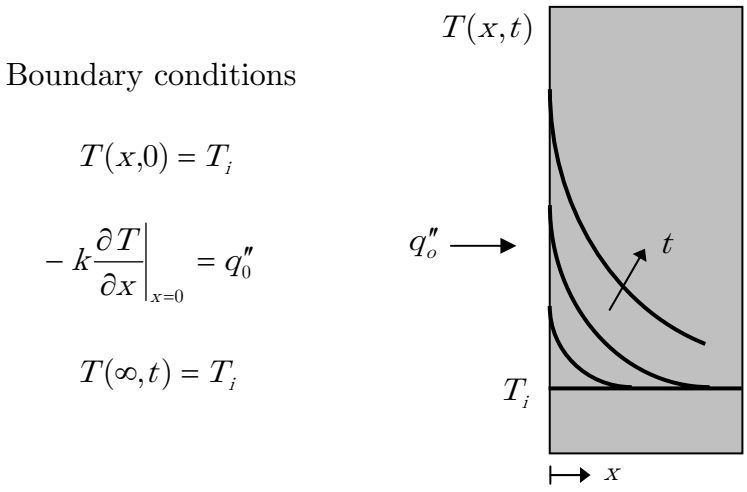

Figure 6.5: Transient temperature distributions is a semi-infinite solid subject to a constant heat flux

Figure 6.5 represents the case of a semi-infinite solid subject to an imposed heat flux at its surface. The solution to the time dependant surface temperature yields the characteristic heat time. Assuming one dimensional heat conduction and no internal heat generation, the following energy equation can be written,

$$\frac{\partial^2 T}{\partial x^2} = \frac{1}{\alpha}\frac{\partial T}{\partial x} = \frac{\rho c}{k}\frac{\partial T}{\partial x} \tag{6.15}$$

with boundary conditions defined as

$$-k\left.\frac{\partial T}{\partial x}\right|_{x=0} = q_0'' = q_s'' - h_T(T - T_i) \tag{6.16}$$

$$T(x,t) = T_i \tag{6.17}$$

Conducting a Laplace transformation $L\big(T(t)\big) = \overline{T}(s)$ and replacing $\rho cs/k$ with k^2, allows equation 6.15 to be written as,

$$\frac{\partial^2 \overline{T}}{\partial x^2} - \frac{\rho c}{k}s\overline{T} = \frac{\partial^2 \overline{T}}{\partial x^2} - k^2\overline{T} = 0 \tag{6.18}$$

Solving this ordinary homogenous differential equation with constant properties gives,

$$\begin{aligned}\overline{T}(x,s) &= \frac{q_0''}{s\left(h_T + k\sqrt{\frac{\rho c}{k}s}\right)}\exp\left(-\sqrt{\frac{\rho c}{k}s}x\right) \\ &= \frac{q_0''}{s\left(h_T + \sqrt{k\rho c}\sqrt{s}\right)}\exp\left(-\sqrt{\frac{\rho c}{k}}\sqrt{s}x\right)\end{aligned} \tag{6.19}$$

Inverting this equation gives the following general solution,

$$T - T_i = \frac{q_0''}{h_T}\left[\operatorname{erfc}\left(\frac{x}{\sqrt{4\frac{k}{\rho c}t}}\right) - \exp\left(\frac{h_T x}{\sqrt{\frac{k}{\rho c}}\sqrt{k\rho c}} + \frac{h_T^2 t}{k\rho c}\right)...\right.$$
$$\left.\ldots\operatorname{erfc}\left(\frac{h_T\sqrt{t}}{\sqrt{k\rho c}} + \frac{x}{\sqrt{4\frac{k}{\rho c}t}}\right)\right] \tag{6.20}$$

Noticing that $\operatorname{erfc}(0) = 1 - \operatorname{erf}(0) = 1$ and that $\operatorname{erfc}(\infty) = 0$, this equation can be simplified further by,

$$T = T_i + \frac{q_0''}{h_T}\left[1 - \exp\left(\frac{h_T^2 t}{k\rho c}\right)\operatorname{erfc}\left(\frac{h_T\sqrt{t}}{\sqrt{k\rho c}}\right)\right] \tag{6.21}$$

which in turn can be further simplified to,

$$T = T_i + T_c\left[1 - \exp\left(\frac{t}{t_c}\right)\operatorname{erfc}\left(\sqrt{\left(\frac{t}{t_c}\right)}\right)\right] \tag{6.22}$$

where a characteristic temperature is defined $T_c = \frac{q_0''}{h_T}$ and time $t_c = \frac{k\rho c}{h_T^2}$.

This gives the characteristic heating time for thermally thick solids as,

$$t_{c_{thick}} = \frac{k\rho c}{h_T^2} \tag{6.23}$$

For the materials shown to be thermally thick in the example in section 6.2, the corresponding characteristic time is presented in Table 6.3.

Material	t_c (s)
Concrete	68
Brick	40
Glass	38
Brick/Concrete Block	28
Gypsum Board	4.2
Plywood	4
Fiber Insulation Board	4
Chipboard	4
Aerated Concrete	3
Plasterboard	3
Calcium Silicate Block	2
Alumina Silicate Block	1
Glass Fiber Insulation	0.04
Expanded Polystyrene	0.02

Table 6.3: Characteristic heating times of thermally thick materials with L_c=0.02m

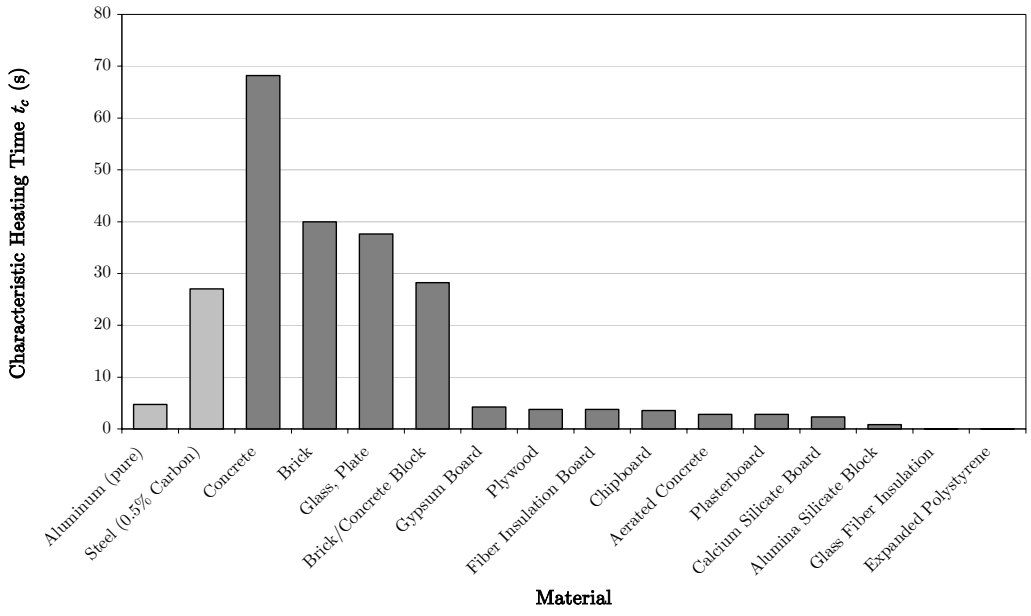

Figure 6.6: Characteristic heating times of typical structural materials. Light grey bars are thermally thin, while dark grey bars are thermally thick materials.

The characteristic heating times of both the thermally thick and thermally thin materials considered above are presented in Figure 6.6. It is evident that thermally thick materials can be split into two different groups. The first are the common structural building materials such as concrete, bricks and glass which all have relatively long characteristic heating times. The second are the insulation materials which, for the case described above all have characteristic times of less than five seconds. Thermally thin characteristic times lie in the range between insulation materials and the more common thermally thick primary structural building materials.

The reason for the large difference in characteristic times for the two thermally thick material types is due to conduction behaviour of the material. Insulation materials are designed to inhibit the transmission of heat through their thickness and achieve this by creating a low thermal inertia ($k\rho c$) generally by having an extremely low thermal conductivity. The result is that large temperature gradients are created near to the surface and indeed the surface temperature is seen to change rapidly with the addition of more energy from an imposed heat flux. In the case of the common primary structural materials, a slightly higher thermal inertia allows for the development of thermal gradients within the solid to a greater depth than seen in cases of insulation. A greater characteristic heating time recognises the fact that temperatures will be conducted into the solid due to the imposed heat flux at the surface and therefore the surface temperature will change at a relatively slower rate than insulation materials. This is represented in Figure 6.7 where the temperature distribution within two semi-infinite solids exposed to a surface heat flux, but with differing thermal inertias is shown. For the lower thermal inertia, strong temperature gradients are seen near to the surface leading to a rapid increase in surface temperature. Figure 6.7 (b) shows that for a larger thermal inertia, temperature gradients are created to a deeper depth

within the solid resulting in the surface temperature rising at a slower rate than observed in (a).

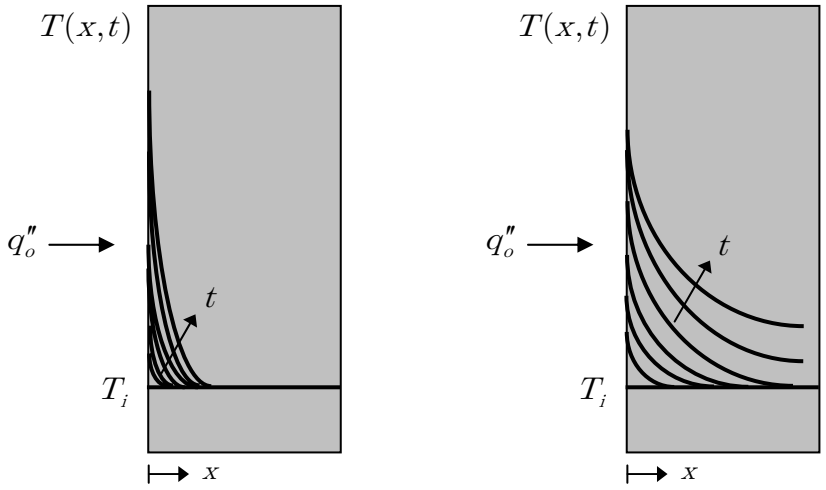

Figure 6.7: Temperature distributions in a semi-finite solid with an imposed surface heat flux for (a) material of low thermal inertia such as insulation and (b) a material with a higher thermal inertia such as concrete

The notion of characteristic heating times can sometimes be somewhat counter-intuative in that it is often percieved that the thicker an element, the longer it takes to heat and therefore the longer the characteristic time. However it is clear from the above discussion, that for *surafce* temperatures this is not always the case.

6.5. Conclusions

A method of determining the thermal thickness of a structural element has been presented with the objective being to determine the characteristic heating time to allow for heat fluxes to be averaged between these intervals. The methodology allows for times to be evaluated for elements

that are thermally thin or thermally thick and incorporates material thermal properties.

The ability to define time intervals over which surface heat fluxes may be averaged allows for greater computational time savings to be made in post-processing data results from the development and evolution of fire.

Chapter Seven

7. Heat Flux Model Development

7.1. Introduction

Although there is an increasing use of CFD tools to evaluate the evolution of fire environment, much structural fire engineering work cannot take advantage of these for defining the temperature rise of structural elements. It has been demonstrated in Chapter 5 that gas temperatures alone are not sufficient to describe the severity of a fire imposed on structural members. It is important to be able to quantify a fire in terms of heat fluxes, incorporating convective and radiative contributions that capture full spatial distributions.

This Chapter outlines the development of a post-processing tool that takes specific results of a CFD calculation and uses them to evaluate incident surface heat fluxes for user specified structural geometries. This process eliminates the need for the resolution of the structural arrangement to be to be used as the length scale for the grid size of the CFD mesh. The use of a CFD tool is important to be able to capture the detailed spatial resolution of the fire.

Chapter 3 demonstrated that convective heat fluxes can be established with knowledge of the convective heat transfer based on gas temperature and flow velocity. Additionally, Chapter 4 demonstrated that radiative fluxes could be evaluated based on knowledge of the local emissivity and gas temperatures. These heat transfer simplifications can be used to create a method of defining structural heat fluxes using simplified computations.

The objective of the model is to act as a heat transfer tool in the intermediary stage within the context of a structural engineering framework that involves all concepts including modelling the fire evolution to prediction of the mechanical behaviour at elevated temperatures. Output generated will provide the boundary condition for the conduction

heat transfer analysis to determine the temperature rise of structural elements. It is not intended within the scope of this study to undertake the conjugate heat transfer that occurs between the gas and solid-phase environments, incorporating radiative feedback and conduction. As a result all surface heat fluxes are evaluated assuming a cold surface.

7.2. Background to the Model

The challenge of the model is to be able to calculate the time and spatially varying incident surface heat flux resulting from a fire. The proposed solution is based on local gas conditions. In essence this means that for the structural component of interest, surface heat fluxes can be evaluated providing it is completely engulfed in smoke and products of combustion or flames. The typical condition for the model is the post-flashover regime whereby the generation of smoke is at its greatest and heat fluxes are at a maximum.

It can be shown that radiation can become the dominant mode of heat transfer to a surface when the element is engulfed in smoke or flames, although convection should never be totally neglected. The evaluation of radiant intensity is achieved by consideration of the optical depth through either products of combustion or the flame itself. From the gas-phase it is possible to extract an extinction coefficient κ from which an optical depth L_e can be evaluated as the reciprocal of the extinction coefficient.

$$L_e = \frac{1}{\kappa} \tag{7.1}$$

Consideration of these two parameters allows a definition of regions that are of radiative interest. For a given path length L, the following limits can be defined,

$$\kappa L >> 1 \quad \text{Optically thick}$$

$$\kappa L << 1 \quad \text{Optically thin}$$

When a region is optically thick surrounding a structural member then the heat flux to its surface can be calculated based on local gas conditions. It is within this limit that the heat flux model described here can be applied. If however a region is optically thin, then the penetration distance is much larger than the path length and radiation can pass entirely through without appreciable extinction. When this is the case, local conditions cannot be applied and radiation from a further distance must be taken into account.

Consider a compartment of dimensions 4m in all directions with a propane fuel fire over the entire floor area and a heat release rate of 1000kW/m^2. Figure 7.1 shows a contour plot of extinction coefficients (a) of the products of combustion and corresponding optical depths (b) using the relationship of equation (7.1).

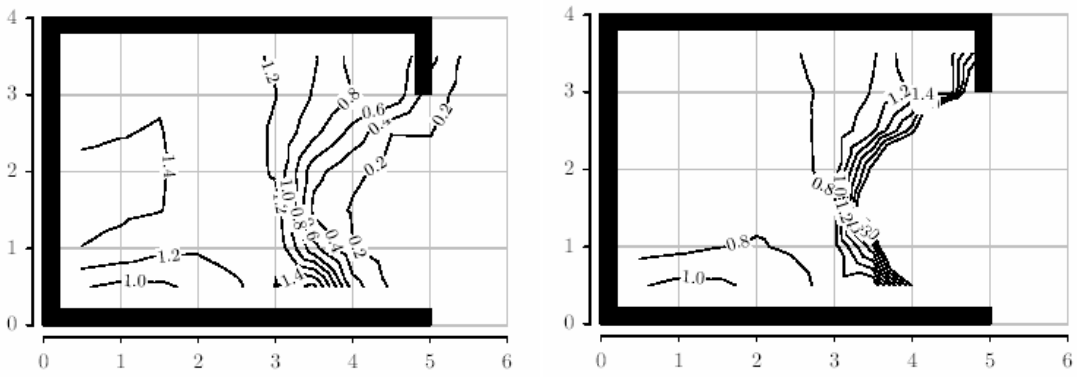

Figure 7.1: Plot of extinction coefficient κ (m^{-1}) in (a) and of optical depth L_e (m) in (b)

If it is required to evaluate the surface heat flux to a structural I-beam placed within this compartment as depicted in Figure 7.2 then it is important to be able to define a control volume from within which the calculation of surface heat flux can be undertaken. The light grey area the represents the optically thick region, where $L_e < 1$. Knowledge of this area confirms that local gas conditions can be used for the calculation. Indeed the darker grey semi-circle represents the region in which the calculation can be confined to. Determination of this control volume's radius, or more accurately, its path length L is described later in this chapter.

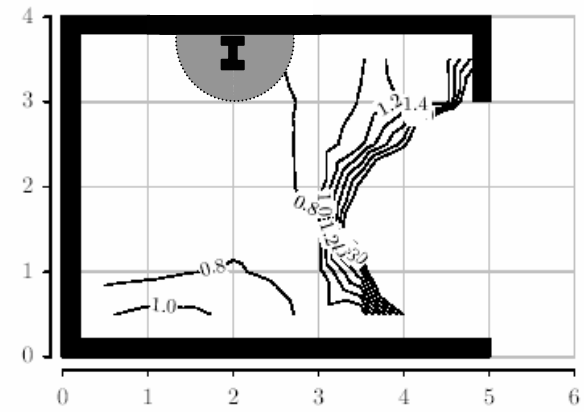

Figure 7.2: Structural I-beam within a fire a compartment. Light grey area represents the optically thick region, while the dark grey area represents the control volume for the heat flux calculation. Contour lines show the optical depth (m)

With a control volume defined, it is possible to calculate the incident surface heat flux by considering the spatial variation of gas parameters including emissivities and temperature. Indeed for the same typical fire scenario outlined above, a contour plot of temperatures reveals large gradients to be present throughout the fire compartment. The model is capable of capturing such levels of detail in its calculation.

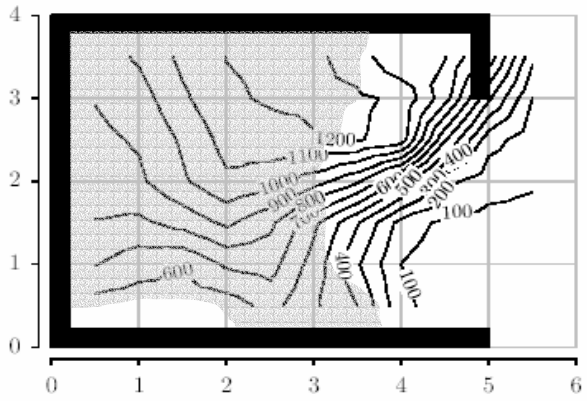

Figure 7.3: Spatial variation in gas-phase temperature for a typical fire. Contour labels are in °C.

Having established the basic premise for the model, the following sections describe in detail each stage of the process to calculate the incident surface heat flux to a structural element using CFD output.

7.3. Exporting Data from CFD Programs

The model is intended to be used as a post-processing tool for any CFD program. However, it is important that appropriate data is structured in the correct format for input to the model. Output parameters are required at two levels; the first requires gas extinction coefficients, velocities in x, y and z and temperatures to be provided at every grid cell for every simulation output time. The second requires wall coordinates to be defined for each wall direction.

Although the method is applicable to any CFD tool, FDS is used as the example in developing the model. In the case of FDS it is important that the following line is added to the input file: -

```
&PL3D DTSAM=n, QUANTITIES='TEMPERATURE','U-VELOCITY',
'V-VELOCITY', 'W-VELOCITY', 'extinction coefficient', /
```

Where 'n' is the number of times these parameters should be written during the simulation, to a maximum of 99. This enables the appropriate gas parameters to be written to a results file.

Coordinates for all wall grid cells can be found by requesting *any* boundary output, such as: -

```
&BNDF QUANTITY='WALL_TEMPERATURE' /
```

Once the simulation has completed, it is necessary that data is extracted from FDS's results file. This is achieved by running the program 'fds2q.exe', the FORTRAN code of which is given in Appendix A. This is a modified version of the fds2ascii.exe program that is supplied with FDS and essentially dumps all required data to .csv files. All gas parameters are written to files named ROOMn_flux.csv where 'n' is the number of the time index at which the data was written as requested on the &PL3D line in the input file. Data in this file is written in columns in the following format: -

x (m), y (m), z (m), temperature (^{o}C), u-velocity (m/s), v-velocity (m/s), w-velocity (m/s), extinction coefficient (m^{-1})

The program also writes out the coordinates of the wall grid cells to files named WALL-3_flux.csv to WALL+3_flux.csv where -3 to +3 represent the directionality given as: -

Direction	Notation
-Z	-3
-Y	-2
-X	-1
+X	+1
+Y	+2
+Z	+3

Table 7.1: Notation in terms of numbers for direction along Cartesian axis

Data in these files are written in columns the following format: -

x (m), y (m), z (m)

The program fds2q.exe also writes a file called Times.csv. This is a two column file in which the first column is the time index 'n' and the second is the simulation time in seconds associated with its corresponding index.

These files can be considered the generic way of providing the heat flux model with the appropriate data needed to carry out the calculation. The model will always need the gas temperature data and the times to be taken from the CFD analysis. The surface coordinates however, can be modified to include only locations that are relevant for the calculation. They can be edited appropriately, ensuring that the same format described above is adhered to. It is important that all six 'wall' files must contain at least one line of coordinates for the calculation to be performed regardless of whether output is required in that direction or not.

This method ensures that any CFD model may be used to define the fire environment, although some data manipulation may be required to achieve the correct format. In the case of FDS, the program fds2q.exe ensures this is the case.

7.4. Analysis of Data

With the CFD data in an appropriate format, the calculation of surface heat fluxes may be undertaken. The programming code MATLAB was used to develop the model and the source code is provided in Appendix B. The following sections define each stage of the model in detail.

7.4.1. Establishing Characteristic Times

In order to save computational time, material characteristic heating times can be used to carry out the calculation at specific time periods. The notion of characteristic heating times and their evaluation is outlined in Chapter 6. The initial step of the model calculates a characteristic time which is used to establish times to import data and intervals over which averaging takes place.

The user is initially asked to define which type of material forms the surface of the structural element in question. Three built-in options are available, namely steel, concrete and gypsum board. The user is asked to choose one of these or to define another. If the latter option is chosen, the user is prompted to enter the material's thermal conductivity k (kW/m.K), its specific heat capacity c (kJ/kg.K) and its density ρ (kg/m^3). Finally, the user is required to enter a conduction characteristic length scale L_c which is defined as the ratio of the solid's volume to its surface area $L_c \equiv V / A_s$. These parameters allow the model to determine the Biot number of the structural element which allows it to be classed as either thermally thin or thermally thick and ultimately for its characteristic heating time to be calculated.

7.4.2. Calculation of Control Volume

The evaluation method of the total incident radiant flux from the gas to the surface considers a series of hemispheres that each radiate to a point source at the centre of the base of the hemisphere. The maximum radius is the path length over which the calculation is undertaken. The user can specify the maximum path length r_n and the number of shells to be considered. This is illustrated in Figure 7.4 where (a) shows the entire control volume for the hemisphere radiating to a point source and (b) shows a cut through the hemisphere as an example with four shells specified.

Having established the limits of the control volume, the user is required to specify the number of points on the surface of each shell at which gas parameters will be evaluated. The user is prompted to enter the number of segments within the circle to consider and also the number of points to be evaluated on each radius. This concept is illustrated in Figure 7.5 (a) where the example shows eight segments within the circle (essentially the base of the hemisphere) and three points on each radius while Figure 7.5 (b) shows the projection of these points onto the surface of the shell. In this case a total of 24 points on the surface of each shell are considered.

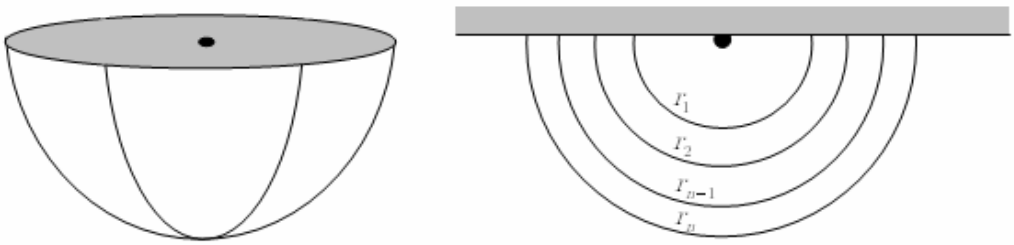

(a) (b)

Figure 7.4: (a) Hemispherical control volume and (b) shells in elevation

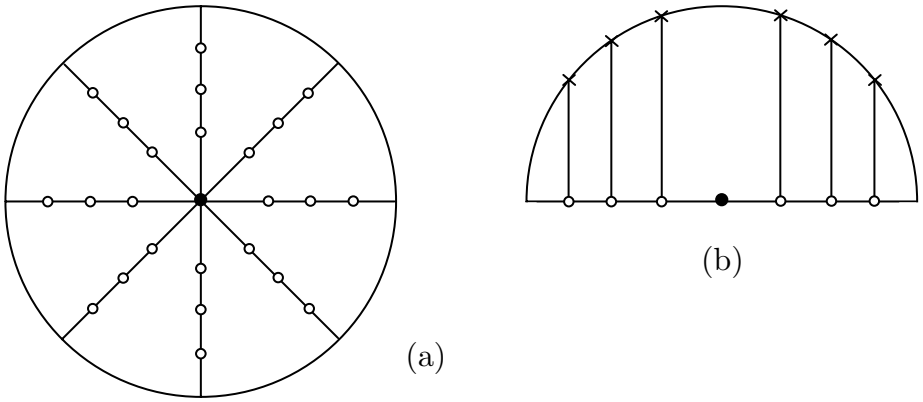

(a) (b)

Figure 7.5: Establishing shell surface coordinates for gas parameters using (a) 8 circle segments and 3 points on each radius and (b) projection of points onto surface

Surface coordinates are generated for all shells and stored in a matrix. This matrix is then used to map the coordinates of the control volume onto each surface coordinate to allow the calculation to be performed.

7.4.3. Establishing Gas Parameters

As the gas data is stored in a three-dimensional matrix, any xyz coordinate can be used to interpolate between the given data locations to provide values at unique points not necessarily considered in the CFD simulation. These xyz coordinates are taken as the surface points on each shell within the control volume. Values of gas temperature T_g and extinction coefficient κ are evaluated and then averaged to give a single value for the surface of each shell. Gas temperatures are averaged to the fourth power for the radiative calculation.

A check on the designated path length is made at this stage. For each shell radius there is a corresponding extinction coefficient. From this value and given an associated acceptable level of error, the required path length can be evaluated and compared. If the shell radius is greater than the required path length then for the given error limit, the calculation is justified. If not, then the radius must be increased (i.e. move to the next shell) to account for the required accuracy. This is further explained below.

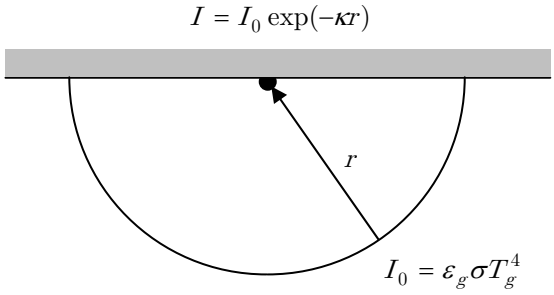

Figure 7.6: Reduction in radiant intensity through a gas of radius r

Figure 7.6 shows how the initial radiant intentsity is reduced through a hemispherical volume of gas to a point source. In this case, the radius to the shell surface r, needs to be checked to determine whether for the

averaged extinction coefficient on its surface, the path length is acceptable. From the equation defining the surface radiative intenstiy,

$$I = I_0 \exp(-\kappa r) \tag{7.2}$$

If the required path length is written as L, and the error limit defined as the ratio of initial radiant energy to incident radiant energy I / I_0, then rearranging equation (7.2) gives,

$$L = \frac{-\ln\left(\frac{I}{I_0}\right)}{\kappa} \tag{7.3}$$

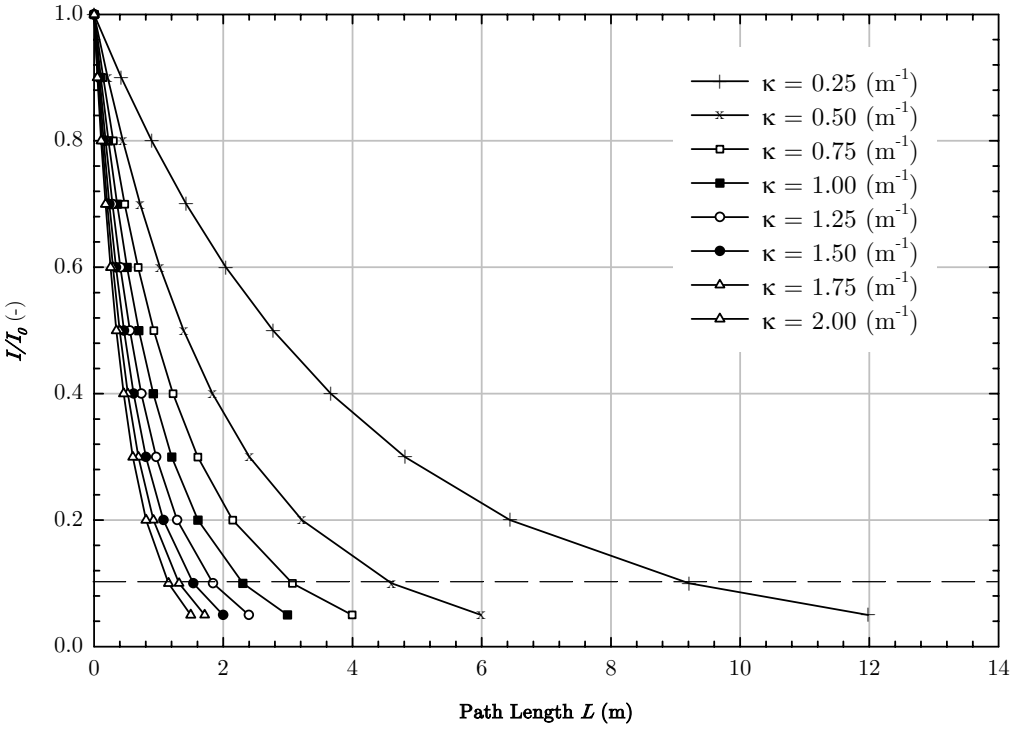

Figure 7.7: Required path lengths based on ratio of radiant intensities and extinction coefficients with an error limit of 10% highlighted

The plot in Figure 7.7 shows the relationship of equation (7.3). This plot has been drawn using extinction coefficients in the range of 0.25 to $2m^{-1}$ as an example only. The dashed line on the plot shows the 10% error limit - reading the x-axis where the extinction coefficient lines cross allows the determination of the required path length. In using this path length an accuracy of 90% can be assured. If the shell radius is greater than this ratio then the calculation can progress to the next surface coordinate, however if it less, then the control volume should extend to another shell and the same check made.

7.4.4. Radiative Fluxes

In calculating incident radiative fluxes to the surface, the contribution from each shell is considered independently and then summed to provide the total radiative flux.

Local gas emissivities are calculated for the distance between each shell as shown in Figure 7.8. Also shown is the path length L_n associated with the transmissivity τ or decay of the radiant intensity as it travels through the gas medium to its point source on the surface of the structural element.

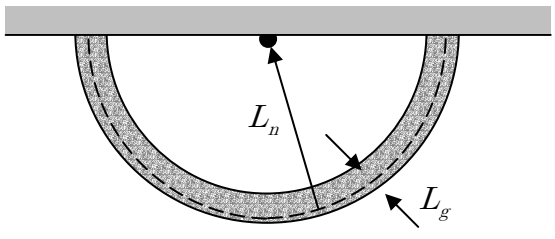

Figure 7.8: Path length L_g through gas for emissivity calculation and L_n to point source for transmissivity

In the case of multiple (n) shells, the transmissivity through the smoke to the surface point source can be written as,

$$\tau = \tau_1 \cdot \tau_2 \cdot \cdots \cdot \tau_n \tag{7.4}$$

where the transmissivity is calculated by,

$$\tau_g = 1 - \exp(-\kappa L_g) \tag{7.5}$$

Local gas emissivities are calculated by;

$$\varepsilon_g = 1 - \exp(-\kappa L_g) \tag{7.6}$$

allowing total radiative fluxes to be calculated for n shells using,

$$I = \sum_{shell=1}^{n} \phi\left(\varepsilon_{g,shell}\sigma(T_{g,shell} + 273)^4 \cdot \tau \cdot A_{shell}\right) \tag{7.7}$$

where A_{shell} is the surface area of the shell and ϕ is the configuration factor required to evaluate the radiative intensity that the point source on the surface receives from the surface area of the hemisphere. Consider Figure 7.9, this shows a finite interior section of a hemisphere A_1 and a finite disk on the base A_2. The configuration factor between the two surfaces is determined using the following relationships,

$$L_i = \frac{l_i}{a} \tag{7.8}$$

$$X_i = \sqrt{\left(4R^2 L_i^2 + \left(1 - R^2\right)^2\right)} \tag{7.9}$$

This allows the configuration factor to be calculated as,

$$F_{1-2} = \frac{1}{4(L_2 - L_1)}(X_2 - X_1) \tag{7.10}$$

For the case of the entire hemisphere radiating to the entire base area as in the model, the configuration factor is simply,

$$F_{1-2} = \frac{1}{2} \tag{7.11}$$

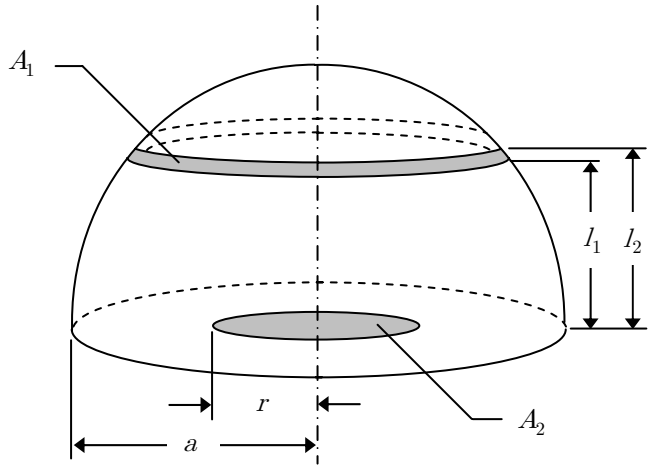

Figure 7.9: Configuration factor of a finite section of interior hemisphere to a disk on its base

This calculation is suitable when the structural element is engulfed in smoke or flames. It cannot be used with accuracy when the element is not engulfed. In this case, radiation from remote locations must be considered. To determine whether an element is engulfed in smoke, an examination of the extinction coefficient is undertaken on the nearest shell to the surface coordinate. If it is found smoke is present, then the calculation is carried out as outlined above. If however, no smoke is found to be present, then an alternative approach is adopted. This involves a very much simplified

approach that involves checking each shell for the presence of smoke. If smoke is found, the check continues for the remaining shells. The number of shells constituting smoke is then used to generate a single volume of constant thickness and uniform emissivity, extinction coefficient and temperature. All shells between the surface and the supposed smoke shells are assumed to be transparent with no noticeable decay factor causing a reduction in the incident radiative intensity. This concept is illustrated in Figure 7.10 where as an example, three shells are found to contain smoke. They can be idealised as a single shell volume with constant properties. When this method is used, it highlights the fact that the original specified path length should be the width of the compartment so as to consider the environment across the room.

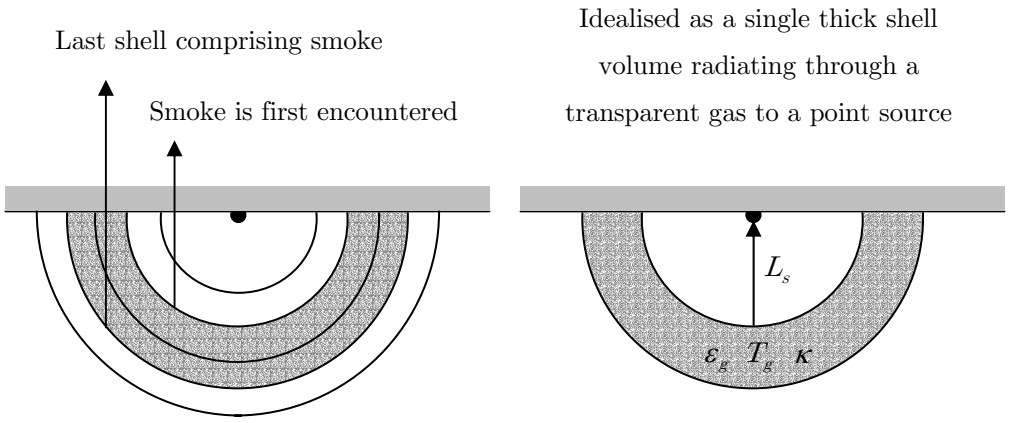

Figure 7.10: Idealisation of smoke shells within the control volume when the surface is not engulfed in smoke

7.4.5. Convective Fluxes

Convective fluxes within the model are calculated using a simplified, yet accurate approach that considers velocity flows within the compartment and gas temperatures. Velocities in each of the Cartesian directions are imported from the CFD analysis at every point in space for the appropriate characteristic heating time intervals. The initial function of

the model is to identify along which nearest Cartesian axis the flow is moving. This is done by considering Figure 7.11 and using spherical polar coordinates to resolve the velocities u, v and w to a single Cartesian axis. Using trigonometry,

$$V_{res} = \sqrt{u^2 + v^2 + w^2} \tag{7.12}$$

$$\tan\theta = \frac{\sqrt{u^2 + v^2}}{w} \tag{7.13}$$

$$\tan\phi = \frac{v}{u} \tag{7.14}$$

Knowledge of the polar angles allows the nearest Cartesian coordinate to be evaluated using,

Condition	Cartesian Axis
If $\phi > 45^o$	x
If $\phi < 45^o$	y
If $\theta < 45^o$	z

Table 7.2: Conditions for determining closest Cartesian axis

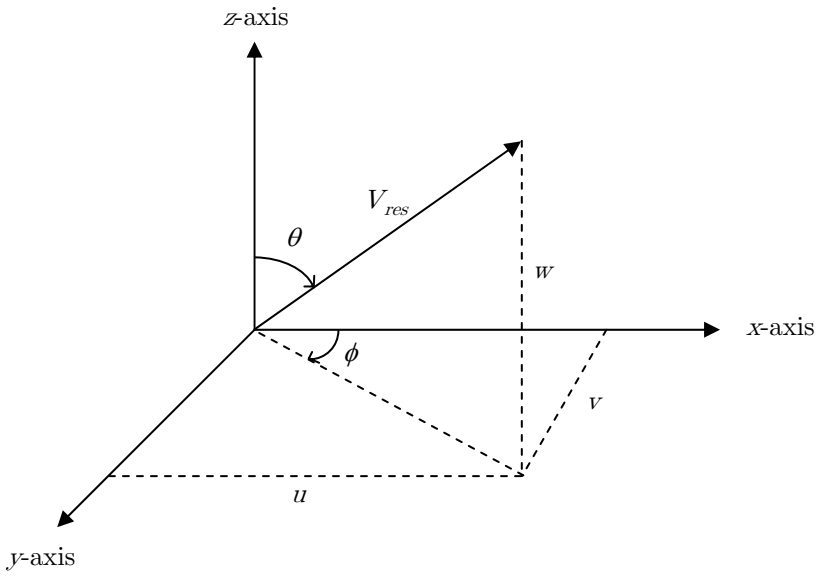

Figure 7.11: Resolving velocity components to a single Cartesian axis

During the heat flux analysis, the user is prompted to enter convective length scales for each Cartesian axis. These are related to the lengths along or past which the velocity field may flow. For example, it could be thickness of truss element, the width or thickness of the flange of an I-beam. Alternate examples could include the entire height of a column or width of a floor slab. The user must decide which length is appropriate for the analysis or alternatively, the convective length scale can be set as the grid cell size. Using this option however, limits the convective length scales to the resolution of the CFD grid and as a result, important convective heating effects may be overlooked.

The calculation of the convective heat flux is based on local temperature conditions and can be expressed to a cold surface by,

$$q_c'' = hT_g \tag{7.15}$$

where h is the convective heat transfer coefficient (W/m^2.K) which can be established from the simplified relationship to the convective length scale and velocity as outlined in Chapter 3 and represented in Figure 7.12.

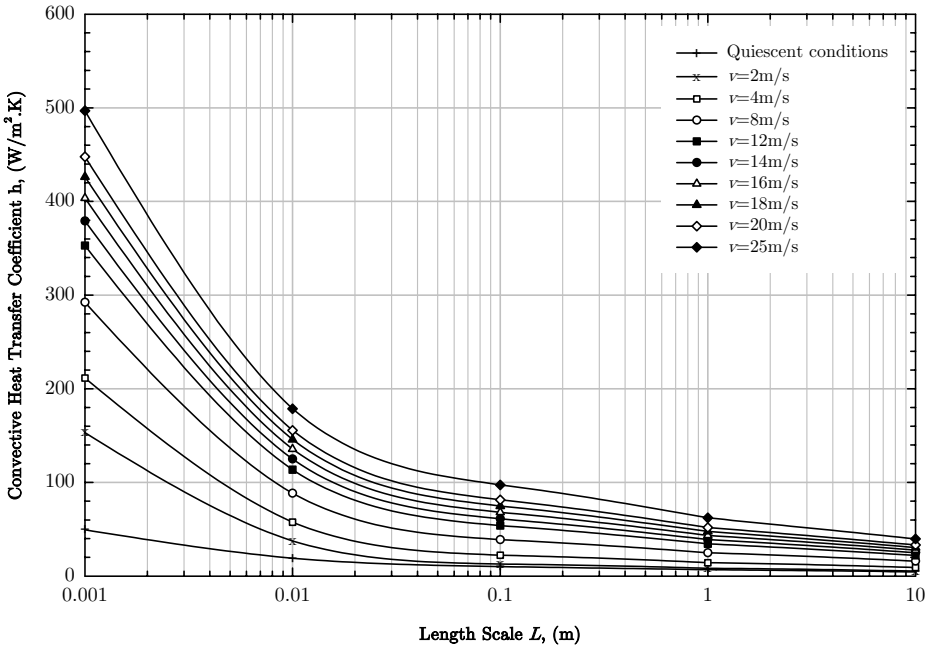

Figure 7.12: Simplified relationship between convective heat transfer coefficient with length scale

7.4.6. Averaging Results and Writing Output

Having established the modelling methodology to determine both radiant and convective heat fluxes to a point source, the output data must be provided in a manner in which it can be readily used as input to a conduction heat transfer analysis. Output is written at every characteristic heating time interval but heat fluxes are averaged between each of these time intervals and held constant throughout the time period. The justification for this approach is detailed in Chapter 6. The result is .csv files for convective, radiative and total heat fluxes with the following format: -

(-)	(-)	(-)	Time (s)					
X	Y	Z	0	t_1	t_1	…	t_n	t_n
(m)	(m)	(m)	Total Gauge Heat Flux (kW/m^2)					
x_0	y_0	z_0	$\frac{q_{t_1}}{2}$	$\frac{q_{t_1}}{2}$	$\frac{q_{t_1}+q_{t_2}}{2}$	…	$\frac{q_{t_{n-1}}+q_{t_n}}{2}$	$\frac{q_{t_{n-1}}+q_{t_n}}{2}$
:	:	:	:	:	:	:	:	:

Figure 7.13: Format of .csv output files

With the output of heat fluxes in this form, curves similar to those in Figure 7.14 can be plotted for each surface coordinate with relative ease and these in turn used as boundary conditions for the heat transfer analysis within structural members.

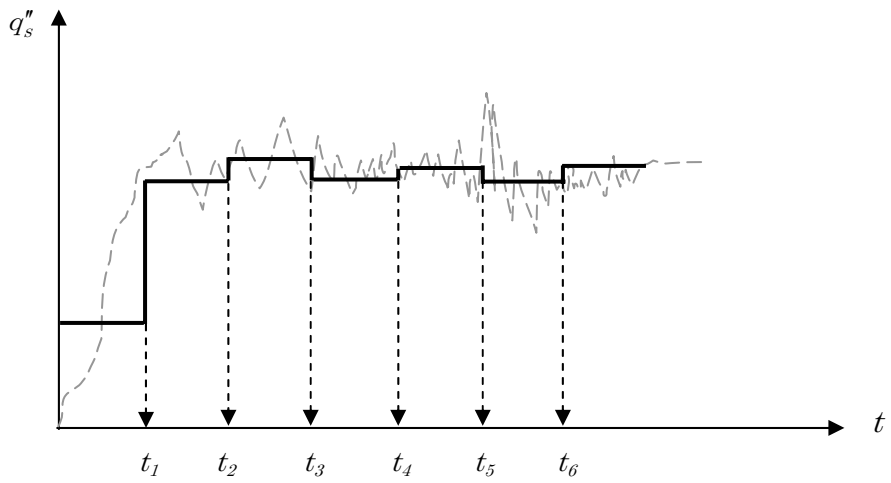

Figure 7.14: Output of heat flux in its final form, kept constant between characteristic heating times

7.5. Conclusions

A simple methodology to calculate the imposed convective, radiative and total heat fluxes using CFD output data has been presented in this chapter. The methodology uses the principle of hemispherical control

volumes to calculate the incident radiant intensity assuming averaged gas parameters over the surface of multiple shells. The method uses interpolation techniques to allow the heat flux at any given coordinate to be calculated. Data is presented in the form of time averaged heat fluxes based on the characteristic heating times of the structural components of interest. This data can be used as the boundary condition for further heat transfer analysis to be undertaken to establish the temperature rise of structural elements.

Chapter Eight

8. Model Validation

8.1. Introduction

This chapter considers output generated from the CFD post-processing program to generate heat fluxes for use as a boundary condition for a structural thermal analysis. The program is validated against output from the results of the Cardington large scale fire tests as presented in Chapter 5.

Initially the parameters within the model are investigated in terms of potential heat flux output with a view to provide guidance on maintaining accuracy within this simplified model.

The model is then applied to an FDS simulation of the Cardington Test 8 fire and comparisons are drawn in terms of heat flux measurements at point locations and heat flux maps representing the compartment boundaries. It is important to note that the purpose of the present Chapter is not to validate FDS but the heat transfer calculations, thus the FDS scenario chosen matches previously published computations where a detailed evaluation of the code was made [22].

A brief study of the time averaging technique is undertaken with output given in terms of heat fluxes and surface temperatures to provide extra validation of the employed method of characteristic times.

For comparison with currently applied methods, the results of the heat transfer calculations are compared to Eurocode solutions. This comparison serves to evaluate the accuracy of these methods and to establish the importance of the present analysis.

8.2. Model Parameters

Within the heat flux model, it is possible to specify both convective and radiative parameters. In this section a systematic evaluation of the effect of changes in these parameters will be presented.

Chapter 3 discussed convection and demonstrated that two main parameters effecting convective fluxes are local velocity and length scales. Convective length scales may be changed according to the dimensions of the structural element being evaluated. The default values are the dimensions of the grid cell which, in many cases can be considered as sufficient for general analyses of large surface areas. Furthermore velocities will be obtained from the output of the CFD tool. Therefore, the sensitivity analysis for the convective heat transfer is one that requires only moderate attention.

The evaluation of radiative heat transfer requires more detailed attention. The primary radiative parameters that may be changed include the maximum path length to be considered and the number of shells to be considered. Default values for the present model are a 2m path length, defined as a typical room height dimension and 20 shells, to provide a shell separation of 0.1m. The following section considers the accuracy of the evaluated surface heat flux when both path length and shell separation parameters are changed. A homogeneous smoke layer is considered with constant extinction coefficient and temperature as shown in Figure 8.1.

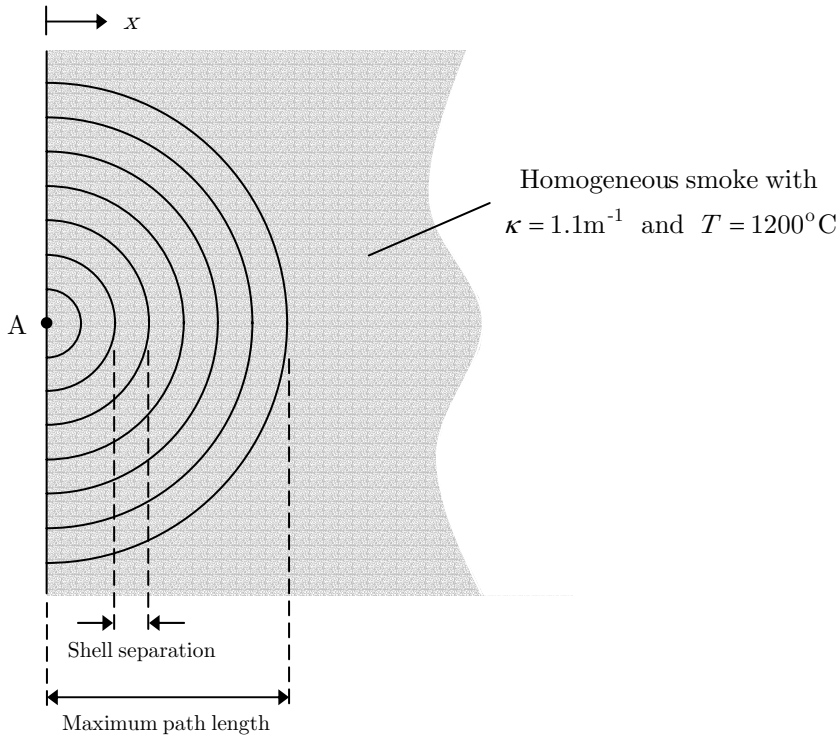

Figure 8.1: Arbitrary smoke environment to investigate model parameters

The gauge heat flux to point A in Figure 8.1 is evaluated for path lengths ranging from 0-5m for a series of constant shell separations (or number of shells) with the results presented in Figure 8.2. The plot shows that as the path length is increased, the heat flux convergences to certain value, however, that value is different for different shell separations. Indeed, for the extinction coefficient of 1.1m^{-1}, a path length greater than 2.1m will lead to variations that will not exceed 10% of the radiative intensity. This is shown in Figure 7.7.

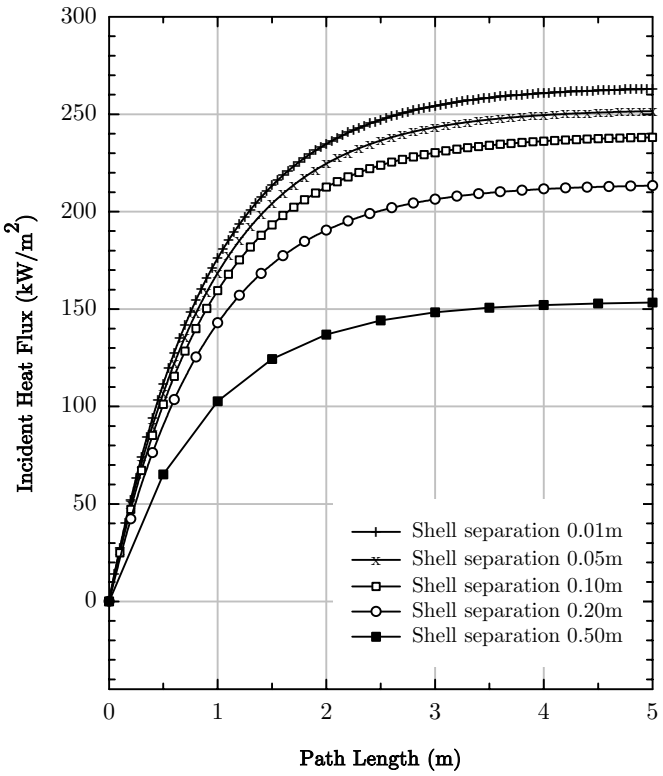

Figure 8.2: Incident heat flux with increasing path length for different shell separations

Figure 8.2 shows that the closer the shell separation or rather, the greater the number of shells, provides a more accurate calculation of the heat flux. The accuracy in heat flux is given in terms of shell separation distances in Figure 8.3 for different paths lengths. This clearly demonstrates that as the number of shells is increased (shell separation decreased), the calculation converges to a specific heat flux. The influence of the path length is also evident in this figure, showing again, that for the conditions of the test, a path length above 2m will lead to discrepancies of less than 10%. An increased number of shells can be considered as similar to evaluating the radiant intensity in terms of a continuous distribution, while an increased shell separation can lead to numerical errors resulting in lower fluxes. Figure 8.3 also indicates that an almost constant value of the heat flux is attained for shell separations below 0.01m and, for the

conditions of the test, shell separations smaller than 0.05m will lead to errors within 10%.

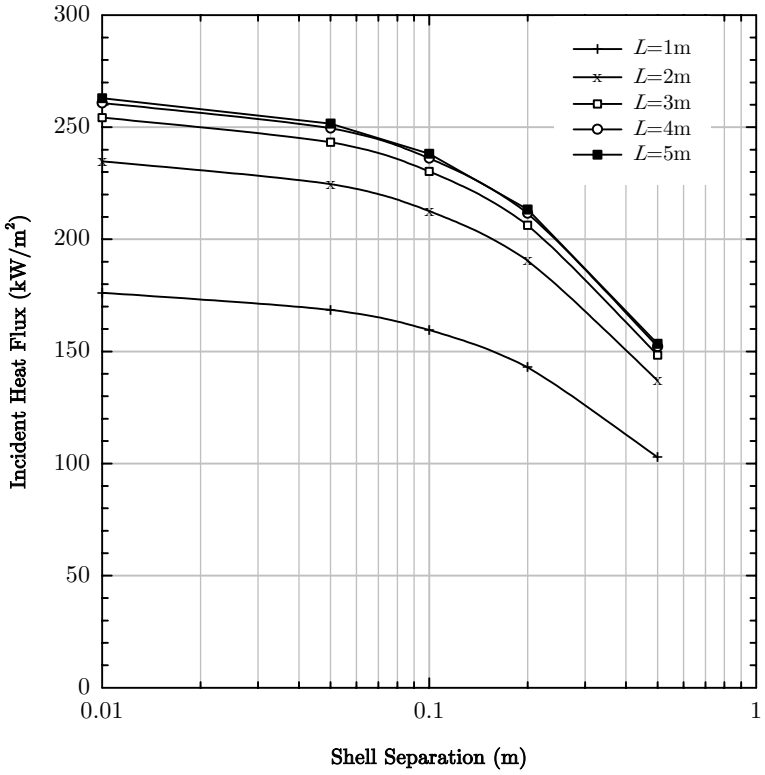

Figure 8.3: Incident heat flux with increasing shell separation for different at different maximum path lengths

For the case considered above, the maximum path length of 2.1m as given Figure 7.7 is confirmed to give at least 90% accuracy in the radiant intensity, providing a shell separation of at least 0.1m, or approximately 20 shells is used. This provides confidence in the default model parameters which adopt a 2m path length and 20 shells. Although the above case is for a homogeneous gas with constant properties, the principles of the accuracies developed with regard to shell separation in this section are applicable to any gas-phase scenario.

8.3. Cardington Large Scale Fire Tests

A CFD analysis of the Cardington large scale fire Test 8 forms the basis of the validation of the proposed heat flux model, the input file of which is given in Appendix C. A detailed outline of the fire test programme is provided in Chapter 5 and as such this section focuses on the development of the CFD simulation, the model for which is shown in Figure 8.4. The study of the heat fluxes using FDS as the underlying model not treated as a validation exercise of FDS. Pope & Bailey [22] conducted a detailed analysis of the capabilities of this code to model the Cardington tests. Their results showing good agreement in the fire growth and development stages together with accurate characterisation of the peak average compartment gas-phase temperatures. Comparison of point gas-temperature measurements showed some deviation, while the decay phase was always under predicted.

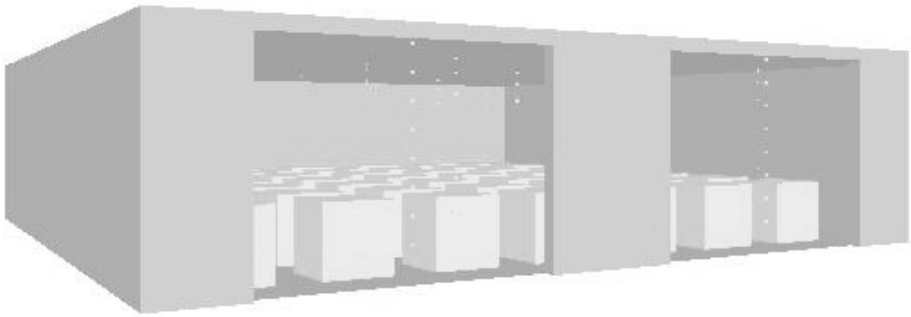

Figure 8.4: FDS model of the Cardington Test 8 scenario

8.3.1. FDS heat release rate

The simulation of these CFD fires is essentially governed by the rate of heat release provided by the user. This is clearly not necessary if sophisticated pyrolysis models are included, but these are currently not

available for CFD simulations of fires. The heat release rate (HRR) is therefore a user-introduced variable.

This section evaluates the heat release rate based on the mass loss data of the burning cribs collected during the test. The HRR, $\dot{Q}_c$, can be evaluated by [3],

$$\dot{Q}_c = \dot{m}\chi\Delta H_c \tag{8.1}$$

in which $\dot{m}$ is the mass flowrate of the fuel vapours, χ is an efficiency factor that takes into account incomplete combustion and ΔH_c is the heat of combustion of the volatiles.

The mass loss of each of the eight load cells is shown in Figure 8.5 with the position of each shown in Figure 8.7. For greater accuracy, data from each load cell could be used to prescribe a HRR for different cribs to allow for systematic ignition of cribs and to capture locations of preferential burning. To maintain simplicity however, an average crib mass loss is defined in Figure 8.6 and this is used for all cribs throughout the compartment.

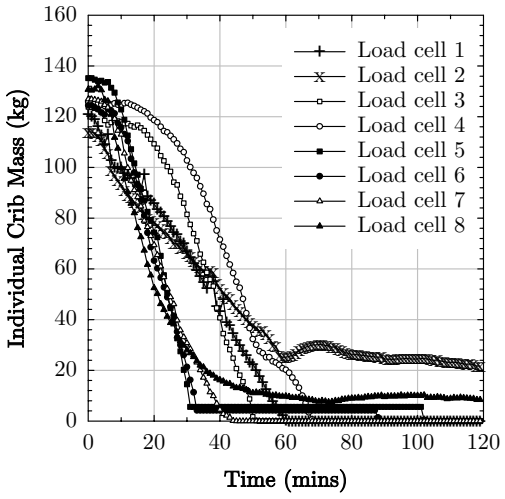

Figure 8.5: Mass of individual cribs throughout the test

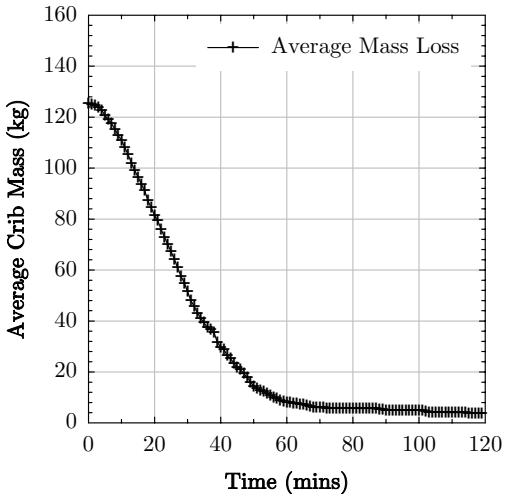

Figure 8.6: Average mass of cribs throughout test

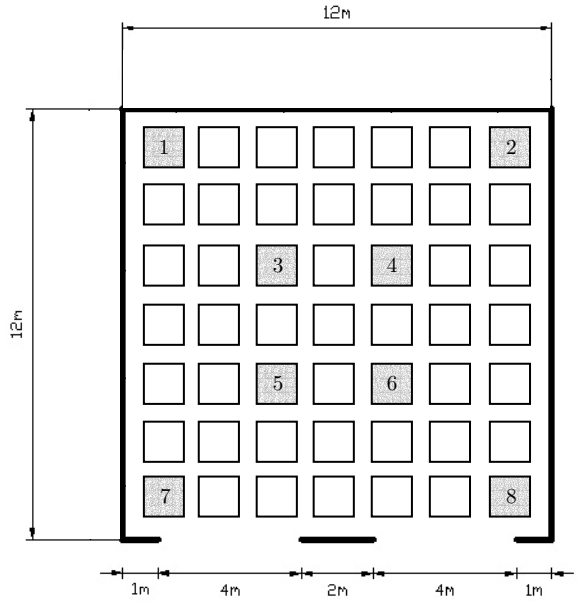

Figure 8.7: Location of wooden cribs within the compartment with load cells shaded and numbered accordingly

The mass flowrate of the fuel vapours is determined by the rate of change of mass of the cribs, given,

$$\dot{m} = \frac{\Delta m_{cribs}}{\Delta t} \tag{8.2}$$

The cribs within the test were known to comprise a total of 490kg of plastic (polypropylene) and 4900kg of wood. By considering the mass flowrate, the consumption rate of the plastic and wood can be evaluated with respect to each other to give the plot shown in Figure 8.8. It is seen that the plastic fuel is very quickly consumed by the fire, while the wood burns away at a far slower rate in comparison. The ratio of the mass consumed for each fuel to its original mass allows for the definition of a burning factor, namely F_{wood} and $F_{plastic}$, for which wood is initially taken to comprise 0.1% of the total burning, therefore allowing the following to be defined,

$$\Delta m_{plastic,t} = \left(1 - F_{wood,t}\right) \cdot \dot{m}_{f,t} \cdot \Delta t \tag{8.3}$$

$$F_{wood} = \min\left(1, \frac{m_{plastic,t}}{m_{plastic,t=0}}\right) \tag{8.4}$$

$$F_{plastic} = 1 - F_{wood} \tag{8.5}$$

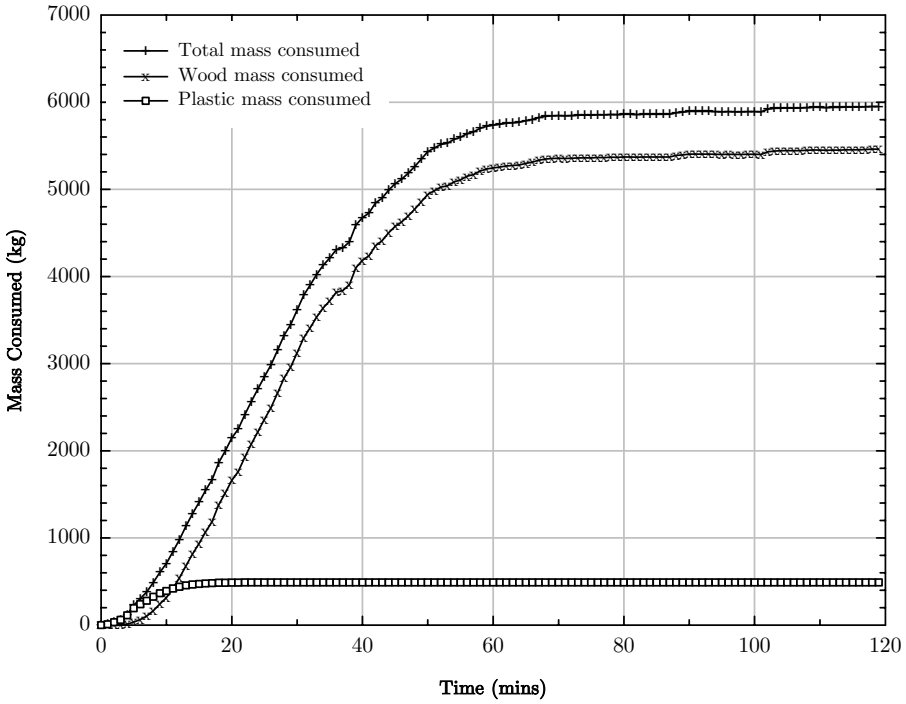

Figure 8.8: Fuel masses consumed throughout fire duration

The efficiency factor, χ is defined as the ratio of the chemical heat of combustion ΔH_{ch} to the net heat of combustion ΔH_c [64], given as,

$$\chi = \frac{\Delta H_{\text{ch}}}{\Delta H_c} \tag{8.6}$$

For wood this is given in Annex E of Eurocode 1 [1] as 0.95 while for polypropylene $\chi = 38.6 / 43.4 = 0.889$.

The net heat of combustion ΔH_c of wood is taken as 17MJ/kg while for polypropylene it is given as 43.4MJ/kg [64]. This allows the HRR to be evaluated by,

$$\dot{Q}_c = \dot{m}\left[\left(F_{\text{plastic}} \cdot \Delta H_{c,\text{plastic}} \cdot \chi_{\text{plastic}}\right) + \left(F_{\text{wood}} \cdot \Delta H_{c,\text{wood}} \cdot \chi_{\text{wood}}\right)\right] \tag{8.7}$$

There are a range of values for the heat of combustion quoted in the literature. Table 8.1 shows typical ranges of the heat of combustion expected for different types of wood. The cribs in the Cardington fire tests comprised pine sticks, therefore the value of 17MJ/kg adopted above is considered to be appropriate.

Wood Type	ΔH_c (MJ/kg)
Plywood – Redwood [121]	5.7 – 15.1
Douglas Fire [64]	16.4
Red Oak [64]	17.1
Pine [64]	17.9
Dry European Beech [3]	19.4

Table 8.1: Heat of combustion values for wood types in the literature

In defining the rate of heat release, it is important to take into account the combustion efficiency of the material. In natural fires, combustion is never complete due to conditions of restricted ventilation in which the products of combustion will contain some species which are partially oxidised and particulate matter in the form of soot smoke. Although the Eurocode presents a value of $\chi = 0.95$, this value could potentially be lower due to the limited availability of oxygen. Table 8.2 presents a range of potential additional values found in the literature. Due to the uncertainty of this parameter, both a low value of $\chi = 0.69$ and a high value of $\chi = 0.95$ have been used in evaluating the heat release rate of the wooden cribs for use in the CFD analysis. The results of these analyses are presented in Figure 8.9.

Wood Type	ΔH_c (MJ/kg)	ΔH_{ch} (MJ/kg)	χ
Douglas Fir	16.4	13.0	0.79
Red Oak	17.1	12.4	0.73
Pine	17.9	12.4	0.69

Table 8.2: Burning efficiency factors for different wood types [64]

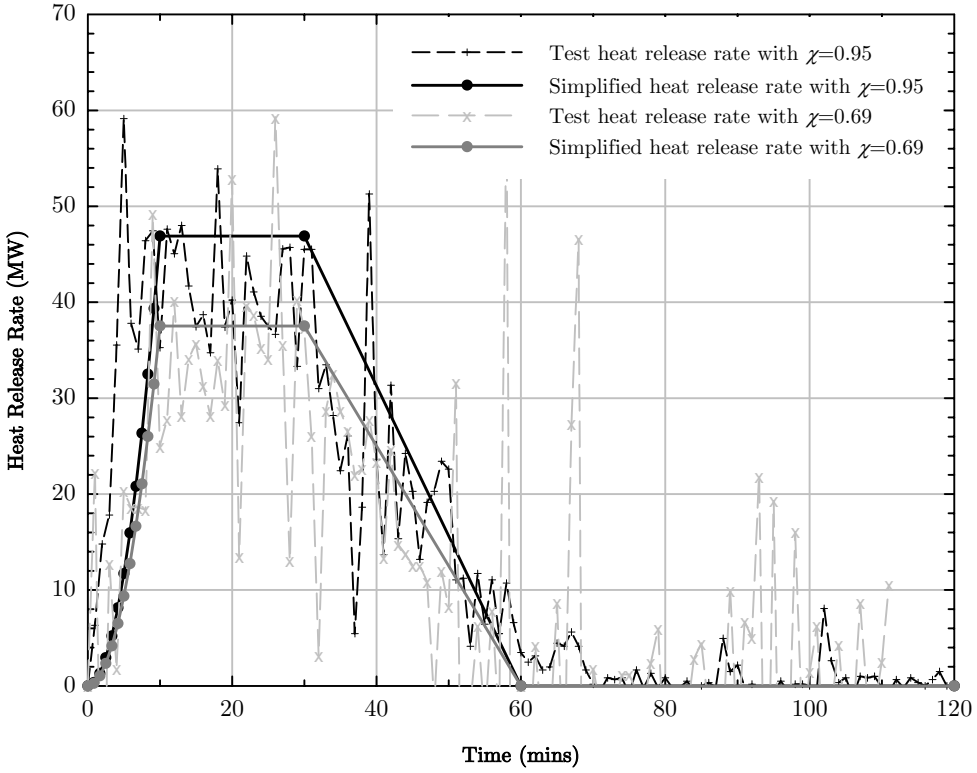

Figure 8.9: Test heat release rate curves for different efficiency factors. The broken lines represent the calculated HRR while the solid lines represent the model input HRR

The HRR to account for all cribs within the compartment is shown in Figure 8.9 for the two given values of combustion efficiency. The large fluctuations shown in the HRR are a result of the numerical solution. The slight changes in gradient of the mass change with time throughout the

test are magnified due to the numerical techniques adopted. These changes in mass can be accounted for by the inaccuracies associated with the crib load cells induced by spalling concrete within the compartment and partial collapses of the crib structures during the fire. The resulting curves are unsuitable to be used as input to the CFD code and thus a simple approximation is given by the solid lines representing a very slow *t*-squared fire ($\alpha_f = 0.00013\text{kW/s}^2$) to 10 mins, a plateau to 30 mins and a linear decay to 60 mins. It is these HRR that are used as the input for the FDS simulation; furthermore it is only applied to the upper face of each crib to account for air entrainment through the cribs themselves. These two HRR curves are approximations that incorporate simple growth periods, peak values and decay periods. Each solid line is simply a subjective curve fit through the original HRR data. It is not the intention to characterise the HRR to a fine level of detail as would be the case in a detailed validation exercise of the CFD code. The requirement for the heat flux model at this stage is to define a simplified and approximate fire environment based on the measured crib data, from which the heat fluxes throughout the compartment can be established. Although two HRR curves are being considered at this stage, that which reproduces the fire environment most accurately in terms of gas temperature comparison to measured data will be used for the heat flux model.

8.3.2. Gas Temperatures

A comparison of the average compartment gas temperature is shown in Figure 8.10. The growth of the fire is well predicted using both efficiency factors, however the lower factor under-predicts the maximum temperature while the higher factor captures the maximum temperature well. In both cases, the duration of the fully-developed period is under-predicted by FDS. Fire development and therefore gas temperatures are influenced by the prescribed rate of heat release. The approximations given in Figure

8.9 and used in the FDS simulation are subjective. It could be argued that the duration of the peak HRR could be extended to 40 minutes which in turn would increase the duration of the peak temperatures achieved in the model. Nonetheless, the FDS simulation provides a limited duration of the fully developed fire period that allows comparison to the test data. The higher temperatures achieved in the test from about 50 minutes onwards is attributed to the glowing embers of the cribs left on the floor of the compartment. FDS assumes that the fuel in completely consumed and is unable to model the characteristics of the glowing embers. Of the two efficiency factors considered, the higher value of $\chi = 0.95$ provides the most accurate representation of the test data and as such, the output generated by this simulation is adopted for all future analyses.

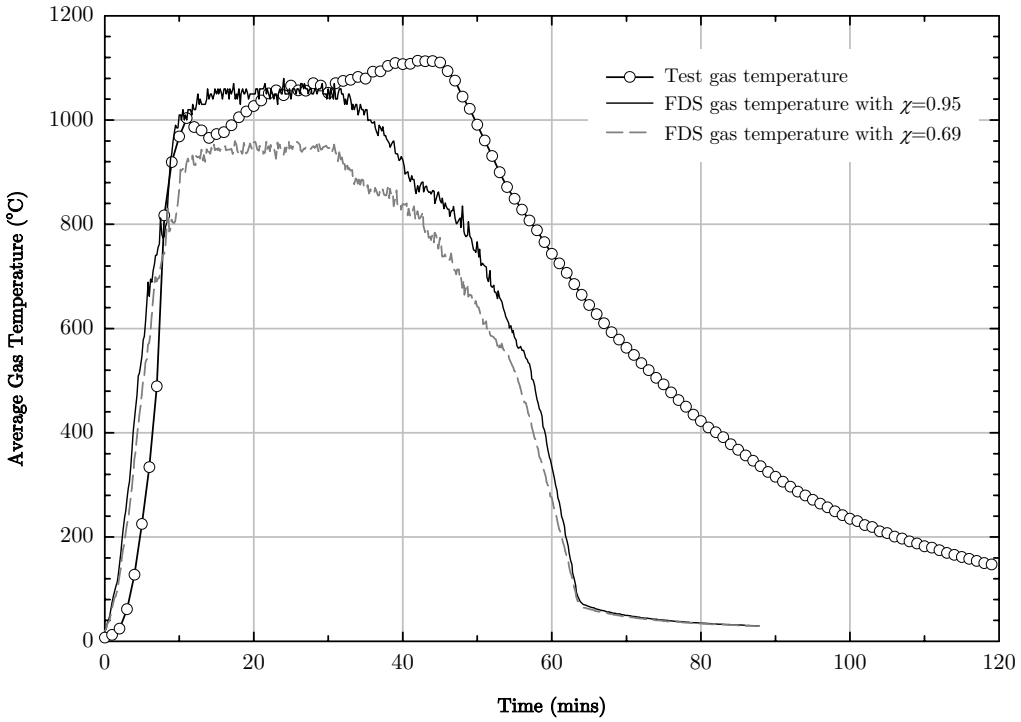

Figure 8.10: Comparison of averaged measured gas temperatures and averaged FDS gas temperatures with different burning efficiencies

While average compartment temperatures provide a useful comparison to the test conditions, it was demonstrated in Chapter 5 that large spatial temporal variations play an important role in the thermal environment and the resultant structural heat fluxes. Therefore it is important to investigate local temperatures at locations within the compartment. In keeping with the test conditions described and the results presented in Chapter 5, three locations of interest are considered; the left and right walls with point measurements at their centres and the ceiling with a point measurement slightly diagonally offset from its centre. Each of these locations is considered separately in the following sections, firstly in terms of predicted gas-phase temperatures and secondly in terms of surface gauge heat fluxes. Where gas-phase temperatures are referred to in the context of test conditions, they have been corrected from the initial thermocouple measurements as per the methodology in Chapter 5.

Left Wall

A single thermocouple tree (Tree 9) near to the left wall is used to compare gas temperatures over its height. Figure 8.11 shows the test and FDS comparison. Very good comparison is seen in the maximum temperature for the upper layer, with the location at 1.8m from the ceiling showing the greatest deviation, although still following the overall trend of the temperature history. Indeed the duration of the fully-developed fire at all points is captured remarkably well considering the under-predicted comparison of the average temperature in Figure 8.10 between 30-50 minutes. The temperature error between the two methods is shown in Figure 8.12, if the initial fire growth period is neglected and focus is given to the full-developed stage of 10-50 minutes then temperatures are generally shown to be predicted to within 200°C. The lowest comparison point of 1.8m from the ceiling shows the greatest deviation which can be attributed to its proximity to the burning cribs and the dynamic nature of the fire at this location due to the inflow of air and smoke layer.

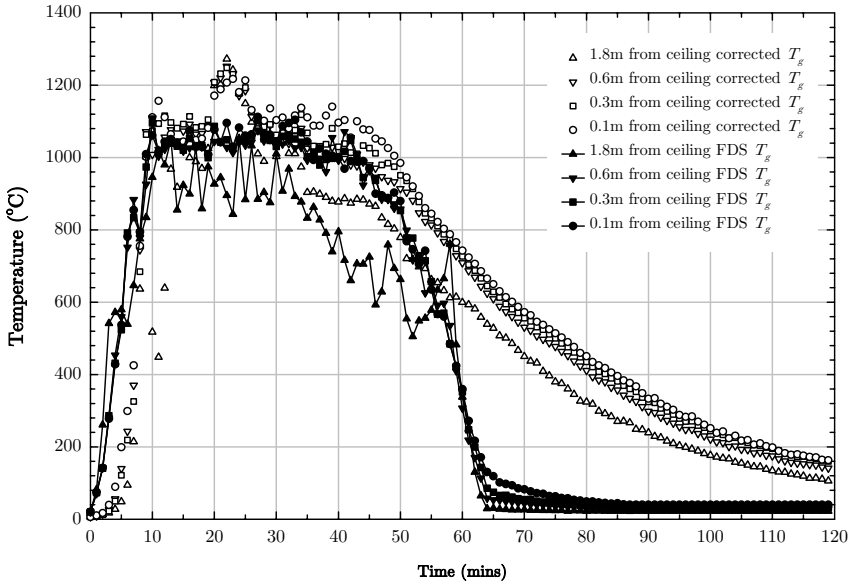

Figure 8.11: Comparison of corrected measured gas and FDS localised temperatures at various heights for Tree 9 near to the left wall of the compartment

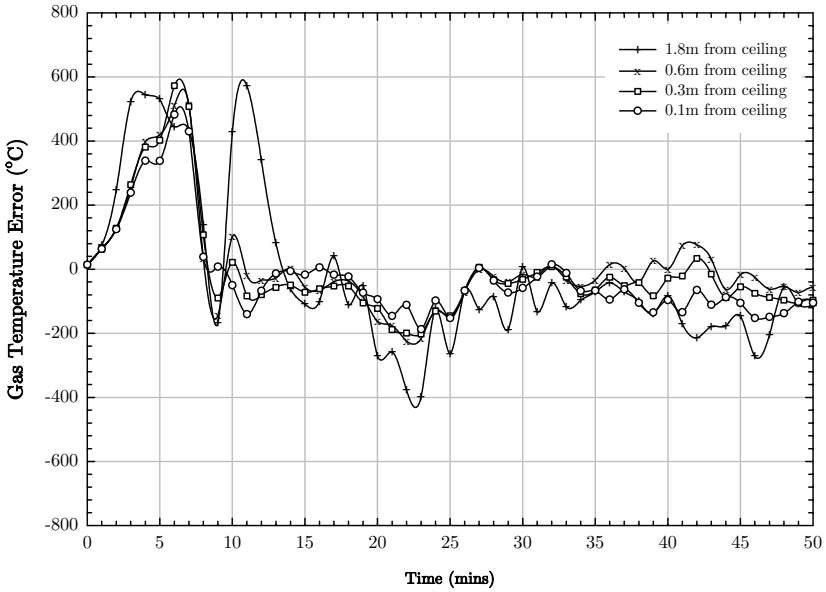

Figure 8.12: Temperature error between corrected measured gas and FDS localised temperatures at various heights for Tree 9 near to the left wall of the compartment

Right Wall

The comparison of temperatures at different heights for Tree 12, near to the left wall is presented in Figure 8.13 with the corresponding temperature difference shown in Figure 8.14 for a the fully-developed fire period. A similar pattern to that of the comparison on the left side of the compartment is seen. The upper layer comparisons are very good, while the point measurement at 1.8m from the ceiling shows the greater error in terms of magnitude, as expected, despite the trend of the fire behaviour being captured reasonably well. The time to flashover is predicted very well and peak temperatures appear to be captured correctly. However, the duration of the fully-developed fire is slightly shorter than the test data which suggests that there was some localised burning and heat release within this area that may be due to some external ventilation condition that the FDS model can not repeat.

It is interesting to note that during the fully-developed period, gas temperatures are slightly higher at this side of the room than at the opposite side. Indeed, these hot temperatures are not only seen in the test data, but are also captured in the model (compare to Figure 8.11) suggesting that the dynamic flows induced in the model have an influence on the local gas temperatures.

For the period 10-20 minutes, following the initial growth of the fire, temperatures in FDS are under-predicted to about 200°C, after this, for about a 15 minute period, upper layer temperatures are over predicted by about 100-150°C after which they revert to being under-predicted. The reduction in temperature in the test seems unusual but may be attributed to ventilation conditions affecting this location. The lack of external ventilation influence in the model means that temperatures in the fully-developed regime are sustained for its entire duration.

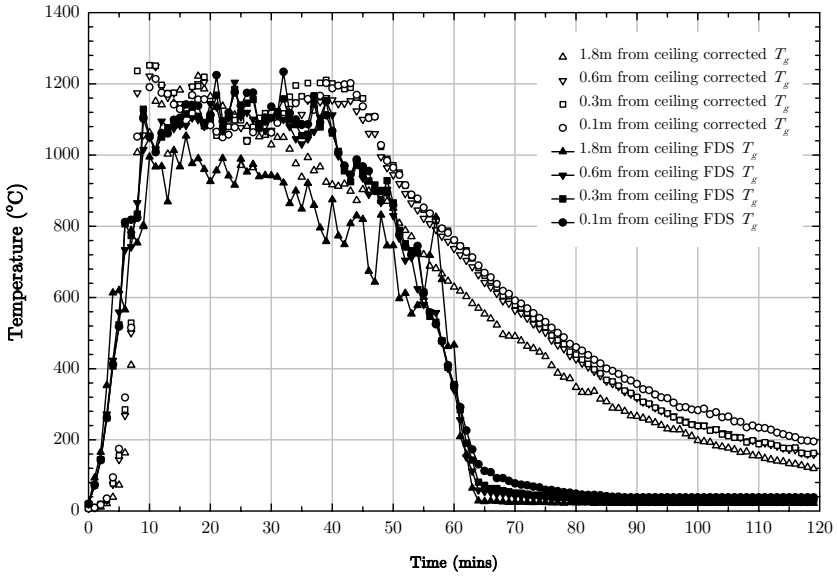

Figure 8.13: Comparison of corrected measured gas and FDS localised temperatures at various heights for Tree 12 near to the right wall of the compartment

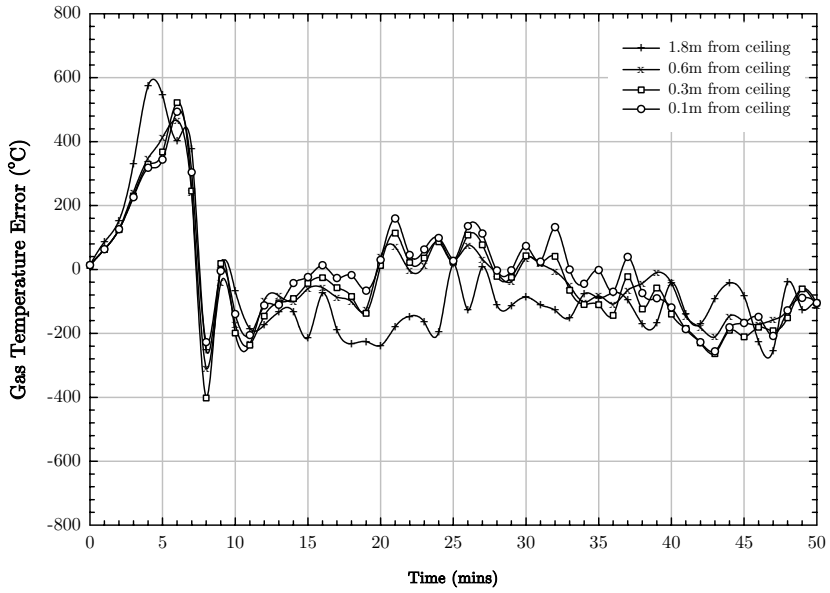

Figure 8.14: Temperature error between corrected measured gas and FDS localised temperatures at various heights for Tree 12 near to the right wall of the compartment

Ceiling

Figure 8.15 and Figure 8.16 show the upper layers temperatures and temperature errors respectively at locations under the ceiling of the compartment. Thermocouple trees 2, 6, 10 and 14 at a distance of 0.1m from the ceiling provide the basis of a comparison between test and simulation gas temperatures from the back of the compartment to the openings at the front.

First impressions given by Figure 8.15 are that flashover at about 7-10 minutes is captured well but that the fully-developed period is not maintained for long enough in comparison to the test data. It is also evident in both the test and simulation data that highest temperatures are observed at the back of the compartment and lowest temperatures towards the front. It is clear that there are some over-predictions and some under-predictions in gas temperatures. The extent of these differences during the fully-developed regime is shown in Figure 8.16.

During the fully-developed fire after approximately 10 minutes, temperatures at the two thermocouple trees nearest the openings are under-predicted by about 200°C while those towards the rear of the compartment are over predicted by up to 300°C. This is due to the energy released by combustion at the top and rear of the compartment being totally absorbed by the products of combustion and generating unrealistic high temperatures. The smoke layer is at its most dense nearest to the ceiling and simulated temperatures in this environment will carry large errors. Indeed, towards the front of the compartment, the soot model employed within FDS is again unable to resolve the energy distribution and in this case temperatures are seen to be lower than expected.

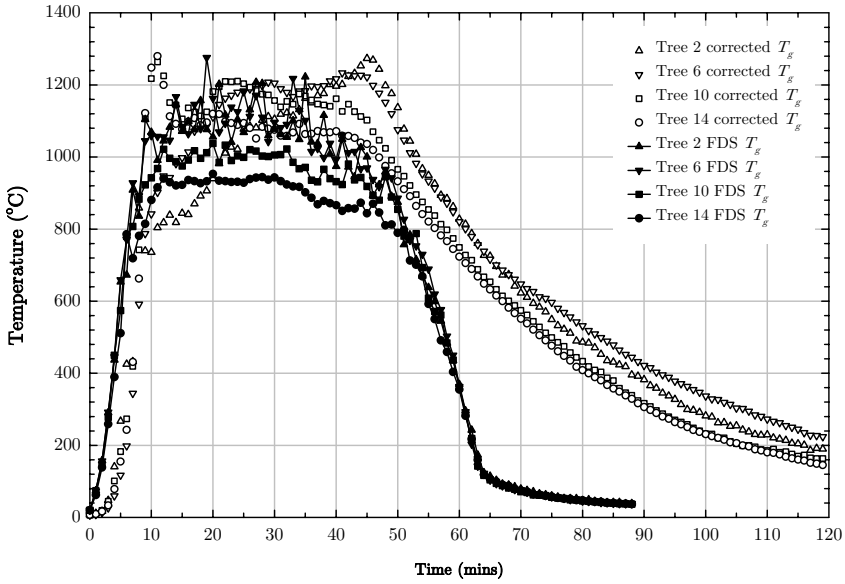

Figure 8.15: Comparison of corrected measured gas and FDS localised temperatures 0.1m from the ceiling from back (Tree 2) to front (Tree 14) of compartment

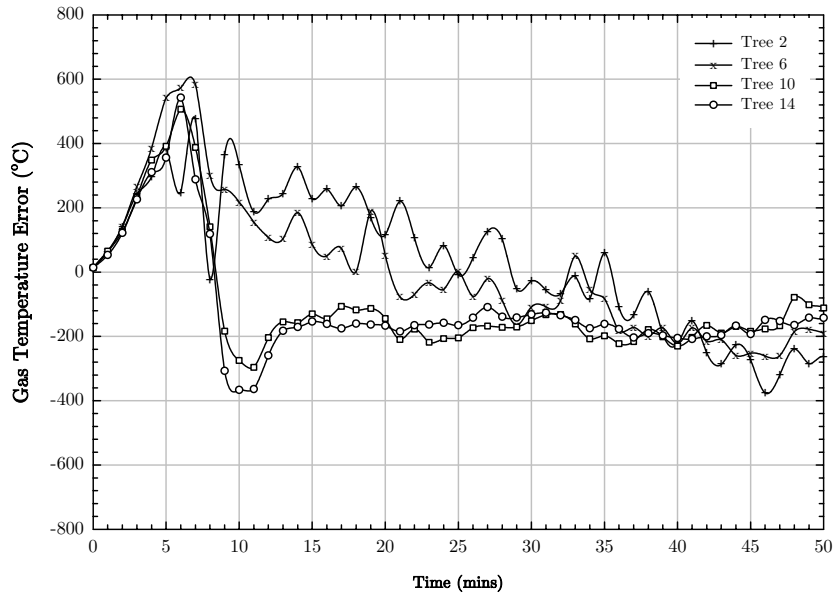

Figure 8.16: Temperature error between corrected measured gas and FDS localised temperatures 0.1m from the ceiling from back (Tree 2) to front (Tree 14) of compartment

8.3.3. Comparison of heat fluxes

The comparison of measured and simulated gas temperatures in the previous section is an important issue in the context of understanding the errors associated with structural heat fluxes produced using CFD tools. Radiative fluxes are dependant on gas-phase temperatures raised to the fourth power. Consequently, any deviation in temperature can have a significant effect of radiative and therefore total and net heat fluxes.

This section again considers the left and right walls and the ceiling for results comparison.

Left Wall

The gauge heat fluxes recorded by the billet and those produced by FDS and the heat flux model are shown in Figure 8.17. The FDS heat flux is slightly higher than that predicted by the model but this can be attributed to FDS incorporating far-field and flame radiation to greater detail. The heat flux model is designed to calculate heat fluxes when the surface element is completely engulfed in dense smoke. The location of the point measurement on the left wall is at its mid-height and therefore is likely to experience flame radiation from the surrounding cribs. In addition the hemispherical approach to averaging the gas data properties at this location would incorporate effects from the cooler lower layer outside the smoke creating reduced average temperatures for the radiant intensity calculation. In general, the heat flux model follows the same trends as FDS which is to be expected as the convective lengths are assumed to be grid cell dimensions.

The measured heat flux during the fully-developed fire period is over-predicted during its initial and latter stages, but the peak value of about 190kW/m^2 at 22 minutes is captured very well. The duration of the peak simulated heat fluxes is about 20 minutes and follows the same shape

as the HRR applied. In reality, the billet shows that there is a definitive peak with strong growth and decay periods. The HRR in the model is applied to all of the cribs at the same time, in reality the ignition of each was at a different time and thus the flame spread characteristics were extremely complex – a factor not captured properly within FDS. The peak recorded heat flux could be the result of flame radiation due to some extreme burning condition in the local area.

In general though, the gauge heat fluxes compare very well at this location on the wall and provide confidence in the simulated CFD fluxes and those defined by the heat flux model.

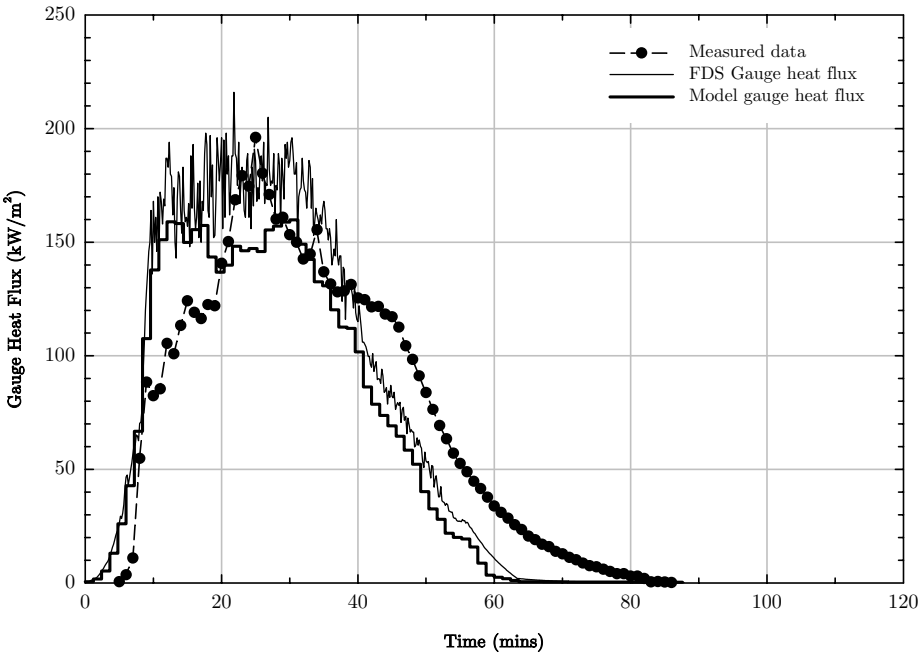

Figure 8.17: Gauge heat flux comparison for billet 7 (left wall) of Test 8 comparing measured data, FDS results and the heat flux model output

Further comparisons are made by creating gauge heat flux maps over the surface of the left wall at various times from the heat flux model output. These in turn can be compared to those created using the methodology of

reconstructing the heat fluxes from the corrected gas temperatures in Chapter 5. Heat flux maps from the model for the time periods of 10, 20, 30 and 40 minutes, corresponding with the fully-developed fire regime, are shown in Figure 8.18. The black square on each plot represents the location of the billet while the value to the left of each plot shows the recorded value at that time interval.

There are definite spots of high flux in each plot at the mid to rear location of the compartment with peak heat fluxes are seen to be 190kW/m^2. The inflow of cool air at the openings on the right of each plot is evident along the entire wall. For all times, the heat flux at the lowest section of the wall is always less than 40kW/m^2. The transition from horizontal stratification at a height of about 1m corresponds with the height of the wooden cribs in the simulation. As there is no reduction in size of the cribs with burning, this horizontal level is maintained for the entire duration of the simulation.

Regions of high heat flux are seen, most notably at 20 minutes and 30 minutes, towards the front of the compartment near to the openings. This is a direct consequence of the external flames produced during the fully-developed fire as burning of the oxygen takes place in this region.

The billet reading at each time provides an indication of the accuracy of the plots, albeit at a precise location. Good accuracy is achieved in all plots, but at 20 minutes and 30 minutes, the comparison is excellent. The plots and readings generated at these point locations are essentially a more detailed reproduction of Figure 8.17.

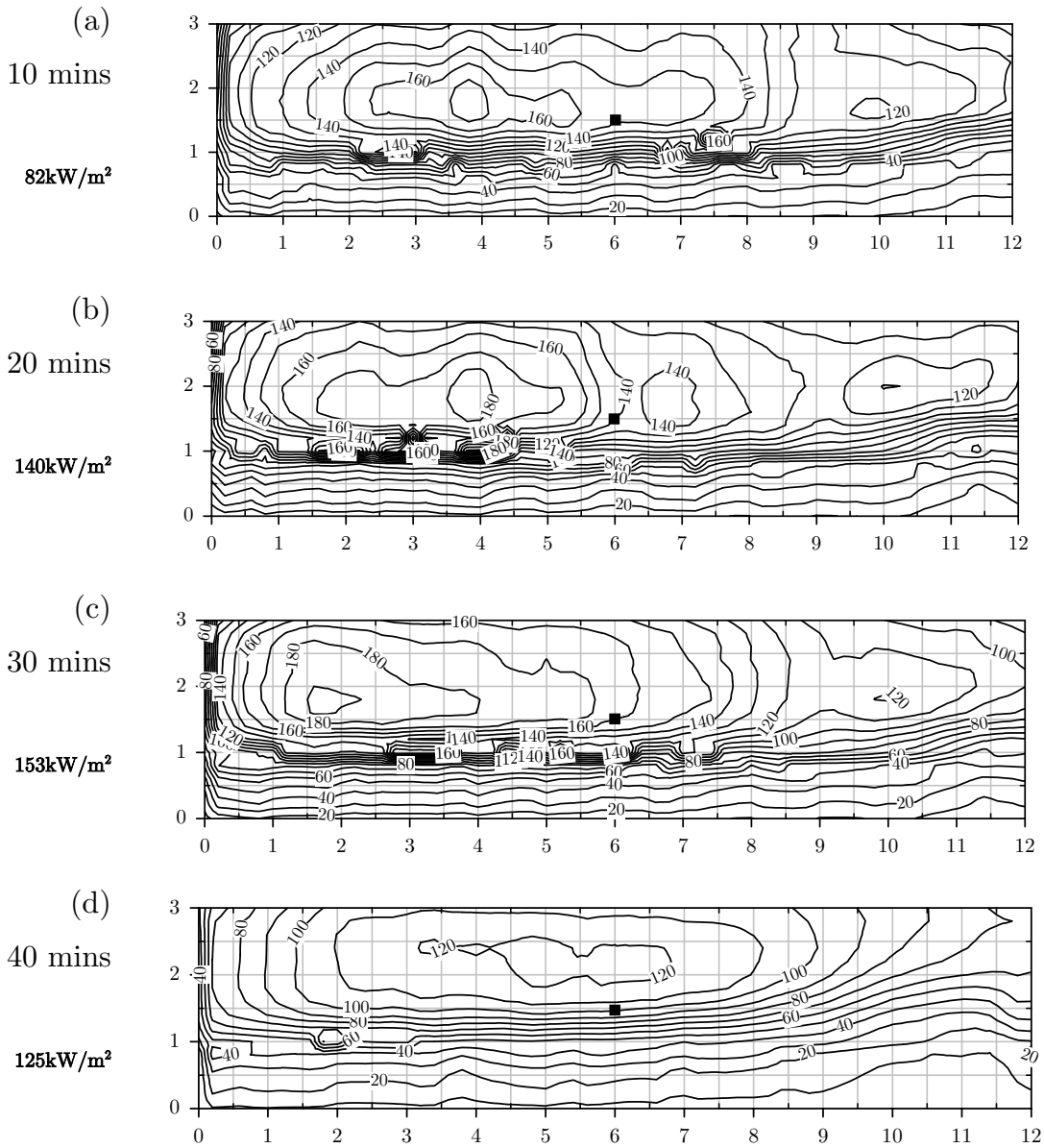

Figure 8.18: Gauge heat flux map over left wall from heat flux model output. Black square indicates location of billet, with the recorded value shown on the left for that time interval. The openings are located on the right of each plot. Contour labels are in kW/m^2 and axis labels of room dimensions are in m.

The percentage error in the gauge heat flux model with respect to the maps produced using the methodology in Chapter 5 is shown in Figure 8.19. Large errors, defined as deviation from the Cardington maps, are seen in the lower section of the wall, although this is to be expected when burn away of the cribs is not accounted for in the CFD model as explained above. Focus is therefore given to the upper sections of the wall.

For all times represented in the plots, the smallest error is seen to be in the centre portions of the wall. As explained earlier, the reliability of the CFD gas temperature predictions in the dense smoke layer are questionable. Higher temperatures are generated at the rear of the compartment and lower temperatures nearer to the openings (see Figure 8.16). At the centre, the errors appear to cancel and good agreement between the temperatures and therefore heat fluxes are found. The largest errors are always found towards the upper-rear of the compartment. The over-predicted temperatures in this location result in high heat fluxes due to the dependence on temperature to the fourth power. During the test, a hot-spot concentration of heat flux on the wall was seen to move progressively towards the rear of the compartment during the fully-developed fire. In the simulated model, at the corresponding times, this concentration is always at the rear of the compartment. As previously discussed, the temperatures and therefore peak heat fluxes follow the HRR curve very closely and therefore these concretions would always be expected in these locations during the simulations.

In general, errors on the left wall in the smoke layer are of the order of 10-50%. The majority of these errors can be attributed to the error in temperature prediction of the CFD model. A more detailed discussion on the relationship between temperatures and heat fluxes follows this section.

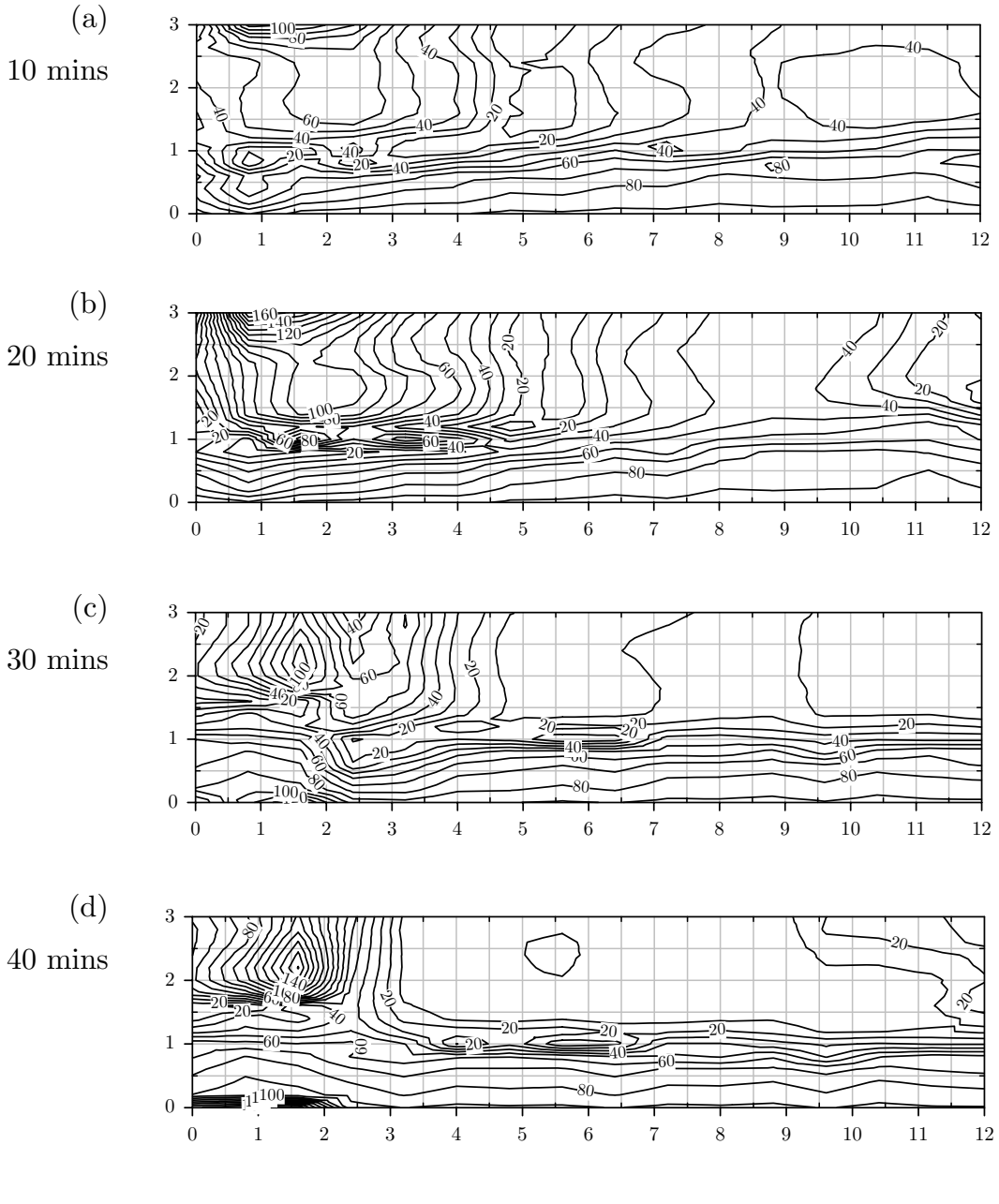

Figure 8.19: Heat flux error map over compartment left wall; comparison of model output to test results for post-flashover conditions. The openings are located on the right of each plot. Contour labels are in % and axis labels of room dimensions are in m

Right Wall

The plot in Figure 8.20 shows a comparison of the measured billet gauge heat flux, the FDS predictions and the heat flux model predictions for the central point on the right wall. It would not be unreasonable to assume that similar conditions on the right wall could be expected to those on the left wall due to symmetry, however, as the plot shows, this is certainly not the case.

For the fully-developed period, the models significantly over-predict the gauge heat flux recorded in the test. The reason for this is the slight over-prediction of gas temperature (see Figure 8.14) at this location producing dramatically exaggerated heat fluxes for the period after 15 minutes. Possible reasons for the reduction in temperature are discussed above, but this plot demonstrates the need to be able to predict temperatures accurately if they are to be used to establish heat fluxes.

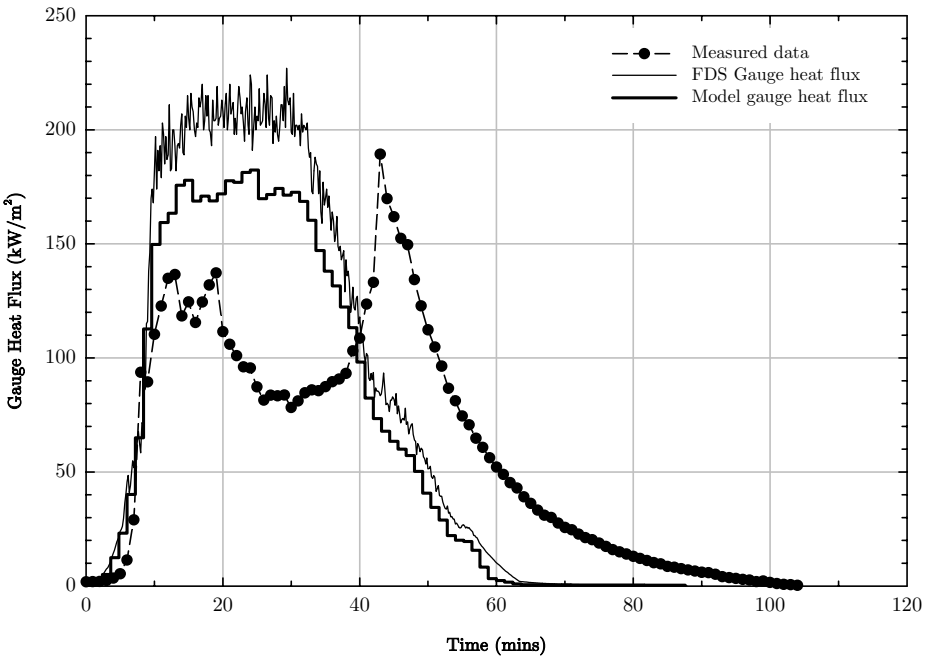

Figure 8.20: Gauge heat flux comparison for billet 8 (right wall) of Test 8 comparing measured data, FDS results and the heat flux model output

Ceiling

The comparison of the point measurement of gauge heat flux and model predictions for the ceiling billet is shown in Figure 8.21. It is clear that both models are significantly under predicting the heat flux at this location. Again, it is the reliability of the CFD upper layer smoke temperatures that is the primary cause of the error. The billet is diagonally offset from the centre of the ceiling towards the opening. As a result, the temperatures here are under-predicted (see Figure 8.16). A comparison towards the rear of the compartment would have seen the model predictions give higher fluxes than the billet due to the over-predicted temperatures in that location.

It is interesting to note that the measured billet gauge heat flux produces a relatively steady peak value throughout the fully-developed fire period in comparison to the other locations considered above. This is due to uniform gas temperatures typical of upper smoke layers.

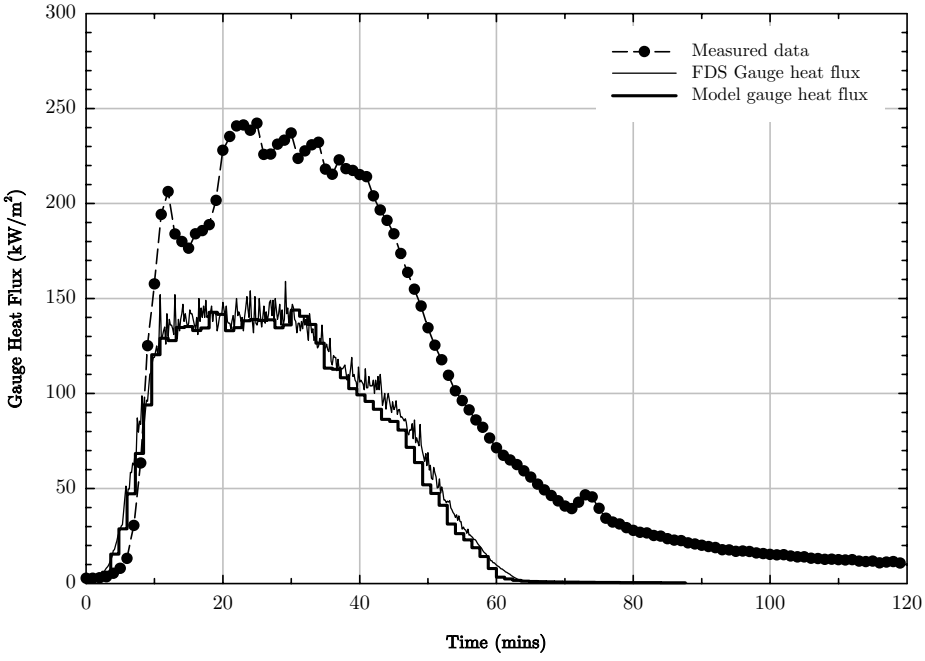

Figure 8.21: Gauge heat flux comparison for billet 6 (ceiling) of Test 8 comparing measured data, FDS results and the heat flux model output

For completeness, gauge heat flux maps for the ceiling, from the heat flux model, are produced at various times through the fully-developed fire period and these are presented in Figure 8.22. The openings in the compartment are located on the right of each plot, while the black square indicates the location of the billet, of which the value at that point in time during the test is given below.

In each plot, the peak heat fluxes are seen to occur at the rear of the compartment, with specific concentration being towards the corners of the room. This is due to the radiative feedback of the compartment walls influencing the gas-phase temperature in these localised areas. Figure 8.22 (a) demonstrates this clearly; towards the centre of the room at the very back of the compartment (left of the plot) the influence of the side walls is decreased relative to the edges of the room, with resultant lower heat fluxes. Indeed, all plots demonstrate to some extent the influence of the two openings at the front of the compartment where the products of combustion can escape, but the impact of flame radiation ensures that high heat fluxes are maintained here.

Peak heat fluxes of 240-260kW/m^2 occur on the ceiling, but it remains evident that there is considerable spatial variation in heat fluxes over the surface of the ceiling. During the fully-developed fire period of 20-30 minutes, ceiling heat fluxes range from 120-260kW/m^2.

At 40 minutes, the HRR is reducing and the resultant heat fluxes appear to remain concentrated towards the rear of the compartment, however, the influence of the surrounding walls seems to have a far lower impact in terms of creating gradients of flux across the surface near to the walls.

(a) 10 mins

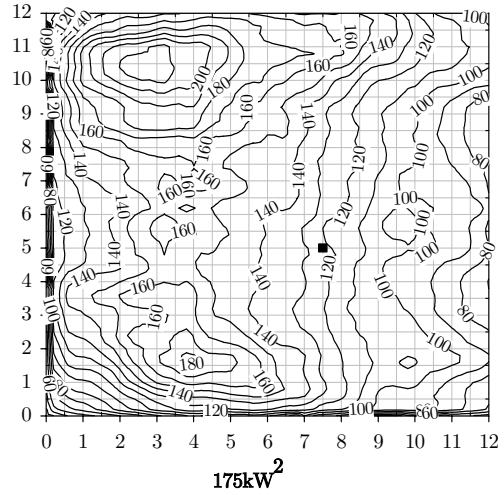

(b) 20 mins

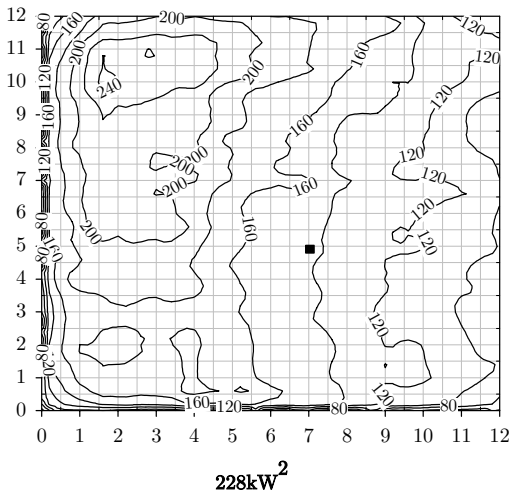

(c) 30 mins

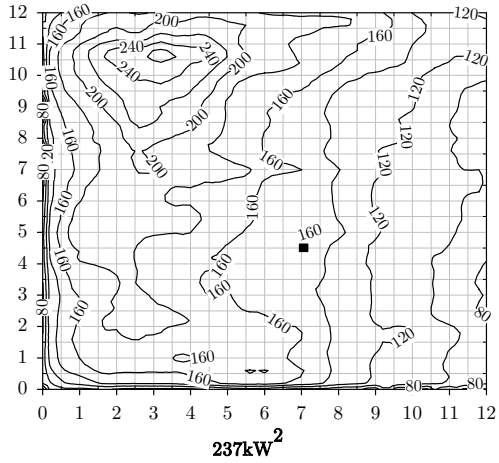

(d) 40 mins

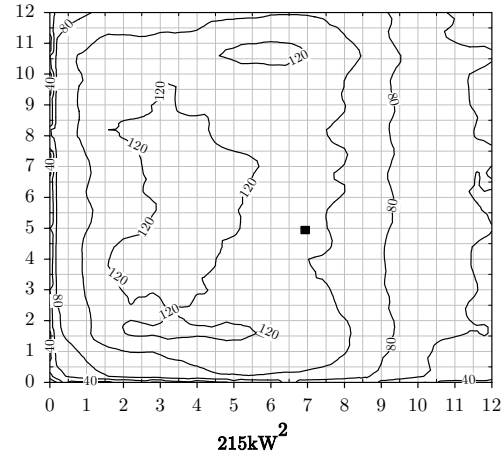

Figure 8.22: Gauge heat flux map over compartment ceiling from the heat flux model. Bold numbers below the plots indicate the measured billet reading at the black square at the corresponding time. The openings are located on the right of each plot. Contour labels are in kW/m^2 and axis labels of room dimensions are in m

(a) 20 mins (b) 30 mins

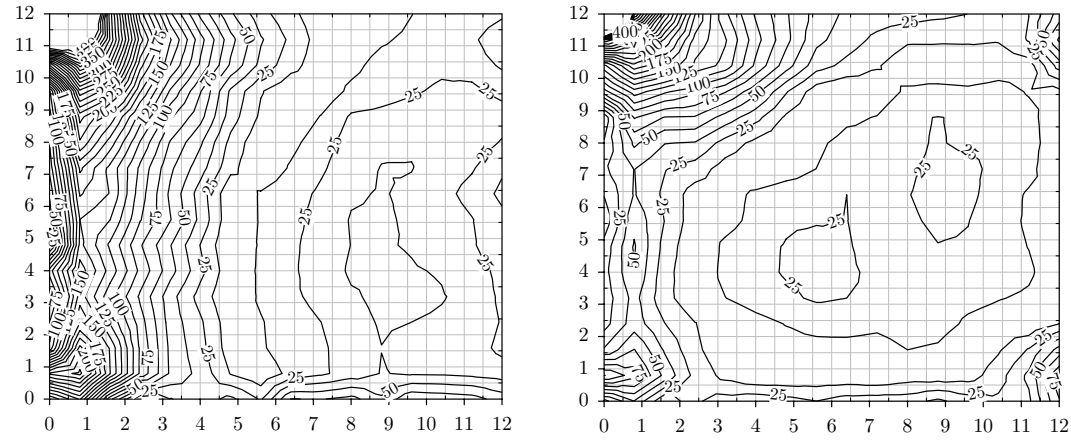

Figure 8.23: Heat flux error map over compartment ceiling; comparison of model output to test results for post-flashover conditions. The openings are located on the right of each plot. Contour labels are in % and axis labels of room dimensions are in m.

The error associated with the ceiling gauge heat flux as defined by the heat flux model and compared against the maps produced for 20 minutes and 30 minutes by the methodology in Chapter 5 is shown in Figure 8.23.

The majority of the ceiling experiences fluxes with errors in the range 20-50%. In the back corners of the room, the largest errors are seen, although these can be accounted for in terms of the curve fitting technique adopted in Chapter 5 that interpolates between limited data points and can therefore lead to misleading fluxes at certain areas of the compartment boundaries.

In general, highest errors are found towards the back of the compartment, while lowest errors are found at mid to front regions on the compartment ceiling. These errors remain a function of the under and over-predicted gas temperatures by the CFD model in the upper smoke filled layer.

8.3.4. Time Averaging

The methodology behind averaging heat fluxes between characteristic times for the solid was introduced and discussed in Chapter 6. The model uses this methodology to speed up computational time yet still remain a required level of accuracy. This section considers different time averaging intervals for gauge heat fluxes and then evaluates the variation of the surface temperature for each interval.

When running the heat flux model for the Cardington scenario, a conduction length scale of 0.2m is assumed for the thickness of the walls. The walls themselves are taken as concrete. This allows a characteristic time of 68 seconds to be defined, however, as FDS is limited to 99 data output requests, the minimum available time averaging interval is 72 seconds (7200s/99). Figure 8.24 shows a typical Cardington gauge heat flux curve overlaid with numerous equivalent time averaged responses ranging from 100s to 1000s.

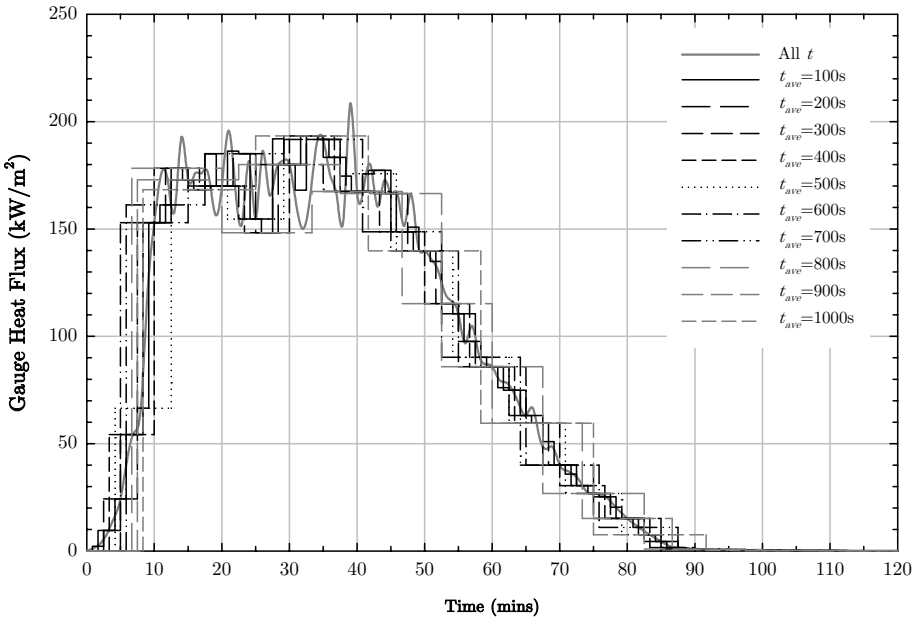

Figure 8.24: Time averaged gauge heat fluxes for different time averages

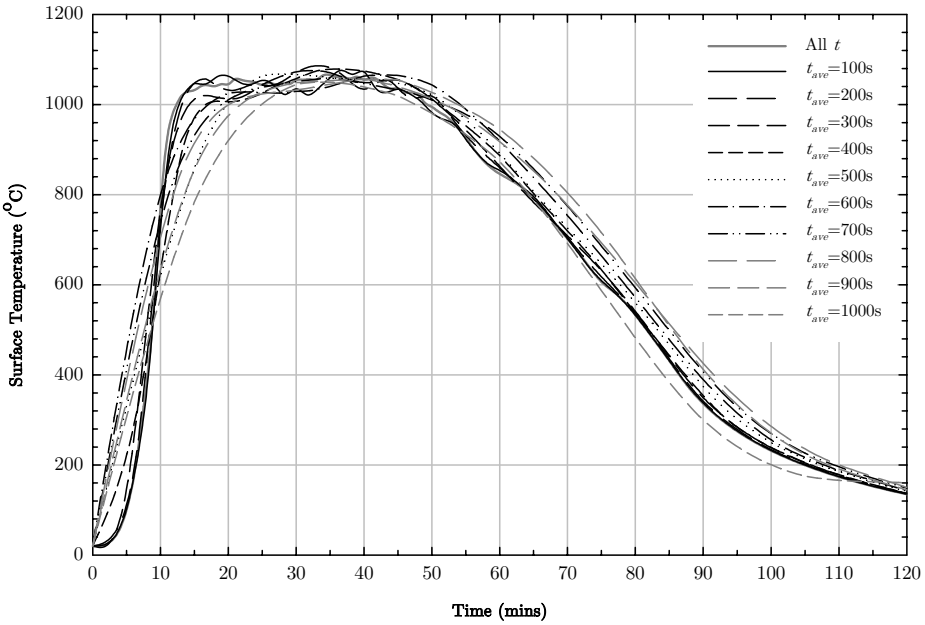

Figure 8.25: Structural temperatures assuming thermally-thin steel ($H_p / A = 200\text{m}^{-1}$) with different time averaging intervals

The corresponding structural temperatures for a thermally-thin steel section with an H_p / A value of 200m^{-1} are shown in Figure 8.25. As the time averaging interval is increased, the initial steel temperature deviates largely from the actual value during the growth of the fire. The peak steel temperatures during the fully-developed fire for all the time averaging intervals correspond very well to the expect temperatures, while in the decay phase, an increased time average interval results in higher steel temperatures.

The error in using a small (100s) and a large (1000s) interval is shown in Figure 8.26. A 100s interval evaluates steel temperatures that are always less than 10% of the actual value, while a 1000s interval produces errors of up to 30% when the gas temperature is seen to vary with time, or rather during the growth and decay periods.

It would appear then the methodology of using characteristic times for averaging heat fluxes is extremely robust and that the characteristic time of 72 seconds used in the Cardington scenario would yield a heat flux evolution that could be used to define structural surface temperatures that would have a temperature error of far less than 10% of the anticipated value.

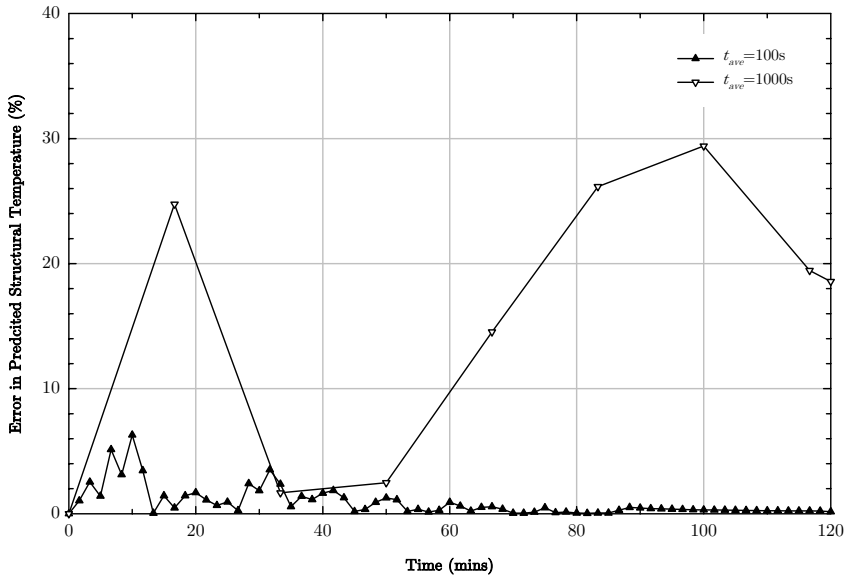

Figure 8.26: Error in predicted structural temperature over fire duration for different time averaged gauge heat fluxes

8.4. Eurocodes

A comparison to heat fluxes predicted by the Eurocodes to the model predictions allows an assessment of the validity of this prescribed design approach. Figure 8.27 shows the average compartment gas temperature for the Cardington scenario together with the standard fire and a parametric temperature-time curve. The parametric curve, which considers ventilation and fuel load characteristics over-predicts the fire growth slightly under-predicts the peak temperatures during the fully-developed period, and again under-predicts temperatures during the

decay phase of the fire. It also significantly under-predicts the end of the fully-developed period. In comparison, the standard fire is seen to under-predict temperatures by around 200°C during the fully-developed period. The standard fire does not consider a decay period and as such the gas-phase temperatures remain at a high value for the entire duration considered.

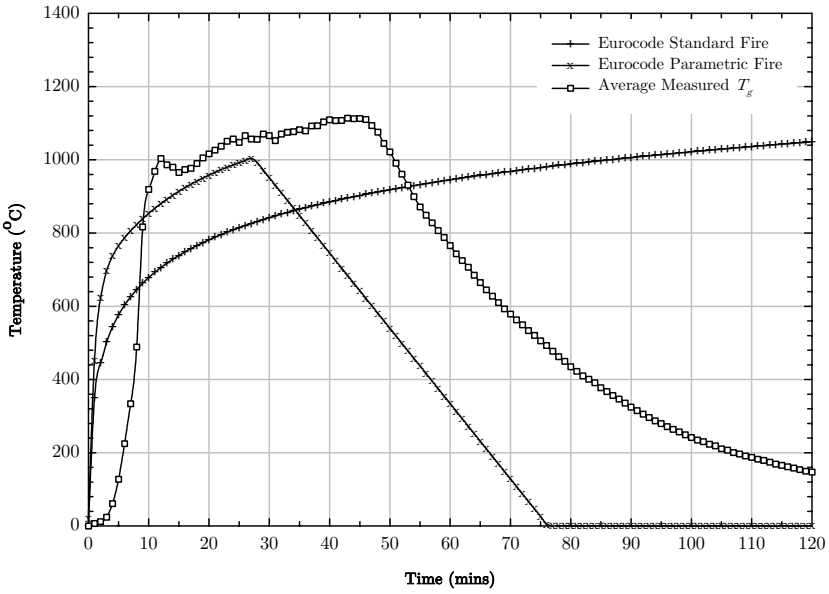

Figure 8.27: Average gas temperatures within the compartment for Eurocode predictions and measured test data

It is common practice to use the Eurocode gas temperatures and calculate heat fluxes assuming a constant emissivity of 1 and some specified convective heat transfer coefficient. This allows convective, radiative and total heat fluxes (gauge heat fluxes) to be evaluated to gain an idea of their relative magnitude. Gauge heat fluxes for the parametric and standard fires are shown in Figure 8.28. As expected, the pattern of heat fluxes corresponds closely to that of the gas temperatures. In the time period up the 30 minutes, convective fluxes, based on a constant coefficient of 25W/m^2.K, for both fires are of a very similar magnitude, however, radiative and total fluxes are far greater for the parametric fire. It is only

after two hours that the standard fire reaches the peak heat fluxes achieved in the parametric fire.

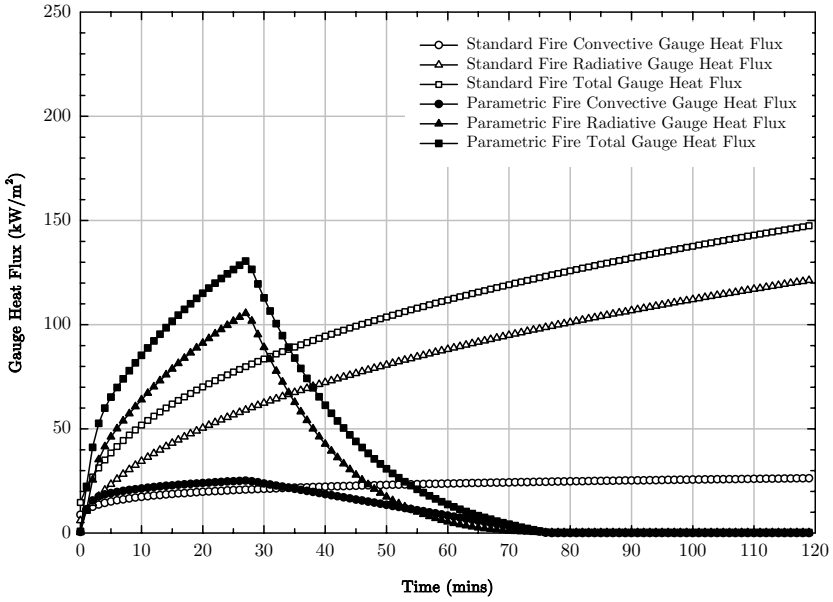

Figure 8.28: Convective, radiative and total gauge heat fluxes expected within the compartment as a result of the Eurocode parametric and standard fires

Figure 8.29 shows a comparison between gauge heat fluxes predicted by the model and those predicted by the parametric Eurocode fire. This comparison is for the left wall of the compartment where very good CFD agreement was found when compared to experimental measurements. For convective, radiative and total fluxes, the magnitude of the peak values are slightly under-predicted by the Eurocode method, although the time at which they occur in comparison to the model is very good. Figure 8.30 shows the same comparison but for the ceiling where poor predictions between the model and test data were found. Again it is clear that the Eurocode predictions match the model data well in terms of magnitude, growth and decay periods. It is evident that the Eurocode method is always slightly under-predicting the intensity of the total heat flux in

comparison to the model, however the model results would be provide a conservative account for the severity of the fire on structural members.

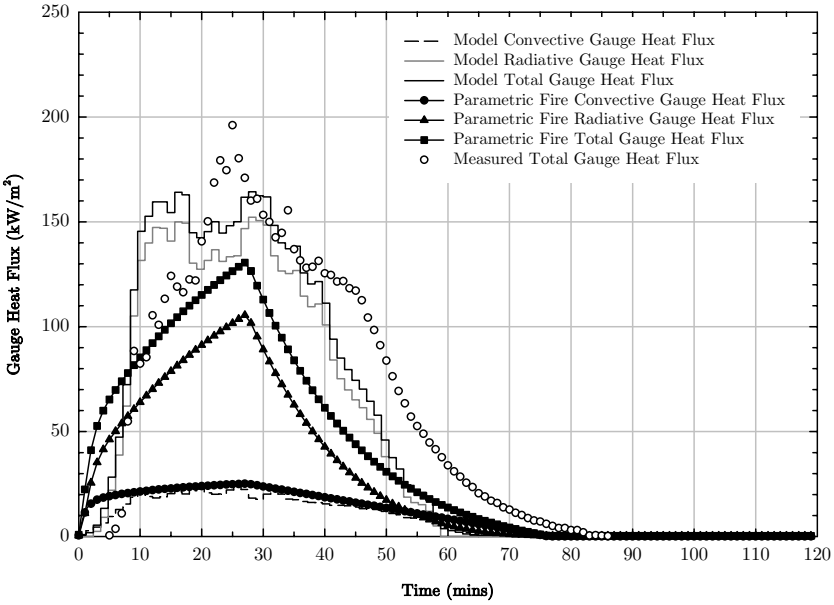

Figure 8.29: Comparison of Eurocode parametric heat fluxes with model output and measured test billet data for left wall of compartment

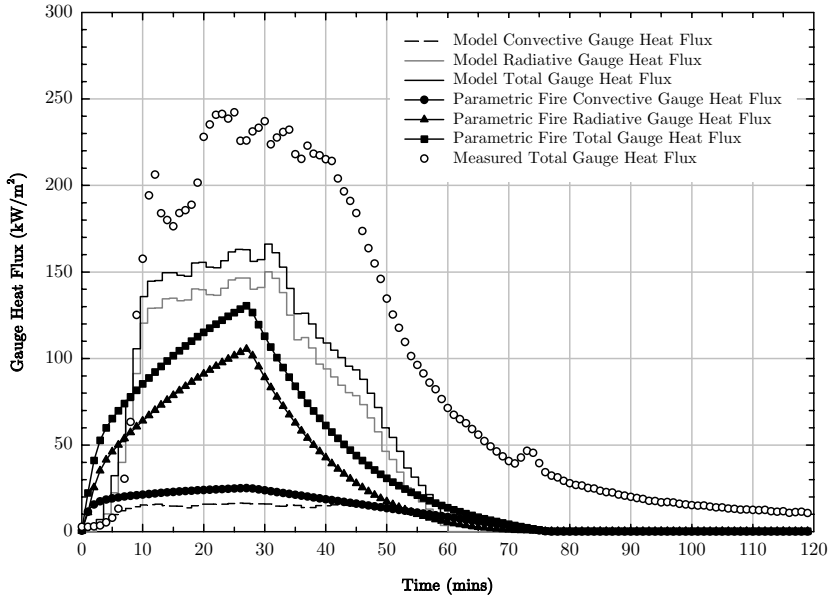

Figure 8.30: Comparison of Eurocode parametric heat fluxes with model output and measured test billet data for ceiling of compartment

The main outcome of the Eurocode approach is that the range of heat fluxes found in the wall is much broader than the values obtained from assuming an average to represent the entire compartment.

8.5. Conclusions

A comparison of the heat flux model has been undertaken with respect to measurements taken during Test 8 of the large scale Cardington fires, a CFD simulation of the fire and Eurocode design fires.

The heat flux model matches the results of FDS accurately for locations in the upper smoke layer, while at lower levels it slightly under-predicts the total flux due to its inability to correctly model far-field radiation from flames and the effect of lower temperatures outside the smoke layer influencing the average gas temperature on the surface of the shell. As the model is intended to evaluate surface heat fluxes in the smoke layer for structural elements (which are generally in close proximity to the ceiling), the heat flux model can be considered to give an accurate representation based on the CFD results. In addition, the use of characteristic times for averaging heat fluxes has been shown to be robust.

As the heat flux model uses results generated by the CFD model, the CFD model must be compared to experimental data. In doing so, it is evident that heat fluxes can have large variations in error at different points in the compartment. The reason for the error is due to the inability of the CFD code to accurately predict localised gas temperatures. The average gas temperature of the compartment compares well to the experimental measurements, however this can often give misleading results. The greatest temporal errors and hence heat flux errors were found to be in the upper section of the compartment where temperatures towards the back were significantly over-predicted and also at the front where they were

significantly under-predicted. Overall, heat flux errors of the order 20-50% were observed throughout the majority of the compartment boundaries.

As it is regarded that given adequate soot yields as inputs, the spatial distribution of the soot fractions within CFD codes are relatively accurate, the heat flux errors can be attributed purely to temperature errors. Since heat fluxes are dependent on temperatures raised to the fourth power, it is vital that temperatures are predicted accurately at all locations within the compartment. The importance of this accuracy is demonstrated by the figures on the following pages.

Figure 8.31 shows the potential gauge radiant heat flux error that may be produced when the gas temperature is under or over-predicted by a specific amount from a series of different initial temperatures. This is replicated in terms of a percentage error in Figure 8.32 which shows that if the temperature is under-predicted then the heat flux error can be significant, although never more than 100%. In contrast, if it is over-predicted, far greater errors in the heat flux may be induced.

If limits in the radiant heat flux errors are defined, then it is possible to establish allowable temperature errors for different predicted gas temperatures. This is shown in Figure 8.33 with limits of 10%, 20% and 50% in the radiant intensity. This data is replicated in terms of percentage error in Figure 8.34 and shows that for low gas temperatures and wider range of error is allowable to maintain the accuracy limits. As the gas temperature increases, that error limit becomes smaller.

As an example, consider a typical gas temperature of 1000°C. If it required to predict the radiant intensity within 10% then Figure 8.34 shows that the temperature needs to predicted to within approximately

2-3% which translates as approximately +/-30°C. This degree of accuracy is very difficult to achieve within CFD models.

A comparison to the Eurocode gas temperature to that recorded in the test shows that temperatures, duration of the full-developed fire and its decay are all under-predicted. The use of a single temperature to represent the compartment hides the important spatial temporal distributions that are required to evaluate the heat fluxes correctly. By analysing the Eurocode fire in terms of convective, radiative and total heat fluxes, a comparison to the heat flux model can be undertaken. This reveals that despite capturing the growth and decay phases well, the Eurocode is always slightly under-predicting the magnitude of the radiant and therefore total heat fluxes.

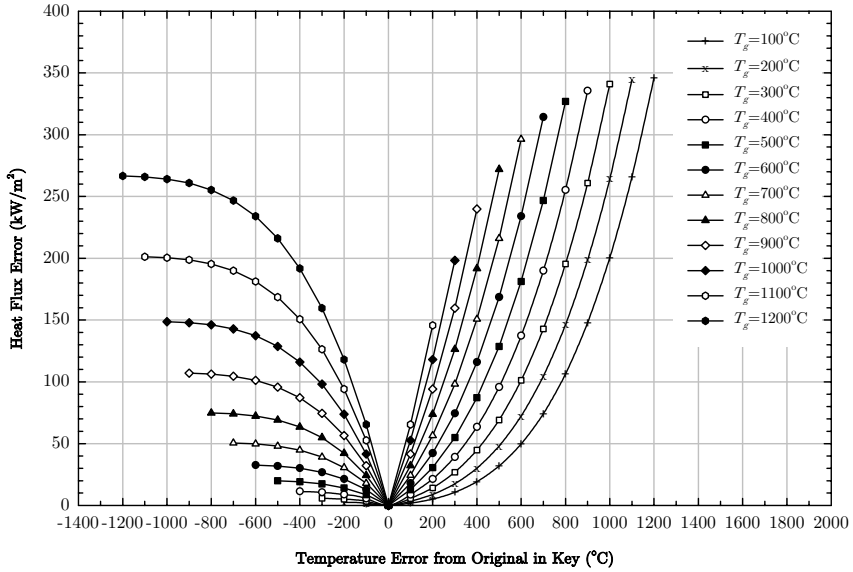

Figure 8.31: Gauge heat flux error for different gas temperature errors based on original gas temperatures as shown in the key for a constant gas mixture emissivity of 1

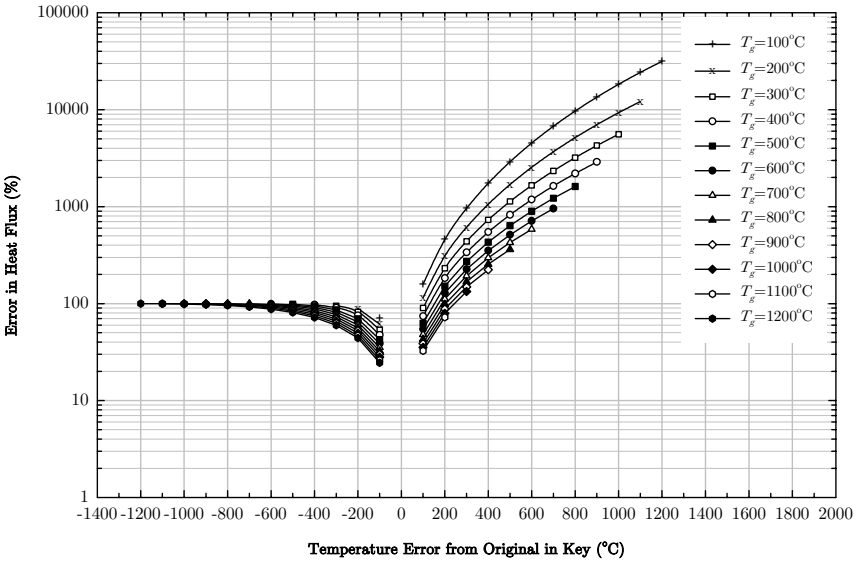

Figure 8.32: Percentage error in gauge heat flux for different gas temperature errors based on original gas temperatures as shown in the key for a constant gas mixture emissivity of 1

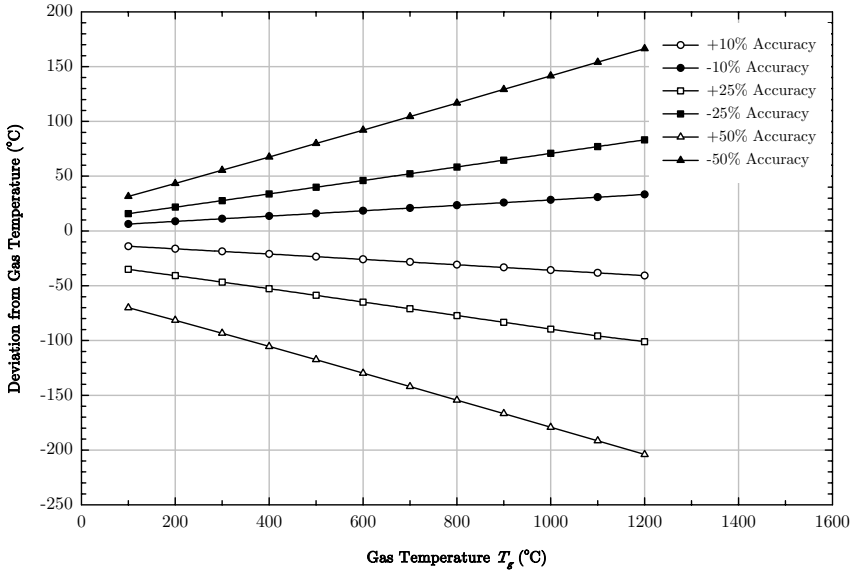

Figure 8.33: Possible deviation from original gas temperatures to maintain accuracies of 10%, 20% and 50% in the gauge heat flux

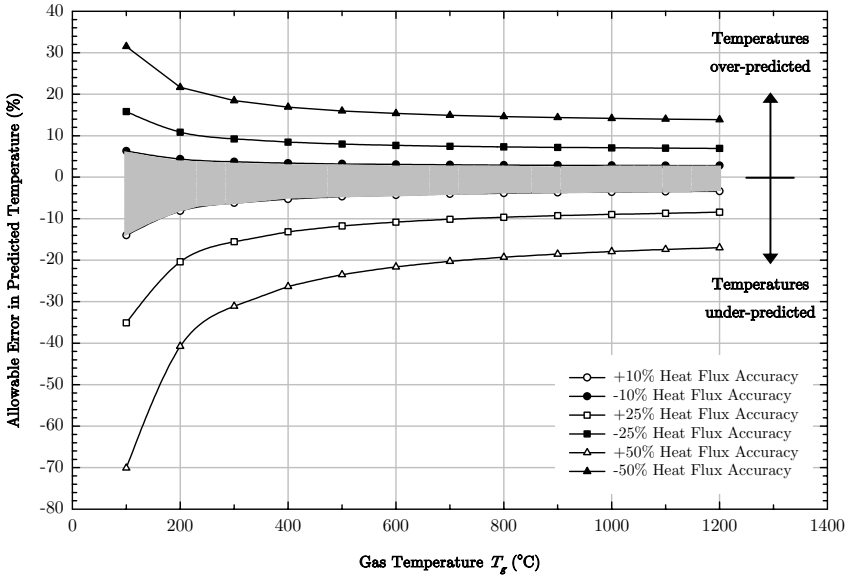

Figure 8.34: Allowable predicted temperature error for a range of gas temperatures with limits for 10% (shaded), 25% and 50% accuracy of the gauge heat flux

Chapter Nine

9. Structural Analysis Applications

9.1. Introduction

In order to demonstrate how the defined heat fluxes calculated by the model can be transferred into a structural analysis, it is applied here with the intention of evaluating the performance of a hypothetical multi-storey building in fire. A brief methodology provides the basis of the analysis which involves thorough consideration of potential structural weaknesses, consideration of the possible fires, modelling of fires, heat transfer and structural analysis.

In addition, the use of structural systems with complex geometries is discussed in terms of potential heat transfer implications and thus their general performance in fire.

9.2. Analysis Methodology

The methodology outlined here allows potential weaknesses in buildings due to fire exposure to be established. Initially, a screening process allows structural vulnerabilities to be identified. In a similar approach, potential fire areas within the building can be defined. It is the matching of critical structural elements together with fire locations in which severe fires may occur that identifies specific scenarios for detailed study. For these scenarios a parametric study of the potential fires can be undertaken. Heat transfer to the structural elements, capturing full spatial and temporal resolution provides the basis for the mechanical response to be evaluated. A series of local studies establishes the behaviour of structural elements that may define specific failure features. A global analysis of the structure serves to validate these failure modes and determine whether any individual failure can induce total collapse of the structure. The following sections briefly outline each of the individual aspects of the methodology.

9.2.1. Structural weakness and fire locations

The initial part of the methodology involves identifying key structural components and assemblies within the building that could potentially cause disproportionate damage if they were to fail under fire conditions. This process is essentially very similar to that used to evaluate the robustness of the building at ambient temperatures including the response due to occasional anticipated loads such as blast or impact. Consideration must also be given to the general behaviour of the structural elements in fire. For example, the response due to thermal expansion together with regions of high restraint can lead to problematic scenarios. In addition it is likely that more than one structural element may fail due to the effect of fire and as such it can be difficult to accurately define specific structural locations. Ideally a fire engineer would work closely with a structural engineer to come up with a series of locations that require further investigation. The focus of this methodology does not consider local failures leading to life threatening situations, such as failure of fire barriers, but focuses on issues associated to partial or total collapse. Therefore, the characteristic features that relate to collapse are significantly reduced in number. Typical things to consider are unfavourable load ratios on columns, long spans structural systems including truss and cellular beam arrangements, irregular geometry and load transfer truss systems amongst others.

In parallel with the definition of areas of potential structural concern, consideration must also be given to possible areas of fire development. This is commonly undertaken with respect to the likely fuel loads in relation to the occupancy type in specific locations throughout the building. It is also important to consider ventilation characteristics of a fire area as these can have large influences on the size and duration of potential fires. When assessing structural performance in fire, it is important to note that the fires of most interest are those of long duration

and/or high temperatures. Structural elements have generally large thermal inertia, thus their heating response is a slow process compared to the time scales of the fire. Because of this particular characteristic, many fires, that will have to be studied for life safety purposes, can be excluded when evaluating structural performance.

These screening processes can be combined and where an overlap in potential structural failures and possible critical fire areas is seen, further analysis to demonstrate expected the fire severities and the local and global structural response should be established.

9.2.2. Fire modelling

Chapter 2 outlined many tools available to the structural engineer for evaluating the development of the fire, ranging from simplified temperature-time relationships through to complex computational fluid dynamics models. The choice of method to use, as previously discussed depends greatly on the level of detail required together with a fundamental knowledge of the limitations of each model and the appropriate error bars with which they are associated. Whichever model is chosen, the objective is to define the worst-case fire scenario that will affect the structural members deemed to have the potential to fail. The result may be a maximum temperature, a long duration of heating or some combination of both. By undertaking a parametric fire study of the localised fire area these conditions can be properly evaluated. This study involves systematically varying the fuel load within acceptable error bars and ventilation parameters across the range of potential ventilation conditions. In the case of the Eurocode parametric equations and zone modelling techniques this will always yield a uniform temperature-time curve for the gas phase environment. In the case of CFD modelling a parametric study of this type can be used to define a scenario in which high heat fluxes

result around the structural elements of interest with the outcome being a spatially well-defined thermal gas phase environment.

9.2.3. Heat transfer to structural elements

Having established the gas-phase thermal environment, it is required to evaluate the solid-phase temperature rise of the structural elements due the fire. It is this output that is passed to the mechanical structural response analysis. When CFD tools are used to evaluate the evolution of the fire, the heat flux model developed in Chapter 7 as part of this study can be used to provide the gauge heat flux to the structural elements of interest.

9.2.4. Structural modelling

With the definition of heat fluxes to the structure and resulting temperature-time relationships (uniform or spatially sensitive), a mechanical analysis may be undertaken. These analyses are only carried out for those areas defined in the initial screening processes that overlap with potential fire areas. Once again, the structural fire engineer has different tools available for this purpose ranging from simple hand calculations through to complex numerical finite element models. The choice of model depends on the level of detail to which the study takes into account together with consideration of irregular structural frames and unusual assemblies.

Initially a series of local studies to establish the behaviour of structural elements within a sub-structure assembly may define specific failure features. A global analysis of the structure would serve to validate such potential failure modes and help determine whether any individual failure can induce total collapse of the structure.

9.3. Multi-Storey Building

The application of the above methodology is applied to the case of a hypothetical multi-storey building in which potentially weak structural members are present together with potential fire compartments.

9.3.1. Structural details

The building dimensions are taken as 100m long by 43m wide and 185m in height with the footprint of the building representing that of a trapezoid. There are a total of 47 stories, with the upper 40 stories assumed as office type occupancies. The lower 7 stories comprise typical mechanical, electrical and storage rooms together with entrance lobbies. Figure 9.1 shows the numerical model representation of the building up to and including floor 15.

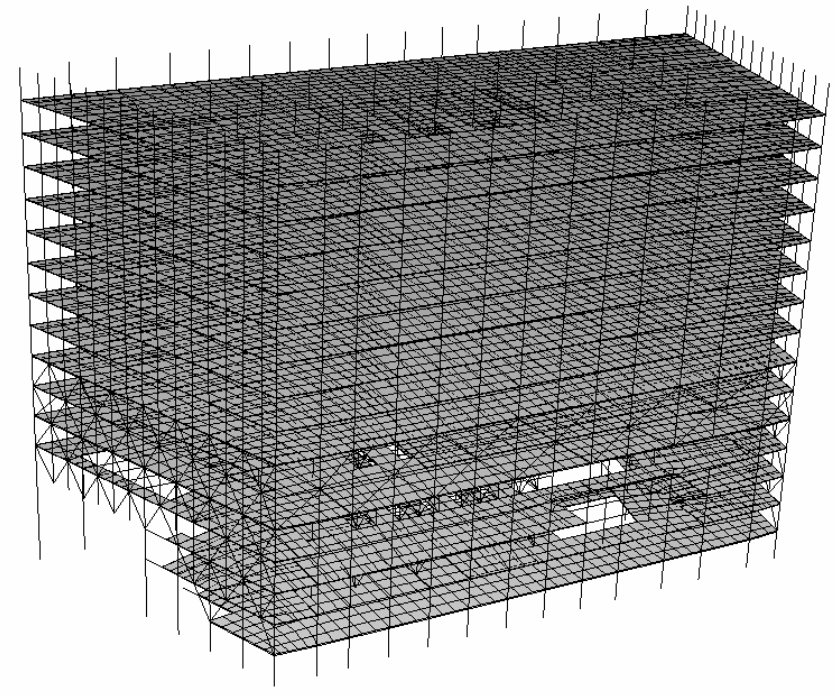

Figure 9.1: Complete numerical model of the structure used in analysis, representing the lower 15 floors of the building

A standard structural floor beam layout is adopted for floors 8 to 45 with beams generally spanning from the central core to the perimeter. Floors 1 to 8 each comprise a unique layout. The structural frame used in the numerical model is shown in Figure 9.2.

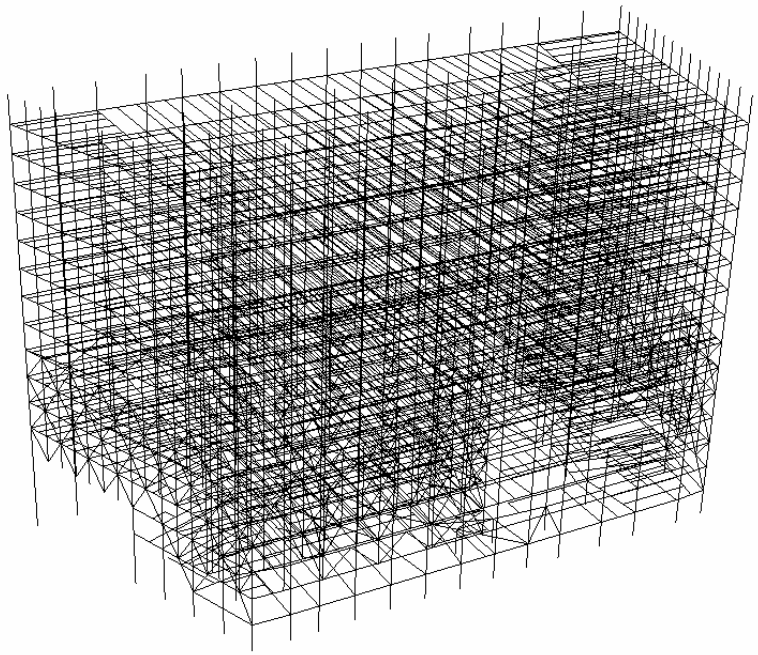

Figure 9.2: Numerical model without floor slabs to show structural frame

A total of four perimeter moment frames carry lateral wind loads and are located on each exterior wall. In addition to these, two-story belt trusses between the 5th to 7th floors and 22nd to 24th floors are incorporated to maintain structural stability. Additional trusses on the east and west elevations together with an interior braced core extend from the ground to the 7th floor.

While lower concrete floor slabs varied in thickness, horizontal shear was transferred to the core at the 5th and 7th floors by means of thick reinforced concrete slabs. Total slab depth above floor 7 was 140mm. Floors 2 and 3 have an opening on one side to form an atrium above the ground level

lobby. In addition, floor 4 had an opening on one side to form a double-height space above the 3rd floor lobby. Floor 6 has a principle opening to form a double height mechanical space at its right side.

Core columns comprise mainly large I-beam shapes ($H_p / A = 17\text{m}^{-1}$), increasing in size towards the base of the building through the use of built-up shapes.

In some locations, columns do not run continuously through the complete height of the building. In these instances, large transfer trusses are designed to take loads from the building and pass them into alternative columns and finally to the foundations. The most significant of these are three interior gravity column transfers between floors 5 and 7, shown in Figure 9.3 the location of which is shown in Figure 9.4.

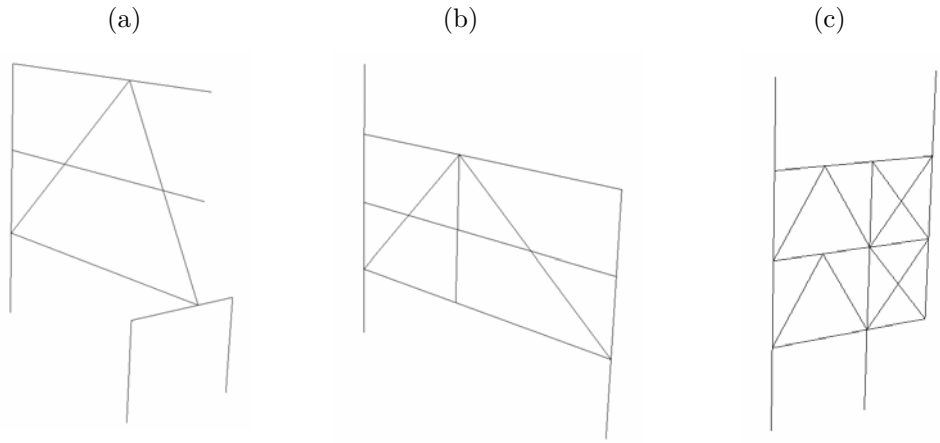

Figure 9.3: Internal truss systems of (a) Truss 1, (b) Truss 2 and (c) Truss 3. Their locations are shown in Figure 9.4.

Truss 1 supported 41 floors and transfers its load through a triangular truss system into a beam and column at the 5th floor.

Truss 2 is a single transfer located in close proximity to Truss 1. Again, loads from the upper stories of the building are transferred at floor 7 through a triangular truss, this time into two separate existing columns at the 5th floor. This truss is located within a slab opening forming the double-height room at one side of the building.

Truss 3 is a two-story transfer structure adjacent to the core but located at the opposite side of the building to Trusses 1 and 2. Loads at the 7th floor are transferred to adjacent columns.

In accordance with the methodology for assessing structural weaknesses in the building, these three truss systems are a typical example in which, were they to fail, the loads they carry may be unable to be fully redistributed with a possible result being total structural collapse. Therefore subsequent analyses are concentrated around their locations.

An examination of possible fire locations within the building reveals that a two-storey compartment is situated between floors 5 and 7 in which Trusses 1 and 2 are located. The compartment location is shown in Figure 9.4 which also shows the locations of the two truss systems and also Figure 9.5 which shows its location in terms of the floor slab. In addition these figures show that the compartment has a boundary with the perimeter of the building. At this perimeter location there is a source of ventilation which could influence the severity of a fire. The location of other possible fire compartments is not presented here as the intention is to demonstrate the application of the heat flux model in a structural application. The overlap of a potential fire compartment and a potential structural weakness completes the screening process to allow for a more detailed analysis to be focused in a specific location.

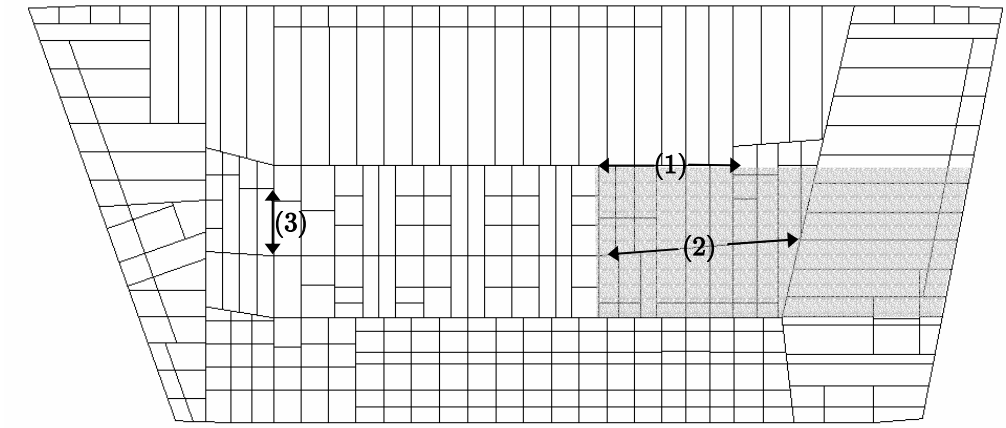

Figure 9.4: Structural beam layout of Floor 5, with Trusses 1-3 indicated. The shaded area represents the compartment fire.

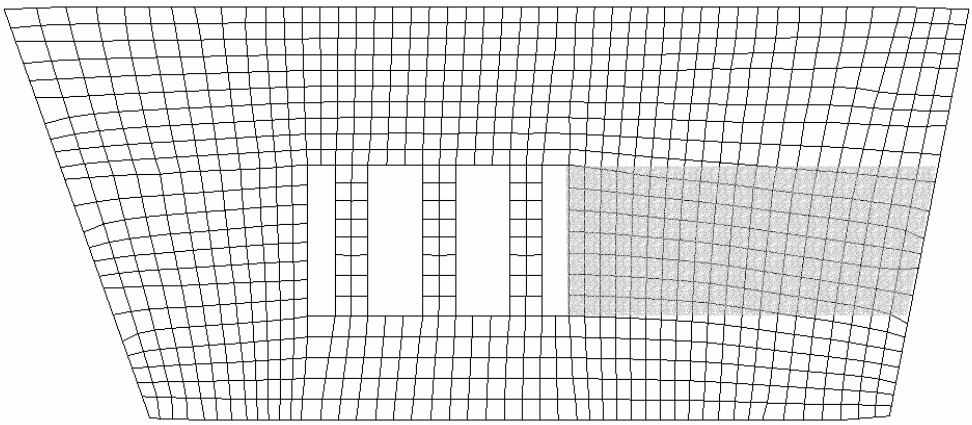

Figure 9.5: Slab mesh used for Floor 5 including core service shaft openings with the shaded area representing the dimensions of the compartment

9.3.2. Fire modelling

The fire within this compartment is modelled using FDS as shown in Figure 9.6, assuming an infinite supply of fuel, taken as a pool fire over the entire floor area. A sensitivity study including varying the ventilation and

fuel loads allowed for the identification of the conditions required to establish the most severe fire around the structural members of interest. These members are defined in Figure 9.6 as individual columns which are associated with the structural trusses outlined above. Again, the sensitivity study is not presented here as the objective is the illustration of the method of the heat transfer from the gas to the structural elements.

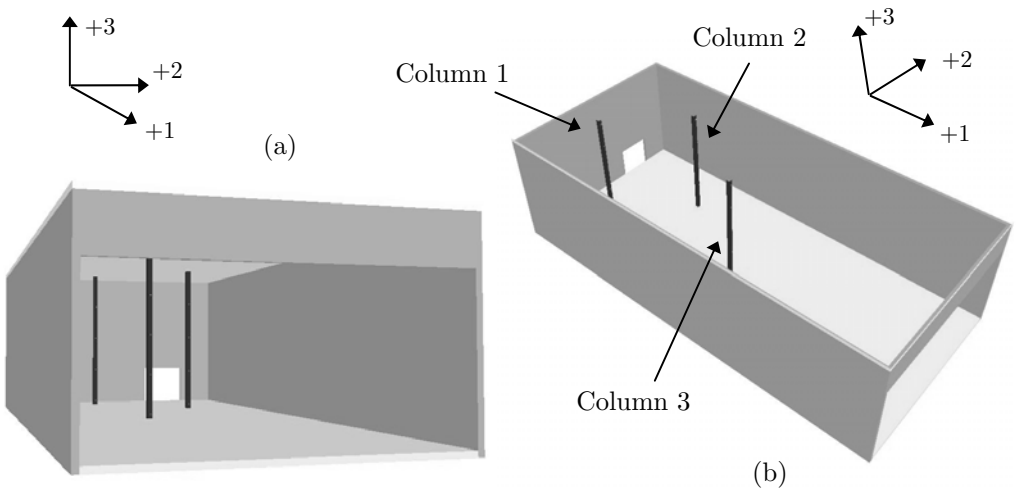

Figure 9.6: (a) FDS compartment and (b) with ceiling removed for clarity and location of columns 1, 2 and 3 indicated. In both cases approximate positive axis directions are shown.

The heat release rate in FDS is defined as a constant, with the intention of creating post-flashover conditions from the onset of the analysis. The fuel used in the model is kerosene and by assuming a pool fire covering the entire floor the intention is to simulate the leakage of a fuel pipe or the event of an intentional fire. Fuel pipes are common in buildings where power generation units are available. An infinite supply of fuel is assumed, however, the simulation time is limited to 600s during which steady-state thermal conditions in the gas-phase should be achieved. This method provides an almost steady-state fire but does not eliminate the need for

time averaging. The fluctuations of the fire as shown in Figure 9.7 provide an inherent unsteadiness that needs to be accounted for while spatial variation within the compartment is shown in Figure 9.8. The validity of the time averaging procedures was established in the previous Chapter, thus these calculations will only be used to define the time period to where structural integrity could be jeopardised.

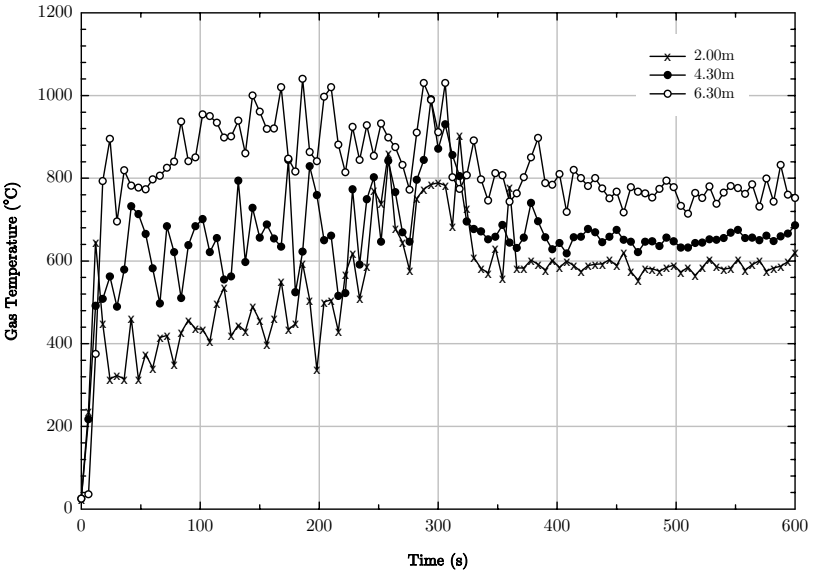

Figure 9.7: Gas temperature at with simulation time at various heights from the ground in the room in the location of column 3.

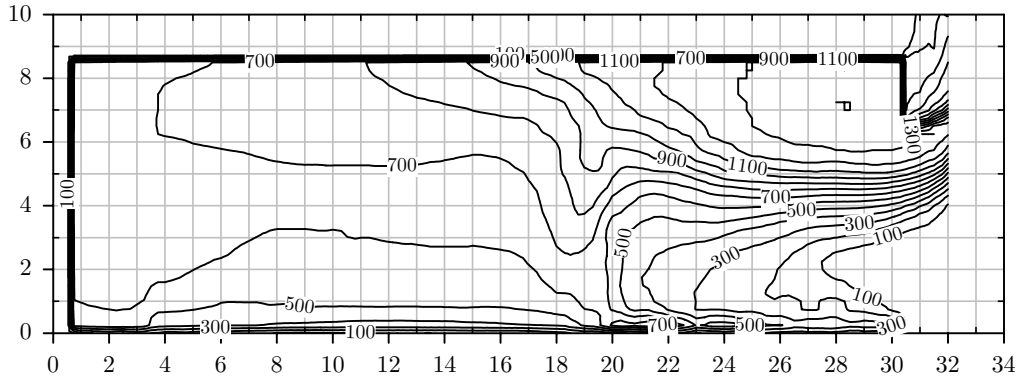

Figure 9.8: Gas temperature slice through centre of compartment from back (left) to opening (right) for t=500s. Contours are in °C while axis represent the room dimensions in m.

9.3.3. Heat transfer

The heat flux model is applied to the CFD analyses for a steel material with a characteristic heating length of 0.02m. This provides a characteristic time of 27 seconds to make the analysis more computationally efficient in terms of the averaging techniques previously discussed.

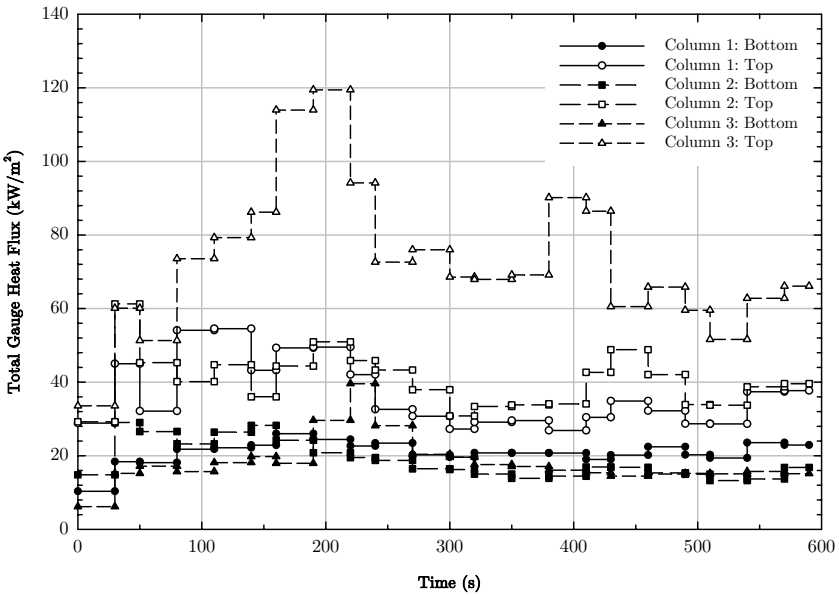

Figure 9.9: Total gauge heat flux (-2 direction) for each column at a low height (1.2m from floor) and a high height (7.9m from floor). Total room height is 8.6m.

Figure 9.9 shows the total gauge heat flux with time, in direction -2 (see Figure 9.6) at a low and high point on each of the three columns. It is clear that lower heat fluxes are found towards the base of the column, while higher heat fluxes occur at the top. This is a direct consequence of the generated smoke layer within the compartment. Additionally, column 3 is seen to experience the most severe heat flux due to the influence of the ventilation producing preferential burning in its location. As this column experiences the most severe heat flux, it provides the basis for the

following calculations, henceforth the term 'column' is taken to mean column 3 unless specifically otherwise stated. For the sake of completion, the methodology was applied to all other columns in the compartment.

The column resembles an I-section and as such, it has four distinct faces, each pointing in a different axis direction. Radiative fluxes therefore have the potential to be significantly different depending on what radiation each face can 'see'. In the case of fully-developed fires it is unlikely, but not impossible, that localised hot spots will result in different incident radiation intensities for a similar location facing different directions. It is more likely that the result of shielding of the element by some other structural form will influence the intensity. In this example, all columns are well spaced within the compartment and fully-developed conditions have been defined. This allows incident radiation on all faces to be accounted for by a single representative radiative heat flux. Figure 9.10 shows a comparison of the incident radiation on each face of the column at the same height. It is evident that neglecting the dynamic nature of the fire that creates the fluctuations in intensity, a single curve may be used to define radiation to account for all faces.

Convective fluxes are accounted for by changing the convective length scale parameter in the model. The potential variation in convective fluxes for lengths scales of 0.4m and 0.02m representing the flange width and flange thickness respectively are shown in Figure 9.11 for a low and high point on the column. The smaller length scale results in convective fluxes that are double those implied by the larger length scale. A detailed conduction study of the column cross-section would highlight further the influence of these higher fluxes on the overall member temperature, but this is beyond the scope of the present study. As such the larger length scale is adopted for further calculations.

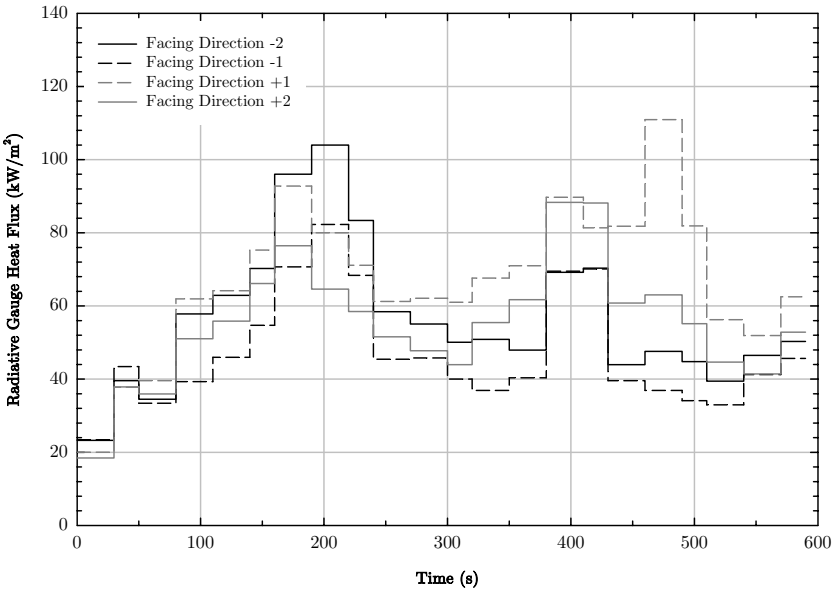

Figure 9.10: Comparison of radiative gauge heat fluxes on each face for column 3 at 7.9m from the ground

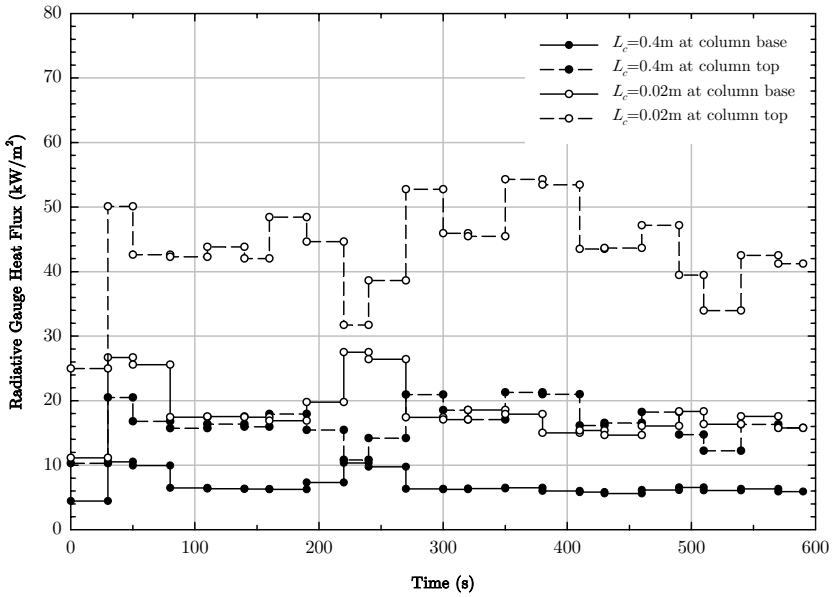

Figure 9.11: Convective fluxes with varying length scale for column 3 at a low height (1.2m from floor) and a high height (7.9m from floor)

Total gauge heat flux from the model for different heights along the column is shown Figure 9.12. Despite a constant rate of heat release in the model, the heat fluxes exhibit a rise in intensity to a peak value at about 200 seconds after which time they begin to adopt a steady-state value.

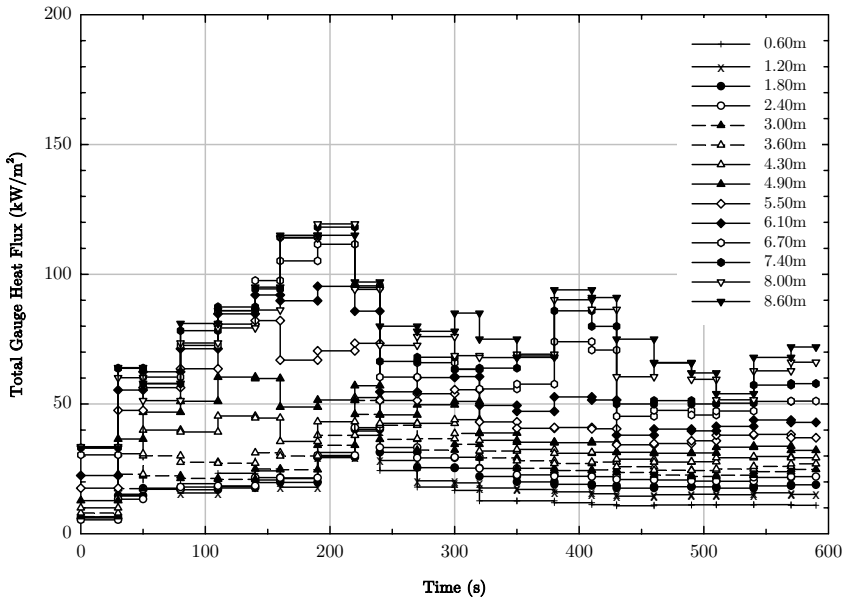

Figure 9.12: Total gauge heat fluxes on column 3 at various heights from the ground

Once a steady-state heat flux has been achieved, a single representative value for each height along the column can be defined. This has been done for all columns in Figure 9.13 highlighting further the fact that column 3 experiences the most severe fire conditions. The definition of a single heat flux allows the determination of the steel temperature evolution to be determined for different heights and this is shown Figure 9.14 for an arbitrarily long time period.

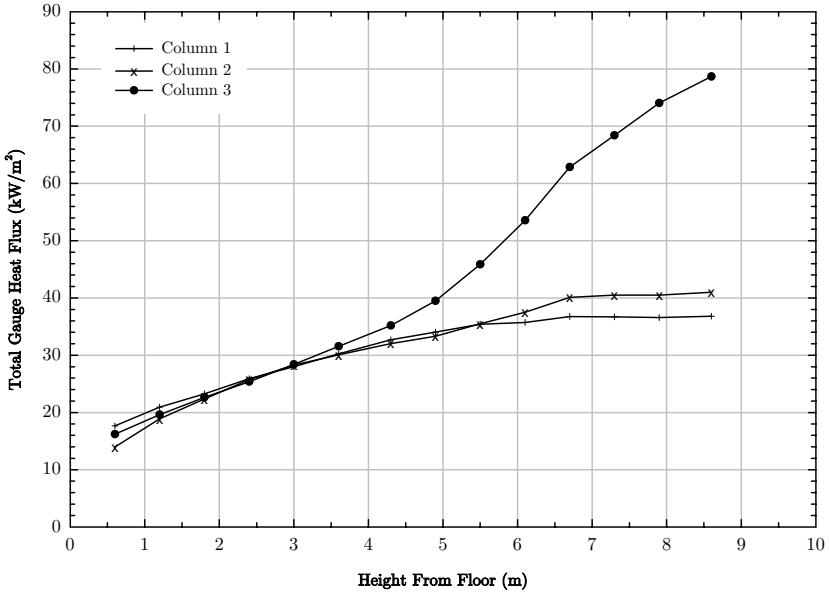

Figure 9.13: Steady-state total gauge heat fluxes for each column over its total height

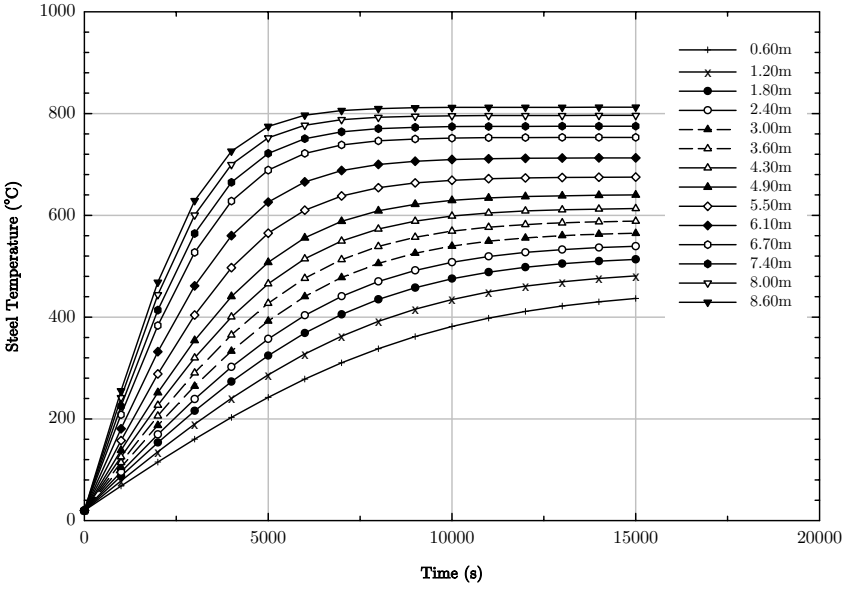

Figure 9.14: Steel temperatures for column 3 based on steady-state total heat fluxes at various heights from the ground

In general, the heating of the structural elements can be divided into two parts, a transient heating stage and a steady-state stage. It is important to note that this treatment is not necessary since a numerical code can resolve the transient problem completely. Nevertheless, for practical applications it is important to establish analytical methodologies that could enable the design engineer to concentrate on a parametric study of the different scenarios instead of investing all resources in a complete numerical analysis of the problem. In this application, the gain of a transient numerical analysis is deemed marginal, given the high thermal inertia of the structural elements, thus a simple methodology to couple the numerical simulations of the gas-phase to those of the solid-phase is developed. The time for the structural temperatures to reach steady-state conditions is established by conducting a lumped capacity analysis of the cross-section (see Figure 9.14) and defining a characteristic time as the time to reach an arbitrary limit 90% of the steady-state gas temperature as shown in Figure 9.7. This is shown in Figure 9.15 for a column height of 5.5m, taken as a representative value for the entire range of heights along the column.

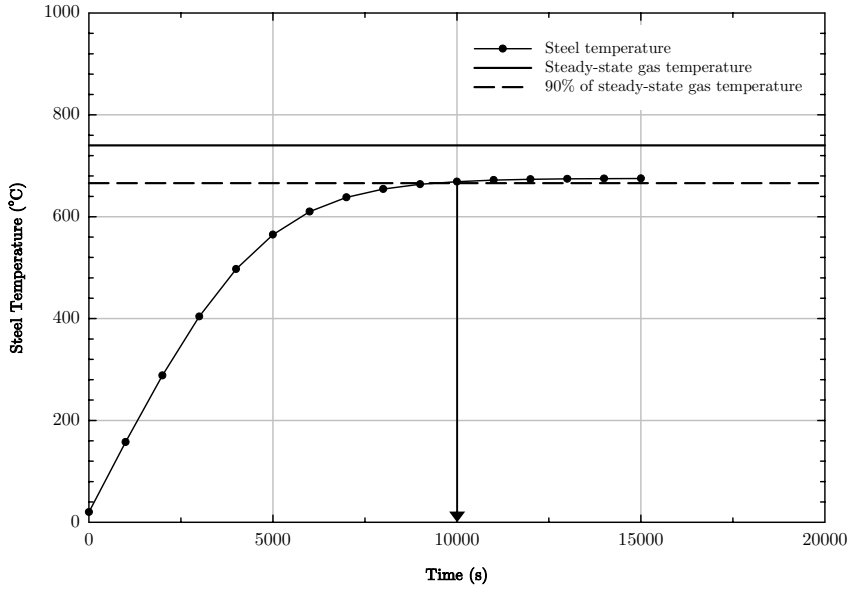

Figure 9.15: Establishment of 'transient' heating time based on a location 5.5m from the ground at column 3

The establishment of a characteristic time of 10,000s as shown in Figure 9.15 allows the transient temperature to be simplified to a linear increase to this time, after which the steel temperature is taken to remain at a steady-state value. Figure 9.16 shows the time dependent steel temperatures applied to the column for the structural analysis. The methodology outlined above can be applied to all structural elements in the compartment to quickly establish curves similar to those in Figure 9.16.

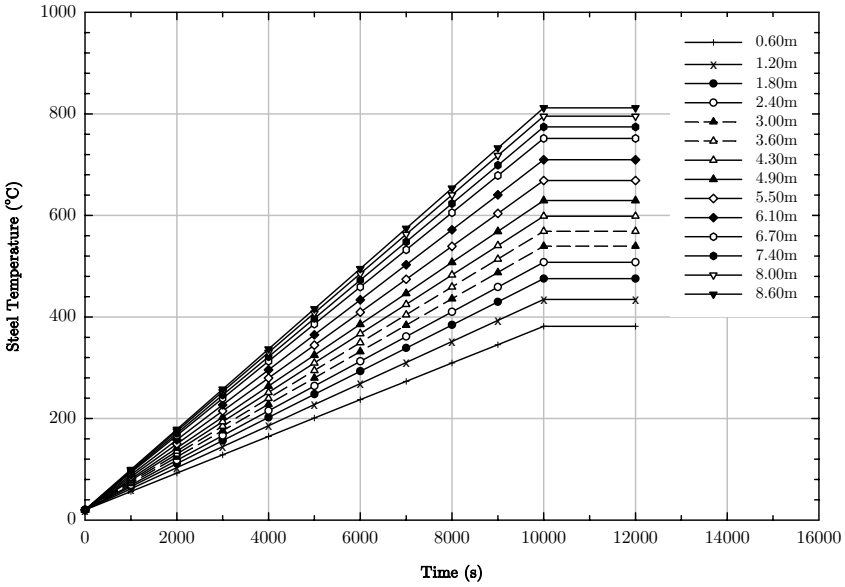

Figure 9.16: Steel temperature at various heights within the compartment where distances in the key denote the height from the ground

The heat flux model was also applied to the ceiling of the compartment where the material is taken as concrete with a conduction length of 0.2m. This results in a characteristic time of 68s, allowing very efficient computational efforts with regards to the speed of calculation in the model. Again, a steady-state heat flux can be established for all points on the ceiling, a contour plot of which is shown in Figure 9.17. For each location, a one-dimensional heat transfer can be undertaken to establish the structural temperature rise of points through the depth of the concrete

slab based on its steady-state heat flux, in a similar manner that adopted for the steel temperature.

Both the steel and concrete temperature evolutions are used as a boundary condition for the structural analysis.

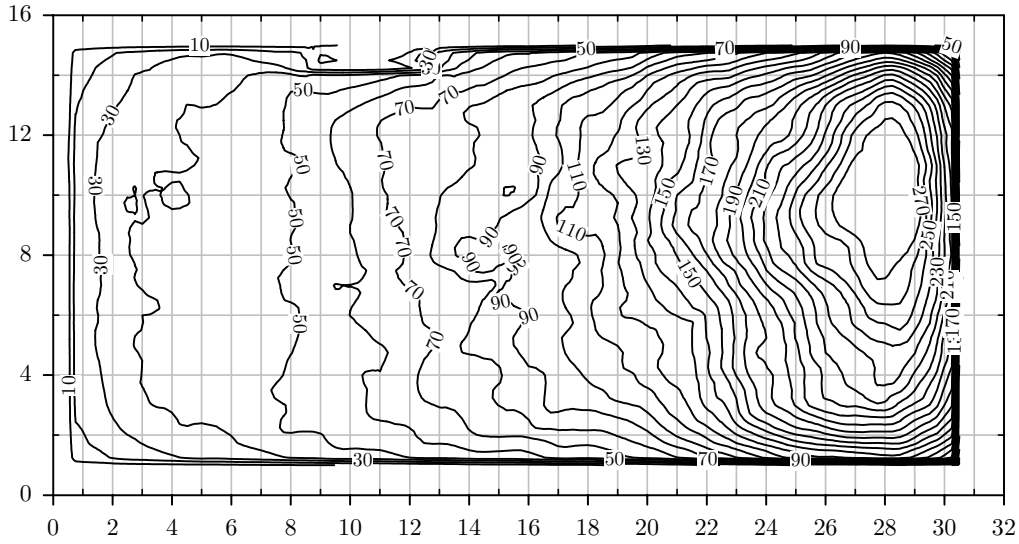

Figure 9.17: Steady-state total gauge heat flux distribution on the ceiling of the compartment. The ventilation opening is on the right of the plot. Axes represent the compartment dimensions in m, while contour lines are in kW/m^2.

9.3.4. Structural analysis

In order to understand the full structural response of the building in fire, a large computational model of the building is required. Indeed, to show the effect of localised fires in the building, this model needs to be sufficiently large to capture the force redistribution throughout the structural frame and if applicable, to ultimately demonstrate total collapse. Figure 9.1 shows the numerical finite element model used for the analyses, while Figure 9.2 depicting the structural frame highlights the level of complexity to which this model was built. Indeed the model incorporates 239,040 nodes and 87,674 elements resulting in 522,210 degrees of freedom.

As previously stated, the objective of this Chapter is to demonstrate the use of the heat-flux model in structural applications. As such, a detailed structural evaluation of the building is not included here, however, indications of its global response in fire is briefly reviewed.

The final deflected shape using the thermal inputs outlined above is shown in Figure 9.18 and for an elevation view in Figure 9.19. It is clear that a kink is forming across building in the location directly above the heated truss systems. Initial indications from this model are that areas of the structure away from Trusses 1 and 2 begin to react due to the effect of force redistribution when the trusses reach their highest temperatures and lose a considerable amount of their structural integrity. Furthermore, specific effects of the force redistribution show that the central columns across the long dimension of the building take considerably more compressive forces when this happens. Figure 9.20 shows the final deflected shapes of the three truss system, while the rate of maximum defection in the building is shown in Figure 9.21. Indeed, this shows that following the effects of thermal expansion, a rapid rate of deformation is achieved, suggesting that if the structural temperatures were to continue to rise, global failure may be the result.

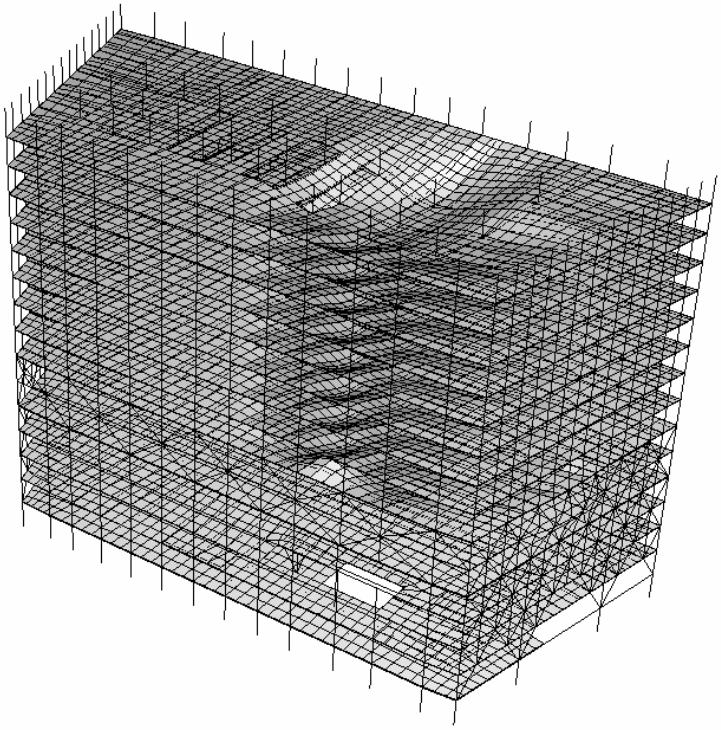

Figure 9.18: Final deflected shape (scale 3:1) of the building following heating

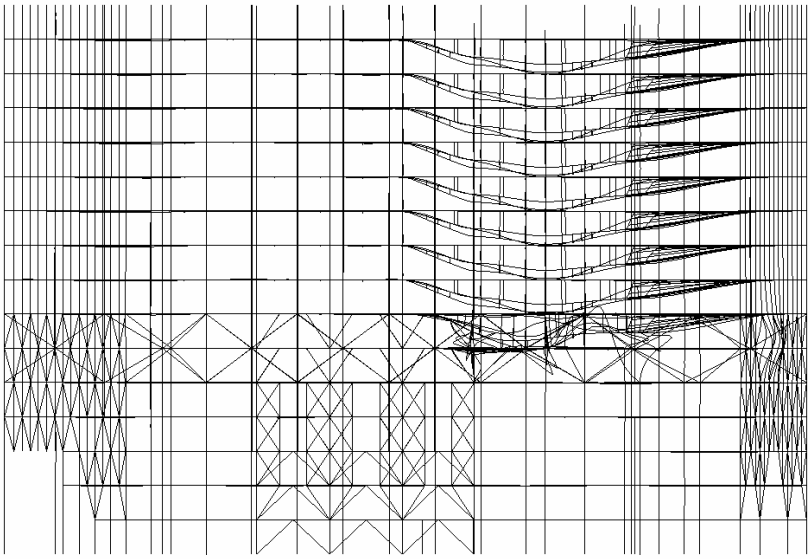

Figure 9.19: Elevation view of the deflections (scale 3:1) in the frame

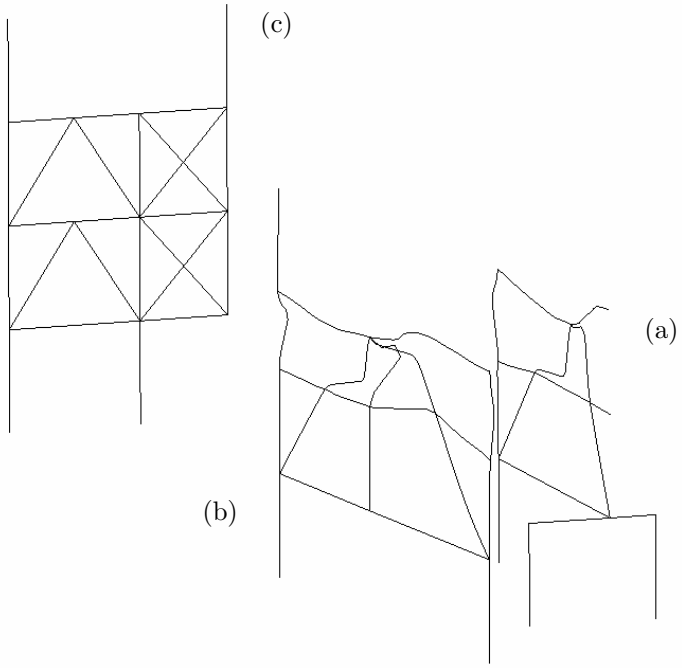

Figure 9.20: Deflections (scale 1:1) of (a) Truss 1, (b) Truss 2 and (c) Truss 3

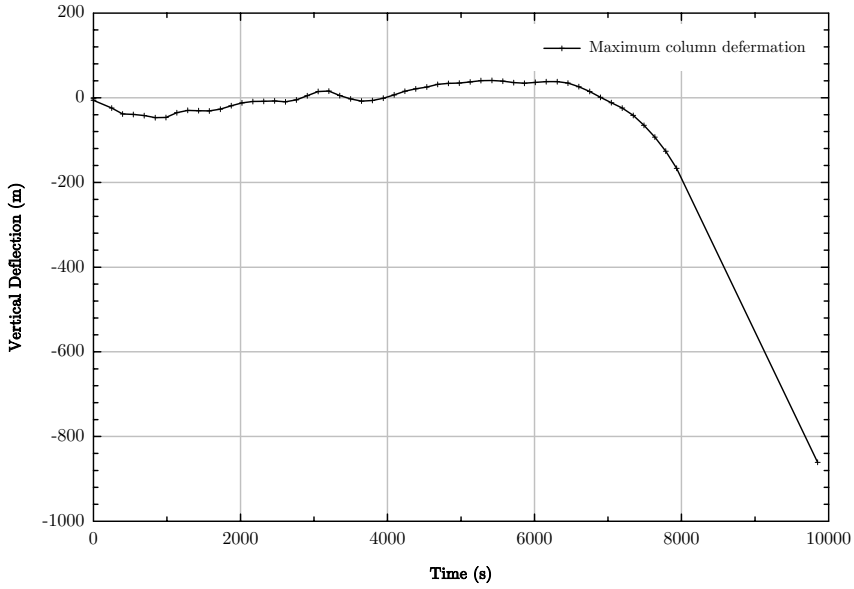

Figure 9.21: Maximum vertical deflection within the model throughout the simulation

9.4. Complex Geometry

The effect of convective length scale has been discussed in Chapter 3 and its relevance to a structural engineering application highlighted above. Figure 9.22 shows two typical long span structural systems, each with their own unique complex geometry comprising small characteristic length scales. The temperature distribution over the web of cellular beams has been investigated by Bailey [122]. The tests in his study revealed higher temperatures around the perimeter of the cells which he attributes to the 'pull-back' of the intumescent protection. It is entirely plausible however, that this increase could also be attributed to convective fluxes due to an increased flow velocity of hot gases through the cell opening, passing across the small length scale defined by the width of the web. In the same sense, the convective heat fluxes can play an important role in the heating of truss elements that can have extremely small length scales. Changes in the characteristic length scale, given the orientation of the flow, can cover a range from 'mm' (if the flow is through the cell opening or perpendicular to the truss bars) to 'cm' (if the flow is perpendicular to the flanges) to 'm' (if the flow is parallel to the axis of the beam), these changes can have a important impact on the magnitude of convective flux. Current methods to evaluate convective heat transfer may be significantly under-predicting the rate of temperature increase of such structural elements.

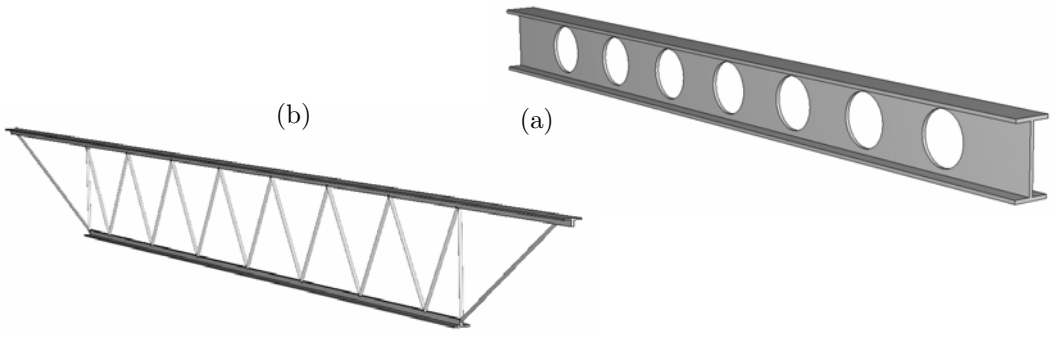

Figure 9.22: Typical long span structural systems comprising complex geometries in the form of (a) cellular holes (b) truss elements

In order to assess the structural implications of capturing the full resolution of heat flux distributions, three typical structural members are subjected to the Cardington large scale fire test exposures as defined by the heat transfer model. Each structural element is assumed to span centrally 12m from the back of the compartment to the front at roof level as depicted in Figure 9.23.

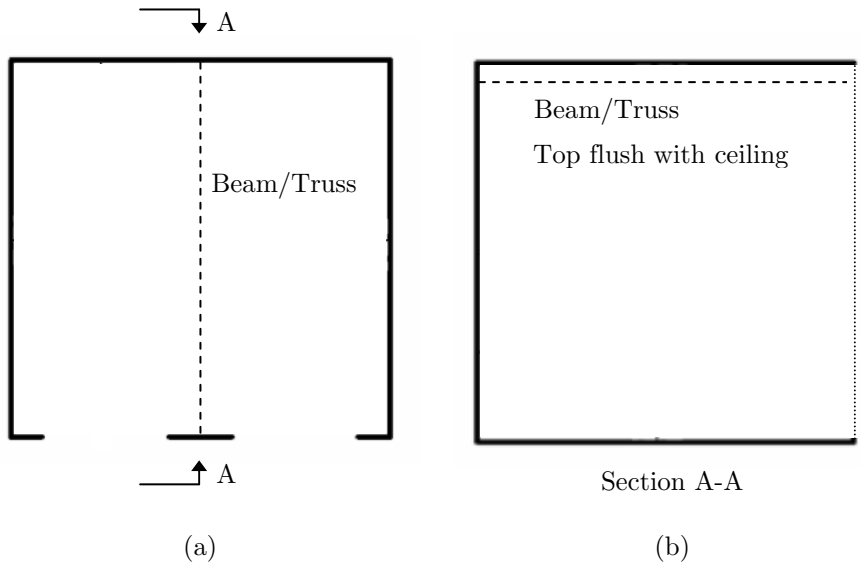

Figure 9.23: Location of structural member within the Cardington compartment (a) Plan view (b) Elevation

The three members include a truss system, a solid I-beam shape and a cellular beam, the dimensions of which are shown in Figure 9.24. In each case, a load of 10kN/m is applied to the top of the member, while each end is assumed to be pinned. Modelling a single member in this way can only give indicative results in terms of structural behaviour. A full and comprehensive assessment of behaviour would need to incorporate a composite concrete slab and realistic boundary conditions provided in the form of a more complete structural frame. Nonetheless, the intention of this study is demonstrate possible differences in terms of behaviour when a detailed resolution of the fire is considered on the structural member. For

each case, the total gauge heat flux is obtained using appropriate characteristic length scales to define the structural member geometry. These heat fluxes are in turn used to evaluate the steel temperature based on a lumped capacitance approach as defined in the Eurocodes. This method assumes that conduction through the member's thickness is negligible in comparison to the distribution along the member's length. The resultant temperature-time curves are passed directly to the finite element analysis.

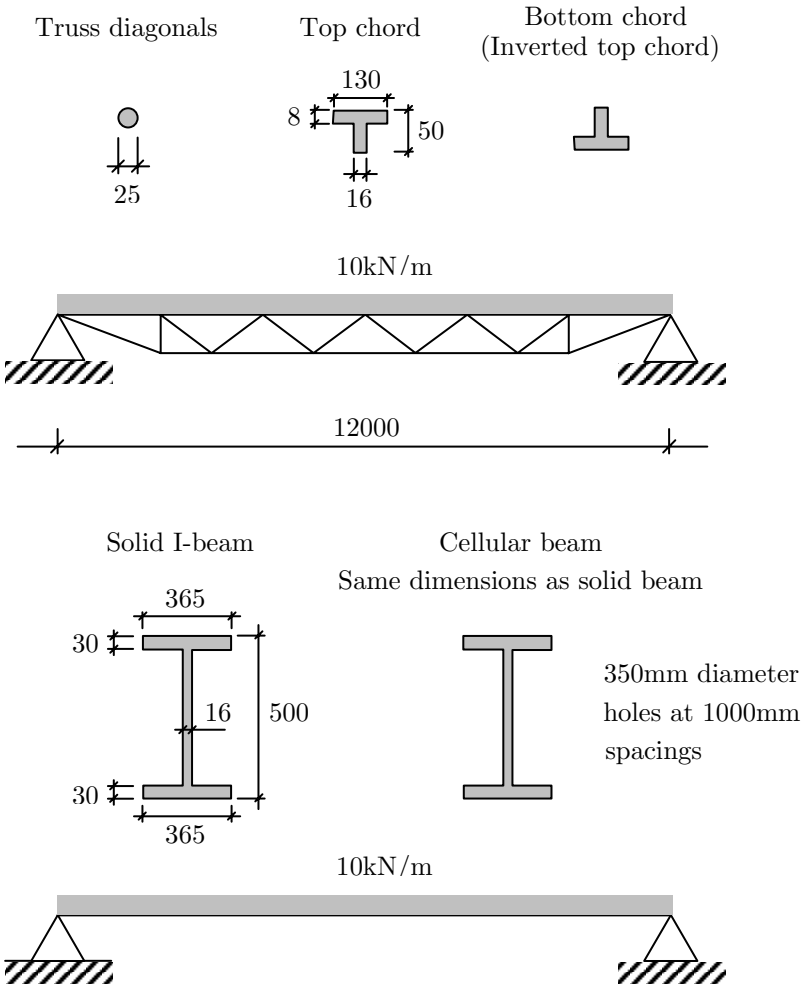

Figure 9.24: Structural members and arrangement for analysis. All dimensions are in mm. For location within compartment, see Figure 9.23.

9.4.1. Truss behaviour

The heat flux evolution of only three locations on the truss is presented for clarity. In this case, the characteristic length scale is primarily that defined by the diameter of the diagonal truss bars, specifically 0.025m in each direction. The locations of the heat flux verses time curves are presented in Figure 9.25, with the corresponding curves presented in Figure 9.26 together with a comparison of the total heat flux as defined in the Eurocode for the characteristics of this compartment.

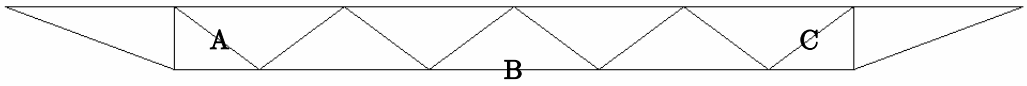

Figure 9.25: Locations on the truss for heat flux curves shown in Figure 9.26 and temperature time curves represented in Figure 9.27

The heat flux curve at each location is seen to be significantly greater than that given by the parametric fire in the Eurocodes for the period of the fully-developed fire while the decay period is underestimated by the Eurocodes. As expected the highest heat fluxes are found at the left of the element (point A) as this is at the rear of the compartment where the fire is at its most severe. There is a decay in the heat flux from left to right (towards the ventilation) opening.

The resulting steel temperature at each given location on the truss is presented in Figure 9.27. Similar trends to that of heat flux are seen in this plot, however the maximum steel temperature during the peak of the fire is seen to be under-predicted at all locations by the Eurocode approach.

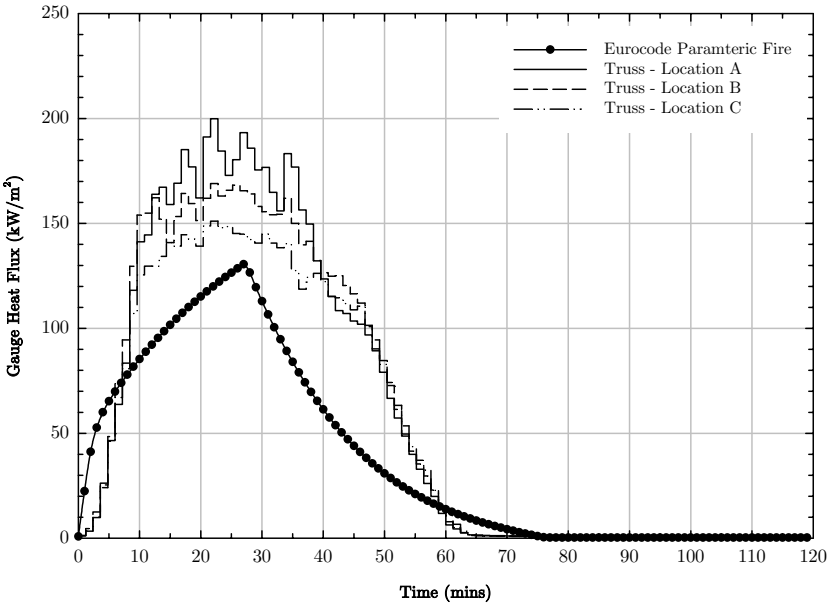

Figure 9.26: Gauge heat flux histories at locations on the truss compared with the Eurocode gauge heat flux for the entire compartment. For locations of A, B and C see Figure 9.25.

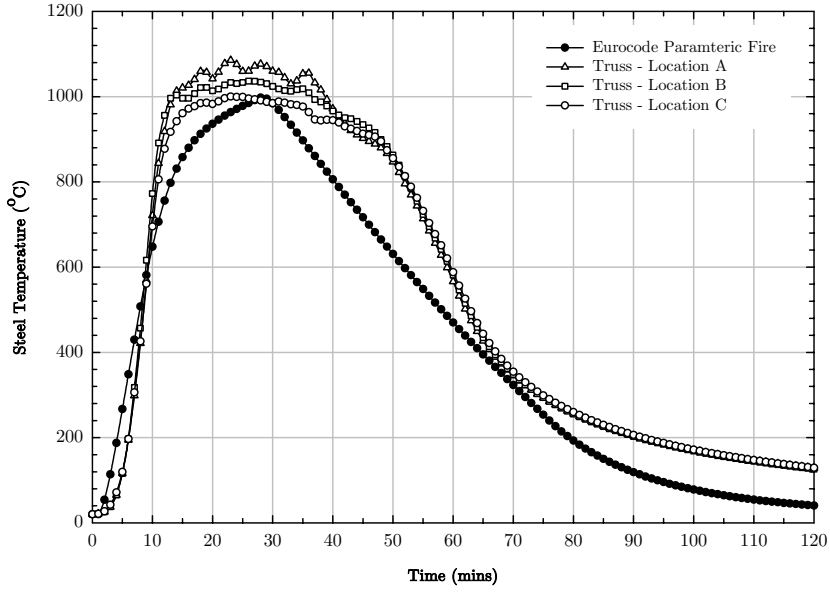

Figure 9.27: Steel temperature histories for locations on the truss compared with to the Eurocode resultant steel temperature. For locations of A, B and C see Figure 9.25.

The final deflected shape of the truss shown in Figure 9.28 after cooling for both the Eurocode and the heat flux model approach. The Eurocode method results in a symmetrical deflected shape due to its uniform heating while the heat flux model heating produces a shape with greater deflections at the rear of the compartment. It should also be noted that extreme torsional effects are seen with the heat flux method due to the higher associated steel temperatures causing greater thermal expansion.

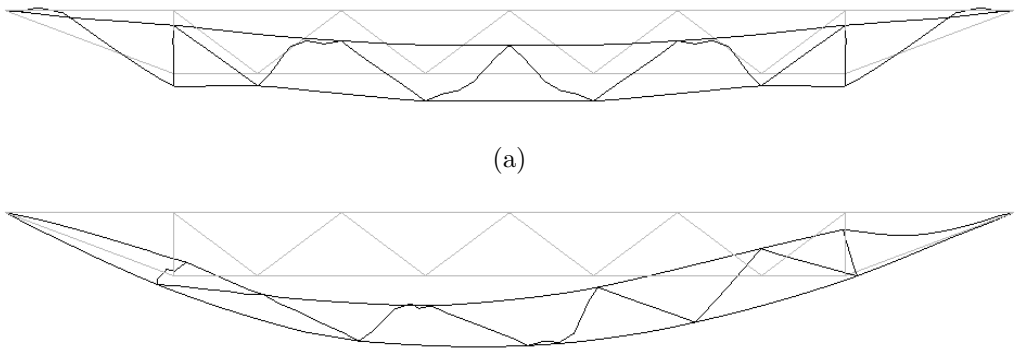

(a)

(b)

Figure 9.28: Final deflected shape of the truss after 2 hours of fire including the cooling phase (a) Eurocode heating (b) Heat flux model

The truss vertical deflection with time is presented in Figure 9.29. Using the Eurocode approach, the truss is seen to deflect downwards and then reverse its movement during cooling, however, the heat flux model results in slightly higher steel temperatures and this has a dramatic effect of inducing failure in the truss shown by the sudden vertical displacement shortly after 20 minutes from which it is unable to recover. This is also shown in terms of lateral connection forces in Figure 9.30 whereby following initial loading and thermal expansion, the heat flux model produces comparatively little lateral force as the majority is carried by the vertical component.

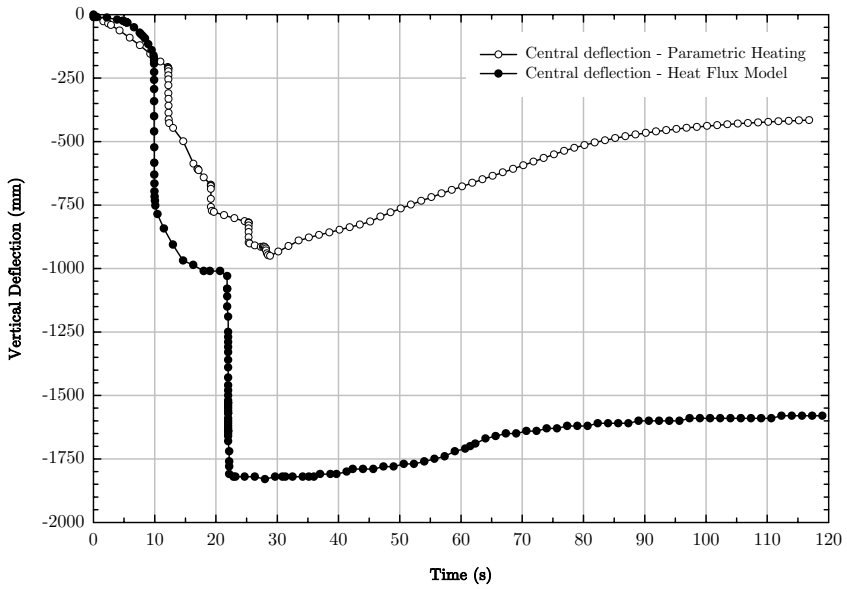

Figure 9.29: Mid-span vertical deflection of the truss throughout the duration of the fire comparing uniform heating with spatially resolved heating

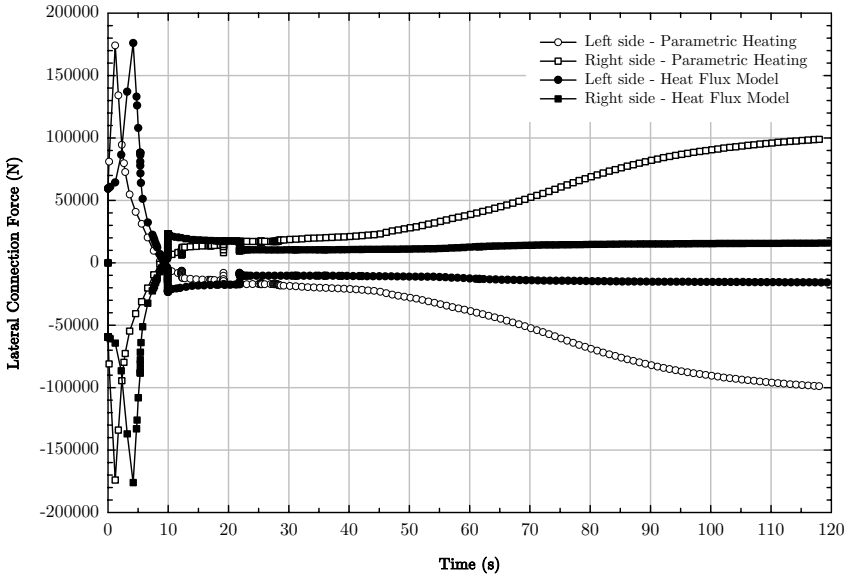

Figure 9.30: Lateral (horizontal) force experienced by the connections at either end of the truss for uniform heating and spatially resolved heating

9.4.2. Solid I-beam

Again, only three points are shown for clarity on the structural member; in this case, a solid I-beam. The locations are shown in Figure 9.31 and for each of these the convective length scale was taken as 0.4m to account for flow against the web of the beam.

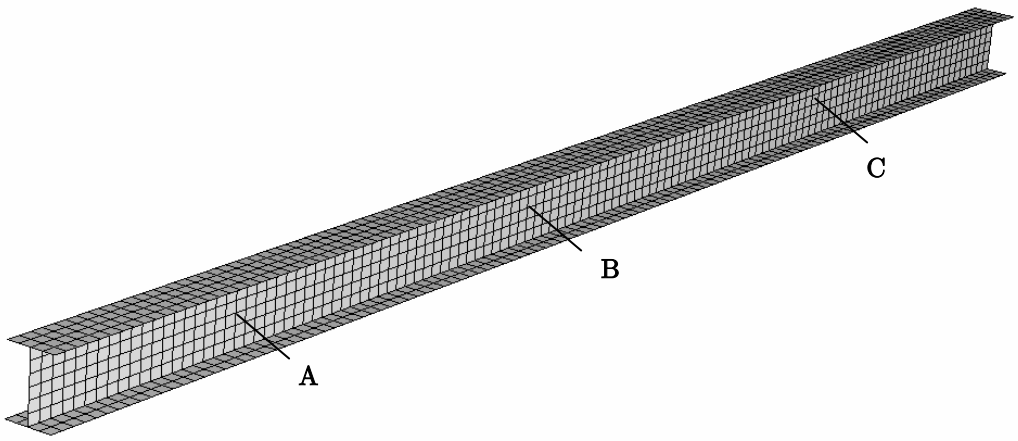

Figure 9.31: Locations on the I-beam for heat flux curves shown in Figure 9.32 and temperature time curves represented in Figure 9.33

The total gauge heat flux evolution of the three locations on the beam is presented in Figure 9.32. During the peak of the fire, the Eurocode is seen to both under-predict and over-predict the heat flux model output depending on location along the beam. As has been discussed in previous sections, the Eurocode does not predict either the duration of the fully developed fire or the decay phase with sufficient accuracy. The errors associated with the heat flux definition are less pronounced for the structural steel temperature, with the peak temperatures in Figure 9.33 reasonably well captured by the Eurocode, although not their duration or that of the decay period. Again, it is clear that there is a variation in temperature evolutions along the length of the beam that would normally be neglected by the Eurocode approach.

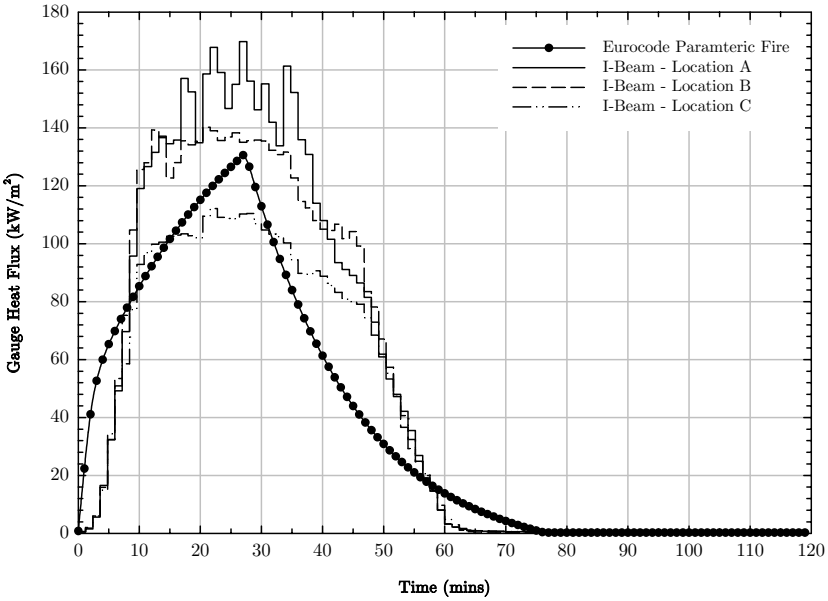

Figure 9.32: Gauge heat flux histories at locations on the I-beam compared with the Eurocode gauge heat flux for the entire compartment. For locations of A, B and C see Figure 9.31.

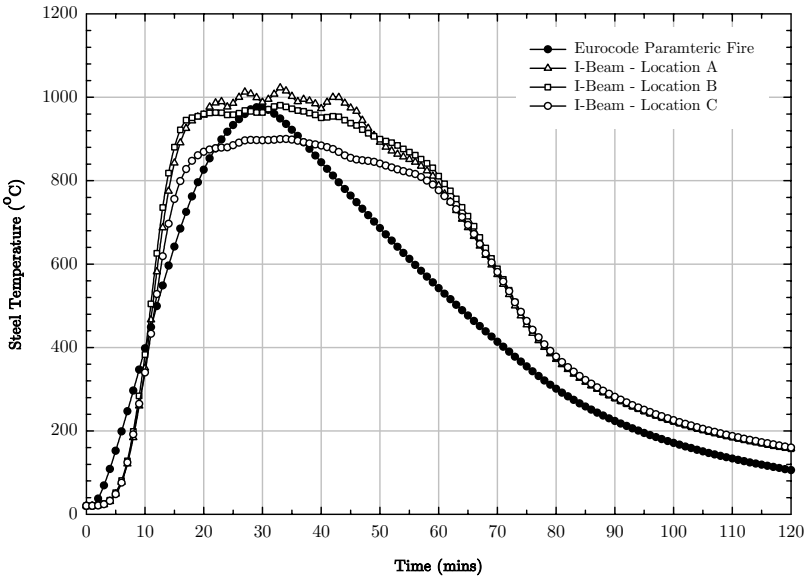

Figure 9.33: Steel temperature histories for locations on the I-beam compared with to the Eurocode resultant steel temperature. For locations of A, B and C see Figure 9.31.

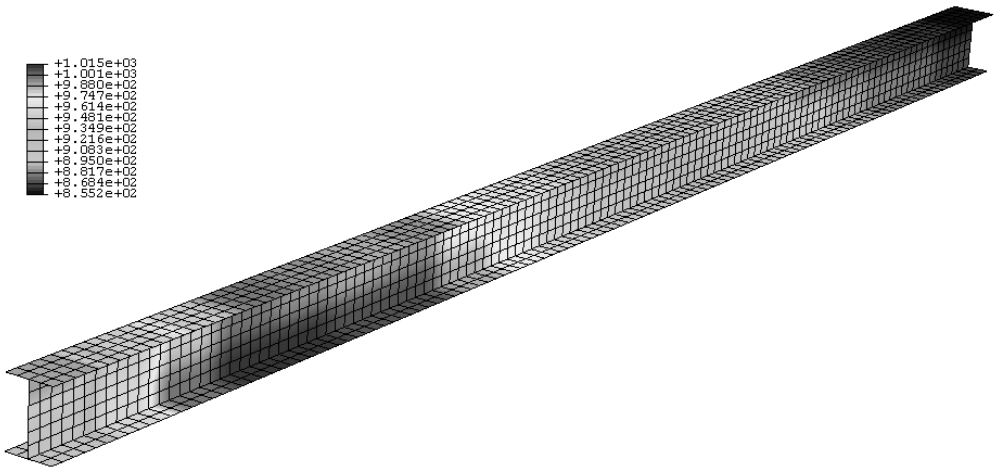

Figure 9.34: Temperature contours (°C) on the I-beam during the fully-developed fire period, 35 minutes into the fire

The contour plot of temperature variation over the I-beam is shown in Figure 9.34 for a single instance in time during the fully-developed fire period. It shows a hot spot towards the left end of the beam (rear of compartment) with a temperature difference of approximately 150°C from the between the hottest and coolest parts of the member.

The mid-span deflections of the I-beam are presented in Figure 9.35. This plot shows that greater deflections are the result when the Eurocode fire provides the thermal input. The lower deflections given by the heat flux model are a direct result of the effects of localised heating. While Figure 9.33 shows location A to have a peak temperature in excess of those predicted by the Eurocode, the majority of the beam experiences temperatures lower than the Eurocode prediction and therefore the effects of thermal expansion and material degradation are less pronounced. This has further implications in terms of lower peak lateral connection forces experienced by using the detailed fire resolution as shown in Figure 9.36.

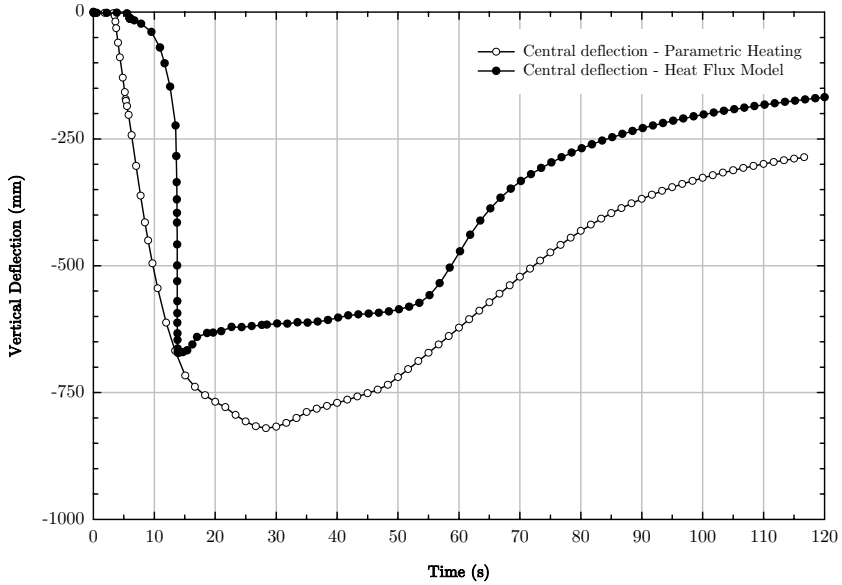

Figure 9.35: Mid-span vertical deflection of the I-beam throughout the duration of the fire comparing uniform heating with spatially resolved heating

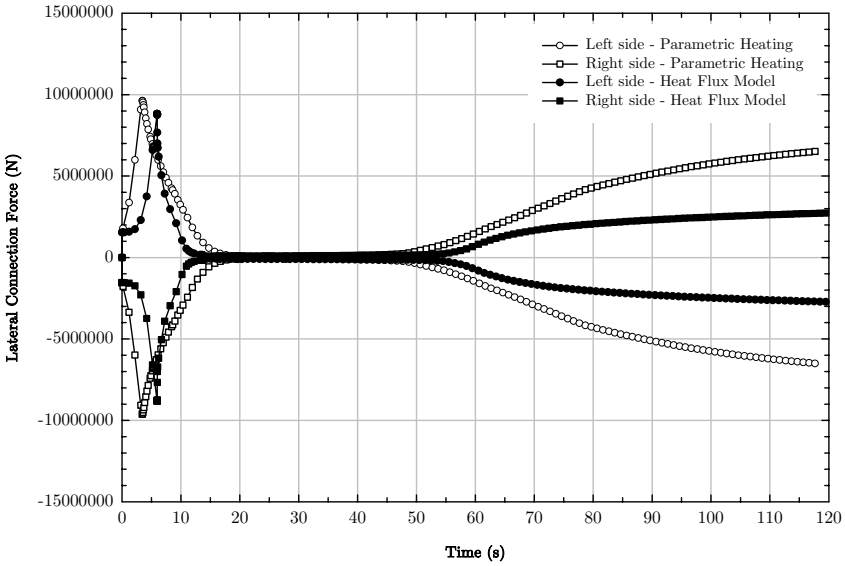

Figure 9.36: Lateral (horizontal) force experienced by the connections at either end of the I-beam for uniform heating and spatially resolved heating

9.4.3. Cellular beam

The cellular beam in this application is simply the I-beam from the previous section with the addition of the cells in the web. The reason for analysing this type of structural member is due to the potentially high convective heat fluxes that may be present around the perimeter of the cells when the flow of gases passes over their thickness. Figure 9.37 shows three locations that are examined in terms of heat flux and temperature.

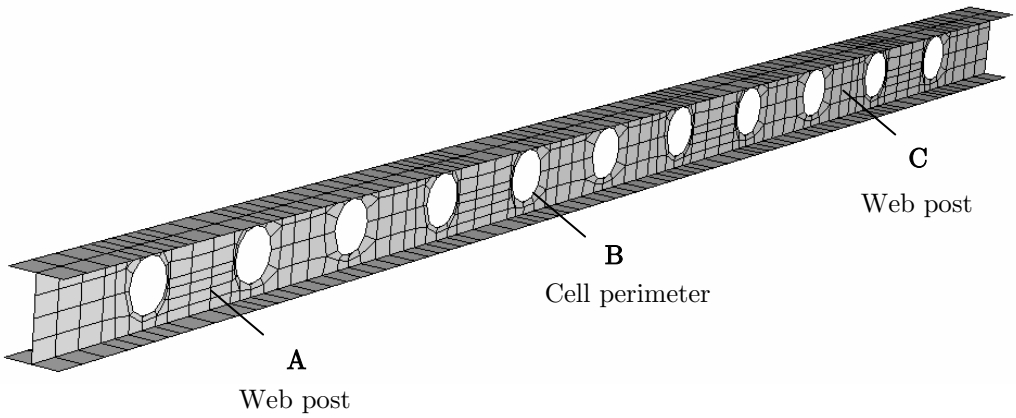

Figure 9.37: Locations on cellular beam for heat flux curves shown in Figure 9.38 and temperature time curves represented in Figure 9.39

The heat fluxes from the three points are shown in Figure 9.38 together with those expected by using the Eurocode approach. Curves A and C in this case are identical to A and C for the I-beam as the convective length remains the same. Point B on the cellular beam however, represents a typical location on the perimeter of a cell opening. The characteristic length scale associated with this point is 0.016m which as the plot below shows, results in a high total heat flux with a longer duration in comparison to the other points due to the convective fraction.

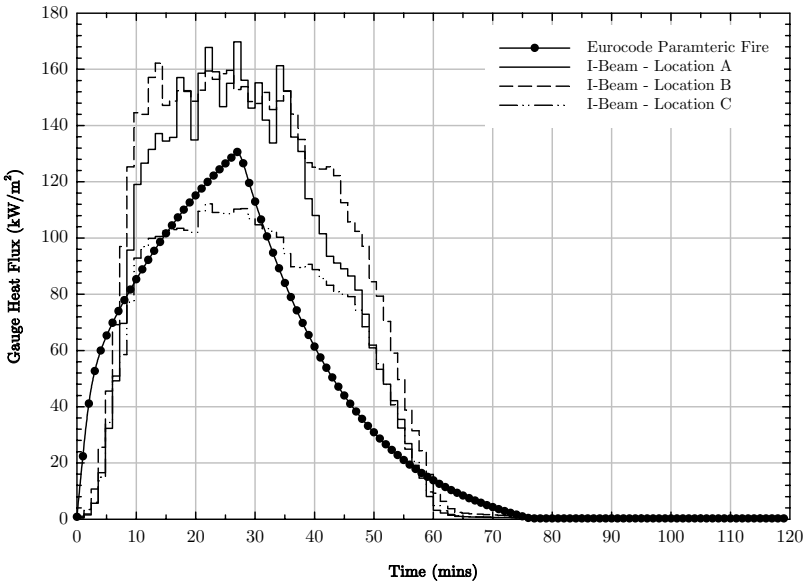

Figure 9.38: Gauge heat flux histories at locations on the cellular beam compared with the Eurocode gauge heat flux for the entire compartment. For locations of A, B and C see Figure 9.37.

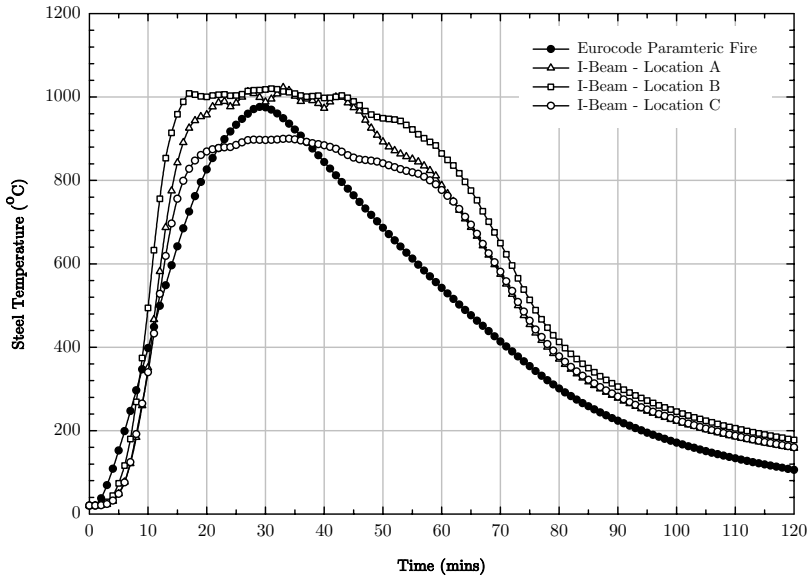

Figure 9.39: Steel temperature histories for locations on the cellular beam compared with to the Eurocode resultant steel temperature. For locations of A, B and C see Figure 9.37

The steel temperature histories in Figure 9.39 show that the perimeter of the hole (location B) heats at a faster rate and to the highest value in comparison to the other points. A variation along the length of the beam remains evident. The influence of the heating around the perimeter of the cell openings is apparent when the temperature contours over the structural member are considered, as in Figure 9.40. A temperature difference of 150°C is found distributed over the member although cell perimeters are distinctly hotter.

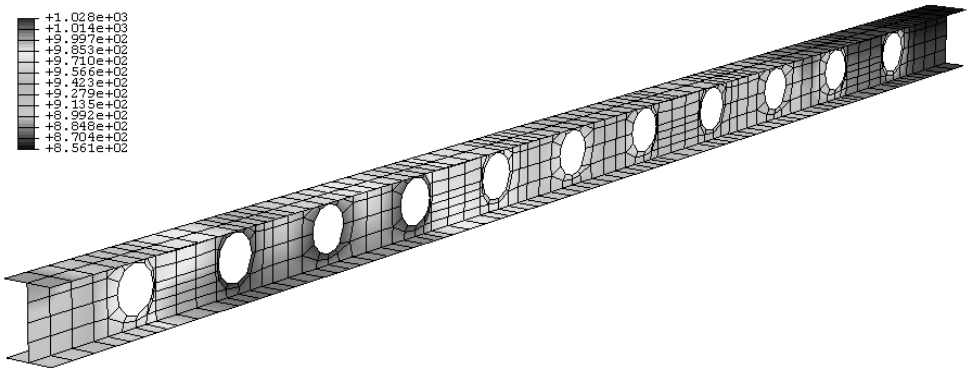

Figure 9.40: Temperature contours (°C) on the cellular beam during the fully-developed fire period, 35 minutes into the fire

Although the only difference between the I-beam model and the cellular beam is the introduction of the holes, Figure 9.41 shows that the increased temperatures around their perimeters can have a marked effect on the load carrying capacity of the beam. The mid-span central deflection for the heat flux model thermal input shows a more severe behaviour compared to the Eurocode temperatures indicating the potential that localised heating effects may cause. The overall increased web heating due to the effect of the holes in comparison to the I-beam results in greater thermal expansion and therefore greater lateral connection forces as shown in Figure 9.42.

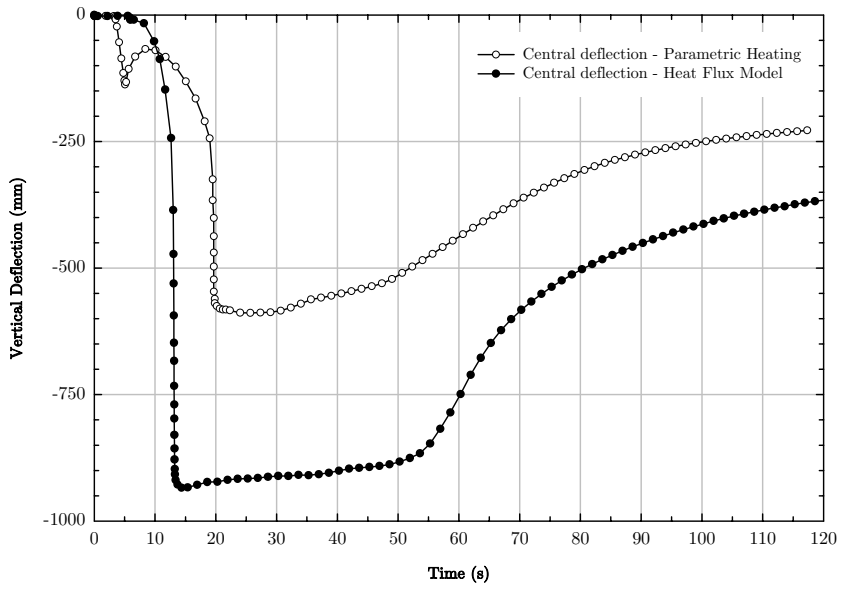

Figure 9.41: Mid-span vertical deflection of the cellular beam throughout the duration of the fire comparing uniform heating with spatially resolved heating

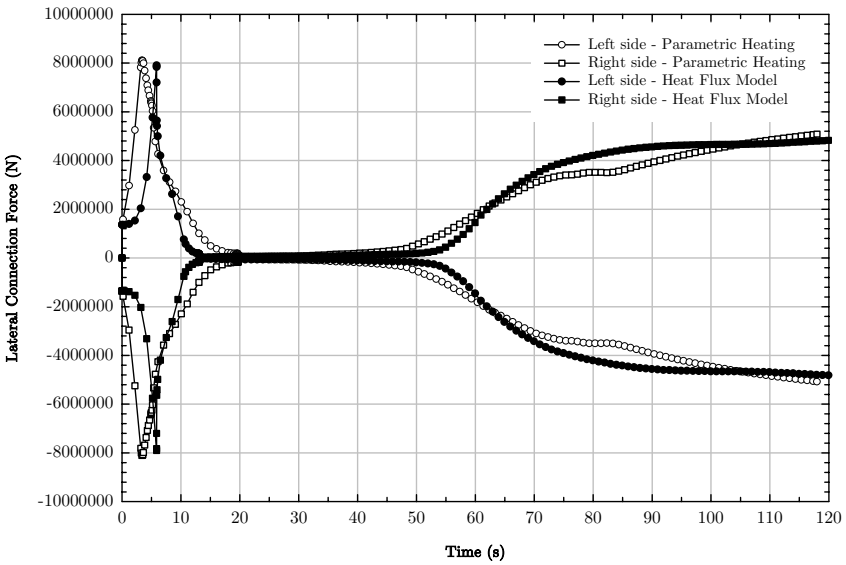

Figure 9.42: Lateral (horizontal) force experienced by the connections at either end of the cellular beam for uniform heating and spatially resolved heating

9.5. Summary

The use of the heat flux model has been presented in the context of a structural fire engineering application. The methodology to undertake the structural fire analysis is illustrated by a large hypothetical multi-storey building that incorporates potential structural weaknesses and potential fire areas. Detailed modelling of the possible anticipated worst case fire scenario is achieved through a parametric study in which fuel loading and ventilation are variables. The heat flux model is used to evaluate convective, radiative and total gauge heat fluxes from which a methodology to evaluate the structural temperature evolution is described. The structural temperatures are in turn passed into a structural analysis to evaluate the performance of the building in fire, which indicates a potential global failure mechanism in the lower floor force redistribution structural systems.

The method of characteristic times is shown to provide computational speed-up in the calculation of the heat fluxes, while the range of convective heat fluxes for a specific structural member are highlighted.

The issue of under-predicting convective heat fluxes is illustrated in terms of structural members with complex geometries for which current methods in structural fire safety design could potentially result in non-conservative solutions.

The heat flux model methodology of defining structural thermal input has been applied to three structural members incorporating small length scales and complex geometries, namely a truss, an I-beam and a cellular beam. Each member was exposed to a realistic fire defined by that of the Cardington large scale tests allowing full spatial and temporal resolution to be captured. A comparison against the thermal input as defined by the Eurocode provided the basis to undertake a mechanical analysis. In the

case of the truss, the small length scales associated with the truss diagonals resulted in high convective heat fluxes that ultimately relate to higher steel temperatures with the impact being failure of the truss. An interesting comparison was observed in the case of the Eurocode thermal input, where the truss was found to behave well. The I-beam was found to behave better during the heat flux model thermal input than the Eurocode input despite higher heat fluxes and temperatures being seen at locations along the beam. The improved behaviour was attributed to localised heating effects in that the majority of the beam experienced a thermal exposure lower than that of the parametric fire. The cellular beam behaved worse with the heat flux model definition in comparison to the parametric fire. This is attributed directly to the effects of the increased convective heat fluxes around the perimeter of the cell openings resulting in higher temperatures along the web in comparison to the solid I-beam.

This study has demonstrated that it can be important to capture the proper resolution of the fire over the geometry of a structural member. The current method of assuming a uniform fire exposure may under-estimate or indeed over-estimate the structural integrity of the element.

Chapter Ten

10. Conclusions and Further Work

10.1. Introduction

This research has been diverse and wide ranging. It has covered in detail all areas necessary to determine the heat fluxes imposed by fire on structural elements with the aim to use them as boundary conditions in structural mechanical analyses. Methods of generating the fire environment and its evolution have been reviewed from simplified approaches through to complex numerical methods. Current methods implicit in the determination of surface heat fluxes have been reviewed with focus given to characteristic extinction distances, gas temperatures, velocities and length scales found in post-flashover compartment fires. A review of the heat transfer mechanisms associated with convective and radiative transfer has been undertaken together with a parametric study of each to define the importance of their underlying parameters on the magnitude of the generated heat fluxes. A study of the typical characteristic heating time-scales of solids with respect to those of the gas-phase demonstrates the ability to average structural heat fluxes over large time intervals. The preceding studies provided the background for the development of a model to determine surface heat fluxes to structural elements based on CFD simulations of a post-flashover fire. The model ephasises spatial resolution of heat flusex averaged over adequate periods of time. This model was then validated against one of the Cardington Large Scale Fire Tests before being applied to hypothetical multi-storey building to demonstrate its applicability to design scenarios. The purpose of this chapter is to summarise and appraise the conclusions of this research. Suggestions for possible further work are also made.

10.2. Summary and Conclusions

This work has provided a means by which surface convective, radiative and total heat fluxes can be evaluated on a structural member based on a CFD fire environment. The spatial distribution is fully accounted for over the member and provides the input for a structural thermal analysis to be undertaken. This method allows a more precise evaluation of the structural response that can properly incorporate a realistic fire scenario. This is in direct comparison to the current methods that assume a spatially uniform temperature-time curve to represent the fire which may be a very severe assumption and result in uneconomical (or non-conservative) design solutions. In addition, the ability to predict the spatially resolved heat fluxes may highlight areas where local heating may be more detrimental to structural behaviour than uniform heating.

The advantage of this work is that the structural member does need to be directly modelled within the CFD analysis. The CFD grid sizes required to define elements of the structure and to properly model heat transfer would need to be of a very small scale and thus, the simulation time and resources required could be extremely demanding. The simple method of the heat flux model enables structural elements to be analysed very quickly without the need to re-run the CFD code.

Both designers and researchers alike can make use of this work in defining realistic thermal responses of structures. The advantage this can bring is an increased understanding in terms of structural behaviour due to the effect of localised heating. An increased understanding in this area can lead to more economical design solutions through the ability to refine the fire protection measures applied, for example; refined location of insulation materials or localised increases in structural member capacities.

Some of the key summary points and conclusions raised by this work are highlighted by the bullet point list below: -

- It is well known that large spatial temporal variations can occur within a compartment during post flashover conditions, yet for the purpose of structural analysis, fires are assumed to follow a single temperature-time curve to represent the average gas temperature in the compartment. It is only by using compartment fire models such as CFD tools that the detailled temperature/heat flux distributions can be captured.

- Structural temperatures are often determined using simplified approaches, many of which are based on a single temperature-time curve to define the thermal environment. Their use is therefore limited by the design fire adopted for the compartment of interest.

- The Eurocodes adopt a lumped capacitance approach in which the net heat flux is calculated assuming a constant emissivity representing the thermal environment account for radiation, while a constant heat transfer coefficient accounts for all possible convective heat fluxes.

- Field fire models allow for time and spatially varying characteristics to be accounted for. However, the combustion and soot models employed in CFD tools are generally sensitive to the burning conditions of solids within the compartment and their ability to provide reasonable predictions under fully developed fire conditions remains largely untested, mainly due to a lack of appropriate test data. Indeed, common validations rely on simple comparisons with temperature measurements that may be decades old. This study has not focused on the development of improved CFD tools but on

a model to post-process their output. Thus the accuracy of the present modelling approach is defined by the accuracy of the CFD tool used as input.

- The convective heat transfer coefficient is largely independent of gas temperature, but has strong dependencies on length-scale and velocity. Different correlations are available for different geometries, however, for individual velocities, a single curve-fit can be applied to all correlations. The overall result is that the heat transfer coefficient can be evaluated with knowledge of the length-scale over which the gas is flowing and the velocity of the flow itself. The length scale being a defined geometrical variable and the local velocity the output of the CFD tool.

- Radiative intensities on structural elements can be evaluated with knowledge of the gas emissivities and temperatures of the local products of combustion. The mixture emissivities are defined by the extinction coefficients which are in turn defined by the localised concentration of soot or the soot volume fraction. Knowledge of the extinction coefficient and an acceptable level of error in the calculation of radiative intensity allows for a limit in the path length through the products of combustion that needs to be considered.

- A study of the characteristic heating time-scales of different solids allows a time interval for different materials to be defined. Between these time periods, heat fluxes can be averaged without loss of accuracy. This conduction study in terms of thermal thickness, allow transient environments to be transformed into quasi-steady-state conditions to simplify the analysis into a summation of a series of steady-state solutions.

- A simplified heat transfer model is developed with its principles based on the outcomes of the convective and radiative heat transfer studies. The model acts as a post-processing tool for any CFD model and captures the full spatial resolution of the gas environment. The model can account for any structural member and any complex geometry expressed in terms of a characteristic length scale. The aim of the model is to act as an intermediary stage between modelling of the fire and modelling of the structure.

- Validation of the model was conduted using the Cardington Large Scale Fire Tests.

- The availability of test data in post-flashover fires is extremely limited. It has been shown using the Cardington Large Scale Fire Tests, that given a limited set of temperature measurements, it is possible to reconstruct entire true gas temperature fields within the compartment by taking into account interactions between the temperature measurement device and the local environement. The resolved temperature fields allow for the creation of radiative intensity distribution maps on all surfaces of the compartment. This methodology has been used to generate experimental data to establish information on the spatial distribution of radiative fluxes during a fully-developed fire. Additionally it provides data against which computer models can be validated.

- The Cardington Large Scale Fire Test study showed that during the post-flashover stage of the fire, significant variations in radiant intensity were observed on all compartment boundaries with the highest values recorded on the ceilings. Walls of the compartment experienced fluxes in the range 60-220kW/m^2, while the ceiling

experienced severities ranging from 40-270kW/m^2. In both cases regions of peak flux were clearly defined and could be seen to migrate towards the back of the compartment during the fully developed period. These observations validate the need for spatial resolution and adequate time averaging.

- The vast spatial thermal severities and temperature variations observed in the Cardington Large Scale Fire Tests were shown to be hidden when the concept of an average compartment temperature was used. The net result is that all temperature errors cancel, as would be expected due to the conservation of energy. By using an average compartment temperature, a flux gradient of more than 100% is lost within the compartment. This highlights just how misleading an average temperature approach can be.

- The heat flux model is then validated against the data set generated by the Cardington Large Scale Fire Tests. The input used was an FDS simulation that was deemed to provide consistent results with the experimental measurements. FDS did not produce a perfect representation of the compartment, nevertheless, minimisation of the errors of the CFD was considered unnecessary and beyond the scope of this work.

- The total imposed heat fluxes predicted by the model compare very well to the results predicted by the detailed heat flux calculations conducted by FDS, especially for regions deep in the smoke layer, which is the scenario for which it has been developed. This good comparison is to be expected as there as no geometrically complex structural members within the compartment used for validation. Complex geometrical items will have local, but important, effects on the convective heat flux.

- The validation exercise of the heat flux model relies on the validity of FDS in post-flashover conditions. In some locations on the compartment walls, heat fluxes are predicted well, but in others there is a poor comparison. The worst comparison is found at locations on the ceiling where they are under-predicted near to openings and over-predicted towards the rear of the compartment. The spatial variation temperature error between the CFD tool and the measured data is directly linked to the error in the resultant heat flux. In turn, this error can be attributed to a poor definition of the initial fire input, the combustion process and the spatial distribution of the release of energy resulting from the process of combustion. These aspects were explored by other authors for the same tests and this work relies upon their conclusions and sensitivity analyses.

- A comparison of heat fluxes generated by the Eurocode standard and parametric fire curves shows that there is a strong likelihood that significant errors may be induced by using this methodology. Quantification of the errors is scenario specific thus no attempt is made here to estacblish the general accuracy of this methodology.

- The heat flux model is placed within the context of a structural analysis application comprising a hypothetical multi-storey building with significant potential structural weaknesses located within areas that could sustain an intense and long fire. The process of identifying these areas, undertaking a sensitivity study to model the worst case fires, performing the heat transfer using the heat flux model and passing the results to a structural analysis program to evaluate the building's response illustrates the methodology required to undertake a comprehensive structural fire analysis.

- The spatially resolved heat fluxes along three different structural members are defined for a realistic fire. For the different geometries associated with each member, different heat fluxes are achieved due to the variation in the convective heat flux portion. The structural response due to this heating definition is compared to that defined by the Eurocode uniform heating. For each cases considered, it is apparent that there is a different response to that expected with uniform heating. It has been shown that by assuming uniform heating, certain structural member capacities in fire are under-predicted leading to non-conservative behaviour, while for others they may be over-predicted leading to conservative and possibly uneconomical designs. These behaviours highlight the need to define spatially resolved heat fluxes on structural members in order to accurately assess their performance in fire.

10.3. Further Work

The last 20 years has seen the development of fire and structural models increase at a rapid rate with their use today commonplace in everyday Fire Safety Engineering design. Although the research described in this thesis has helped to develop the understanding regarding heat transfer from fire to structures, there are inevitably many issues that remain inadequately or as yet, totally unresolved.

Testing

Increased full-scale testing of compartments throughout the entire duration of a fire, including sustained post-flashover periods would lead to a greater source of data against which more validation exercise can be carried out. Nevertheless, instrumentation for these tests has to be consistent with the precision of the models they intent to validate. Typical measurements to

be taken during the test would need to require significant spatial and temporal resolution and would include: -

- convective, radiative and total heat fluxes
- gas temperatures
- gas flow velocities within the compartment
- soot volume fractions
- optical limits in smoke
- structural temperatures of;
    - thermally-thin and thermally-thick materials
    - geometrically complex shaped members
    - different fire protection materials

CFD Sub-Models

The accuracy of the present model is limited by the accuracy of CFD tools. Many limitations of these tools have been discussed here. Improvements and further validation in all these areas will enhance the value of the present heat transfer model.

References

[1] BS EN 1991-1-2:2002. Eurocode 1: Actions of Structures - Part 1-2: General Actions - Actions on Structures Exposed to Fire. 2002.

[2] Pettersson O., Magnusson S., & Thor J. Fire Engineering Design of Steel Structures. Bulletin 52. 1976. Division of Structural Mechanics and Concrete Construction, Lund Institute of Technology, Lund, Sweden.

[3] Drysdale D.D. An Introduction to Fire Dynamics. 2000. John Wiley & Sons Ltd, Chichester.

[4] Usmani A.S. & Lamont S. Key Events in the Structural Response of a Composite Steel Frame Structure in Fire. *Fire and Materials* **28,** 281-297. 2004.

[5] Moss P.J & Clifton G.C. Modelling of the Cardington LBTF Steel Frame Building Fire Tests. *Fire and Materials* **28,** -177. 2004.

[6] Waterman T.E. Room Flashover - Criteria and Synthesis. *Fire Technology* **4,** 25-31. 1968.

[7] Heselden A.J.M. & Melinek S.J. The Early Stages of Fire Growth in a Compartment. A Co-operative Research Programme of the CIB (Commission W14). First Phase. Fire Research Note No. 1029. 1975.

[8] Thomas P.H. & Bullen M.L. On the Role of $k\rho c$ of Room Lining Materials in the Growth of Room Fires. *Fire and Materials* **3,** 68-73. 1979.

[9] Alpert R.L. Ceiling Jet Flows. In SFPE Handbook of Fire Protection Engineering pp. 2-18-2-31. 2002. SFPE.

[10] Kawagoe K. Fire Behaviour in Rooms. Report No. 27. 1958. Building Research Institute, Tokyo.

[11] Thomas P.H. & Heselden A.J.M. Fully Developed Fires in Single Compartments. A Cooperative Research Programme of the Conseil Internationale du Batiment. Conseil Internationale du Batiment Report No. 20, Fire Research Note No. 923. 1972.

[12] Law M. & O.Brien T. Fire Safety of Bare External Structural Steel. The Steel Construction Institute. SCI Publication 009. 1989.

[13] Magnusson S. & Thelandersson S. Temperature-Time Curves of Complete Process of Fire Development. ACTA Polytechnica Scandinavica, Civil Engineering and Building Construction Series No. 65, Stockholm. 1970.

[14] Kawagoe K. & Sekine T. Estimation of Fire Temperatures-Time Curves in Rooms. BRI Occasional Report No. 11. 1963. Building Research Institute, Ministry of Construction, Tokyo.

[15] Lie T.T. Fire Temperature-Time Relations. In The SFPE Handbook of Fire Protection Engineering pp. 4-201-4-208. 2002. NFPA, Quincy Massachusetts.

[16] Babrauskas V. & Williamson R.B. Post Flashover Compartment Fires: Basis of a Theoretical Model. *Fire and Materials* **2,** 39-53. 1978.

[17] Law M. A Basis for the Design of Fire Protection of Building Structures. *The Structural Engineer* **61A**. 1983.

[18] Ma Z. & Makelainen P. Parametric Temperature-Time Curves of Medium Compartment Fires for Structural Design. *Fire Safety Journal* **34,** 361-375. 2000.

[19] SFPE. Fire Engineering Guide to Fire Exposed Structures. Ballot Draft. 2003.

[20] Barnett C.R. BFD Curve: A New Empirical Model for Fire Compartment Temperatures. *Fire Safety Journal* **37,** 437-463. 2002.

[21] Barnett C.R. & Clifton G.C. Examples of Fire Engineering Design for Steel Members, Using a Standard Curve Versus a New Parametric Curve. *Fire and Materials* **28,** 309-322. 2004.

[22] Pope N.D. & Bailey C Quantitative Comparison of FDS and Parametric Fire Curves With Post-Flashover Compartment Fire Test Data. *Fire Safety Journal* **41,** 99-110. 2006.

[23] Franssen J.M. & Zaharia R. Design of Steel Structures Subjected to Fire. Background and Design Guide to Eurocode 3. 2005. Les Editions de l'Universite de Liege, Liege.

[24] Heskestad G. Virtual Origins of Fire Plumes. *Fire Safety Journal* **5,** 109-114. 1983.

[25] Milke J.A. Analytical Methods for Determining Fire Resistance of Steel Members. In The SFPE Handbook of Fire Protection Engineering - 3rd Edition pp. 4-209-4-238. 2002.

[26] BS EN 1993-1-2:2005. Eurocode 3: Design of Steel Structures - Part 1-2: General Rules - Structural Fire Design. 2005.

[27] Malhotra H.L. Design of Fire Resisting Structures. 1982. Surrey University Press.

[28] Jeanes D.C. Technical Report 84-1. 1984. Society of Fire Protection Engineers.

[29] ASTM Standard Test Method for Determining Material Ignition and Flame Spread Properties. In ASTM Standards pp. 774-789. 1990.

[30] Lie T.T. Fire and Buildings. 1972. Applied Science, London.

[31] Wickstrom U. Comments on Calculation of Temperature in Fire-Exposed Bare Steel Structures in prEN 1993-1-2: Eurocode 3 - Design of Steel Structures - Part 1-2: General Rules - Structural Fire Design. *Fire Safety Journal* **40,** 191-192. 2005.

[32] Melinek S.J. & Thomas P.H. Heat Flow to Insulated Steel. *Fire Safety Journal* **12,** 1-8. 1987.

[33] Wickstrom U. Temperature Analysis of Heavily-Insulated Steel Structures Exposed to Fire. *Fire Safety Journal* **9,** 281-285. 1985.

[34] Wong M.B. & Ghojel J.I. Spreadsheet Method for Temperature Calculation of Unprotected Steelwork Subject to Fire. *The Structural Design of Tall and Special Buildings* **12,** 83-92. 2003.

[35] Lie T.T. & Harmathy T.Z. Fire Study No. 28. 1972. National Research Council of Canada, Ottawa.

[36] Iding R.H., Nizamuddin Z., & Bresler B. Computer Program for the FIre REsponse of Structures - Thermal Three-Dimensional Version. UCB FRD 77-15. 1977. University of California, Berkeley.

[37] Paulsson M. TASEF-2. 1983. Lund Institute of Technology, Lund, Sweden.

[38] Usmani A.S., Rotter M., Lamont S., Sanad A.M., & Gillie M. Fundamental Principles of Structural Behaviour Under Thermal Effects. *Fire Safety Journal* **36,** 721-744. 2001.

[39] Cox G. & Kumar S. Field Modelling of Fire in Forced Ventilated Enclosures. *Combustion Science and Technology* **5,** 7-23. 1987.

[40] Friedman J.N. An International Survey of Computer Models for Fire and Smoke. *SFPE Journal of Fire Protection Engineering* **4,** 81-92. 1992.

[41] Olenick S.M. & Carpenter D.J. An Updated International Survey of Computer Models for Fire and Smoke. *SFPE Journal of Fire Protection Engineering* **13,** 87-110. 2003.

[42] Walton W.D. Zone Computer Fire Models for Enclosures. In The SFPE Handbook for Fire Protection Engineering pp. 3-189-3-193. 2002. NFPA, Quincy, Massachusetts.

[43] Novozhilov V. Computational Fluid Dynamics Modelling of Compartment Fires. *Progress in Energy and Combustion Science* **27,** 611-666. 2001.

[44] Luo K.H. New Opportunities and Challenges in Fire Dynamics Modelling. Fourth International Seminar on Fire and Explosion Hazards. Fire and Explosion Hazards 1, 39-52. 2003. Londonderry, Northern Ireland, UK.

[45] Jones W.W., Forney G.P., Peacock R.D., & Reneke P.A. A Technical Reference for CFAST: Engineering Tools for Estimating Fire Growth and Smoke Transport. 2000. NIST.

[46] Cooper L.Y. Fire-Plume Generated Ceiling Characteristics and Convective Heat Transfer to Ceiling and Wall Surfaces in a Two-Layer Zone-Type of Environment. NISTIR 4705. 1991. NIST.

[47] Atreya A. Convection Heat Transfer. In The SFPE Handbook of Fire Protection Engineering pp. 1-44-1-72. 2002. NFPA, Quincy, Massachusetts.

[48] Siegel R. & Howell J.R. Thermal Radiation Heat Transfer. 1992. Taylor & Francis, New York.

[49] Forney G.P. Computing Radiative Heat Transfer Occuring in a Zone Fire Model. BFRL, NIST. NISTIR 4709. 1991.

[50] Joulain P. Convective and Radiative Transport in Pool and Wall Fires: 20 Years of Research in Poitiers. *Fire Safety Journal* **26,** 99-149. 1996.

[51] Smagorinsky J. General Circulation Experiments with Primitive Equations - I: The Basic Experiment. *Monthly Weather Review* **91,** 99-164. 1963.

[52] Deardorff J.W. A Three-Dimensional Numerical Study of Turbulent Channel Flow at Large Reynold's Numbers. *Journal of Fluid Mechanics* **41,** 453-480. 1970.

[53] Orszag S., Staroselsky I., & Yakhot V. Some Basic Challenges for Large Eddy Simulation Research. In Large Eddy Simulation of Complex Engineering and Geophysical Flows pp. 55-78. 1993. Cambridge University Press, New York.

[54] Bilger R.W. The Structure of Turbulent Nonpremixed Flames. *Proceedings of the Combustion Institute, 22nd Symposium (International) on Combustion* 477-488. 1988.

[55] Cox G. & Kumar S. Modeling Enclosure Fires Using CFD. In The SFPE Handbook of Fire Protection Engineering pp. 3-194-3-218. 2002. NFPA, Quincy, Massachusetts.

[56] Lautenberger C.W., de Ris J.L., Dembsey N.A., Barnett J.R., & Baum H.R. A Simplified Model for Soot Formation and Oxidation in CFD Simulation of Non-Premixed Hydrocarbon Fires. *Fire Safety Journal* **40,** 141-176. 2005.

[57] Grandison A.J., Galea E.R., & Patel M.K. Development of Standards for Fire Models: Report on SMARTFIRE Phase 2 Simulations. FRD Publication Number 2/2003. 2003. Office of the Deputy Prime Minister.

[58] Grandison A.J., Galea E.R., & Patel M.K. Development of Standards for Fire Models: Report on SMARTFIRE Phase 1 Simulations. FRD Publication Number 1/2003. 2003. Office of the Deputy Prime Minister.

[59] Steckler K.D. Flow Induced by Fire in a Compartment. NBSIR-82-25-20. 1982. National Bureau of Standards.

[60] Kumar S., Welch S., Miles S.D., Cajot L.G., Ojanguren M., Barco J., Hostikka S., Max U., & Rohrle A. Natural Fire Safety Concept - The development and validation of a CFD-based engineering methodology for evaluating thermal action on steel and composite structures. European Commission Report EUR 21444 EN. 2005.

[61] Miles S.D., Kumar S., & Cox G. Comparison of 'Blind Predictions' of a CFD Model With Experimental Data. Fire Safety Science - Proceedings of the 6th International Symposium , 543-554. 1999.

[62] Thomas P.H. Burning Behaviour in Room Fires - Some Recent Observations. *Proceedings of the Combustion Institute, 14th Symposium (International) on Combustion* 1007-1020. 1972.

[63] Quintiere J.G. Smoke Measurements: An Assessment of Correlations Between Laboratory and Full-Scale Experiments. *Fire and Materials* **5,** 52-60. 1982.

[64] Tewarson A. Generation of Heat and Chemical Compounds in Fires. In The SFPE Handbook of Fire Protection Engineering pp. 3-82-3-161. 2002. NFPA, Quincy, Massachusetts.

[65] Hostikka S. & Keski-Rahkonen O. Results of CIB W14 Round Robin for Code Assessment Scenario B. 1998. VTT Technical Research Centre of Finland.

[66] McGrattan K. Fire Dynamics Simulator (Version 4) Technical Reference Guide. NIST Special Publication 1018. 2004.

[67] Grosshandler W.L. RADCAL: A Narrow-Band Model for Radiation Calculations in a Combustion Environment. NIST Technical Note 1402. 1993.

[68] Lim L., Buchanan A.H., & Moss P.J Restraint of Fire-Exposed Concrete Floor Systems. *Fire and Materials* **28,** 95-125. 2004.

[69] Usmani A.S., Chung Y.C., & Torero J.L. How Did the WTC Towers Collapse: A New Theory. *Fire Safety Journal* **38,** 501-533. 2003.

[70] Franssen J.M. Numerical Determination of 3D Temperature Fields in Steel Joints. *Fire and Materials* **28,** 63-82. 2004.

[71] Liew J.Y.R. & Ma K.Y. Advanced Analysis of 3D Steel Framework Exposed to Compartment Fire. *Fire and Materials* **28,** 253-267. 2004.

[72] Prasad K. & Baum H.R. Coupled Fire Dynamics and Thermal Response of Complex Building Structures. *Proceedings of the Combustion Institute* **30,** 2255-2262. 2005.

[73] Tofilo P., Delichatsios M.A., & Silcock G.W.H. Effect of Fuel Sootiness on the Heat Fluxes to the Walls in Enclosure Fires. Proceedings of the 8th International Symposium on Fire Safety Science 1, 987-998. 2005.

[74] Lattimer B.Y. Heat Fluxes From Fires to Surfaces. In The SFPE Handbook of Fire Protection Engineering pp. 2-269-2-297. 2002. NFPA, Quincy, Massachusetts.

[75] Lattimer B.Y. & Sorathia U. Thermal Characteristics of Fires in a Noncombustible Corner. *Fire Safety Journal* **38,** 709-745. 2003.

[76] Lattimer B.Y., Hunt S.P., Wright M., & Sorathia U. Modelling Fire Growth in a Combustible Corner. *Fire Safety Journal* **38,** 771-796. 2003.

[77] Lattimer B.Y. & Sorathia U. Thermal Characteristics of Fires in a Combustible Corner. *Fire Safety Journal* **38,** 770. 2003.

[78] Back G., Beyler C., & Dinenno P. Wall Incident Heat Flux Distributions Resulting From an Adjacent Fire. Proceedings of the Fourth IAFSS International Symposium , 241-252. 1994.

[79] Floyd J.E. & Lattimer B.Y. Validation of FDS v4 Boundary Heat Flux Predictions for a Corner Fire. Interflam 2004 2, 1281-1292. 2004.

[80] Adiutori E.F. Origins of the Heat Transfer Coefficient. *Mechanical Engineering* **112,** 46-50. 1990.

[81] Burmeister L.C. Convective Heat Transfer. 1993. John Wiley and Sons.

[82] Incropera F.P. & DeWitt D.P Fundamentals of Heat and Mass Transfer. 2002. John Wiley & Sons, Inc., New York.

[83] Churchill S.W. & Ozoe H. Correlations for Laminar Forced Convection in Flow Over an Isothermal Flat Plate and in Developing and Fully Developed Flow in an Isothermal Tube. *Journal of Heat Transfer* **95**. 1973.

[84] Hilpert R. Correlations for Laminar Forced Convection in Flow Over an Isothermal Flat Plate and in Developing and Fully Developed Flow in an Isothermal Tube. *Forsch Gebiete Ingenieurwes* **4**. 1933.

[85] Knudsen J.D. & Katz D.L. Fluid Dynamics and Heat Transfer. 1958. McGraw-Hill, New York.

[86] Jakob M. Heat Transfer. 1949. Wiley, New York.

[87] Churchill S.W. & Bernstein M. A Correlating Equation for Forced Convection from Gases and Liquids to a Circular Cylinder in Cross Flow. *Journal of Heat Transfer* **99,** 300-306. 1977.

[88] Whitaker S. Forced Convection Heat Transfer Correlations for Flow in Pipes, Past Flat Plates, Single Cylinders, Single Spheres, and for Flow in Packed Beds and Tube Bundles. *AIChE J* **18,** 361-371. 1972.

[89] Rohsenow W.M., Hartnett J.P., & Ganic E.N. Handbook of Heat Transfer Fundamentals. 1973. McGraw-Hill Book Company.

[90] Madrzykowski D. & Vettori R.L. Simulation of the Dynamics of the Fire at 3146 Cherry Road NE Washington D.C., May 30, 1999. BFRL, NIST. NISTR 6510. 2000. Gaithersberg, MD.

[91] Welch S., Jowsey A., Deeny S., Morgan R., & Torero J.L. BRE Large Scale Compartment Fire Tests - Characterising Post-Flashover Fires For Model Validation. *Fire Safety Journal*. 2006.

[92] Bayley F.J. An Analysis pf Turbulent Free Convection Heat Transfer. *Proceedings of the Institute of Mechanical Engineers* **169,** 361. 1955.

[93] McAdams W.H. Heat Transmission. 1954. McGraw-Hill, New York.

[94] Warner C.Y. & Arpaci V.S. An Experimental Investigation of Turbulent Natural Convection in Air at Low Pressure for a Vertical Heated Flat Plate. *International Journal of Heat and Mass Transfer* **11,** 397. 1968.

[95] Churchill S.W. & Chu H.H.S Correlating Equations for Laminar and Turbulent Free Convection from a Vertical Plate. *International Journal of Heat and Mass Transfer* **18,** 1323. 1975.

[96] Morgan V.T. The Overall Convective Heat Transfer from Smooth Circular Cylinders. In Advances in Heat Transfer pp. 199-264. 1975. Academic Press, New York.

[97] Churchill S.W. & Chu H.H.S Correlating Equations for Laminar and Turbulent Free Convection from a Horizontal Cylinder. *International Journal of Heat and Mass Transfer* **18,** 1049. 1975.

[98] Churchill S.W. Free Convection Around Immersed Bodies. In Heat Exchange Design Handbook - Section 2.5.7 1983.

[99] Hottel H.C. & Sarofim A.F. Radiative Transfer. 1967. McGraw-Hill Book Company, USA.

[100] Edwards D.K. & Menard W.A. Comparison of Models for Correlation of Total Band Absorption. *Applied Optics* **3,** 621-625. 1964.

[101] Edwards D.K. & Balakrishnan A. Thermal Radiation by Combustion Gases. *International Journal of Heat and Mass Transfer* **16,** 25-40. 1972.

[102] Edwards D.K. & Balakrishnan A. Self Absorption of Radiation in Turbulent Molecular Gases. *Combustion and Flame* **20,** 401-417. 1973.

[103] Smith T.F., Shen Z.F., & Friedman J.N. Evaluation of Coefficients for the Weighted Sum of Grey Gases Model. *Journal of Heat Transfer* **104,** 602-608. 1982.

[104] Lee S.C. & Tien C.L. Optical Constants of Soot in Hydrocarbon Flames. *Proceedings of the Combustion Institute, 18th Symposium (International) on Combustion* 1159-1166. 1981.

[105] Tien C.L., Lee K.Y., & Stretton A.J. Radiation Heat Transfer. In The SFPE Handbook of Fire Protection Engineering pp. 1-73-1-89. 2002. NFPA, Quincy, Massachusetts.

[106] Felske J.D. & Tien C.L. Calculation of the Emissivity of Luminous Flames. *Combustion Science and Technology* **7,** 25-31. 1973.

[107] Abramowitz M. & Stegun I.A. Handbook of Mathematical Functions with Formulas, Graphs and Mathematical Tables. pp. 228-230. 1964. National Bureau of Standards, AMS 55.

[108] Yuen W.W. & Tien C.L. A Simple Calculation Scheme for the Luminous-Flame Emissivity. Proceedings of the Combustion Institute, 16th Symposium (International) on Combustion , 1481-1487. 1976.

[109] Modak A.T. Radiation from Products of Combustion. *Fire Research* **1,** 339-361. 1978.

[110] Modak A.T. Nonluminous Radiation from Hydrocarbon - Air Diffusion Flames. *Combustion Science and Technology* **10,** 245-259. 1975.

[111] Schleich J.-B., Cajot L.G., Pierre M., Moore D., Lennon T., Kruppa J., Joyeux D., Huller V., Hosser D., Dobbernack R., Kirchner U., Eger U., Twilt L., Van Oerle J., Kokkala M., & Hostikka S. Natural Fire Safety Concept - Full Scale Tests, Implementation in the Eurocodes and Development of a User Friendly Design Tool. Office for Official Publications of the European Communities. 2003. Luxembourg.

[112] Lennon T. & Moore D. The Natural Fire Safety Concept - Full-Scale Tests at Cardington. *Fire Safety Journal* **38,** 623-643. 2003.

[113] Cajot L.G. & Schleich J.-B. Natural Fire Safety for Buildings. InterFlam 2001 , 359-368. 2001.

[114] Masson L. The Use of an Instrumented Steel Billet to Measure Incident Heat Flux. 2003. University of Ulster.

[115] Blevins L.G. & Pitts W.M. Modelling of Bare and Aspirated Thermocouples in Compartment Fires. Fire Safety Journal 33, 239-259. 1999.

[116] Luo M. Effects of Radiation on Temperature Measurement in a Fire Environment. *Journal of Fire Science* **15,** 443-461. 1999.

[117] Jones J.C. On the Use of Metal Sheathed Thermocouples in a Hot Gas Layer Originating From a Room Fire. *Journal of Fire Science* **13,** 257-260. 1995.

[118] Holmann J.P. Heat Transfer. 1997. McGraw-Hill Book Co., London.

[119] Jones W.P. & Whitelaw J.H. Calculation Methods for Reacting Turbulent Flow: A Review. *Combustion and Flame* **48,** 1-26. 1982.

[120] Anderson D., Tannehill J., & Pletcher R. Computational Fluid Mechanics and Heat Transfer. 1994. McGraw-Hill, New York.

[121] Tran H.C. Experimental Data on Wood Materials. In Heat Release in Fires 1992. Elsevier Applied Science, New York.

[122] Bailey C Indicative Fire Tests to Investigate the Behaviour of Cellular Beams Protected With Intumescent Coatings. *Fire Safety Journal* **39,** 689-709. 2004.

Appendix A

FORTRAN source code for *fds2q.exe* to extract required data from FDS. A modified version of *fds2ascii.exe* provided with FDS.

```
      PROGRAM fds2q
C
C     Program to extract data from PL3D and BNDF files for surface
heat flux calculation
C
C     This program extracts TEMPERATURE, VELOCITIES and EXTINCTION
COEFFICIENTS from the PL3D files and also extracts
C     the surface coordinates for each orientation from the BNDF
files.
C
C     All output generated by FDS for the PL3D files is output to
ROOM##_flux.csv files where ## is the index number
C     Just 1 csv file for each orientation is generated WALL**.csv
where ** is the orientation.
C
C     There must be a BNDF line in the FDS input file
C     There must be a PL3D file specifying TEMPERATURE, VELOCITIES
and EXTINCTION COEFFICIENT as outputs
C
C
      INTEGER, PARAMETER :: FB = SELECTED_REAL_KIND(6)
C
      TYPE MESH_TYPE
      REAL(FB), POINTER, DIMENSION(:) :: X,Y,Z
      REAL(FB) :: D1,D2,D3,D4
      INTEGER :: IBAR,JBAR,KBAR,IERR,NXP,NYP,NZP,INDEX
      END TYPE MESH_TYPE
C
      TYPE (MESH_TYPE), DIMENSION(:), ALLOCATABLE, TARGET :: MESH
      TYPE(MESH_TYPE), POINTER :: M
C
      INTEGER,         ALLOCATABLE,         DIMENSION(:)         ::
IOR,I1B,I2B,J1B,J2B,K1B,K2B
      REAL(FB), ALLOCATABLE, DIMENSION(:,:,:,:) :: Q
      REAL(FB), ALLOCATABLE, DIMENSION(:,:,:) :: F
      CHARACTER(1) ANS
      CHARACTER(40) GRIDFILE,QNAME,CHID,QFILE,JUNK,FRMT
      CHARACTER(6)FILE, NUMBER
      CHARACTER(40),               DIMENSION(100)               ::
PL3D_FILE,SLCF_FILE,BNDF_FILE,
     .                                  SLCF_TEXT,BNDF_TEXT,
     .                                  SLCF_UNIT,BNDF_UNIT
      INTEGER,  DIMENSION(6) :: IB,IS
      INTEGER,  DIMENSION(100) :: PL3D_MESH,SLCF_MESH,BNDF_MESH
      REAL(FB), DIMENSION(100) :: PL3D_TIME
C
      WRITE(6,*) ' Enter Job ID string (CHID):'
      READ(5,'(a)') CHID
      GRIDFILE = TRIM(CHID)//'.smv'
C
C
      ************************************************************
**************************
C     Allan Jowsey's additions to create output files
C
C     The following sets up the initial values to be used: -
C
      IFILE=1
```

```
      NSAM=1
      TBEG=0
      TEND=1
      ANS='n'
      IOR_INPUT=-3
C
C     This starts a loop to perform all the iterations to get the
7 output files
C
      DO INDEX=1,7
C
C     This starts a loop to dump all the PL3D files to .csv
formats

      DO ITS=1,99

      if (index.eq.1) THEN

      IF (ITS<10) THEN
      write(NUMBER,'(I1)') ITS
      FILE='ROOM0'//NUMBER
      ELSE
      write(NUMBER,'(I2)') ITS
      FILE='ROOM'//NUMBER
      ENDIF

      ENDIF

C
      ************************************************************
**************************
c
C Open grid file
C
      OPEN(11,FILE=GRIDFILE,STATUS='OLD',FORM='FORMATTED')
C
      CALL SEARCH('VERSION',7,11,IERR)
      IF (IERR.EQ.1) THEN
c         WRITE(6,*) ' WARNING: Assuming FDS version 2 or less'
c         VERSION = 2.
      ELSE
c         READ(11,*) VERSION
c
      VERSION=4
c
      ENDIF
C
      REWIND(11)
C
      CALL SEARCH('NMESHES',7,11,IERR)
      IF (IERR.EQ.1) THEN
         WRITE(6,*) ' WARNING: Assuming 1 mesh'
         NMESHES = 1
      ELSE
         READ(11,*) NMESHES
      ENDIF
      ALLOCATE(MESH(NMESHES))
C
```

```
      REWIND(11)
C
      READ_SMV: DO NM=1,NMESHES
      M=>MESH(NM)
      CALL SEARCH('GRID',4,11,IERR)
      READ(11,*) M%IBAR,M%JBAR,M%KBAR
      ALLOCATE(M%X(0:M%IBAR))
      ALLOCATE(M%Y(0:M%JBAR))
      ALLOCATE(M%Z(0:M%KBAR))
C
      CALL SEARCH('TRNX',4,11,IERR)
      READ(11,*) NOC
      DO I=1,NOC
      READ(11,*)
      ENDDO
      DO I=0,M%IBAR
      READ(11,*) IDUM,M%X(I)
      ENDDO
C
      CALL SEARCH('TRNY',4,11,IERR)
      READ(11,*) NOC
      DO I=1,NOC
      READ(11,*)
      ENDDO
      DO J=0,M%JBAR
      READ(11,*) IDUM,M%Y(J)
      ENDDO
C
      CALL SEARCH('TRNZ',4,11,IERR)
      READ(11,*) NOC
      DO I=1,NOC
      READ(11,*)
      ENDDO
      DO K=0,M%KBAR
      READ(11,*) IDUM,M%Z(K)
      ENDDO
C
      ENDDO READ_SMV
C
C     WRITE(6,*) ' What type of file to parse?'
C     WRITE(6,*) ' PL3D file? Enter 1'
C     WRITE(6,*) ' SLCF file? Enter 2'
C     WRITE(6,*) ' BNDF file? Enter 3'
C     READ(5,*) IFILE
C
C      WRITE(6,*) ' Enter Sampling Factor for Data?'
C        WRITE(6,*) ' (1 for all data, 2 for every other point,
etc.)'
C     READ(5,*) NSAM
C
      FILETYPE: SELECT CASE(IFILE)
C
      CASE(1) FILETYPE
C
C Read a PLOT3D file and print out the values in ASCII text
C
      PL3D_MESH = 1
      REWIND(11)
```

```
      SEARCH_PL3D: DO I=1,99
      CALL SEARCH('PL3D',4,11,IERR)
      IF (IERR.EQ.1) EXIT SEARCH_PL3D
      BACKSPACE(11)
      IF (VERSION.LE.2.) READ(11,*) JUNK,PL3D_TIME(I)
      IF (VERSION.GT.2.) READ(11,*) JUNK,PL3D_TIME(I),PL3D_MESH(I)
      READ(11,'(A)') PL3D_FILE(I)
      DO II=1,5
      IS(II) = II
      READ(11,'(A)') SLCF_TEXT(II)
      READ(11,*)
      READ(11,'(A)') SLCF_UNIT(II)
      ENDDO
c      WRITE(6,'(I3,3X,A,A,I2,A,F5.0)') I,TRIM(PL3D_FILE(I)),
c     .    ', MESH ',PL3D_MESH(I),', Time: ',PL3D_TIME(I)

C
      ************************************************************
**************************

      IF (ITS.eq.1) THEN
      WRITE(QNAME,'(A)') 'Times.csv'
      OPEN(44,FILE=QNAME,STATUS='UNKNOWN')
      WRITE(44,*) I,',',PL3D_TIME(I)
      ENDIF



      ENDDO SEARCH_PL3D
C
C      WRITE(6,'(/A)') ' Choose PLOT3D ``q'' file by its index:'

      TIMES=I-1


      if (ITS.gt.TIMES) THEN
      DEALLOCATE(MESH)
      ENDIF
      if (ITS.gt.TIMES) EXIT

      I=ITS

C
      ************************************************************
**************************

C      READ(5,*) I
      QFILE = PL3D_FILE(I)
      NM = PL3D_MESH(I)
      M=>MESH(NM)
C
      I1 = 0
      I2 = M%IBAR
      J1 = 0
      J2 = M%JBAR
      K1 = 0
      K2 = M%KBAR
      NV = 5
```

```
      ALLOCATE(Q(0:M%IBAR,0:M%JBAR,0:M%KBAR,5))
C
      OPEN(12,FILE=QFILE,FORM='UNFORMATTED',STATUS='OLD')
c      WRITE(6,*) ' Reading PLOT3D data file...'
      READ(12) NXP,NYP,NZP
      READ(12) D1,D2,D3,D4
      READ(12)
((((Q(I,J,K,N),I=0,M%IBAR),J=0,M%JBAR),K=0,M%KBAR),N=1,5)
      CLOSE(12)
C
      CASE(2) FILETYPE
C
C The following program averages up to six variables per section
dumped
C to a slice file.  The data is then dumped to ASCII file(s) in
the form
C of the coordinate(s) and averaged variables.
C Example:  for two-dimensional data, the form is  x,y,t,u,v,
where x,y
C are the coordinates, and t,u,v are averaged scalar variables.
C
      SLCF_MESH = 1
      REWIND(11)
      SEARCH_SLCF: DO I=1,100
      CALL SEARCH('SLCF',4,11,IERR)
      IF (IERR.EQ.1) EXIT SEARCH_SLCF
      BACKSPACE(11)
      IF (VERSION.LE.2.) READ(11,*) JUNK
      IF (VERSION.GT.2.) READ(11,*) JUNK,SLCF_MESH(I)
      READ(11,'(A)') SLCF_FILE(I)
      READ(11,'(A)') SLCF_TEXT(I)
      READ(11,*)
      READ(11,'(A)') SLCF_UNIT(I)
      OPEN(12,FILE=SLCF_FILE(I),FORM='UNFORMATTED',STATUS='OLD')
      READ(12)
      READ(12)
      READ(12)
      READ(12) I1,I2,J1,J2,K1,K2
      CLOSE(12)
      NM=SLCF_MESH(I)
      M=>MESH(NM)
      IF (I1.EQ.I2) THEN
      WRITE(6,'(I3,3X,A,I2,A,F8.2,A,A)') I,'MESH ',SLCF_MESH(I),
     .     ', x=',M%X(I1),', ',TRIM(SLCF_TEXT(I))
      ELSEIF (J1.EQ.J2) THEN
      WRITE(6,'(I3,3X,A,I2,A,F8.2,A,A)') I,'MESH ',SLCF_MESH(I),
     .     ', y=',M%Y(J1),', ',TRIM(SLCF_TEXT(I))
      ELSE
      WRITE(6,'(I3,3X,A,I2,A,F8.2,A,A)') I,'MESH ',SLCF_MESH(I),
     .     ', z=',M%Z(K1),', ',TRIM(SLCF_TEXT(I))
      ENDIF
      ENDDO SEARCH_SLCF
C
      WRITE(6,*) ' Enter starting and ending time for averaging
(s)'
      READ(5,*) TBEG,TEND
      WRITE(6,*) ' Enter number of variables: (6 max)'
      READ(5,*) NV
```

```
C
      VARLOOP: DO MV=1,NV
C
      WRITE(6,'(A,I2)')  '  Enter  Index  for  slice  file  for
variable',MV
      READ(5,*) I
      IS(MV) = I
      QFILE = SLCF_FILE(I)
C
      IF (MV.EQ.1) THEN
      NM = SLCF_MESH(I)
      M=>MESH(NM)
      ALLOCATE(Q(0:M%IBAR,0:M%JBAR,0:M%KBAR,NV))
      ALLOCATE(F(0:M%IBAR,0:M%JBAR,0:M%KBAR))
      F = 0.
      Q = 0.
      ELSE
      IF (SLCF_MESH(I).NE.NM) THEN
        WRITE(6,*) ' ERROR: All slices must have the same mesh'
        STOP
        ENDIF
      ENDIF
C
      OPEN(12,FILE=QFILE,FORM='UNFORMATTED',STATUS='OLD')
C
      READ(12)
      READ(12)
      READ(12)
      READ(12) I1,I2,J1,J2,K1,K2
C
      IF (MV.EQ.1) THEN
      I10=I1 ; I20=I2 ; J10=J1 ; J20=J2 ; K10=K1 ; K20=K2
      ELSE
      IF (I1.NE.I10 .OR. I2.NE.I20 .OR.
     .    J1.NE.J10 .OR. J2.NE.J20 .OR.
     .    K1.NE.K10 .OR. K2.NE.K20) THEN
         WRITE(6,*) ' ERROR: Slice files are incompatible'
         STOP
         ENDIF
      ENDIF
C
      NCOUNT = 0
      READ_LOOP: DO
      READ(12,END=99) TIME
      READ(12,END=99) (((F(I,J,K),I=I1,I2),J=J1,J2),K=K1,K2)
      IF (TIME.LT.TBEG) CYCLE READ_LOOP
      IF (TIME.GT.TEND) EXIT READ_LOOP
      NCOUNT = NCOUNT + 1
      Q(I1:I2,J1:J2,K1:K2,MV) = Q(I1:I2,J1:J2,K1:K2,MV)+
     .                          F(I1:I2,J1:J2,K1:K2)
      ENDDO READ_LOOP

99    CLOSE(12)

      DO K=K1,K2
      DO J=J1,J2
      DO I=I1,I2
      Q(I,J,K,MV) = Q(I,J,K,MV)/REAL(NCOUNT)
```

```
      ENDDO
      ENDDO
      ENDDO
c
      ENDDO VARLOOP
C
C
      CASE(3) FILETYPE
C
      BNDF_MESH = 1
      REWIND(11)
      SEARCH_BNDF: DO I=1,100
      CALL SEARCH('BNDF',4,11,IERR)
      IF (IERR.EQ.1) EXIT SEARCH_BNDF
      BACKSPACE(11)
      IF (VERSION.LE.2.) READ(11,*) JUNK
      IF (VERSION.GT.2.) READ(11,*) JUNK,BNDF_MESH(I)
      READ(11,'(A)') BNDF_FILE(I)
      READ(11,'(A)') BNDF_TEXT(I)
      READ(11,*)
      READ(11,'(A)') BNDF_UNIT(I)
c      WRITE(6,'(I3,3X,A,I2,A,A)') I,'MESH ',BNDF_MESH(I),
c     .     ', ',TRIM(BNDF_TEXT(I))
      ENDDO SEARCH_BNDF
C
C       WRITE(6,*) ' Enter starting and ending time for averaging
(s)'
C      READ(5,*) TBEG,TEND
C      WRITE(6,*) ' Enter orientation: (plus or minus 1, 2 or 3)'
C      READ(5,*) IOR_INPUT
c      IF (VERSION.LE.2.0) IOR_INPUT = ABS(IOR_INPUT)
C      WRITE(6,*) ' Limit the domain size? (y or n)'
C      READ(5,'(A)') ANS
c
      IF (ANS.EQ.'y' .OR. ANS.EQ.'Y') THEN
         WRITE(6,*) ' Enter min/max x, y and z'
         READ(5,*) XS,XF,YS,YF,ZS,ZF
      ELSE
         XS = -100000.
         XF =  100000.
         YS = -100000.
         YF =  100000.
         ZS = -100000.
         ZF =  100000.
      ENDIF
C
C      WRITE(6,*) ' Enter number of variables'
C      READ(5,*) NV
c
      NV=1
C
      BVARLOOP: DO MV=1,NV
C
C          WRITE(6,'(A,I2)')  ' Enter boundary file index for
variable',MV
C     READ(5,*) I
      I=1
      IB(MV) = I
```

```
      QFILE = BNDF_FILE(I)
      OPEN(12,FILE=QFILE,FORM='UNFORMATTED',STATUS='OLD')
C
      IF (MV.EQ.1) THEN
      NM = BNDF_MESH(I)
      M=>MESH(NM)
      ALLOCATE(Q(0:M%IBAR,0:M%JBAR,0:M%KBAR,NV))
      Q = 0.
      ELSE
      IF (BNDF_MESH(I).NE.NM) THEN
        WRITE(6,*) ' ERROR: All boundary files must have the same
mesh'
        STOP
        ENDIF
      ENDIF
C
      READ(12)
      READ(12)
      READ(12)
      READ(12) NPATCH
C


      IF (MV.EQ.1) THEN
      ALLOCATE(IOR(1:NPATCH))
      ALLOCATE(I1B(1:NPATCH))
      ALLOCATE(I2B(1:NPATCH))
      ALLOCATE(J1B(1:NPATCH))
      ALLOCATE(J2B(1:NPATCH))
      ALLOCATE(K1B(1:NPATCH))
      ALLOCATE(K2B(1:NPATCH))
      ENDIF
C
      DO I=1,NPATCH
      IF (VERSION.LE.2.0) THEN
      READ(12) I1B(I),I2B(I),J1B(I),J2B(I),K1B(I),K2B(I)
      IF (I1B(I).EQ.I2B(I)) IOR(I) = 1
      IF (J1B(I).EQ.J2B(I)) IOR(I) = 2
      IF (K1B(I).EQ.K2B(I)) IOR(I) = 3
      ELSE
      READ(12) I1B(I),I2B(I),J1B(I),J2B(I),K1B(I),K2B(I),IOR(I)
      ENDIF
      ENDDO
C
      IF (MV.EQ.1) THEN
      IJBAR = MAX(M%IBAR,M%JBAR)
      JKBAR = MAX(M%JBAR,M%KBAR)
      ALLOCATE(F(0:IJBAR,0:JKBAR,NPATCH))
      ENDIF
      F = 0.
C
      NCOUNT = 0
      READ_BLOOP: DO
      READ(12,END=199) TIME
      DO II=1,NPATCH
      SELECT CASE(ABS(IOR(II)))
      CASE(1)
```

```
      READ(12,END=199)
((F(J,K,II),J=J1B(II),J2B(II)),K=K1B(II),K2B(II))
      CASE(2)
      READ(12,END=199)
((F(I,K,II),I=I1B(II),I2B(II)),K=K1B(II),K2B(II))
      CASE(3)
      READ(12,END=199)
((F(I,J,II),I=I1B(II),I2B(II)),J=J1B(II),J2B(II))
      END SELECT
      ENDDO
      IF (TIME.LT.TBEG) CYCLE READ_BLOOP
      IF (TIME.GT.TEND) EXIT READ_BLOOP
C
      NCOUNT = NCOUNT + 1
C
      REC_PATCH: DO II=1,NPATCH
      IF (IOR(II).NE.IOR_INPUT) CYCLE REC_PATCH
      SELECT CASE(ABS(IOR(II)))
      CASE(1)
      DO K=K1B(II),K2B(II)
      DO J=J1B(II),J2B(II)
      Q(I1B(II),J,K,MV) = Q(I1B(II),J,K,MV) + F(J,K,II)
      ENDDO
      ENDDO
      CASE(2)
      DO K=K1B(II),K2B(II)
      DO I=I1B(II),I2B(II)
      Q(I,J1B(II),K,MV) = Q(I,J1B(II),K,MV) + F(I,K,II)
      ENDDO
      ENDDO
      CASE(3)
      DO J=J1B(II),J2B(II)
      DO I=I1B(II),I2B(II)
      Q(I,J,K1B(II),MV) = Q(I,J,K1B(II),MV) + F(I,J,II)
      ENDDO
      ENDDO
      END SELECT
      ENDDO REC_PATCH
C
      ENDDO READ_BLOOP

199   CLOSE(12)
C
      DO K=0,M%KBAR
      DO J=0,M%JBAR
      DO I=0,M%IBAR
      Q(I,J,K,MV) = Q(I,J,K,MV)/REAL(NCOUNT)
      ENDDO
      ENDDO
      ENDDO
C
      ENDDO BVARLOOP
C
      END SELECT FILETYPE
C
C Write out the data to an ASCII file
C
c     WRITE(QNAME,'(A,A)') TRIM(CHID),'_fds2ascii.csv'
```

```
      WRITE(QNAME,'(A,A)') FILE, '_flux.csv'
      OPEN(44,FILE=QNAME,FORM='FORMATTED',STATUS='UNKNOWN')
C
      WRITE(6,*) ' Writing flux data to file...      ',QNAME
C
      SELECT CASE(IFILE)
C
      CASE(1:2)
C
      I3 = I2 - I1 + 1
      J3 = J2 - J1 + 1
      K3 = K2 - K1 + 1
C
C One-dimensional section file
C
      IF (I1.EQ.I2 .AND. J1.EQ.J2 .AND. K1.NE.K2) then
        WRITE(FRMT,'(A,I1.1,A)') "(1X,",NV,"(A,','),A)"
        WRITE(44,FRMT) 'Z',(TRIM(SLCF_TEXT(IS(L))),L=1,NV)
        WRITE(44,FRMT) 'm',(TRIM(SLCF_UNIT(IS(L))),L=1,NV)
        WRITE(FRMT,'(A,I1.1,A)') "(",NV,"(E12.5,','),E12.5)"
        DO K=K1,K2,NSAM
        write(44,FRMT) M%Z(K),(Q(I2,J2,K,L),L=1,NV)
        enddo
        endif

        if(i1.eq.i2.and.j1.ne.j2.and.k1.eq.k2) then
        WRITE(FRMT,'(A,I1.1,A)') "(1X,",NV,"(A,','),A)"
        WRITE(44,FRMT) 'Y',(TRIM(SLCF_TEXT(IS(L))),L=1,NV)
        WRITE(44,FRMT) 'm',(TRIM(SLCF_UNIT(IS(L))),L=1,NV)
        WRITE(FRMT,'(A,I1.1,A)') "(",NV,"(E12.5,','),E12.5)"
        DO J=J1,J2,NSAM
        write(44,FRMT) M%y(j),(q(i2,j,k2,l),l=1,nv)
        enddo
        endif

        if(i1.ne.i2.and.j1.eq.j2.and.k1.eq.k2) then
        WRITE(FRMT,'(A,I1.1,A)') "(1X,",NV,"(A,','),A)"
        WRITE(44,FRMT) 'X',(TRIM(SLCF_TEXT(IS(L))),L=1,NV)
        WRITE(44,FRMT) 'm',(TRIM(SLCF_UNIT(IS(L))),L=1,NV)
        WRITE(FRMT,'(A,I1.1,A)') "(",NV,"(E12.5,','),E12.5)"
        DO I=I1,I2,NSAM
        write(44,FRMT) M%x(i),(q(i,j2,k2,l),l=1,nv)
        enddo
        endif

c ... Two-dimensional section file
        if(i1.eq.i2.and.j1.ne.j2.and.k1.ne.k2) then
        WRITE(FRMT,'(A,I1.1,A)') "(1X,",NV+1,"(A,','),A)"
        WRITE(44,FRMT) 'Y','Z',(TRIM(SLCF_TEXT(IS(L))),L=1,NV)
        WRITE(44,FRMT) 'm','m',(TRIM(SLCF_UNIT(IS(L))),L=1,NV)
        WRITE(FRMT,'(A,I1.1,A)') "(",NV+1,"(E12.5,','),E12.5)"
        DO K=K1,K2,NSAM
        DO J=J1,J2,NSAM
        write(44,FRMT) M%y(j),M%z(k),(q(i2,j,k,l),l=1,nv)
        enddo
        enddo
```

```
        endif

        if (j1.eq.j2.and.i1.ne.i2.and.k1.ne.k2) then
        WRITE(FRMT,'(A,I1.1,A)') "(1X,",NV+1,"(A,','),A)"
        WRITE(44,FRMT) 'X','Z',(TRIM(SLCF_TEXT(IS(L))),L=1,NV)
        WRITE(44,FRMT) 'm','m',(TRIM(SLCF_UNIT(IS(L))),L=1,NV)
        WRITE(FRMT,'(A,I1.1,A)') "(",NV+1,"(E12.5,','),E12.5)"
        DO K=K1,K2,NSAM
        DO I=I1,I2,NSAM
        write(44,FRMT) M%x(i),M%z(k),(q(i,j2,k,l),l=1,nv)
        enddo
        enddo
        endif

        if(k1.eq.k2.and.i1.ne.i2.and.j1.ne.j2) then
        WRITE(FRMT,'(A,I1.1,A)') "(1X,",NV+1,"(A,','),A)"
        WRITE(44,FRMT) 'X','Y',(TRIM(SLCF_TEXT(IS(L))),L=1,NV)
        WRITE(44,FRMT) 'm','m',(TRIM(SLCF_UNIT(IS(L))),L=1,NV)
        WRITE(FRMT,'(A,I1.1,A)') "(",NV+1,"(E12.5,','),E12.5)"
        DO J=J1,J2,NSAM
        DO I=I1,I2,NSAM
        write(44,FRMT) M%x(i),M%y(j),(q(i,j,k2,l),l=1,nv)
        enddo
        enddo
        endif

c ... Three-dimensional section file
        if (i1.ne.i2.and.j1.ne.j2.and.k1.ne.k2) then
        WRITE(FRMT,'(A,I1.1,A)') "(1X,",NV+2,"(A,','),A)"
C                                                       WRITE(44,FRMT)
'X','Y','Z',(TRIM(SLCF_TEXT(IS(L))),L=1,NV)
C                                                       WRITE(44,FRMT)
'm','m','m',(TRIM(SLCF_UNIT(IS(L))),L=1,NV)
        WRITE(FRMT,'(A,I1.1,A)') "(",NV+2,"(E12.5,','),E12.5)"
        DO K=K1,K2,NSAM
        DO J=J1,J2,NSAM
        DO I=I1,I2,NSAM
        write(44,FRMT) M%x(i),M%y(j),M%z(k),(q(i,j,k,l),l=1,nv)
        enddo
        enddo
        enddo
        endif
C
      CASE(3)
C
      PATCHES: DO II=1,NPATCH
      IF (IOR(II).NE.IOR_INPUT) CYCLE PATCHES
      IF   (M%X(I1B(II)).GT.XF   .OR.   M%X(I2B(II)).LT.XS)   CYCLE
PATCHES
      IF   (M%Y(J1B(II)).GT.YF   .OR.   M%Y(J2B(II)).LT.YS)   CYCLE
PATCHES
      IF   (M%Z(K1B(II)).GT.ZF   .OR.   M%Z(K2B(II)).LT.ZS)   CYCLE
PATCHES
C      WRITE(44,'(A,I4,5(F7.2,A),F8.2)') 'Patch',II,
C     .   M%X(I1B(II)),'<x<',M%X(I2B(II)),',  ',
C     .   M%Y(J1B(II)),'<y<',M%Y(J2B(II)),',  ',
C     .   M%Z(K1B(II)),'<z<',M%Z(K2B(II))
C      WRITE(FRMT,'(A,I1.1,A)') "(1X,",NV+2,"(A,','),A)"
```

```
C      WRITE(44,FRMT) 'X','Y','Z',(TRIM(BNDF_TEXT(IB(L))),L=1,NV)
C      WRITE(44,FRMT) 'm','m','m',(TRIM(BNDF_UNIT(IB(L))),L=1,NV)
       WRITE(FRMT,'(A,I1.1,A)') "(",NV+2,"(E12.5,','),E12.5)"
       DO K=K1B(II),K2B(II),NSAM
       DO J=J1B(II),J2B(II),NSAM
       ILOOP: DO I=I1B(II),I2B(II),NSAM
       IF (M%X(I).GT.XF .OR. M%X(I).LT.XS) CYCLE ILOOP
       IF (M%Y(J).GT.YF .OR. M%Y(J).LT.YS) CYCLE ILOOP
       IF (M%Z(K).GT.ZF .OR. M%Z(K).LT.ZS) CYCLE ILOOP
       WRITE(44,FRMT) M%X(I),M%Y(J),M%Z(K),(Q(I,J,K,L),L=1,NV)
       ENDDO ILOOP
       ENDDO
       ENDDO
       ENDDO PATCHES
C
       END SELECT
C
C
C
       ************************************************************
****************************

       DEALLOCATE(MESH)
       DEALLOCATE(Q)


       IF (INDEX.gt.1) THEN
             DEALLOCATE(F)
             DEALLOCATE(IOR)
             DEALLOCATE(I1B)
             DEALLOCATE(I2B)
             DEALLOCATE(J1B)
             DEALLOCATE(J2B)
             DEALLOCATE(K1B)
             DEALLOCATE(K2B)
       END IF


       if (index.gt.1) EXIT

       END DO

       IF (INDEX.eq.1) THEN
       IFILE=3
       ELSE
       IOR_INPUT=IOR_INPUT+1
       IF (IOR_INPUT.eq.0) THEN
       IOR_INPUT=1
       END IF
       END IF


       IF(INDEX.eq.1) THEN
       FILE='WALL-3'
       ELSEIF(INDEX.eq.2) THEN
       FILE='WALL-2'
       ELSEIF(INDEX.eq.3) THEN
       FILE='WALL-1'
```

```
      ELSEIF(INDEX.eq.4) THEN
      FILE='WALL+1'
      ELSEIF(INDEX.eq.5) THEN
      FILE='WALL+2'
      ELSEIF(INDEX.eq.6) THEN
      FILE='WALL+3'
      ENDIF

      close(44)

      NULLIFY(M)
      DEALLOCATE(M)




      ENDDO
C
C
C     End of Allan Jowsey's changes
C
      ************************************************************
****************************
C
      ************************************************************
****************************
C
C


      STOP
      END


      SUBROUTINE SEARCH(STRING,LENGTH,LU,IERR)
C
      CHARACTER(*), INTENT(IN) :: STRING
      INTEGER, INTENT(OUT) :: IERR
      CHARACTER(20) :: JUNK
      INTEGER LU,LENGTH
C
      SEARCH_LOOP: DO
      READ(LU,'(A)',END=10) JUNK
      IF (JUNK(1:LENGTH).EQ.STRING(1:LENGTH)) EXIT SEARCH_LOOP
      ENDDO SEARCH_LOOP
C
      IERR = 0
      RETURN
C
   10 IERR = 1
      RETURN
C
      END SUBROUTINE SEARCH
C
C
```

Appendix B

MATLAB source code for *structuralflux.exe* to evaluate surface gauge heat fluxes

```
function structuralflux

%  Program to calculate heat flux to surfaces using a CDF approach
%  Allan Jowsey - May 2006

%  This is the introduction screen
display(' ')
disp('                                          ')
disp('                                *         ***** ')
disp('                                **          *   ')
disp('    CFD Post-Processing Tool                      *   ')
disp('        to Evaluate                *          *   ')
disp('     Gauge Heat Fluxes to           **    *     ***** ')
disp('      Structural Elements          ****  **          ')
disp('                                 ****   **         ')
disp('         Allan Jowsey            *****   *         ')
disp('   The University of Edinburgh     *******            ')
disp('             2006                ********       *    ')
disp('                                 ********      **    ')
disp('                              *   ***********     ***   ')
disp('           *       *     **   ************    *****  ')
disp('          **      **     *** *************** *******  ')
disp('    *     ***     ****   ***************************** ')
disp('    **   *****    ********************************** ')
disp('   ************** ***************************************** ')
disp('  ********************************************************** ')
disp(' ************************************************************')
display(' ')

% This determines at which times the calculation needs to be done
%  This program evaluates the characteristic timescales associated with the
%  heated material.  These times are used to determine when the heat flux
%  calculation needs to be done (to save compuational time) and provides
%  output averaged between them.

%  Define material
disp('****')
disp('Choose type of material to which surface heat fluxes are to be evaluated: -')
disp('1. Steel')
disp('2. Concrete')
disp('3. Gypsum Board')
disp('4. Other (user defined)')
mat=input('Enter a number [1-4]: ');

if mat==1;
   mat_k=0.054;
   mat_c=0.465;
   mat_r=7850;

   else if mat==2;
      mat_k=0.0016;
      mat_c=0.750;
      mat_r=2400;

   else if mat==3;
```

```
        mat_k=0.00017;
        mat_c=1.1;
        mat_r=960;

    else if mat==4;
        disp('***')
        mat_k=input('Enter material thermal conductivity [kW/m-K]: ');
        mat_c=input('Enter material specific heat capacity [kJ/kg-K]: ');
        mat_r=input('Enter material density [kg/m^3]: ');

end
end
end
end
disp('***')

%  Enter a conduction length scale
cond_L=input('Enter conduction length scale (Volume/Area) [m]: ');

%  Assume for now a convective heat transfer coefficient of 25W/m^2-K for
%  characteristic time evaluation.
h_cond=25;

%  Calculate h_rad using maximum possible gas temperature of 1200oC
h_rad=1*5.67e-8*(1200+273)^3;

%  Calculate h_tot for characteristic time evaluation
h_tot=h_cond+h_rad;

%  Evaluate Biot number to determine whether material is thermally thick
%  (Bi>0.1) or thermally thin (Bi<0.1)
Bi=((h_tot/1000)*cond_L)/(mat_k);

if Bi<0.1;
    time_c=cond_L^2/(mat_k/(mat_c*mat_r));
    disp('***')
    disp('Material is thermally thin.  Calculation proceeding... ')
    display(strcat('Characteristic time = ', int2str(time_c), 's'))
    disp('***')
else
    time_c=(mat_k*mat_c*mat_r)/(h_tot/1000)^2;
    disp('***')
    disp('Material is thermally thick.  Calculation proceeding... ')
    display(strcat('Characteristic time = ', int2str(time_c), 's'))
    disp('***')
end


% This imports necessary files from the FDS calculation
%  This file imports the .csv files produced
%  from the FDS analysis following the use of
%  the program fds2heatflux.exe

%  Imports an array with the index and time for each PL3D file
```

```
fds_times=csvread('Times.csv');
max_index=max(fds_times(:,1));
max_time=max(fds_times(:,2));

fds_times2=[0,0];
[a,b]=size(fds_times);
for i=1:a;
   fds_times2(i+1,1)=fds_times(i,1);
   fds_times2(i+1,2)=fds_times(i,2);
end


%  This section works out which time indexes should be read for the
%  calculation of the heat fluxes - based on the characteristic times.

time_dif=fds_times(2,2)-fds_times(1,2);

%  If the origial time step is greater than the characteristic time step,
%  then use original time for calculations.
if time_dif>=time_c;
   time_c=time_dif;
   disp('Warning: characteristic time is less than time steps available - using original time
steps')
   disp('***')
end
%  Otherwise, peform calculation at these characteristic time steps.
calc_times=[time_c:time_c:max_time]';
%  These time steps are rounded to the nearest corresponding time index
calc_times(:,2)=round(interp1(fds_times2(:,2),fds_times2(:,1),calc_times(:,1)));
%  Which in turn are a certain original time value
calc_times(:,3)=interp1(fds_times2(:,1),fds_times2(:,2),calc_times(:,2));
%  The difference between each timestep used is...
calc_times(1,4)=calc_times(1,3);
no_of_calcs=length(calc_times);
for i=2:length(calc_times);
   calc_times(i,4)=calc_times(i,3)-calc_times(i-1,3);
end

for i=1:no_of_calcs+1;
   if i==1;
      times(i)=0;
   else if i<no_of_calcs+1;
         for k=2:no_of_calcs;
         for j=1:2;
            times(2*(k-1)+(j-1))=calc_times(k-1,3);
         end
         end
      else if i==no_of_calcs+1;
            k=i-1;
            times(2*k)=calc_times((k),3);
         end
      end
   end
end
```

```
%  All 3d room coordinates and point values imported into a single matrix
%  called 'room'.  This is a multidimensional array for each time index.
for calc=1:no_of_calcs;
   tc=calc;
   n=calc_times(calc,2);
   if n<10;
      file=strcat('room',int2str(0),int2str(n),'_flux.csv');
   else
      file=strcat('room',int2str(n),'_flux.csv');
   end
   display(strcat('Reading ROOM file _', int2str(n),' of _', int2str(max_index)))
 clear room_data
   room_data(:,:)=csvread(file);
%end
clear n
clear file

%  Each boundary surface coordinate imported.
%  The -3 to +3 extension is changed to a to e in terms of notation
wall_a=csvread('WALL-3_flux.csv');
wall_b=csvread('WALL-2_flux.csv');
wall_c=csvread('WALL-1_flux.csv');
wall_d=csvread('WALL+1_flux.csv');
wall_e=csvread('WALL+2_flux.csv');
wall_f=csvread('WALL+3_flux.csv');

% This sets up a loop to do the calculation for all timesteps
%for tc=2:2;
%for tc=1:no_of_calcs;
   clear room;
   room=room_data(:,:);
   clear room_data
% Ths determines the resultant velocity and its principal direction
%  This program calcualtes the magnitude of the resultant velocity vector.
%  It also determines along which principle axis the flow is nearest to and
%  adopts that as the direction.

for i=1:length(room);  %  For every data point...
   room(i,5)=room(i,5)+0.0000123454321;  %  Add a small value to avoid zero values
   room(i,6)=room(i,6)+0.0000123454321;
   room(i,7)=room(i,7)+0.0000123454321;
   room(i,9)=sqrt((room(i,5)^2+room(i,6)^2+room(i,7)^2));  %  Resultant velocity
   room(i,10)=abs(atan(sqrt(room(i,5)^2+room(i,6)^2)/room(i,7))*(180/pi));  %  Angle from
z-axis to x-y axes
   room(i,11)=abs(atan(room(i,6)/room(i,5))*(180/pi));  %  Angle between x and y axes
   if room(i,10)<45;  %  If nearest to z-axis
      room(i,12)=3;
   else if room (i,11)>45;  %  If nearest to y-axis
         room (i,12)=2;
      else if room(i,11)<45;  %  If nearest to x-axis
            room(i,12)=1;
         end
      end
   end
   if room(i,12)==1;  %  If z-axis
      room(i,13)=room(i,5)/abs(room(i,5));  % Determine whether flow is +'ve or -'ve
```

```
   else if room(i,12)==2;
         room(i,13)=room(i,6)/abs(room(i,6));
      else if room(i,12)==3;
            room(i,13)=room(i,7)/abs(room(i,7));
         end
      end
   end
  room(i,14)=room(i,12)*room(i,13);  % Final direcition (including +'ve or -'ve)
end


% This sets up the convective heat transfer lookup tables
%  The following section creates th lookup table for the convective heat
%  transfer coefficient based on a series of data points from a curve fit.

conv_hL=[0.001 0.01 0.1 1 10];  %  Length scales
conv_hV=[0 2 4 8 12 14 16 18 20 25]; % Velocities
conv_h = [49.4 153 211 292 352 379 403 426 447 496
       19 37.5 57.5 88.3 113.5 124.8 135.6 145.8 155.6 178.6
       10 12.7 22.3 38.9 53.9 61.1 67.98 74.7 81.4 97.4
       6.7 8.13 14.21 24.83 34.4 38.96 43.39 47.7 51.93 62.14
       4.5 5.19 9.07 15.85 21.97 24.87 27.69 30.5 33.14 39.6]; %  Convective heat transfer
coefficient

%  Determines the number of grid cells in each direction
a=find(room(:,1)==0);
b=length(a);
c=length(room);
d=c./b;
a=find(room(:,2)==0);
b=length(a);
e=c./b;
f=c./(d*e);
x_room_size=f;
y_room_size=e;
z_room_size=d;

clear a;
clear b;
clear c;
clear d;
clear e;
clear f;

x_dim=max(room(:,1))/(z_room_size-1);  %  Determines the x cell dimension
y_dim=max(room(:,2))/(x_room_size-1);  %  Determines the y cell dimension
z_dim=max(room(:,3))/(y_room_size-1);  %  Determines the z cell dimension

if tc==1;
disp('***')
   question=input('Do you want to set convective length scales [1] or use grid cell sizes
[2]? ');
disp('***')
end
```

```
if question==1;
if tc==1;
x_L=input('Enter x-dimension length scale to be analysed = ');
if x_L>x_dim;  %  Check on whether length scale given is greater than cell dimension...
   x_L=x_dim;  %  If so, then adopts the cell dimension
end
y_L=input('Enter y-dimension length scale to be analysed = ');
if y_L>y_dim;
   y_L=y_dim;
end
z_L=input('Enter z-dimension length scale to be analysed = ');
if z_L>z_dim;
   z_L=z_dim;
end
end
else
   x_L=x_dim;
   y_L=y_dim;
   z_L=z_dim;
end


clear x_dim
clear y_dim
clear z_dim

h_values(:,1)=[1 2 3]';  %  Sets up a table that stores the convective heat conefficients for
reference later
h_values(1,2)=x_L;  %  Second column stores the length scales for the respective axes
h_values(2,2)=y_L;
h_values(3,2)=z_L;

% This arranges the data for lookups
%  This program converts the room.csv imported data into 3d arrays
%  for use in a 3d interploated lookup command.


%  Goes through the 'room' array element by element and converts
%  to a 3d array the x, y and z coordinates and data values.
room_counter=1;

for i=1:x_room_size
   for j=1:y_room_size
      for k=1:z_room_size
         room_x(j,k,i)=room(room_counter,1);  %  x coords
         room_y(j,k,i)=room(room_counter,2);  %  y coords
         room_z(j,k,i)=room(room_counter,3);  %  z coords
         room_T(j,k,i) = room(room_counter,4);  %  Temperatures
         room_K(j,k,i) = room(room_counter,8);  %  Extinction coefficients
         room_QcV(j,k,i) = room(room_counter,9);  % Resultant velocities
         room_QcA(j,k,i) = room(room_counter,12); % Velocity axis
         room_counter=room_counter+1;
      end
   end
end
```

```
clear i
clear j
clear k
clear room_counter
clear room
clear x_room_size
clear y_room_size
clear z_room_size


% This determines the hemispherical coordinates for given geometry
%  This program evaluates the hemispherical coordinates
%  for a generic point (0,0,0).  The user can specify the path length,
%  number of segments in circle, number of points on each radius and
%  the number of shells comprising the hemisphere.

%  User input questions
if tc==1;

qu=input('Do you want to change radiative calcualtion parameters [1] or use default
values [2]? ');
disp('***')

if qu==1

L = input('Path length? ');
segments = input('How many segments within circle? ');
p = input('Number of points to evaluate on radius? ');
shells=input('Number of shells to analyse? ');

else if qu==2;
   L=2;
   segments=4;
   p=3;
   shells=20;
   end
end

end
%  Generic point
x=0;
y=0;
z=0;


theta_s = 360/segments;  % Segment angle size
angles = (0:segments-1)';  %  Angles to be used in calculation
angles(:,2)=angles(:,1).*theta_s;
clear xyz;

%  Loop for number of shells comprising hemisphere
for j=1:shells

   r=(L/shells)*(shells-(j-1));  %  Radius of shell
```

```
    S_l = r/(p+1);  %  Radius to individual points on radius
    point_list = (1:p)';  %  Number of points in analysis
    points=[point_list S_l.*point_list];  %  Distance of each point along radius
    points(:,3)=sqrt(r.^2-points(:,2).^2);  %  Evaluates distance from surface of each point
    points_3d_list=(2:segments*p+1)';
    angs=angles(:,2);
    points_0=points(:,1);
    z_0=points(:,3);
    S_l_0=points(:,2);

%  Repeats the angles list for use in a later matrix below
    for i=1:p-1;
        angs=cat(1,angs(:,1),angles(:,2));
    end

%  Repeats arrays for use below
    for i=1:segments-1;
        points_0=cat(1,points_0(:,1),points(:,1));
        z_0=cat(1,z_0(:,1),points(:,3));
        S_l_0=cat(1,S_l_0(:,1),points(:,2));
    end

%  Sorts the arrays for ease in understanding
    S_l_0=sort(S_l_0,1);
    z_0=sort(z_0,1);
    z_0 = flipud(z_0);
    points_3d=cat(2,points_3d_list,S_l_0,angs);

%  Points defined for easy look-ups
    k=(j*3-2);
    m=(j*3-1);
    n=(j*3);

%  Evaluates the 'x' and 'y' coordinates for all points in circle
    xyz(:,k)=(x+(points_3d(:,2).*cos(points_3d(:,3).*(pi/180))));
    xyz(:,m)=(x+(points_3d(:,2).*sin(points_3d(:,3).*(pi/180))));

%  Introduces the 'z' coordinates to complete the hemispherical coordinates
    xyz(:,n)=z_0(:,1)+z;
end

% This determines the temps and K values on each shell
%  This program evaluates the gas temperatures and extinction coefficients
%  of every coordinate on every surface for all hemispherical coordinates at each shell
%  surface.  It then finds the averages these values for each shell and writes
%  this into the appropriate wall matrix.

clear wall;


display(strcat('Peforming calculation _', int2str(tc), ' of _', int2str(no_of_calcs), ' please
wait...'))
```

```
% Specifies that calculation will be performed for all 6 directions
for wall=1:6;
   clear XYZ;
   clear w_l;

% Wall 'a'

   if wall==1; % Coniditional statement to determine which wall is being considered
      [w_l,b]=size(wall_a); % Determines the number of coordinates on the wall
      wall_a_T=[wall_a(:,1) wall_a(:,2) wall_a(:,3)]; % Creates a matrix of coords
      wall_a_K=[wall_a(:,1) wall_a(:,2) wall_a(:,3)]; % Creates a matrix of coords

      for w=1:w_l; % Loop for each coordinate to be considered separately
         X=wall_a(w,1); % Gets x coordinate
         Y=wall_a(w,2); % Gets y coordinate
         Z=wall_a(w,3); % Gets z coordinate

         for i=1:shells % Peforms calculation for each shell
            k=(i*5-4); % These variables help with the lookup
            m=(i*5-3);
            n=(i*5-2);
            o=(i*5-1);
            t=(i*5);

            p=(i*3-2);
            q=(i*3-1);
            r=(i*3);

            XYZ(:,k)=X+xyz(:,p); % Maps the hemispherical coords onto original coords
            XYZ(:,m)=Y+xyz(:,q); % The order will change for each wall...
            XYZ(:,n)=Z-xyz(:,r); % ...do to directionality.

            % Interpolates from the 3d room array for the new hemispherical
            % coordinates
            XYZ(:,o)=interp3(room_x,room_y,room_z,room_T,XYZ(:,k),XYZ(:,m),XYZ(:,n));
            XYZ(:,t)=interp3(room_x,room_y,room_z,room_K,XYZ(:,k),XYZ(:,m),XYZ(:,n));
            % The following section takes into account any points on
            % the hemisphere that may lie outside the domain. The
            % calculation is restricted to only those inside.
            is=isnan(XYZ(:,o)); % This determines which are outside (NaN)
            siz=size(XYZ);
            len=siz(1,1);
            for v=1:len;
               if is(v,1)==0; % For those inside...
                  t1(v,1)=(XYZ(v,o)+273)^4; % Write the temperature
               else
                  t1(v,1)=1; % For those outside... write "1"
               end
               if is(v,1)==0;
                  e1(v,1)=XYZ(v,t)^4; % Same as above, but for K values
               else
                  e1(v,1)=1;
               end
            end
```

```
            if (length(is)-sum(is))==0;
               temps2(:,i)=0;
               exts2(:,i)=0;
            else
            % Evaluate the mean temperature on shell within domain
               temps2(:,i)=(((sum(t1)-sum(is))/(length(is)-sum(is)))^0.25-273);
            % Evaluate the mean extinction coefficient on shell within domain
               exts2(:,i)=((sum(e1)-sum(is))/(length(is)-sum(is)))^0.25;
            end
            % Evaluates the % of shell contributing to calculation
            wall_a_s(w,i)=(length(is)-sum(is))/length(is);
            %  Writes the mean temperature to the wall coordinate matrix
            wall_a_T(w,i+3)=temps2(1,i);
            %  Writes the mean extinction coefficients to the wall coordinate matrix
            wall_a_K(w,i+3)=exts2(1,i);
            clear is
            clear t1
            clear e1
         end
      end

%  Calculation is repeated for each wall direction.
%  Main difference in each is the mapping of the hemispherical coordinates
%  onto the original coordinates due to directionality.

%  Wall 'b'

   else if wall==2;
         [w_l,b]=size(wall_b);
         wall_b_T=[wall_b(:,1) wall_b(:,2) wall_b(:,3)];
         wall_b_K=[wall_b(:,1) wall_b(:,2) wall_b(:,3)];

      for w=1:w_l;
         X=wall_b(w,1);
         Y=wall_b(w,2);
         Z=wall_b(w,3);

         for i=1:shells

            k=(i*5-4);
            m=(i*5-3);
            n=(i*5-2);
            o=(i*5-1);
            t=(i*5);

            p=(i*3-2);
            q=(i*3-1);
            r=(i*3);

            XYZ(:,k)=X+xyz(:,p);
            XYZ(:,m)=Y-xyz(:,r);
            XYZ(:,n)=Z+xyz(:,q);
            XYZ(:,o)=interp3(room_x,room_y,room_z,room_T,XYZ(:,k),XYZ(:,m),XYZ(:,n));
            XYZ(:,t)=interp3(room_x,room_y,room_z,room_K,XYZ(:,k),XYZ(:,m),XYZ(:,n));
            is=isnan(XYZ(:,o));
```

```
            siz=size(XYZ);
            len=siz(1,1);
            for v=1:len;
               if is(v,1)==0;
                  t1(v,1)=(XYZ(v,o)+273)^4;
               else
                  t1(v,1)=1;
               end
               if is(v,1)==0;
                  e1(v,1)=XYZ(v,t)^4;
               else
                  e1(v,1)=1;
               end
            end
            if (length(is)-sum(is))==0;
               temps2(:,i)=0;
               exts2(:,1)=0;
            else
            temps2(:,i)=(((sum(t1)-sum(is))/(length(is)-sum(is)))^0.25-273);
            exts2(:,i)=((sum(e1)-sum(is))/(length(is)-sum(is)))^0.25;
            end
            wall_b_s(w,i)=(length(is)-sum(is))/length(is);
            wall_b_T(w,i+3)=temps2(1,i);
            wall_b_K(w,i+3)=exts2(1,i);
            clear is
            clear t1
            clear e1
         end
      end

%  Wall 'c'

else if wall==3;
      [w_l,b]=size(wall_c);
      wall_c_T=[wall_c(:,1) wall_c(:,2) wall_c(:,3)];
      wall_c_K=[wall_c(:,1) wall_c(:,2) wall_c(:,3)];

      for w=1:w_l;
         X=wall_c(w,1);
         Y=wall_c(w,2);
         Z=wall_c(w,3);


         for i=1:shells

            k=(i*5-4);
            m=(i*5-3);
            n=(i*5-2);
            o=(i*5-1);
            t=(i*5);

            p=(i*3-2);
            q=(i*3-1);
            r=(i*3);
```

```
            XYZ(:,k)=X-xyz(:,r);
            XYZ(:,m)=Y+xyz(:,p);
            XYZ(:,n)=Z+xyz(:,q);
            XYZ(:,o)=interp3(room_x,room_y,room_z,room_T,XYZ(:,k),XYZ(:,m),XYZ(:,n));
            XYZ(:,t)=interp3(room_x,room_y,room_z,room_K,XYZ(:,k),XYZ(:,m),XYZ(:,n));
            is=isnan(XYZ(:,o));
            siz=size(XYZ);
            len=siz(1,1);
            for v=1:len;
               if is(v,1)==0;
                  t1(v,1)=(XYZ(v,o)+273)^4;
               else
                  t1(v,1)=1;
               end
               if is(v,1)==0;
                  e1(v,1)=XYZ(v,t)^4;
               else
                  e1(v,1)=1;
               end
            end
             if (length(is)-sum(is))==0;
               temps2(:,i)=0;
               exts2(:,1)=0;
            else
            temps2(:,i)=(((sum(t1)-sum(is))/(length(is)-sum(is)))^0.25-273);
            exts2(:,i)=((sum(e1)-sum(is))/(length(is)-sum(is)))^0.25;
             end
            wall_c_s(w,i)=(length(is)-sum(is))/length(is);
            wall_c_T(w,i+3)=temps2(1,i);
            wall_c_K(w,i+3)=exts2(1,i);
            clear is
            clear t1
            clear e1
         end
      end

%  Wall 'd'

else if wall==4;
      [w_l,b]=size(wall_d);
      wall_d_T=[wall_d(:,1) wall_d(:,2) wall_d(:,3)];
      wall_d_K=[wall_d(:,1) wall_d(:,2) wall_d(:,3)];

      for w=1:w_l;
         X=wall_d(w,1);
         Y=wall_d(w,2);
         Z=wall_d(w,3);

         for i=1:shells

            k=(i*5-4);
            m=(i*5-3);
            n=(i*5-2);
            o=(i*5-1);
            t=(i*5);
```

```
            p=(i*3-2);
            q=(i*3-1);
            r=(i*3);

            XYZ(:,k)=X+xyz(:,r);
            XYZ(:,m)=Y+xyz(:,p);
            XYZ(:,n)=Z+xyz(:,q);
            XYZ(:,o)=interp3(room_x,room_y,room_z,room_T,XYZ(:,k),XYZ(:,m),XYZ(:,n));
            XYZ(:,t)=interp3(room_x,room_y,room_z,room_K,XYZ(:,k),XYZ(:,m),XYZ(:,n));
            is=isnan(XYZ(:,o));
            siz=size(XYZ);
            len=siz(1,1);
            for v=1:len;
               if is(v,1)==0;
                  t1(v,1)=(XYZ(v,o)+273)^4;
               else
                  t1(v,1)=1;
               end
               if is(v,1)==0;
                  e1(v,1)=XYZ(v,t)^4;
               else
                  e1(v,1)=1;
               end
            end
            if (length(is)-sum(is))==0;
               temps2(:,i)=0;
               exts2(:,1)=0;
            else
            temps2(:,i)=(((sum(t1)-sum(is))/(length(is)-sum(is)))^0.25-273);
            exts2(:,i)=((sum(e1)-sum(is))/(length(is)-sum(is)))^0.25;
            end
            wall_d_s(w,i)=(length(is)-sum(is))/length(is);
            wall_d_T(w,i+3)=temps2(1,i);
            wall_d_K(w,i+3)=exts2(1,i);
            clear is
            clear t1
            clear e1
         end
      end

%  Wall 'e'

else if wall==5;
      [w_l,b]=size(wall_e);
      wall_e_T=[wall_e(:,1) wall_e(:,2) wall_e(:,3)];
      wall_e_K=[wall_e(:,1) wall_e(:,2) wall_e(:,3)];

      for w=1:w_l;
         X=wall_e(w,1);
         Y=wall_e(w,2);
         Z=wall_e(w,3);

         for i=1:shells
```

```
            k=(i*5-4);
            m=(i*5-3);
            n=(i*5-2);
            o=(i*5-1);
            t=(i*5);

            p=(i*3-2);
            q=(i*3-1);
            r=(i*3);

            XYZ(:,k)=X+xyz(:,p);
            XYZ(:,m)=Y+xyz(:,r);
            XYZ(:,n)=Z+xyz(:,q);
            XYZ(:,o)=interp3(room_x,room_y,room_z,room_T,XYZ(:,k),XYZ(:,m),XYZ(:,n));
            XYZ(:,t)=interp3(room_x,room_y,room_z,room_K,XYZ(:,k),XYZ(:,m),XYZ(:,n));
            is=isnan(XYZ(:,o));
            siz=size(XYZ);
            len=siz(1,1);
            for v=1:len;
               if is(v,1)==0;
                  t1(v,1)=(XYZ(v,o)+273)^4;
               else
                  t1(v,1)=1;
               end
               if is(v,1)==0;
                  e1(v,1)=XYZ(v,t)^4;
               else
                  e1(v,1)=1;
               end
            end
             if (length(is)-sum(is))==0;
               temps2(:,i)=0;
               exts2(:,1)=0;
            else
            temps2(:,i)=(((sum(t1)-sum(is))/(length(is)-sum(is)))^0.25-273);
            exts2(:,i)=((sum(e1)-sum(is))/(length(is)-sum(is)))^0.25;
             end
            wall_e_s(w,i)=(length(is)-sum(is))/length(is);
            wall_e_T(w,i+3)=temps2(1,i);
            wall_e_K(w,i+3)=exts2(1,i);
            clear is
            clear t1
            clear e1
         end
      end

%  Wall 'f'

else if wall==6;
      [w_l,b]=size(wall_f);
      wall_f_T=[wall_f(:,1) wall_f(:,2) wall_f(:,3)];
      wall_f_K=[wall_f(:,1) wall_f(:,2) wall_f(:,3)];

      for w=1:w_l;
         X=wall_f(w,1);
         Y=wall_f(w,2);
```

```
        Z=wall_f(w,3);

        for i=1:shells

            k=(i*5-4);
            m=(i*5-3);
            n=(i*5-2);
            o=(i*5-1);
            t=(i*5);

            p=(i*3-2);
            q=(i*3-1);
            r=(i*3);

            XYZ(:,k)=X+xyz(:,p);
            XYZ(:,m)=Y+xyz(:,q);
            XYZ(:,n)=Z+xyz(:,r);
            XYZ(:,o)=interp3(room_x,room_y,room_z,room_T,XYZ(:,k),XYZ(:,m),XYZ(:,n));
            XYZ(:,t)=interp3(room_x,room_y,room_z,room_K,XYZ(:,k),XYZ(:,m),XYZ(:,n));
            is=isnan(XYZ(:,o));
            siz=size(XYZ);
            len=siz(1,1);
            for v=1:len;
               if is(v,1)==0;
                  t1(v,1)=(XYZ(v,o)+273)^4;
               else
                  t1(v,1)=1;
               end
               if is(v,1)==0;
                  e1(v,1)=XYZ(v,t)^4;
               else
                  e1(v,1)=1;
               end
            end
             if (length(is)-sum(is))==0;
               temps2(:,i)=0;
               exts2(:,1)=0;
            else
            temps2(:,i)=(((sum(t1)-sum(is))/(length(is)-sum(is)))^0.25-273);
            exts2(:,i)=((sum(e1)-sum(is))/(length(is)-sum(is)))^0.25;
            end
            wall_f_s(w,i)=(length(is)-sum(is))/length(is);
            wall_f_T(w,i+3)=temps2(1,i);
            wall_f_K(w,i+3)=exts2(1,i);
            clear is
            clear t1
            clear e1
         end
      end


               end
            end
         end
      end
   end
end
```

```
end

% This creates a lookup matrix for determining path lengths from K values
%  This program evaluates the ratio of radiant intensity at the surface to
%  initial intensity for different values of extinction coefficient.
%  It returns a corresponding path length.

%  The user is asked to input an allowable error percentage for the ratio
%  This is used as the limiting factor for determining the required path
%  length for individual shells at each point.

clear ratio_lookup


%  Allowable error in radiant intensity
error=10;

ratio=(0.05:0.05:1)';  %  Ratio of radiant intensities
ext_coefs=(0.01:0.25:50);  %  Arbitrary range of extinction coefficients
[A,B]=meshgrid(ext_coefs,ratio);  %  Converts data for lookup command
for i=1:length(ratio);
   for j=1:length(ext_coefs);
      ratio_lookup(i,j)=(-reallog(ratio(i,1)))/ext_coefs(1,j);  %  Calculation of ratio values
   end
end

%  Calculation of limiting path length for given extinction cofficient and
%  and error limit


% This checks the required path lengths against shell radius
%  This program calculates for the mean extinction coefficient on each shell,
%  the corresponding path length required for its value.  It then compares this
%  value with the radius of the shell.  When the radius is greater than the
%  required path length then that value it is stored for that wall coordinate.

clear wall

for wall=1:6;  % Perform calculation for each wall

   if wall==1; % Do for first wall...

      clear paths
      for j=1:shells;  %  Peform for each shell
            k=L/shells;  % Radius distance between shells
         paths=(L/shells:L/shells:L);
           %paths(1,shells-j+1)=L-(k*(j-1));
           paths=fliplr(paths);  %  Creates an array of radius distances
         is=isnan(wall_a_K(:,3+j));  %  Checks if there are any "NaN" values of K
         [a,b]=size(wall_a_K);
         for i=1:a;  %  For every wall coordinate
            if is(i,1)==0;  %  If K is a value, then lookup its path length
               wall_a_K(i,3+shells+j) = interp2(A,B,ratio_lookup,wall_a_K(i,3+j),error/100);
            else
```

```
            wall_a_K(i,3+shells+j)=wall_a_K(i,3+j);
          end
          if wall_a_K(i,3+shells+j)<=paths(1,j); % Check if path length is less than radius
            wall_a_K(i,3+2*shells+j)=paths(1,j); % If so, then write radius
          else
            wall_a_K(i,3+2*shells+j)=99; % If not then write an arbitrarily high value of
"99"
          end
        end
      clear is
      end

  else if wall==2;

      clear paths
      for j=1:shells;
          k=L/shells;
        paths=(L/shells:L/shells:L);
        paths=fliplr(paths);
        is=isnan(wall_b_K(:,3+j));
        [a,b]=size(wall_b_K);
        for i=1:a;
          if is(i,1)==0;
            wall_b_K(i,3+shells+j) = interp2(A,B,ratio_lookup,wall_b_K(i,3+j),error/100);
          else
            wall_b_K(i,3+shells+j)=wall_b_K(i,3+j);
          end
          if wall_b_K(i,3+shells+j)<=paths(1,j);
            wall_b_K(i,3+2*shells+j)=paths(1,j);
          else
            wall_b_K(i,3+2*shells+j)=99;
          end
        end
      clear is
      end

  else if wall==3;

      clear paths
      for j=1:shells;
          k=L/shells;
          paths=(L/shells:L/shells:L);
        paths=fliplr(paths);
        is=isnan(wall_c_K(:,3+j));
        [a,b]=size(wall_c_K);
        for i=1:a;
          if is(i,1)==0;
            wall_c_K(i,3+shells+j) = interp2(A,B,ratio_lookup,wall_c_K(i,3+j),error/100);
          else
            wall_c_K(i,3+shells+j)=wall_c_K(i,3+j);
          end
          if wall_c_K(i,3+shells+j)<=paths(1,j);
            wall_c_K(i,3+2*shells+j)=paths(1,j);
          else
            wall_c_K(i,3+2*shells+j)=99;
          end
```

```
    end
  clear is
  end

  else if wall==4;

  clear paths
  for j=1:shells;
      k=L/shells;
      paths=(L/shells:L/shells:L);
    paths=fliplr(paths);
    is=isnan(wall_d_K(:,3+j));
    [a,b]=size(wall_d_K);
    for i=1:a;
      if is(i,1)==0;
        wall_d_K(i,3+shells+j) = interp2(A,B,ratio_lookup,wall_d_K(i,3+j),error/100);
      else
        wall_d_K(i,3+shells+j)=wall_d_K(i,3+j);
      end
      if wall_d_K(i,3+shells+j)<=paths(1,j);
        wall_d_K(i,3+2*shells+j)=paths(1,j);
      else
        wall_d_K(i,3+2*shells+j)=99;
      end
    end
  clear is
  end

else if wall==5;

  clear paths
  for j=1:shells;
      k=L/shells;
      paths=(L/shells:L/shells:L);
    paths=fliplr(paths);
    is=isnan(wall_e_K(:,3+j));
    [a,b]=size(wall_e_K);
    for i=1:a;
      if is(i,1)==0;
        wall_e_K(i,3+shells+j) = interp2(A,B,ratio_lookup,wall_e_K(i,3+j),error/100);
      else
        wall_e_K(i,3+shells+j)=wall_e_K(i,3+j);
      end
      if wall_e_K(i,3+shells+j)<=paths(1,j);
        wall_e_K(i,3+2*shells+j)=paths(1,j);
      else
        wall_e_K(i,3+2*shells+j)=99;
      end
    end
  clear is
  end

else if wall==6;

  clear paths
```

```
      for j=1:shells;
           k=L/shells;
           paths=(L/shells:L/shells:L);
        paths=fliplr(paths);
        is=isnan(wall_f_K(:,3+j));
        [a,b]=size(wall_f_K);
        for i=1:a;
          if is(i,1)==0;
            wall_f_K(i,3+shells+j) = interp2(A,B,ratio_lookup,wall_f_K(i,3+j),error/100);
          else
            wall_f_K(i,3+shells+j)=wall_f_K(i,3+j);
          end
          if wall_f_K(i,3+shells+j)<=paths(1,j);
            wall_f_K(i,3+2*shells+j)=paths(1,j);
          else
            wall_f_K(i,3+2*shells+j)=99;
          end
        end
      clear is
      end
              end
            end
          end
        end
      end
   end
end

% This detetrmines the minimum path length required at each coordinate
%  This program determines the minimum path length required at each surface
%  coodinate from the previous analysis.

for wall=1:6;  % Perform calculation for each wall

   if wall==1; % Do for first wall...
        [a,b]=size(wall_a_K);
      for i=1:a;  % Do for wall locations on wall
        for j=1:shells; % Do for each shell
          p_check(1,j)=wall_a_K(i,3+2*shells+j);  % Write all path lengths to a variable
          wall_a_K(i,3+3*shells+1)=min(p_check);  % Write minimum path length
required
        end
      end

   else if wall==2;    % Continue for each wall
        [a,b]=size(wall_b_K);
      for i=1:a;
        for j=1:shells;
          p_check(1,j)=wall_b_K(i,3+2*shells+j);
          wall_b_K(i,3+3*shells+1)=min(p_check);
        end
      end

   else if wall==3;
        [a,b]=size(wall_c_K);
      for i=1:a;
```

```
        for j=1:shells;
            p_check(1,j)=wall_c_K(i,3+2*shells+j);
            wall_c_K(i,3+3*shells+1)=min(p_check);
        end
    end

elseif wall==4;
        [a,b]=size(wall_d_K);
    for i=1:a;
        for j=1:shells;
            p_check(1,j)=wall_d_K(i,3+2*shells+j);
            wall_d_K(i,3+3*shells+1)=min(p_check);
        end
    end

elseif wall==5;
        [a,b]=size(wall_e_K);
    for i=1:a;
        for j=1:shells;
            p_check(1,j)=wall_e_K(i,3+2*shells+j);
            wall_e_K(i,3+3*shells+1)=min(p_check);
        end
    end

elseif wall==6;
        [a,b]=size(wall_f_K);
    for i=1:a;
        for j=1:shells;
            p_check(1,j)=wall_f_K(i,3+2*shells+j);
            wall_f_K(i,3+3*shells+1)=min(p_check);
        end
    end
                end
            end
        end
    end
  end
end

% This evaluates the shell areas used in the analyses
% This program evaluates the surface area of each shell at each coordinate

% Creates a table of shell radius and associated surface areas assuming no
% boundary interaction.

clear areas
areas=(shells:-1:1);
areas(2,:)=paths;
areas(3,:)=2.*pi.*areas(2,:).*areas(2,:);
areas(4,:)=pi.*areas(2,:).*areas(2,:);


% This calculated the gas emissivity for each shell layer
% This program calculates the gas mixture emissivity at each shell for each
```

```
% wall coordinate

for wall=1:6;  % Perform calculation for each wall

   if wall==1; % Do for first wall...

      wall_a_e=[wall_a(:,1) wall_a(:,2) wall_a(:,3)];  %  Creates a matrix of coords
        [a,b]=size(wall_a_K);
      for i=1:a;  % Do for wall locations on wall
         for j=1:shells; % Do for each shell
            wall_a_e(i,3+j)=1-exp(-wall_a_K(i,3+j)*(paths(1,1)-paths(1,2)));  % Determines
local emissivity
            wall_a_e(i,3+shells+j)=exp(-wall_a_K(i,3+j)*(paths(1,1)-paths(1,2)));  %
Determine decay factor through gas
         end
         for j=1:shells;
            if j==1;
               wall_a_e(i,3+2*shells+j)=wall_a_e(i,3+shells+j);
            else
               wall_a_e(i,3+2*shells+j)=wall_a_e(i,3+shells+j)*wall_a_e(i,3+2*shells+j-1);
            end
         end

      end

      else if wall==2;    % Continue for each wall

      wall_b_e=[wall_b(:,1) wall_b(:,2) wall_b(:,3)];
               [a,b]=size(wall_b_K);
      for i=1:a;
         for j=1:shells;
            wall_b_e(i,3+j)=1-exp(-wall_b_K(i,3+j)*(paths(1,1)-paths(1,2)));
            wall_b_e(i,3+shells+j)=exp(-wall_b_K(i,3+j)*(paths(1,1)-paths(1,2)));
         end
           for j=1:shells;
            if j==1;
               wall_b_e(i,3+2*shells+j)=wall_b_e(i,3+shells+j);
            else
               wall_b_e(i,3+2*shells+j)=wall_b_e(i,3+shells+j)*wall_b_e(i,3+2*shells+j-1);
            end
         end

      end
           else if wall==3;

      wall_c_e=[wall_c(:,1) wall_c(:,2) wall_c(:,3)];
               [a,b]=size(wall_c_K);
      for i=1:a;
         for j=1:shells;
            wall_c_e(i,3+j)=1-exp(-wall_c_K(i,3+j)*(paths(1,1)-paths(1,2)));
            wall_c_e(i,3+shells+j)=exp(-wall_c_K(i,3+j)*(paths(1,1)-paths(1,2)));
         end
         for j=1:shells;
            if j==1;
               wall_c_e(i,3+2*shells+j)=wall_c_e(i,3+shells+j);
```

```
        else
            wall_c_e(i,3+2*shells+j)=wall_c_e(i,3+shells+j)*wall_c_e(i,3+2*shells+j-1);
        end
    end

    end


    else if wall==4;

wall_d_e=[wall_d(:,1) wall_d(:,2) wall_d(:,3)];
          [a,b]=size(wall_d_K);
for i=1:a;
    for j=1:shells;
        wall_d_e(i,3+j)=1-exp(-wall_d_K(i,3+j)*(paths(1,1)-paths(1,2)));
        wall_d_e(i,3+shells+j)=exp(-wall_d_K(i,3+j)*(paths(1,1)-paths(1,2)));
    end
                for j=1:shells;
        if j==1;
            wall_d_e(i,3+2*shells+j)=wall_d_e(i,3+shells+j);
        else
            wall_d_e(i,3+2*shells+j)=wall_d_e(i,3+shells+j)*wall_d_e(i,3+2*shells+j-1);
        end
    end

end
else if wall==5;

wall_e_e=[wall_e(:,1) wall_e(:,2) wall_e(:,3)];
          [a,b]=size(wall_e_K);
for i=1:a;
    for j=1:shells;
        wall_e_e(i,3+j)=1-exp(-wall_e_K(i,3+j)*(paths(1,1)-paths(1,2)));
        wall_e_e(i,3+shells+j)=exp(-wall_e_K(i,3+j)*(paths(1,1)-paths(1,2)));
    end
                for j=1:shells;
        if j==1;
            wall_e_e(i,3+2*shells+j)=wall_e_e(i,3+shells+j);
        else
            wall_e_e(i,3+2*shells+j)=wall_e_e(i,3+shells+j)*wall_e_e(i,3+2*shells+j-1);
        end
    end

end
else if wall==6;

wall_f_e=[wall_f(:,1) wall_f(:,2) wall_f(:,3)];
          [a,b]=size(wall_f_K);
for i=1:a;
    for j=1:shells;
        wall_f_e(i,3+j)=1-exp(-wall_f_K(i,3+j)*(paths(1,1)-paths(1,2)));
        wall_f_e(i,3+shells+j)=exp(-wall_f_K(i,3+j)*(paths(1,1)-paths(1,2)));
    end
     for j=1:shells;
        if j==1;
```

```
            wall_f_e(i,3+2*shells+j)=wall_f_e(i,3+shells+j);
          else
            wall_f_e(i,3+2*shells+j)=wall_f_e(i,3+shells+j)*wall_f_e(i,3+2*shells+j-1);
          end
      end
        end
        end
        end
          end
        end
   end
end
end

% This determines the radiative fluxes on the surface
%  This program calculates the radiant intensities on each wall surface
%  coordinate.

for wall=1:6;  % Perform calculation for each wall

  if wall==1; % Do for first wall...

      wall_a_qr=[wall_a(:,1) wall_a(:,2) wall_a(:,3)];  %  Creates a matrix of coords
      wall_a_qr2=[wall_a(:,1) wall_a(:,2) wall_a(:,3)];
      [a,b]=size(wall_a);
      for i=1:a;  % Do for wall locations on wall
         for j=1:shells; % Do for each shell
            wall_a_qr(i,3+j)=(0.5*wall_a_s(i,j)*areas(3,j)*1e-3*wall_a_e(i,3+j)*5.67e-
8*(wall_a_T(i,3+j)+273.15)^4*wall_a_e(i,3+2*shells+j))/areas(4,j);
         end
      end

  else if wall==2;    % Continue for each wall

        wall_b_qr=[wall_b(:,1) wall_b(:,2) wall_b(:,3)];
        wall_b_qr2=[wall_b(:,1) wall_b(:,2) wall_b(:,3)];
        [a,b]=size(wall_b);
      for i=1:a;
         for j=1:shells;
            wall_b_qr(i,3+j)=(0.5*wall_b_s(i,j)*areas(3,j)*1e-3*wall_b_e(i,3+j)*5.67e-
8*(wall_b_T(i,3+j)+273.15)^4*wall_b_e(i,3+2*shells+j))/areas(4,j);
         end
      end

      else if wall==3;

        wall_c_qr=[wall_c(:,1) wall_c(:,2) wall_c(:,3)];
        wall_c_qr2=[wall_c(:,1) wall_c(:,2) wall_c(:,3)];
        [a,b]=size(wall_c);
      for i=1:a;
         for j=1:shells;
            wall_c_qr(i,3+j)=(0.5*wall_c_s(i,j)*areas(3,j)*1e-3*wall_c_e(i,3+j)*5.67e-
8*(wall_c_T(i,3+j)+273.15)^4*wall_c_e(i,3+2*shells+j))/areas(4,j);
         end
      end
```

```
      else if wall==4;

        wall_d_qr=[wall_d(:,1) wall_d(:,2) wall_d(:,3)];
        wall_d_qr2=[wall_d(:,1) wall_d(:,2) wall_d(:,3)];
        [a,b]=size(wall_d);
      for i=1:a;
        for j=1:shells;
          wall_d_qr(i,3+j)=(0.5*wall_d_s(i,j)*areas(3,j)*1e-3*wall_d_e(i,3+j)*5.67e-
8*(wall_d_T(i,3+j)+273.15)^4*wall_d_e(i,3+2*shells+j))/areas(4,j);
        end
      end

      else if wall==5;

        wall_e_qr=[wall_e(:,1) wall_e(:,2) wall_e(:,3)];
        wall_e_qr2=[wall_e(:,1) wall_e(:,2) wall_e(:,3)];
        [a,b]=size(wall_e);
      for i=1:a;
        for j=1:shells;
          wall_e_qr(i,3+j)=(0.5*wall_e_s(i,j)*areas(3,j)*1e-3*wall_e_e(i,3+j)*5.67e-
8*(wall_e_T(i,3+j)+273.15)^4*wall_e_e(i,3+2*shells+j))/areas(4,j);
        end
      end

      else if wall==6;

        wall_f_qr=[wall_f(:,1) wall_f(:,2) wall_f(:,3)];
        wall_f_qr2=[wall_f(:,1) wall_f(:,2) wall_f(:,3)];
        [a,b]=size(wall_f);
      for i=1:a;
        for j=1:shells;
          wall_f_qr(i,3+j)=(0.5*wall_f_s(i,j)*areas(3,j)*1e-3*wall_f_e(i,3+j)*5.67e-
8*(wall_f_T(i,3+j)+273.15)^4*wall_f_e(i,3+2*shells+j))/areas(4,j);
        end
      end
        end
        end
        end
        end
    end
  end
end

% This writes the radiant, convective and net heat flux for the surfaces
% and also considers what happens when outside the smoke layer
%  This program evaluates the radiant intensities when the surface is
%  outside the smoke layer.  It writes the convective and total heat fluxes
%  to appropriate arrays.

extlimit=0.5;  % Extinction coefficient limit for smoke

for wall=1:6;  % Perform calculation for each wall

  if wall==1; % Do for first wall...
```

```
    if tc==1;
     wall_a_q_r=[wall_a(:,1) wall_a(:,2) wall_a(:,3)];  %  Creates a matrix of coords
     wall_a_q_c=[wall_a(:,1) wall_a(:,2) wall_a(:,3)];
     wall_a_q_t=[wall_a(:,1) wall_a(:,2) wall_a(:,3)];
    end
                [a,b]=size(wall_a);
    for i=1:a;  %  For wall points on wall
        if wall_a_K(i,3+shells)>extlimit;  % If in the smoke layer
         qr=0;
         for j=1:shells; % Do for each shell
            qr=qr+wall_a_qr(i,3+j);  % Sum radiant intensities
         end
         wall_a_q_r(i,3+tc)=qr;  % Write total radiant intensity
        else  %  If outside the smoke...
        for n=shells:-1:1;  %  Start at first shell from wall
           extvalue=wall_a_K(i,3+n);
           if extvalue>extlimit;  % Check K value
              break  % Stop checking K value
           end
        end
        smoke_start=shells+1-n;  % Identifies which at which shell the smoke starts
        smoke_check=n;
        for n=smoke_check:-1:1; % Continue checking till smoke ends
           extvalue=wall_a_K(i,3+n);
           if extvalue<extlimit;
              break  %  Stop when smoke ends
           end
        end
        smoke_end=shells+1-n;  %  Identifies shell at which smoke ends
        smoke_shells=abs(smoke_start-smoke_end);  % No. of smoke shells
        smoke_length=smoke_shells*(paths(1,1)-paths(1,2)); % Distance of smoke
        clear_shells=smoke_start-1;  % No. of clear shells before smoke
        clear_length=clear_shells*(paths(1,1)-paths(1,2));  % Distance of clear shells

        ambK=0;
        for j=1:clear_shells;
           ambK=ambK+wall_a_K(i,3+shells+1-j);
        end
        clear_ave_K=ambK/clear_shells;  % Average K value outside the smoke
        decay_factor=exp(-clear_ave_K*clear_length);  % Associated decay factor
outside smoke

        smokeK=0;
        smokeT=0;
        for j=1:smoke_shells; % In the smoke...
           smokeK=smokeK+wall_a_K(i,3+shells-clear_shells-j+1);
           smokeT=smokeT+(wall_a_T(i,3+shells-clear_shells-j+1));
        end
        smoke_ave_K=smokeK/(smoke_shells+0.0001); % Ave smoke K value
        smoke_emissivity=1-exp(-smoke_ave_K*smoke_length); % Smoke emissivity
        smoke_ave_T=(smokeT)/(smoke_shells+0.0001); % Average smoke
temperature
        if smoke_start==shells;
        radiative =0;  % If no smoke, then zero radiative flux
        else % Else calculate the radiative intensity due to the smoke
```

```
radiative=(wall_a_s(i,smoke_end)*areas(3,smoke_end)*smoke_emissivity*5.67E-
8*(smoke_ave_T+273)^4*decay_factor*0.001)/areas(4,smoke_end);
            end
            wall_a_q_r(i,3+tc)=radiative;  % Write radiative intensity to array
          end
       end

       %  Convective heat fluxes

wall_a_q_cV(:,tc)=interp3(room_x,room_y,room_z,room_QcV,wall_a_q_c(:,1),wall_a_q_c
(:,2),wall_a_q_c(:,3));

wall_a_q_cA(:,tc)=round(interp3(room_x,room_y,room_z,room_QcA,wall_a_q_c(:,1),wall
_a_q_c(:,2),wall_a_q_c(:,3)));

wall_a_q_cT(:,tc)=interp3(room_x,room_y,room_z,room_T,wall_a_q_c(:,1),wall_a_q_c(:,2
),wall_a_q_c(:,3));

Lw=size(wall_a_q_c);
for i=1:Lw(1,1);
   if abs(wall_a_q_cA(i,tc))==1;

wall_a_q_c(i,3+tc)=0.001*interp2(conv_hV,conv_hL,conv_h,wall_a_q_cV(i,tc),x_L)*wall_
a_q_cT(i,tc);
   else if abs(wall_a_q_cA(i,tc))==2;

wall_a_q_c(i,3+tc)=0.001*interp2(conv_hV,conv_hL,conv_h,wall_a_q_cV(i,tc),y_L)*wall_
a_q_cT(i,tc);
      else if abs(wall_a_q_cA(i,tc))==3;

wall_a_q_c(i,3+tc)=0.001*interp2(conv_hV,conv_hL,conv_h,wall_a_q_cV(i,tc),z_L)*wall_
a_q_cT(i,tc);
         end
      end
   end
end

      %  Net heat fluxes
      wall_a_q_t(:,3+tc)=wall_a_q_r(:,3+tc)+wall_a_q_c(:,3+tc);

   else if wall==2;    % Continue for each wall

         if tc==1;
         wall_b_q_r=[wall_b(:,1) wall_b(:,2) wall_b(:,3)];
         wall_b_q_c=[wall_b(:,1) wall_b(:,2) wall_b(:,3)];
         wall_b_q_t=[wall_b(:,1) wall_b(:,2) wall_b(:,3)];
         end
               [a,b]=size(wall_b);
      for i=1:a;
         if wall_b_K(i,3+shells)>extlimit;
         qr=0;
          for j=1:shells;
             qr=qr+wall_b_qr(i,3+j);
          end
          wall_b_q_r(i,3+tc)=qr;
```

```
        else
           for n=shells:-1:1;
              extvalue=wall_b_K(i,3+n);
              if extvalue>extlimit;
                 break
              end
           end
           smoke_start=shells+1-n;
           smoke_check=n;
           for n=smoke_check:-1:1;
              extvalue=wall_b_K(i,3+n);
              if extvalue<extlimit;
                 break
              end
           end
           smoke_end=shells+1-n;
           smoke_shells=abs(smoke_start-smoke_end);
           smoke_length=smoke_shells*(paths(1,1)-paths(1,2));
           clear_shells=smoke_start-1;
           clear_length=clear_shells*(paths(1,1)-paths(1,2));

           ambK=0;
           for j=1:clear_shells;
              ambK=ambK+wall_b_K(i,3+shells+1-j);
           end
           clear_ave_K=ambK/clear_shells;
           decay_factor=exp(-clear_ave_K*clear_length);

           smokeK=0;
           smokeT=0;
           for j=1:smoke_shells;
              smokeK=smokeK+wall_b_K(i,3+shells-clear_shells-j+1);
              smokeT=smokeT+(wall_b_T(i,3+shells-clear_shells-j+1));
           end
           smoke_ave_K=smokeK/(smoke_shells+0.0001);
           smoke_emissivity=1-exp(-smoke_ave_K*smoke_length);
           smoke_ave_T=(smokeT)/(smoke_shells+0.0001);
           if smoke_start==shells;
           radiative =0;
           else

radiative=(wall_b_s(i,smoke_end)*areas(3,smoke_end)*smoke_emissivity*5.67E-
8*(smoke_ave_T+273)^4*decay_factor*0.001)/areas(4,smoke_end);
           end
           wall_b_q_r(i,3+tc)=radiative;
        end
     end


wall_b_q_cV(:,tc)=interp3(room_x,room_y,room_z,room_QcV,wall_b_q_c(:,1),wall_b_q_c
(:,2),wall_b_q_c(:,3));

wall_b_q_cA(:,tc)=round(interp3(room_x,room_y,room_z,room_QcA,wall_b_q_c(:,1),wall
_b_q_c(:,2),wall_b_q_c(:,3)));
```

```
wall_b_q_cT(:,tc)=interp3(room_x,room_y,room_z,room_T,wall_b_q_c(:,1),wall_b_q_c(:,2
),wall_b_q_c(:,3));

Lw=size(wall_b_q_c);
for i=1:Lw(1,1);
   if abs(wall_b_q_cA(i,tc))==1;

wall_b_q_c(i,3+tc)=0.001*interp2(conv_hV,conv_hL,conv_h,wall_b_q_cV(i,tc),x_L)*wall_
b_q_cT(i,tc);
   else if abs(wall_b_q_cA(i,tc))==2;

wall_b_q_c(i,3+tc)=0.001*interp2(conv_hV,conv_hL,conv_h,wall_b_q_cV(i,tc),y_L)*wall_
b_q_cT(i,tc);
      else if abs(wall_b_q_cA(i,tc))==3;

wall_b_q_c(i,3+tc)=0.001*interp2(conv_hV,conv_hL,conv_h,wall_b_q_cV(i,tc),z_L)*wall_
b_q_cT(i,tc);
         end
      end
   end
end
      wall_b_q_t(:,3+tc)=wall_b_q_r(:,3+tc)+wall_b_q_c(:,3+tc);


   else if wall==3;

         if tc==1;
      wall_c_q_r=[wall_c(:,1) wall_c(:,2) wall_c(:,3)];
      wall_c_q_c=[wall_c(:,1) wall_c(:,2) wall_c(:,3)];
      wall_c_q_t=[wall_c(:,1) wall_c(:,2) wall_c(:,3)];
        end
                  [a,b]=size(wall_c);
     for i=1:a;
        if wall_c_K(i,3+shells)>extlimit;
       qr=0;
           for j=1:shells;
            qr=qr+wall_c_qr(i,3+j);
        end
        wall_c_q_r(i,3+tc)=qr;
       else
          for n=shells:-1:1;
             extvalue=wall_c_K(i,3+n);
             if extvalue>extlimit;
                break
             end
          end
          smoke_start=shells+1-n;
          smoke_check=n;
          for n=smoke_check:-1:1;
             extvalue=wall_c_K(i,3+n);
             if extvalue<extlimit;
                break
             end
          end
          smoke_end=shells+1-n;
          smoke_shells=abs(smoke_start-smoke_end);
```

```
            smoke_length=smoke_shells*(paths(1,1)-paths(1,2));
            clear_shells=smoke_start-1;
            clear_length=clear_shells*(paths(1,1)-paths(1,2));

            ambK=0;
            for j=1:clear_shells;
               ambK=ambK+wall_c_K(i,3+shells+1-j);
            end
            clear_ave_K=ambK/clear_shells;
            decay_factor=exp(-clear_ave_K*clear_length);

            smokeK=0;
            smokeT=0;
            for j=1:smoke_shells;
               smokeK=smokeK+wall_c_K(i,3+shells-clear_shells-j+1);
               smokeT=smokeT+(wall_c_T(i,3+shells-clear_shells-j+1));
            end
            smoke_ave_K=smokeK/(smoke_shells+0.0001);
            smoke_emissivity=1-exp(-smoke_ave_K*smoke_length);
            smoke_ave_T=(smokeT)/(smoke_shells+0.0001);
            if smoke_start==shells;
            radiative =0;
            else

radiative=(wall_c_s(i,smoke_end)*areas(3,smoke_end)*smoke_emissivity*5.67E-
8*(smoke_ave_T+273)^4*decay_factor*0.001)/areas(4,smoke_end);
            end
            wall_c_q_r(i,3+tc)=radiative;
         end
      end


wall_c_q_cV(:,tc)=interp3(room_x,room_y,room_z,room_QcV,wall_c_q_c(:,1),wall_c_q_c
(:,2),wall_c_q_c(:,3));

wall_c_q_cA(:,tc)=round(interp3(room_x,room_y,room_z,room_QcA,wall_c_q_c(:,1),wall_
c_q_c(:,2),wall_c_q_c(:,3)));

wall_c_q_cT(:,tc)=interp3(room_x,room_y,room_z,room_T,wall_c_q_c(:,1),wall_c_q_c(:,2
),wall_c_q_c(:,3));

Lw=size(wall_c_q_c);
for i=1:Lw(1,1);
   if abs(wall_c_q_cA(i,tc))==1;

wall_c_q_c(i,3+tc)=0.001*interp2(conv_hV,conv_hL,conv_h,wall_c_q_cV(i,tc),x_L)*wall_c
_q_cT(i,tc);
   else if abs(wall_c_q_cA(i,tc))==2;

wall_c_q_c(i,3+tc)=0.001*interp2(conv_hV,conv_hL,conv_h,wall_c_q_cV(i,tc),y_L)*wall_c
_q_cT(i,tc);
      else if abs(wall_c_q_cA(i,tc))==3;

wall_c_q_c(i,3+tc)=0.001*interp2(conv_hV,conv_hL,conv_h,wall_c_q_cV(i,tc),z_L)*wall_c
_q_cT(i,tc);
         end
```

```
      end
   end
end
      wall_c_q_t(:,3+tc)=wall_c_q_r(:,3+tc)+wall_c_q_c(:,3+tc);

   else if wall==4;

         if tc==1;
      wall_d_q_r=[wall_d(:,1) wall_d(:,2) wall_d(:,3)];
      wall_d_q_c=[wall_d(:,1) wall_d(:,2) wall_d(:,3)];
      wall_d_q_t=[wall_d(:,1) wall_d(:,2) wall_d(:,3)];
      end
                  [a,b]=size(wall_d);
     for i=1:a;
        if wall_d_K(i,3+shells)>extlimit;
        qr=0;
           for j=1:shells;
            qr=qr+wall_d_qr(i,3+j);
         end
         wall_d_q_r(i,3+tc)=qr;
        else
           for n=shells:-1:1;
              extvalue=wall_d_K(i,3+n);
              if extvalue>extlimit;
                 break
              end
           end
           smoke_start=shells+1-n;
           smoke_check=n;
           for n=smoke_check:-1:1;
              extvalue=wall_d_K(i,3+n);
              if extvalue<extlimit;
                 break
              end
           end
           smoke_end=shells+1-n;
           smoke_shells=abs(smoke_start-smoke_end);
           smoke_length=smoke_shells*(paths(1,1)-paths(1,2));
           clear_shells=smoke_start-1;
           clear_length=clear_shells*(paths(1,1)-paths(1,2));

           ambK=0;
           for j=1:clear_shells;
              ambK=ambK+wall_d_K(i,3+shells+1-j);
           end
           clear_ave_K=ambK/clear_shells;
           decay_factor=exp(-clear_ave_K*clear_length);

           smokeK=0;
           smokeT=0;
           for j=1:smoke_shells;
              smokeK=smokeK+wall_d_K(i,3+shells-clear_shells-j+1);
              smokeT=smokeT+(wall_d_T(i,3+shells-clear_shells-j+1));
           end
           smoke_ave_K=smokeK/(smoke_shells+0.0001);
           smoke_emissivity=1-exp(-smoke_ave_K*smoke_length);
```

```
            smoke_ave_T=(smokeT)/(smoke_shells+0.0001);
            if smoke_start==shells;
            radiative =0;
            else

radiative=(wall_d_s(i,smoke_end)*areas(3,smoke_end)*smoke_emissivity*5.67E-
8*(smoke_ave_T+273)^4*decay_factor*0.001)/areas(4,smoke_end);
            end
            wall_d_q_r(i,3+tc)=radiative;
         end
      end


wall_d_q_cV(:,tc)=interp3(room_x,room_y,room_z,room_QcV,wall_d_q_c(:,1),wall_d_q_c
(:,2),wall_d_q_c(:,3));

wall_d_q_cA(:,tc)=round(interp3(room_x,room_y,room_z,room_QcA,wall_d_q_c(:,1),wall
_d_q_c(:,2),wall_d_q_c(:,3)));

wall_d_q_cT(:,tc)=interp3(room_x,room_y,room_z,room_T,wall_d_q_c(:,1),wall_d_q_c(:,2
),wall_d_q_c(:,3));

Lw=size(wall_d_q_c);
for i=1:Lw(1,1);
   if abs(wall_d_q_cA(i,tc))==1;

wall_d_q_c(i,3+tc)=0.001*interp2(conv_hV,conv_hL,conv_h,wall_d_q_cV(i,tc),x_L)*wall_
d_q_cT(i,tc);
   else if abs(wall_d_q_cA(i,tc))==2;

wall_d_q_c(i,3+tc)=0.001*interp2(conv_hV,conv_hL,conv_h,wall_d_q_cV(i,tc),y_L)*wall_
d_q_cT(i,tc);
      else if abs(wall_d_q_cA(i,tc))==3;

wall_d_q_c(i,3+tc)=0.001*interp2(conv_hV,conv_hL,conv_h,wall_d_q_cV(i,tc),z_L)*wall_
d_q_cT(i,tc);
         end
      end
   end
end
         wall_d_q_t(:,3+tc)=wall_d_q_r(:,3+tc)+wall_d_q_c(:,3+tc);

   else if wall==5;

         if tc==1;
        wall_e_q_r=[wall_e(:,1) wall_e(:,2) wall_e(:,3)];
         wall_e_q_c=[wall_e(:,1) wall_e(:,2) wall_e(:,3)];
         wall_e_q_t=[wall_e(:,1) wall_e(:,2) wall_e(:,3)];
        end
             [a,b]=size(wall_e);
      for i=1:a;
        if wall_e_K(i,3+shells)>extlimit;
         qr=0;
         for j=1:shells;
            qr=qr+wall_e_qr(i,3+j);
         end
```

```
        wall_e_q_r(i,3+tc)=qr;
      else
        for n=shells:-1:1;
          extvalue=wall_e_K(i,3+n);
          if extvalue>extlimit;
            break
          end
        end
        smoke_start=shells+1-n;
        smoke_check=n;
        for n=smoke_check:-1:1;
          extvalue=wall_e_K(i,3+n);
          if extvalue<extlimit;
            break
          end
        end
        smoke_end=shells+1-n;
        smoke_shells=abs(smoke_start-smoke_end);
        smoke_length=smoke_shells*(paths(1,1)-paths(1,2));
        clear_shells=smoke_start-1;
        clear_length=clear_shells*(paths(1,1)-paths(1,2));

        ambK=0;
        for j=1:clear_shells;
          ambK=ambK+wall_e_K(i,3+shells+1-j);
        end
        clear_ave_K=ambK/clear_shells;
        decay_factor=exp(-clear_ave_K*clear_length);

        smokeK=0;
        smokeT=0;
        for j=1:smoke_shells;
          smokeK=smokeK+wall_e_K(i,3+shells-clear_shells-j+1);
          smokeT=smokeT+(wall_e_T(i,3+shells-clear_shells-j+1));
        end
        smoke_ave_K=smokeK/(smoke_shells+0.0001);
        smoke_emissivity=1-exp(-smoke_ave_K*smoke_length);
        smoke_ave_T=(smokeT)/(smoke_shells+0.0001);
        if smoke_start==shells;
        radiative =0;
        else

radiative=(wall_e_s(i,smoke_end)*areas(3,smoke_end)*smoke_emissivity*5.67E-
8*(smoke_ave_T+273)^4*decay_factor*0.001)/areas(4,smoke_end);
        end
        wall_e_q_r(i,3+tc)=radiative;
      end
    end


wall_e_q_cV(:,tc)=interp3(room_x,room_y,room_z,room_QcV,wall_e_q_c(:,1),wall_e_q_c
(:,2),wall_e_q_c(:,3));

wall_e_q_cA(:,tc)=round(interp3(room_x,room_y,room_z,room_QcA,wall_e_q_c(:,1),wall
_e_q_c(:,2),wall_e_q_c(:,3)));
```

```
wall_e_q_cT(:,tc)=interp3(room_x,room_y,room_z,room_T,wall_e_q_c(:,1),wall_e_q_c(:,2
),wall_e_q_c(:,3));

Lw=size(wall_e_q_c);
for i=1:Lw(1,1);
   if abs(wall_e_q_cA(i,tc))==1;

wall_e_q_c(i,3+tc)=0.001*interp2(conv_hV,conv_hL,conv_h,wall_e_q_cV(i,tc),x_L)*wall_
e_q_cT(i,tc);
   else if abs(wall_e_q_cA(i,tc))==2;

wall_e_q_c(i,3+tc)=0.001*interp2(conv_hV,conv_hL,conv_h,wall_e_q_cV(i,tc),y_L)*wall_
e_q_cT(i,tc);
      else if abs(wall_e_q_cA(i,tc))==3;

wall_e_q_c(i,3+tc)=0.001*interp2(conv_hV,conv_hL,conv_h,wall_e_q_cV(i,tc),z_L)*wall_
e_q_cT(i,tc);
         end
      end
   end
end

      wall_e_q_t(:,3+tc)=wall_e_q_r(:,3+tc)+wall_e_q_c(:,3+tc);

   else if wall==6;

         if tc==1;
      wall_f_q_r=[wall_f(:,1) wall_f(:,2) wall_f(:,3)];
      wall_f_q_c=[wall_f(:,1) wall_f(:,2) wall_f(:,3)];
      wall_f_q_t=[wall_f(:,1) wall_f(:,2) wall_f(:,3)];
      end
            [a,b]=size(wall_f);
     for i=1:a;
        if wall_f_K(i,3+shells)>extlimit;
         qr=0;
         for j=1:shells;
            qr=qr+wall_f_qr(i,3+j);
         end
         wall_f_q_r(i,3+tc)=qr;
        else
           for n=shells:-1:1;
              extvalue=wall_f_K(i,3+n);
              if extvalue>extlimit;
                 break
              end
           end
           smoke_start=shells+1-n;
           smoke_check=n;
           for n=smoke_check:-1:1;
              extvalue=wall_f_K(i,3+n);
              if extvalue<extlimit;
                 break
              end
           end
           smoke_end=shells+1-n;
```

```
            smoke_shells=abs(smoke_start-smoke_end);
            smoke_length=smoke_shells*(paths(1,1)-paths(1,2));
            clear_shells=smoke_start-1;
            clear_length=clear_shells*(paths(1,1)-paths(1,2));

            ambK=0;
            for j=1:clear_shells;
               ambK=ambK+wall_f_K(i,3+shells+1-j);
            end
            clear_ave_K=ambK/clear_shells;
            decay_factor=exp(-clear_ave_K*clear_length);

            smokeK=0;
            smokeT=0;
            for j=1:smoke_shells;
               smokeK=smokeK+wall_f_K(i,3+shells-clear_shells-j+1);
               smokeT=smokeT+(wall_f_T(i,3+shells-clear_shells-j+1));
            end
            smoke_ave_K=smokeK/(smoke_shells+0.0001);
            smoke_emissivity=1-exp(-smoke_ave_K*smoke_length);
            smoke_ave_T=(smokeT)/(smoke_shells+0.0001);
            if smoke_start==shells;
            radiative =0;
            else

radiative=(wall_f_s(i,smoke_end)*areas(3,smoke_end)*smoke_emissivity*5.67E-
8*(smoke_ave_T+273)^4*decay_factor*0.001)/areas(4,smoke_end);
            end
            wall_f_q_r(i,3+tc)=radiative;
         end
      end


wall_f_q_cV(:,tc)=interp3(room_x,room_y,room_z,room_QcV,wall_f_q_c(:,1),wall_f_q_c(:,
2),wall_f_q_c(:,3));

wall_f_q_cA(:,tc)=round(interp3(room_x,room_y,room_z,room_QcA,wall_f_q_c(:,1),wall_f
_q_c(:,2),wall_f_q_c(:,3)));

wall_f_q_cT(:,tc)=interp3(room_x,room_y,room_z,room_T,wall_f_q_c(:,1),wall_f_q_c(:,2),
wall_f_q_c(:,3));

Lw=size(wall_f_q_c);
for i=1:Lw(1,1);
   if abs(wall_f_q_cA(i,tc))==1;

wall_f_q_c(i,3+tc)=0.001*interp2(conv_hV,conv_hL,conv_h,wall_f_q_cV(i,tc),x_L)*wall_f_
q_cT(i,tc);
   else if abs(wall_f_q_cA(i,tc))==2;

wall_f_q_c(i,3+tc)=0.001*interp2(conv_hV,conv_hL,conv_h,wall_f_q_cV(i,tc),y_L)*wall_f_
q_cT(i,tc);
      else if abs(wall_f_q_cA(i,tc))==3;

wall_f_q_c(i,3+tc)=0.001*interp2(conv_hV,conv_hL,conv_h,wall_f_q_cV(i,tc),z_L)*wall_f_
q_cT(i,tc);
```

```
        end
      end
   end
end
        wall_f_q_t(:,3+tc)=wall_f_q_r(:,3+tc)+wall_f_q_c(:,3+tc);


      end
            end
          end
        end
      end
  end
end


end

% This program averages fluxes over given times
% This program averages the fluxes between the characteristic times.
clear tc;
for tc=1:no_of_calcs;

for wall=1:6;  % Perform calculation for each wall

  if wall==1; % Do for first wall...

     if tc==1;
      wall_a_q_r_ave=[wall_a(:,1) wall_a(:,2) wall_a(:,3)];  %  Creates a matrix of coords
      wall_a_q_c_ave=[wall_a(:,1) wall_a(:,2) wall_a(:,3)];
      wall_a_q_t_ave=[wall_a(:,1) wall_a(:,2) wall_a(:,3)];
     end
          [a,b]=size(wall_a);
     for i=1:a;  %  For wall points on wall
        if tc==1;
        wall_a_q_r_ave(i,(2*tc)+1+tc)=wall_a_q_r(i,3+tc)/2;
        wall_a_q_r_ave(i,(2*tc)+2+tc)=wall_a_q_r_ave(i,(2*tc)+1+tc);
        wall_a_q_c_ave(i,(2*tc)+1+tc)=wall_a_q_c(i,3+tc)/2;
        wall_a_q_c_ave(i,(2*tc)+2+tc)=wall_a_q_c_ave(i,(2*tc)+1+tc);
        wall_a_q_t_ave(i,(2*tc)+1+tc)=wall_a_q_t(i,3+tc)/2;
        wall_a_q_t_ave(i,(2*tc)+2+tc)=wall_a_q_t_ave(i,(2*tc)+1+tc);
        else
           wall_a_q_r_ave(i,(2*tc)+2)=(wall_a_q_r(i,3+tc-1)+wall_a_q_r(i,3+tc))/2;
           wall_a_q_r_ave(i,(2*tc)+3)=wall_a_q_r_ave(i,(2*tc)+2);
           wall_a_q_c_ave(i,(2*tc)+2)=(wall_a_q_c(i,3+tc-1)+wall_a_q_c(i,3+tc))/2;
           wall_a_q_c_ave(i,(2*tc)+3)=wall_a_q_c_ave(i,(2*tc)+2);
           wall_a_q_t_ave(i,(2*tc)+2)=(wall_a_q_t(i,3+tc-1)+wall_a_q_t(i,3+tc))/2;
           wall_a_q_t_ave(i,(2*tc)+3)=wall_a_q_t_ave(i,(2*tc)+2);
        end
     end

  else if wall==2;  % Continue for all walls...

     if tc==1;
      wall_b_q_r_ave=[wall_b(:,1) wall_b(:,2) wall_b(:,3)];  %  Creates a matrix of coords
```

```
    wall_b_q_c_ave=[wall_b(:,1) wall_b(:,2) wall_b(:,3)];
    wall_b_q_t_ave=[wall_b(:,1) wall_b(:,2) wall_b(:,3)];
  end
              [a,b]=size(wall_b);
  for i=1:a;  %  For wall points on wall
     if tc==1;
     wall_b_q_r_ave(i,(2*tc)+1+tc)=wall_b_q_r(i,3+tc)/2;
     wall_b_q_r_ave(i,(2*tc)+2+tc)=wall_b_q_r_ave(i,(2*tc)+1+tc);
     wall_b_q_c_ave(i,(2*tc)+1+tc)=wall_b_q_c(i,3+tc)/2;
     wall_b_q_c_ave(i,(2*tc)+2+tc)=wall_b_q_c_ave(i,(2*tc)+1+tc);
     wall_b_q_t_ave(i,(2*tc)+1+tc)=wall_b_q_t(i,3+tc)/2;
     wall_b_q_t_ave(i,(2*tc)+2+tc)=wall_b_q_t_ave(i,(2*tc)+1+tc);
     else
        wall_b_q_r_ave(i,(2*tc)+2)=(wall_b_q_r(i,3+tc-1)+wall_b_q_r(i,3+tc))/2;
        wall_b_q_r_ave(i,(2*tc)+3)=wall_b_q_r_ave(i,(2*tc)+2);
        wall_b_q_c_ave(i,(2*tc)+2)=(wall_b_q_c(i,3+tc-1)+wall_b_q_c(i,3+tc))/2;
        wall_b_q_c_ave(i,(2*tc)+3)=wall_b_q_c_ave(i,(2*tc)+2);
        wall_b_q_t_ave(i,(2*tc)+2)=(wall_b_q_t(i,3+tc-1)+wall_b_q_t(i,3+tc))/2;
        wall_b_q_t_ave(i,(2*tc)+3)=wall_b_q_t_ave(i,(2*tc)+2);
     end
  end

else if wall==3;

  if tc==1;
   wall_c_q_r_ave=[wall_c(:,1) wall_c(:,2) wall_c(:,3)];  %  Creates a matrix of coords
   wall_c_q_c_ave=[wall_c(:,1) wall_c(:,2) wall_c(:,3)];
   wall_c_q_t_ave=[wall_c(:,1) wall_c(:,2) wall_c(:,3)];
  end
            [a,b]=size(wall_c);
  for i=1:a;  %  For wall points on wall
     if tc==1;
     wall_c_q_r_ave(i,(2*tc)+1+tc)=wall_c_q_r(i,3+tc)/2;
     wall_c_q_r_ave(i,(2*tc)+2+tc)=wall_c_q_r_ave(i,(2*tc)+1+tc);
     wall_c_q_c_ave(i,(2*tc)+1+tc)=wall_c_q_c(i,3+tc)/2;
     wall_c_q_c_ave(i,(2*tc)+2+tc)=wall_c_q_c_ave(i,(2*tc)+1+tc);
     wall_c_q_t_ave(i,(2*tc)+1+tc)=wall_c_q_t(i,3+tc)/2;
     wall_c_q_t_ave(i,(2*tc)+2+tc)=wall_c_q_t_ave(i,(2*tc)+1+tc);
     else
        wall_c_q_r_ave(i,(2*tc)+2)=(wall_c_q_r(i,3+tc-1)+wall_c_q_r(i,3+tc))/2;
        wall_c_q_r_ave(i,(2*tc)+3)=wall_c_q_r_ave(i,(2*tc)+2);
        wall_c_q_c_ave(i,(2*tc)+2)=(wall_c_q_c(i,3+tc-1)+wall_c_q_c(i,3+tc))/2;
        wall_c_q_c_ave(i,(2*tc)+3)=wall_c_q_c_ave(i,(2*tc)+2);
        wall_c_q_t_ave(i,(2*tc)+2)=(wall_c_q_t(i,3+tc-1)+wall_c_q_t(i,3+tc))/2;
        wall_c_q_t_ave(i,(2*tc)+3)=wall_c_q_t_ave(i,(2*tc)+2);
     end
  end

else if wall==4;

  if tc==1;
   wall_d_q_r_ave=[wall_d(:,1) wall_d(:,2) wall_d(:,3)];  %  Creates a matrix of coords
   wall_d_q_c_ave=[wall_d(:,1) wall_d(:,2) wall_d(:,3)];
   wall_d_q_t_ave=[wall_d(:,1) wall_d(:,2) wall_d(:,3)];
  end
          [a,b]=size(wall_d);
```

```
    for i=1:a;  %  For wall points on wall
       if tc==1;
       wall_d_q_r_ave(i,(2*tc)+1+tc)=wall_d_q_r(i,3+tc)/2;
       wall_d_q_r_ave(i,(2*tc)+2+tc)=wall_d_q_r_ave(i,(2*tc)+1+tc);
       wall_d_q_c_ave(i,(2*tc)+1+tc)=wall_d_q_c(i,3+tc)/2;
       wall_d_q_c_ave(i,(2*tc)+2+tc)=wall_d_q_c_ave(i,(2*tc)+1+tc);
       wall_d_q_t_ave(i,(2*tc)+1+tc)=wall_d_q_t(i,3+tc)/2;
       wall_d_q_t_ave(i,(2*tc)+2+tc)=wall_d_q_t_ave(i,(2*tc)+1+tc);
       else
          wall_d_q_r_ave(i,(2*tc)+2)=(wall_d_q_r(i,3+tc-1)+wall_d_q_r(i,3+tc))/2;
          wall_d_q_r_ave(i,(2*tc)+3)=wall_d_q_r_ave(i,(2*tc)+2);
          wall_d_q_c_ave(i,(2*tc)+2)=(wall_d_q_c(i,3+tc-1)+wall_d_q_c(i,3+tc))/2;
          wall_d_q_c_ave(i,(2*tc)+3)=wall_d_q_c_ave(i,(2*tc)+2);
          wall_d_q_t_ave(i,(2*tc)+2)=(wall_d_q_t(i,3+tc-1)+wall_d_q_t(i,3+tc))/2;
          wall_d_q_t_ave(i,(2*tc)+3)=wall_d_q_t_ave(i,(2*tc)+2);
       end
    end

else if wall==5;

    if tc==1;
     wall_e_q_r_ave=[wall_e(:,1) wall_e(:,2) wall_e(:,3)];  %  Creates a matrix of coords
     wall_e_q_c_ave=[wall_e(:,1) wall_e(:,2) wall_e(:,3)];
     wall_e_q_t_ave=[wall_e(:,1) wall_e(:,2) wall_e(:,3)];
    end
              [a,b]=size(wall_e);
    for i=1:a;  %  For wall points on wall
       if tc==1;
       wall_e_q_r_ave(i,(2*tc)+1+tc)=wall_e_q_r(i,3+tc)/2;
       wall_e_q_r_ave(i,(2*tc)+2+tc)=wall_e_q_r_ave(i,(2*tc)+1+tc);
       wall_e_q_c_ave(i,(2*tc)+1+tc)=wall_e_q_c(i,3+tc)/2;
       wall_e_q_c_ave(i,(2*tc)+2+tc)=wall_e_q_c_ave(i,(2*tc)+1+tc);
       wall_e_q_t_ave(i,(2*tc)+1+tc)=wall_e_q_t(i,3+tc)/2;
       wall_e_q_t_ave(i,(2*tc)+2+tc)=wall_e_q_t_ave(i,(2*tc)+1+tc);
       else
          wall_e_q_r_ave(i,(2*tc)+2)=(wall_e_q_r(i,3+tc-1)+wall_e_q_r(i,3+tc))/2;
          wall_e_q_r_ave(i,(2*tc)+3)=wall_e_q_r_ave(i,(2*tc)+2);
          wall_e_q_c_ave(i,(2*tc)+2)=(wall_e_q_c(i,3+tc-1)+wall_e_q_c(i,3+tc))/2;
          wall_e_q_c_ave(i,(2*tc)+3)=wall_e_q_c_ave(i,(2*tc)+2);
          wall_e_q_t_ave(i,(2*tc)+2)=(wall_e_q_t(i,3+tc-1)+wall_e_q_t(i,3+tc))/2;
          wall_e_q_t_ave(i,(2*tc)+3)=wall_e_q_t_ave(i,(2*tc)+2);
       end
    end

else if wall==6;

    if tc==1;
     wall_f_q_r_ave=[wall_f(:,1) wall_f(:,2) wall_f(:,3)];  %  Creates a matrix of coords
     wall_f_q_c_ave=[wall_f(:,1) wall_f(:,2) wall_f(:,3)];
     wall_f_q_t_ave=[wall_f(:,1) wall_f(:,2) wall_f(:,3)];
    end
               [a,b]=size(wall_f);
    for i=1:a;  %  For wall points on wall
       if tc==1;
       wall_f_q_r_ave(i,(2*tc)+1+tc)=wall_f_q_r(i,3+tc)/2;
       wall_f_q_r_ave(i,(2*tc)+2+tc)=wall_f_q_r_ave(i,(2*tc)+1+tc);
```

```
        wall_f_q_c_ave(i,(2*tc)+1+tc)=wall_f_q_c(i,3+tc)/2;
        wall_f_q_c_ave(i,(2*tc)+2+tc)=wall_f_q_c_ave(i,(2*tc)+1+tc);
        wall_f_q_t_ave(i,(2*tc)+1+tc)=wall_f_q_t(i,3+tc)/2;
        wall_f_q_t_ave(i,(2*tc)+2+tc)=wall_f_q_t_ave(i,(2*tc)+1+tc);
        else
           wall_f_q_r_ave(i,(2*tc)+2)=(wall_f_q_r(i,3+tc-1)+wall_f_q_r(i,3+tc))/2;
           wall_f_q_r_ave(i,(2*tc)+3)=wall_f_q_r_ave(i,(2*tc)+2);
           wall_f_q_c_ave(i,(2*tc)+2)=(wall_f_q_c(i,3+tc-1)+wall_f_q_c(i,3+tc))/2;
           wall_f_q_c_ave(i,(2*tc)+3)=wall_f_q_c_ave(i,(2*tc)+2);
           wall_f_q_t_ave(i,(2*tc)+2)=(wall_f_q_t(i,3+tc-1)+wall_f_q_t(i,3+tc))/2;
           wall_f_q_t_ave(i,(2*tc)+3)=wall_f_q_t_ave(i,(2*tc)+2);
        end
     end
     end
     end
     end
     end
     end
  end
end
end

% This writes the output to .csv files
% writing_data

disp('***')
disp('Calculation complete - Writing output to .csv files...')
disp('***')

for wall=1:6;  % Perform calculation for each wall

  if wall==1; % Do for first wall...

% Write total gauge heat flux
fid=fopen('wall-3_qt.csv', 'w+');
fprintf(fid, ' -, -, -,Time (s) \n');
fprintf(fid, 'X,Y,Z,');
for i=1:length(times);
       fprintf(fid, '%8.5f,', times(1,i));
end
fprintf(fid, '\n');
fprintf(fid, '(m),(m),(m),Total Gauge Heat Flux (kW/m^2) \n');
[r,c]=size(wall_a_q_t_ave);
for i=1:r;
   for j=1:c;
      fprintf(fid, '%8.5f,', wall_a_q_t_ave(i,j));
   end
   fprintf(fid, '\n');
end
fclose(fid);

% Write convective gauge heat flux
fid=fopen('wall-3_qc.csv', 'w+');
fprintf(fid, ' -, -, -,Time (s) \n');
fprintf(fid, 'X,Y,Z,');
```

```
for i=1:length(times);
      fprintf(fid, '%8.5f,', times(1,i));
end
fprintf(fid, '\n');
fprintf(fid, '(m),(m),(m),Convective Gauge Heat Flux (kW/m^2) \n');
[r,c]=size(wall_a_q_c_ave);
for i=1:r;
   for j=1:c;
      fprintf(fid, '%8.5f,', wall_a_q_c_ave(i,j));
   end
   fprintf(fid, '\n');
end
fclose(fid);

% Write radiative gauge heat flux
fid=fopen('wall-3_qr.csv', 'w+');
fprintf(fid, ' -, -, -,Time (s) \n');
fprintf(fid, 'X,Y,Z,');
for i=1:length(times);
      fprintf(fid, '%8.5f,', times(1,i));
end
fprintf(fid, '\n');
fprintf(fid, '(m),(m),(m),Radiative Gauge Heat Flux (kW/m^2) \n');
[r,c]=size(wall_a_q_r_ave);
for i=1:r;
   for j=1:c;
      fprintf(fid, '%8.5f,', wall_a_q_r_ave(i,j));
   end
   fprintf(fid, '\n');
end
fclose(fid);

  else if wall==2;  % Continue with other walls...

fid=fopen('wall-2_qt.csv', 'w+');
fprintf(fid, ' -, -, -,Time (s) \n');
fprintf(fid, 'X,Y,Z,');
for i=1:length(times);
      fprintf(fid, '%8.5f,', times(1,i));
end
fprintf(fid, '\n');
fprintf(fid, '(m),(m),(m),Total Gauge Heat Flux (kW/m^2) \n');
[r,c]=size(wall_b_q_t_ave);
for i=1:r;
   for j=1:c;
      fprintf(fid, '%8.5f,', wall_b_q_t_ave(i,j));
   end
   fprintf(fid, '\n');
end
fclose(fid);

fid=fopen('wall-2_qc.csv', 'w+');
fprintf(fid, ' -, -, -,Time (s) \n');
fprintf(fid, 'X,Y,Z,');
for i=1:length(times);
      fprintf(fid, '%8.5f,', times(1,i));
```

```
end
fprintf(fid, '\n');
fprintf(fid, '(m),(m),(m),Convective Gauge Heat Flux (kW/m^2) \n');
[r,c]=size(wall_b_q_c_ave);
for i=1:r;
   for j=1:c;
      fprintf(fid, '%8.5f,', wall_b_q_c_ave(i,j));
   end
   fprintf(fid, '\n');
end
fclose(fid);

fid=fopen('wall-2_qr.csv', 'w+');
fprintf(fid, ' -, -, -,Time (s) \n');
fprintf(fid, 'X,Y,Z,');
for i=1:length(times);
      fprintf(fid, '%8.5f,', times(1,i));
end
fprintf(fid, '\n');
fprintf(fid, '(m),(m),(m),Radiative Gauge Heat Flux (kW/m^2) \n');
[r,c]=size(wall_b_q_r_ave);
for i=1:r;
   for j=1:c;
      fprintf(fid, '%8.5f,', wall_b_q_r_ave(i,j));
   end
   fprintf(fid, '\n');
end
fclose(fid);

  else if wall==3;

fid=fopen('wall-1_qt.csv', 'w+');
fprintf(fid, ' -, -, -,Time (s) \n');
fprintf(fid, 'X,Y,Z,');
for i=1:length(times);
      fprintf(fid, '%8.5f,', times(1,i));
end
fprintf(fid, '\n');
fprintf(fid, '(m),(m),(m),Total Gauge Heat Flux (kW/m^2) \n');
[r,c]=size(wall_c_q_t_ave);
for i=1:r;
   for j=1:c;
      fprintf(fid, '%8.5f,', wall_c_q_t_ave(i,j));
   end
   fprintf(fid, '\n');
end
fclose(fid);

fid=fopen('wall-1_qc.csv', 'w+');
fprintf(fid, ' -, -, -,Time (s) \n');
fprintf(fid, 'X,Y,Z,');
for i=1:length(times);
      fprintf(fid, '%8.5f,', times(1,i));
end
fprintf(fid, '\n');
fprintf(fid, '(m),(m),(m),Convective Gauge Heat Flux (kW/m^2) \n');
```

```
[r,c]=size(wall_c_q_c_ave);
for i=1:r;
   for j=1:c;
      fprintf(fid, '%8.5f,', wall_c_q_c_ave(i,j));
   end
   fprintf(fid, '\n');
end
fclose(fid);

fid=fopen('wall-1_qr.csv', 'w+');
fprintf(fid, ' -, -, -,Time (s) \n');
fprintf(fid, 'X,Y,Z,');
for i=1:length(times);
      fprintf(fid, '%8.5f,', times(1,i));
end
fprintf(fid, '\n');
fprintf(fid, '(m),(m),(m),Radiative Gauge Heat Flux (kW/m^2) \n');
[r,c]=size(wall_c_q_r_ave);
for i=1:r;
   for j=1:c;
      fprintf(fid, '%8.5f,', wall_c_q_r_ave(i,j));
   end
   fprintf(fid, '\n');
end
fclose(fid);

  else if wall==4;

fid=fopen('wall+1_qt.csv', 'w+');
fprintf(fid, ' -, -, -,Time (s) \n');
fprintf(fid, 'X,Y,Z,');
for i=1:length(times);
      fprintf(fid, '%8.5f,', times(1,i));
end
fprintf(fid, '\n');
fprintf(fid, '(m),(m),(m),Total Gauge Heat Flux (kW/m^2) \n');
[r,c]=size(wall_d_q_t_ave);
for i=1:r;
   for j=1:c;
      fprintf(fid, '%8.5f,', wall_d_q_t_ave(i,j));
   end
   fprintf(fid, '\n');
end
fclose(fid);

fid=fopen('wall+1_qc.csv', 'w+');
fprintf(fid, ' -, -, -,Time (s) \n');
fprintf(fid, 'X,Y,Z,');
for i=1:length(times);
      fprintf(fid, '%8.5f,', times(1,i));
end
fprintf(fid, '\n');
fprintf(fid, '(m),(m),(m),Convective Gauge Heat Flux (kW/m^2) \n');
[r,c]=size(wall_d_q_c_ave);
for i=1:r;
   for j=1:c;
```

```
        fprintf(fid, '%8.5f,', wall_d_q_c_ave(i,j));
    end
    fprintf(fid, '\n');
end
fclose(fid);

fid=fopen('wall+1_qr.csv', 'w+');
fprintf(fid, ' -, -, -,Time (s) \n');
fprintf(fid, 'X,Y,Z,');
for i=1:length(times);
        fprintf(fid, '%8.5f,', times(1,i));
end
fprintf(fid, '\n');
fprintf(fid, '(m),(m),(m),Radiative Gauge Heat Flux (kW/m^2) \n');
[r,c]=size(wall_d_q_r_ave);
for i=1:r;
    for j=1:c;
        fprintf(fid, '%8.5f,', wall_d_q_r_ave(i,j));
    end
    fprintf(fid, '\n');
end
fclose(fid);

  else if wall==5;

fid=fopen('wall+2_qt.csv', 'w+');
fprintf(fid, ' -, -, -,Time (s) \n');
fprintf(fid, 'X,Y,Z,');
for i=1:length(times);
        fprintf(fid, '%8.5f,', times(1,i));
end
fprintf(fid, '\n');
fprintf(fid, '(m),(m),(m),Total Gauge Heat Flux (kW/m^2) \n');
[r,c]=size(wall_e_q_t_ave);
for i=1:r;
    for j=1:c;
        fprintf(fid, '%8.5f,', wall_e_q_t_ave(i,j));
    end
    fprintf(fid, '\n');
end
fclose(fid);

fid=fopen('wall+2_qc.csv', 'w+');
fprintf(fid, ' -, -, -,Time (s) \n');
fprintf(fid, 'X,Y,Z,');
for i=1:length(times);
        fprintf(fid, '%8.5f,', times(1,i));
end
fprintf(fid, '\n');
fprintf(fid, '(m),(m),(m),Convective Gauge Heat Flux (kW/m^2) \n');
[r,c]=size(wall_e_q_c_ave);
for i=1:r;
    for j=1:c;
        fprintf(fid, '%8.5f,', wall_e_q_c_ave(i,j));
    end
    fprintf(fid, '\n');
```

```
end
fclose(fid);

fid=fopen('wall+2_qr.csv', 'w+');
fprintf(fid, ' -, -, -,Time (s) \n');
fprintf(fid, 'X,Y,Z,');
for i=1:length(times);
      fprintf(fid, '%8.5f,', times(1,i));
end
fprintf(fid, '\n');
fprintf(fid, '(m),(m),(m),Radiative Gauge Heat Flux (kW/m^2) \n');
[r,c]=size(wall_e_q_r_ave);
for i=1:r;
   for j=1:c;
      fprintf(fid, '%8.5f,', wall_e_q_r_ave(i,j));
   end
   fprintf(fid, '\n');
end
fclose(fid);

  else if wall==6;

fid=fopen('wall+3_qt.csv', 'w+');
fprintf(fid, ' -, -, -,Time (s) \n');
fprintf(fid, 'X,Y,Z,');
for i=1:length(times);
      fprintf(fid, '%8.5f,', times(1,i));
end
fprintf(fid, '\n');
fprintf(fid, '(m),(m),(m),Total Gauge Heat Flux (kW/m^2) \n');
[r,c]=size(wall_f_q_t_ave);
for i=1:r;
   for j=1:c;
      fprintf(fid, '%8.5f,', wall_f_q_t_ave(i,j));
   end
   fprintf(fid, '\n');
end
fclose(fid);

fid=fopen('wall+3_qc.csv', 'w+');
fprintf(fid, ' -, -, -,Time (s) \n');
fprintf(fid, 'X,Y,Z,');
for i=1:length(times);
      fprintf(fid, '%8.5f,', times(1,i));
end
fprintf(fid, '\n');
fprintf(fid, '(m),(m),(m),Convective Gauge Heat Flux (kW/m^2) \n');
[r,c]=size(wall_f_q_c_ave);
for i=1:r;
   for j=1:c;
      fprintf(fid, '%8.5f,', wall_f_q_c_ave(i,j));
   end
   fprintf(fid, '\n');
end
fclose(fid);
```

```
fid=fopen('wall+3_qr.csv', 'w+');
fprintf(fid, ' -, -, -,Time (s) \n');
fprintf(fid, 'X,Y,Z,');
for i=1:length(times);
        fprintf(fid, '%8.5f,', times(1,i));
end
fprintf(fid, '\n');
fprintf(fid, '(m),(m),(m),Radiative Gauge Heat Flux (kW/m^2) \n');
[r,c]=size(wall_f_q_r_ave);
for i=1:r;
    for j=1:c;
        fprintf(fid, '%8.5f,', wall_f_q_r_ave(i,j));
    end
    fprintf(fid, '\n');
end
fclose(fid);

      end
      end
      end
      end
      end
   end
end
disp('End');
```

Appendix C

FDS data file for the Cardington Large Scale Fire Test 8

```
&HEAD CHID='cardington_test8',TITLE='Cardington Large Scale Fire
Tests - TEST 8' /
&GRID IBAR=72,JBAR=62,KBAR=24 /
&PDIM XBAR0=0,XBAR=14.4,YBAR0=0,YBAR=12.4,ZBAR0=0,ZBAR=4.8 /
&TIME TWFIN=7200 /

&MISC NFRAMES=7200 /

&RAMP ID='cribs', T=0, F=0 /
&RAMP ID='cribs', T=100, F=0.029 /
&RAMP ID='cribs', T=200, F=0.117 /
&RAMP ID='cribs', T=300, F=0.263 /
&RAMP ID='cribs', T=400, F=0.467 /
&RAMP ID='cribs', T=500, F=0.729 /
&RAMP ID='cribs', T=600, F=1.000 /
&RAMP ID='cribs', T=1800, F=1.000 /
&RAMP ID='cribs', T=3800, F=0 /

&SURF ID     = 'GYPSUM BOARD',
      FYI    = 'Quintiere, Fire Behavior',
      RGB    = 0.80,0.80,0.70,
      HRRPUA = 100., RAMP_Q = 'GB',
      KS     = 0.48,
      C_P    = 0.84,
      DENSITY= 1440.,
      DELTA  = 0.013,
      TMPIGN = 400. /
      &RAMP ID='GB',T= 0.0,F=0.0 /
      &RAMP ID='GB',T= 1.0,F=0.5 /
      &RAMP ID='GB',T= 2.0,F=1.0 /
      &RAMP ID='GB',T=10.0,F=1.0 /
      &RAMP ID='GB',T=20.0,F=0.0 /
      &RAMP ID='GB',T=30.0,F=0.0 /

&SURF ID='Burner',HRRPUA=792, RGB=1,1,0, RAMP_Q='cribs' /
&SURF ID='Crib', RGB=1,1,0, /

&VENT CB='XBAR0',SURF_ID='OPEN' /
&VENT CB='XBAR' ,SURF_ID='OPEN' /
&VENT CB='YBAR0',SURF_ID='OPEN' /
&VENT CB='YBAR' ,SURF_ID='OPEN' /
&VENT CB='ZBAR0' ,SURF_ID='OPEN' /
&VENT CB='ZBAR' ,SURF_ID='OPEN' /

&OBST  XB=12.2,12.4,5.2,7.2,0.0,3  SURF_ID='GYPSUM  BOARD'  /  Front
Middle
&OBST XB=0.0,12.4,12.2,12.4,0.0,3 SURF_ID='GYPSUM BOARD' /  Right
Wall
&OBST  XB=0.0,0.2,0.2,12.2,0.0,3  SURF_ID='GYPSUM  BOARD'  /   Back
Wall
&OBST  XB=12.2,12.4,0.2,1.2,0.0,3  SURF_ID='GYPSUM  BOARD'  /   Front
Left
&OBST  XB=0.0,12.4,0.0,0.2,0.0,3  SURF_ID='GYPSUM  BOARD'  /   Left
Wall
&OBST XB=12.2,12.4,11.2,12.2,0.0,3 SURF_ID='GYPSUM BOARD' /  Front
Right
&OBST XB=0.2,12.2,0.2,12.2,0.0,0.0 SURF_ID='GYPSUM BOARD' /  Floor
&OBST XB=0.0,12.4,0.0,12.4,3,3.2 SURF_ID='GYPSUM BOARD' /  Roof
```

```
&OBST XB=0.8,1.8,0.8,1.8,0,0.80 SURF_ID='Crib' / Crib
&OBST XB=2.4,3.4,0.8,1.8,0,0.80 SURF_ID='Crib' / Crib
&OBST XB=4,5,0.8,1.8,0,0.80 SURF_ID='Crib' / Crib
&OBST XB=5.6,6.6,0.8,1.8,0,0.80 SURF_ID='Crib' / Crib
&OBST XB=7.2,8.2,0.8,1.8,0,0.80 SURF_ID='Crib' / Crib
&OBST XB=8.8,9.8,0.8,1.8,0,0.80 SURF_ID='Crib' / Crib
&OBST XB=10.4,11.4,0.8,1.8,0,0.80 SURF_ID='Crib' / Crib
&OBST XB=0.8,1.8,2.4,3.4,0,0.80 SURF_ID='Crib' / Crib
&OBST XB=2.4,3.4,2.4,3.4,0,0.80 SURF_ID='Crib' / Crib
&OBST XB=4,5,2.4,3.4,0,0.80 SURF_ID='Crib' / Crib
&OBST XB=5.6,6.6,2.4,3.4,0,0.80 SURF_ID='Crib' / Crib
&OBST XB=7.2,8.2,2.4,3.4,0,0.80 SURF_ID='Crib' / Crib
&OBST XB=8.8,9.8,2.4,3.4,0,0.80 SURF_ID='Crib' / Crib
&OBST XB=10.4,11.4,2.4,3.4,0,0.80 SURF_ID='Crib' / Crib
&OBST XB=0.8,1.8,4,5,0,0.80 SURF_ID='Crib' / Crib
&OBST XB=2.4,3.4,4,5,0,0.80 SURF_ID='Crib' / Crib
&OBST XB=4,5,4,5,0,0.80 SURF_ID='Crib' / Crib
&OBST XB=5.6,6.6,4,5,0,0.80 SURF_ID='Crib' / Crib
&OBST XB=7.2,8.2,4,5,0,0.80 SURF_ID='Crib' / Crib
&OBST XB=8.8,9.8,4,5,0,0.80 SURF_ID='Crib' / Crib
&OBST XB=10.4,11.4,4,5,0,0.80 SURF_ID='Crib' / Crib
&OBST XB=0.8,1.8,5.6,6.6,0,0.80 SURF_ID='Crib' / Crib
&OBST XB=2.4,3.4,5.6,6.6,0,0.80 SURF_ID='Crib' / Crib
&OBST XB=4,5,5.6,6.6,0,0.80 SURF_ID='Crib' / Crib
&OBST XB=5.6,6.6,5.6,6.6,0,0.80 SURF_ID='Crib' / Crib
&OBST XB=7.2,8.2,5.6,6.6,0,0.80 SURF_ID='Crib' / Crib
&OBST XB=8.8,9.8,5.6,6.6,0,0.80 SURF_ID='Crib' / Crib
&OBST XB=10.4,11.4,5.6,6.6,0,0.80 SURF_ID='Crib' / Crib
&OBST XB=0.8,1.8,7.2,8.2,0,0.80 SURF_ID='Crib' / Crib
&OBST XB=2.4,3.4,7.2,8.2,0,0.80 SURF_ID='Crib' / Crib
&OBST XB=4,5,7.2,8.2,0,0.80 SURF_ID='Crib' / Crib
&OBST XB=5.6,6.6,7.2,8.2,0,0.80 SURF_ID='Crib' / Crib
&OBST XB=7.2,8.2,7.2,8.2,0,0.80 SURF_ID='Crib' / Crib
&OBST XB=8.8,9.8,7.2,8.2,0,0.80 SURF_ID='Crib' / Crib
&OBST XB=10.4,11.4,7.2,8.2,0,0.80 SURF_ID='Crib' / Crib
&OBST XB=0.8,1.8,8.8,9.8,0,0.80 SURF_ID='Crib' / Crib
&OBST XB=2.4,3.4,8.8,9.8,0,0.80 SURF_ID='Crib' / Crib
&OBST XB=4,5,8.8,9.8,0,0.80 SURF_ID='Crib' / Crib
&OBST XB=5.6,6.6,8.8,9.8,0,0.80 SURF_ID='Crib' / Crib
&OBST XB=7.2,8.2,8.8,9.8,0,0.80 SURF_ID='Crib' / Crib
&OBST XB=8.8,9.8,8.8,9.8,0,0.80 SURF_ID='Crib' / Crib
&OBST XB=10.4,11.4,8.8,9.8,0,0.80 SURF_ID='Crib' / Crib
&OBST XB=0.8,1.8,10.4,11.4,0,0.80 SURF_ID='Crib' / Crib
&OBST XB=2.4,3.4,10.4,11.4,0,0.80 SURF_ID='Crib' / Crib
&OBST XB=4,5,10.4,11.4,0,0.80 SURF_ID='Crib' / Crib
&OBST XB=5.6,6.6,10.4,11.4,0,0.80 SURF_ID='Crib' / Crib
&OBST XB=7.2,8.2,10.4,11.4,0,0.80 SURF_ID='Crib' / Crib
&OBST XB=8.8,9.8,10.4,11.4,0,0.80 SURF_ID='Crib' / Crib
&OBST XB=10.4,11.4,10.4,11.4,0,0.80 SURF_ID='Crib' / Crib

&OBST XB=0.8,1.8,0.8,1.8,0.80,1.00 SURF_ID='Burner' / Crib
&OBST XB=2.4,3.4,0.8,1.8,0.80,1.00 SURF_ID='Burner' / Crib
&OBST XB=4,5,0.8,1.8,0.80,1.00 SURF_ID='Burner' / Crib
&OBST XB=5.6,6.6,0.8,1.8,0.80,1.00 SURF_ID='Burner' / Crib
&OBST XB=7.2,8.2,0.8,1.8,0.80,1.00 SURF_ID='Burner' / Crib
&OBST XB=8.8,9.8,0.8,1.8,0.80,1.00 SURF_ID='Burner' / Crib
&OBST XB=10.4,11.4,0.8,1.8,0.80,1.00 SURF_ID='Burner' / Crib
```

```
&OBST XB=0.8,1.8,2.4,3.4,0.80,1.00 SURF_ID='Burner' / Crib
&OBST XB=2.4,3.4,2.4,3.4,0.80,1.00 SURF_ID='Burner' / Crib
&OBST XB=4,5,2.4,3.4,0.80,1.00 SURF_ID='Burner' / Crib
&OBST XB=5.6,6.6,2.4,3.4,0.80,1.00 SURF_ID='Burner' / Crib
&OBST XB=7.2,8.2,2.4,3.4,0.80,1.00 SURF_ID='Burner' / Crib
&OBST XB=8.8,9.8,2.4,3.4,0.80,1.00 SURF_ID='Burner' / Crib
&OBST XB=10.4,11.4,2.4,3.4,0.80,1.00 SURF_ID='Burner' / Crib
&OBST XB=0.8,1.8,4,5,0.80,1.00 SURF_ID='Burner' / Crib
&OBST XB=2.4,3.4,4,5,0.80,1.00 SURF_ID='Burner' / Crib
&OBST XB=4,5,4,5,0.80,1.00 SURF_ID='Burner' / Crib
&OBST XB=5.6,6.6,4,5,0.80,1.00 SURF_ID='Burner' / Crib
&OBST XB=7.2,8.2,4,5,0.80,1.00 SURF_ID='Burner' / Crib
&OBST XB=8.8,9.8,4,5,0.80,1.00 SURF_ID='Burner' / Crib
&OBST XB=10.4,11.4,4,5,0.80,1.00 SURF_ID='Burner' / Crib
&OBST XB=0.8,1.8,5.6,6.6,0.80,1.00 SURF_ID='Burner' / Crib
&OBST XB=2.4,3.4,5.6,6.6,0.80,1.00 SURF_ID='Burner' / Crib
&OBST XB=4,5,5.6,6.6,0.80,1.00 SURF_ID='Burner' / Crib
&OBST XB=5.6,6.6,5.6,6.6,0.80,1.00 SURF_ID='Burner' / Crib
&OBST XB=7.2,8.2,5.6,6.6,0.80,1.00 SURF_ID='Burner' / Crib
&OBST XB=8.8,9.8,5.6,6.6,0.80,1.00 SURF_ID='Burner' / Crib
&OBST XB=10.4,11.4,5.6,6.6,0.80,1.00 SURF_ID='Burner' / Crib
&OBST XB=0.8,1.8,7.2,8.2,0.80,1.00 SURF_ID='Burner' / Crib
&OBST XB=2.4,3.4,7.2,8.2,0.80,1.00 SURF_ID='Burner' / Crib
&OBST XB=4,5,7.2,8.2,0.80,1.00 SURF_ID='Burner' / Crib
&OBST XB=5.6,6.6,7.2,8.2,0.80,1.00 SURF_ID='Burner' / Crib
&OBST XB=7.2,8.2,7.2,8.2,0.80,1.00 SURF_ID='Burner' / Crib
&OBST XB=8.8,9.8,7.2,8.2,0.80,1.00 SURF_ID='Burner' / Crib
&OBST XB=10.4,11.4,7.2,8.2,0.80,1.00 SURF_ID='Burner' / Crib
&OBST XB=0.8,1.8,8.8,9.8,0.80,1.00 SURF_ID='Burner' / Crib
&OBST XB=2.4,3.4,8.8,9.8,0.80,1.00 SURF_ID='Burner' / Crib
&OBST XB=4,5,8.8,9.8,0.80,1.00 SURF_ID='Burner' / Crib
&OBST XB=5.6,6.6,8.8,9.8,0.80,1.00 SURF_ID='Burner' / Crib
&OBST XB=7.2,8.2,8.8,9.8,0.80,1.00 SURF_ID='Burner' / Crib
&OBST XB=8.8,9.8,8.8,9.8,0.80,1.00 SURF_ID='Burner' / Crib
&OBST XB=10.4,11.4,8.8,9.8,0.80,1.00 SURF_ID='Burner' / Crib
&OBST XB=0.8,1.8,10.4,11.4,0.80,1.00 SURF_ID='Burner' / Crib
&OBST XB=2.4,3.4,10.4,11.4,0.80,1.00 SURF_ID='Burner' / Crib
&OBST XB=4,5,10.4,11.4,0.80,1.00 SURF_ID='Burner' / Crib
&OBST XB=5.6,6.6,10.4,11.4,0.80,1.00 SURF_ID='Burner' / Crib
&OBST XB=7.2,8.2,10.4,11.4,0.80,1.00 SURF_ID='Burner' / Crib
&OBST XB=8.8,9.8,10.4,11.4,0.80,1.00 SURF_ID='Burner' / Crib
&OBST XB=10.4,11.4,10.4,11.4,0.80,1.00 SURF_ID='Burner' / Crib

&SLCF PBY=3.2 , QUANTITY='TEMPERATURE' /
&SLCF PBY=3.2 , QUANTITY='water vapour' /
&SLCF PBY=3.2 , QUANTITY='carbon dioxide' /
&SLCF PBY=3.2 , QUANTITY='soot volume fraction' /
&SLCF PBY=3.2 , QUANTITY='extinction coefficient' /
&SLCF PBY=3.2 , QUANTITY='soot density' /

&BNDF QUANTITY='HEAT_FLUX' /
&BNDF QUANTITY='GAUGE_HEAT_FLUX' /
&BNDF QUANTITY='RADIATIVE_FLUX' /
&BNDF QUANTITY='CONVECTIVE_FLUX' /
&BNDF QUANTITY='WALL_TEMPERATURE' /

&THCP XYZ=1.7,1.7,1.2, QUANTITY='TEMPERATURE', LABEL='G1a' /
&THCP XYZ=1.7,1.7,2.4, QUANTITY='TEMPERATURE', LABEL='G1b' /
```

```
&THCP XYZ=1.7,1.7,2.7, QUANTITY='TEMPERATURE', LABEL='G1c' /
&THCP XYZ=1.7,1.7,2.9, QUANTITY='TEMPERATURE', LABEL='G1d' /
&THCP XYZ=4.7,1.7,1.2, QUANTITY='TEMPERATURE', LABEL='G5a' /
&THCP XYZ=4.7,1.7,2.4, QUANTITY='TEMPERATURE', LABEL='G5b' /
&THCP XYZ=4.7,1.7,2.7, QUANTITY='TEMPERATURE', LABEL='G5c' /
&THCP XYZ=4.7,1.7,2.9, QUANTITY='TEMPERATURE', LABEL='G5d' /
&THCP XYZ=7.7,1.7,1.2, QUANTITY='TEMPERATURE', LABEL='G9a' /
&THCP XYZ=7.7,1.7,2.4, QUANTITY='TEMPERATURE', LABEL='G9b' /
&THCP XYZ=7.7,1.7,2.7, QUANTITY='TEMPERATURE', LABEL='G9c' /
&THCP XYZ=7.7,1.7,2.9, QUANTITY='TEMPERATURE', LABEL='G9d' /
&THCP XYZ=10.7,1.7,1.2, QUANTITY='TEMPERATURE', LABEL='G13a' /
&THCP XYZ=10.7,1.7,2.4, QUANTITY='TEMPERATURE', LABEL='G13b' /
&THCP XYZ=10.7,1.7,2.7, QUANTITY='TEMPERATURE', LABEL='G13c' /
&THCP XYZ=10.7,1.7,2.9, QUANTITY='TEMPERATURE', LABEL='G13d' /
&THCP XYZ=1.7,4.7,1.2, QUANTITY='TEMPERATURE', LABEL='G2a' /
&THCP XYZ=1.7,4.7,2.4, QUANTITY='TEMPERATURE', LABEL='G2b' /
&THCP XYZ=1.7,4.7,2.7, QUANTITY='TEMPERATURE', LABEL='G2c' /
&THCP XYZ=1.7,4.7,2.9, QUANTITY='TEMPERATURE', LABEL='G2d' /
&THCP XYZ=4.7,4.7,1.2, QUANTITY='TEMPERATURE', LABEL='G6a' /
&THCP XYZ=4.7,4.7,2.4, QUANTITY='TEMPERATURE', LABEL='G6b' /
&THCP XYZ=4.7,4.7,2.7, QUANTITY='TEMPERATURE', LABEL='G6c' /
&THCP XYZ=4.7,4.7,2.9, QUANTITY='TEMPERATURE', LABEL='G6d' /
&THCP XYZ=7.7,4.7,1.2, QUANTITY='TEMPERATURE', LABEL='G10a' /
&THCP XYZ=7.7,4.7,2.4, QUANTITY='TEMPERATURE', LABEL='G10b' /
&THCP XYZ=7.7,4.7,2.7, QUANTITY='TEMPERATURE', LABEL='G10c' /
&THCP XYZ=7.7,4.7,2.9, QUANTITY='TEMPERATURE', LABEL='G10d' /
&THCP XYZ=10.7,4.7,1.2, QUANTITY='TEMPERATURE', LABEL='G14a' /
&THCP XYZ=10.7,4.7,2.4, QUANTITY='TEMPERATURE', LABEL='G14b' /
&THCP XYZ=10.7,4.7,2.7, QUANTITY='TEMPERATURE', LABEL='G14c' /
&THCP XYZ=10.7,4.7,2.9, QUANTITY='TEMPERATURE', LABEL='G14d' /
&THCP XYZ=1.7,7.7,1.2, QUANTITY='TEMPERATURE', LABEL='G3a' /
&THCP XYZ=1.7,7.7,2.4, QUANTITY='TEMPERATURE', LABEL='G3b' /
&THCP XYZ=1.7,7.7,2.7, QUANTITY='TEMPERATURE', LABEL='G3c' /
&THCP XYZ=1.7,7.7,2.9, QUANTITY='TEMPERATURE', LABEL='G3d' /
&THCP XYZ=4.7,7.7,1.2, QUANTITY='TEMPERATURE', LABEL='G7a' /
&THCP XYZ=4.7,7.7,2.4, QUANTITY='TEMPERATURE', LABEL='G7b' /
&THCP XYZ=4.7,7.7,2.7, QUANTITY='TEMPERATURE', LABEL='G7c' /
&THCP XYZ=4.7,7.7,2.9, QUANTITY='TEMPERATURE', LABEL='G7d' /
&THCP XYZ=7.7,7.7,1.2, QUANTITY='TEMPERATURE', LABEL='G11a' /
&THCP XYZ=7.7,7.7,2.4, QUANTITY='TEMPERATURE', LABEL='G11b' /
&THCP XYZ=7.7,7.7,2.7, QUANTITY='TEMPERATURE', LABEL='G11c' /
&THCP XYZ=7.7,7.7,2.9, QUANTITY='TEMPERATURE', LABEL='G11d' /
&THCP XYZ=10.7,7.7,1.2, QUANTITY='TEMPERATURE', LABEL='G15a' /
&THCP XYZ=10.7,7.7,2.4, QUANTITY='TEMPERATURE', LABEL='G15b' /
&THCP XYZ=10.7,7.7,2.7, QUANTITY='TEMPERATURE', LABEL='G15c' /
&THCP XYZ=10.7,7.7,2.9, QUANTITY='TEMPERATURE', LABEL='G15d' /
&THCP XYZ=1.7,10.7,1.2, QUANTITY='TEMPERATURE', LABEL='G4a' /
&THCP XYZ=1.7,10.7,2.4, QUANTITY='TEMPERATURE', LABEL='G4b' /
&THCP XYZ=1.7,10.7,2.7, QUANTITY='TEMPERATURE', LABEL='G4c' /
&THCP XYZ=1.7,10.7,2.9, QUANTITY='TEMPERATURE', LABEL='G4d' /
&THCP XYZ=4.7,10.7,1.2, QUANTITY='TEMPERATURE', LABEL='G8a' /
&THCP XYZ=4.7,10.7,2.4, QUANTITY='TEMPERATURE', LABEL='G8b' /
&THCP XYZ=4.7,10.7,2.7, QUANTITY='TEMPERATURE', LABEL='G8c' /
&THCP XYZ=4.7,10.7,2.9, QUANTITY='TEMPERATURE', LABEL='G8d' /
&THCP XYZ=7.7,10.7,1.2, QUANTITY='TEMPERATURE', LABEL='G12a' /
&THCP XYZ=7.7,10.7,2.4, QUANTITY='TEMPERATURE', LABEL='G12b' /
&THCP XYZ=7.7,10.7,2.7, QUANTITY='TEMPERATURE', LABEL='G12c' /
&THCP XYZ=7.7,10.7,2.9, QUANTITY='TEMPERATURE', LABEL='G12d' /
```

```
&THCP XYZ=10.7,10.7,1.2, QUANTITY='TEMPERATURE', LABEL='G16a' /
&THCP XYZ=10.7,10.7,2.4, QUANTITY='TEMPERATURE', LABEL='G16b' /
&THCP XYZ=10.7,10.7,2.7, QUANTITY='TEMPERATURE', LABEL='G16c' /
&THCP XYZ=10.7,10.7,2.9, QUANTITY='TEMPERATURE', LABEL='G16d' /

&THCP    XYZ=6.2,0.2,1.5,    QUANTITY='RADIATIVE_FLUX',    IOR=+2,
LABEL='Left Wall' /
&THCP    XYZ=6.2,0.2,1.5,    QUANTITY='CONVECTIVE_FLUX',    IOR=+2,
LABEL='Left Wall' /
&THCP  XYZ=6.2,0.2,1.5,  QUANTITY='HEAT_FLUX',  IOR=+2,  LABEL='Left
Wall' /
&THCP    XYZ=6.2,0.2,1.5,    QUANTITY='GAUGE_HEAT_FLUX',    IOR=+2,
LABEL='Left Wall' /
&THCP   XYZ=6.2,0.2,1.5,   QUANTITY='INCIDENT_HEAT_FLUX',   IOR=+2,
LABEL='Left Wall' /
&THCP    XYZ=6.2,0.2,1.5,    QUANTITY='WALL_TEMPERATURE',    IOR=+2,
LABEL='Left Wall' /

&THCP    XYZ=6.2,12.2,1.5,    QUANTITY='RADIATIVE_FLUX',    IOR=-2,
LABEL='Right Wall' /
&THCP    XYZ=6.2,12.2,1.5,    QUANTITY='CONVECTIVE_FLUX',    IOR=-2,
LABEL='Right Wall' /
&THCP XYZ=6.2,12.2,1.5, QUANTITY='HEAT_FLUX', IOR=-2, LABEL='Right
Wall' /
&THCP    XYZ=6.2,12.2,1.5,    QUANTITY='GAUGE_HEAT_FLUX',    IOR=-2,
LABEL='Right Wall' /
&THCP   XYZ=6.2,12.2,1.5,   QUANTITY='INCIDENT_HEAT_FLUX',   IOR=-2,
LABEL='Right Wall' /
&THCP    XYZ=6.2,12.2,1.5,    QUANTITY='WALL_TEMPERATURE',    IOR=-2,
LABEL='Right Wall' /

&THCP    XYZ=0.2,6.2,1.5,    QUANTITY='RADIATIVE_FLUX',    IOR=+1,
LABEL='Back Wall' /
&THCP    XYZ=0.2,6.2,1.5,    QUANTITY='CONVECTIVE_FLUX',    IOR=+1,
LABEL='Back Wall' /
&THCP  XYZ=0.2,6.2,1.5,  QUANTITY='HEAT_FLUX',  IOR=+1,  LABEL='Back
Wall' /
&THCP    XYZ=0.2,6.2,1.5,    QUANTITY='GAUGE_HEAT_FLUX',    IOR=+1,
LABEL='Back Wall' /
&THCP   XYZ=0.2,6.2,1.5,   QUANTITY='INCIDENT_HEAT_FLUX',   IOR=+1,
LABEL='Back Wall' /
&THCP    XYZ=0.2,6.2,1.5,    QUANTITY='WALL_TEMPERATURE',    IOR=+1,
LABEL='Back Wall' /

&THCP     XYZ=7.7,4.7,3,     QUANTITY='RADIATIVE_FLUX',     IOR=-3,
LABEL='Ceiling' /
&THCP     XYZ=7.7,4.7,3,     QUANTITY='CONVECTIVE_FLUX',     IOR=-3,
LABEL='Ceiling' /
&THCP XYZ=7.7,4.7,3, QUANTITY='HEAT_FLUX', IOR=-3, LABEL='Ceiling'
/
&THCP     XYZ=7.7,4.7,3,     QUANTITY='GAUGE_HEAT_FLUX',     IOR=-3,
LABEL='Ceiling' /
&THCP    XYZ=7.7,4.7,3,    QUANTITY='INCIDENT_HEAT_FLUX',    IOR=-3,
LABEL='Ceiling' /
&THCP     XYZ=7.7,4.7,3,     QUANTITY='WALL_TEMPERATURE',     IOR=-3,
LABEL='Ceiling' /

&THCP XYZ=12.3,3.2,2.95, QUANTITY='TEMPERATURE', LABEL='T1a' /
```

```
&THCP XYZ=12.3,3.2,2.60, QUANTITY='TEMPERATURE', LABEL='T2a' /
&THCP XYZ=12.3,3.2,2.25, QUANTITY='TEMPERATURE', LABEL='T3a' /
&THCP XYZ=12.3,3.2,1.90, QUANTITY='TEMPERATURE', LABEL='T4a' /
&THCP XYZ=12.3,3.2,1.55, QUANTITY='TEMPERATURE', LABEL='T5a' /
&THCP XYZ=12.3,3.2,1.20, QUANTITY='TEMPERATURE', LABEL='T6a' /
&THCP XYZ=12.3,3.2,0.85, QUANTITY='TEMPERATURE', LABEL='T7a' /
&THCP XYZ=12.3,3.2,0.50, QUANTITY='TEMPERATURE', LABEL='T8a' /

&THCP XYZ=12.3,3.2,2.95, QUANTITY='VELOCITY', LABEL='V1a' /
&THCP XYZ=12.3,3.2,2.60, QUANTITY='VELOCITY', LABEL='V2a' /
&THCP XYZ=12.3,3.2,2.25, QUANTITY='VELOCITY', LABEL='V3a' /
&THCP XYZ=12.3,3.2,1.90, QUANTITY='VELOCITY', LABEL='V4a' /
&THCP XYZ=12.3,3.2,1.55, QUANTITY='VELOCITY', LABEL='V5a' /
&THCP XYZ=12.3,3.2,1.20, QUANTITY='VELOCITY', LABEL='V6a' /
&THCP XYZ=12.3,3.2,0.85, QUANTITY='VELOCITY', LABEL='V7a' /
&THCP XYZ=12.3,3.2,0.50, QUANTITY='VELOCITY', LABEL='V8a' /

&THCP XYZ=12.3,9.2,2.95, QUANTITY='TEMPERATURE', LABEL='T1b' /
&THCP XYZ=12.3,9.2,2.60, QUANTITY='TEMPERATURE', LABEL='T2b' /
&THCP XYZ=12.3,9.2,2.25, QUANTITY='TEMPERATURE', LABEL='T3b' /
&THCP XYZ=12.3,9.2,1.90, QUANTITY='TEMPERATURE', LABEL='T4b' /
&THCP XYZ=12.3,9.2,1.55, QUANTITY='TEMPERATURE', LABEL='T5b' /
&THCP XYZ=12.3,9.2,1.20, QUANTITY='TEMPERATURE', LABEL='T6b' /
&THCP XYZ=12.3,9.2,0.85, QUANTITY='TEMPERATURE', LABEL='T7b' /
&THCP XYZ=12.3,9.2,0.50, QUANTITY='TEMPERATURE', LABEL='T8b' /

&THCP XYZ=12.3,9.2,2.95, QUANTITY='VELOCITY', LABEL='V1b' /
&THCP XYZ=12.3,9.2,2.60, QUANTITY='VELOCITY', LABEL='V2b' /
&THCP XYZ=12.3,9.2,2.25, QUANTITY='VELOCITY', LABEL='V3b' /
&THCP XYZ=12.3,9.2,1.90, QUANTITY='VELOCITY', LABEL='V4b' /
&THCP XYZ=12.3,9.2,1.55, QUANTITY='VELOCITY', LABEL='V5b' /
&THCP XYZ=12.3,9.2,1.20, QUANTITY='VELOCITY', LABEL='V6b' /
&THCP XYZ=12.3,9.2,0.85, QUANTITY='VELOCITY', LABEL='V7b' /
&THCP XYZ=12.3,9.2,0.50, QUANTITY='VELOCITY', LABEL='V8b' /

&PL3D  DTSAM=72,  WRITE_XYZ=.TRUE.,  QUANTITIES='TEMPERATURE','U-
VELOCITY', 'V-VELOCITY', 'W-VELOCITY', 'extinction coefficient', /
```